Adaptive Single To Three-Phase Converter Using Variable Passive Elements

By

Sh.I Ashrafi-Monfared

Thesis submitted to the
Department of Electrical and Electronics Engineering,
University of Cape Town,
In fulfillment of the requirements for the degree of
MASTER OF SCIENCE

Acknowledgments

The author would like to thank the following people for the assistance and contribution towards the completion of this project.

Mr. Malengret, for the knowledge, ideas, and time spent with the project.
Mr. A.Khan, for assistance and time given for long discussions not always related to his field of specialty.
Mr. C.Wozniak, for technical support on instrumentation.
Mr. Z.B Gxikixa, Head of our department at Eastern-Cape Technikon, for providing me with a dedicated laboratory and the necessary equipment to complete the work.
Mr D. Gertze, my dedicated colleague, for introducing me to Virtual-Instrumentation and allowing me the use of his personal hardware.
Finally, my wife, for moral support and patience throughout the slow stages of preparation of this report.

Terms of Reference

This thesis was supervised by Mr. M.Malengret, senior lecturer at the department of electrical engineering at the University of Cape-Town. The scope and objectives of the work are:

a) To study and conduct a literature survey on the theory of three-phase unbalanced voltages including causes and long-term effects on loads.
b) To further develop the above theory for the specific case of extreme voltage unbalance. This would be in the complete absence of two phases, which would lead to conversion of a single to three-phase supply.
c) To apply the above theory to a small 3-phase centrifugal pump fed by a single-phase supply.
d) To include modern techniques of 3-phase load parameter measurement such as conductance and succeptances.
e) To develop a solution for the above, based on passive elements.
f) To design and construct a general adaptive controller suitable for centrifugal pumps.
g) To provide simulated and experimental results for the above objectives.

Synopsis

The main objective of this thesis is to investigate the possible methods of converting a single-phase supply to a three-phase balanced voltage, using passive elements. Three distinct methodologies have been developed, each with its own merits and constructed prototypes. The seven chapters of this thesis contain large amount of non-real time and real-time simulated results. These results were then compared with the experimental results.

In chapter one, a brief review of past and presently available single to three-phase technology is presented. The methods of operation, some advantages and disadvantages and finally some prices have been included.

Chapter 2 starts with the theory behind voltage asymmetry. The conditions for voltage balancing in terms of load parameters are deduced. After confirmation of the theory using simulations, several techniques for producing variable shunt succeptances have been explored, among which the old saturable reactor has been paid particular attention to. For each case, experimental results in the form of oscilloscope captured waveforms and/or graphs, have been shown. In all of the above methods, harmonic distortion is a critical issue and therefore it has been meticulously investigated.

Chapter 3 describes the construction of the proposed converter for a small centrifugal pump. Feedback control strategy with two voltages and two current feed back loops were used. After the tests and with better understanding on the effect of the loads characteristics on the controller, it was realized that in such application a simpler method could be adapted. A simple solution is offered.

Chapter 4 focuses on a general simulation technique for the measurement of load parameters and the corresponding size and nature of passive elements required to establish and maintain a three-phase balanced voltage across a variable load.

Chapter 5 deals with prototyping an adaptive converter. The converter is built with discrete components and is capable of dynamically monitoring the load parameters such as average active and reactive power, conductance, and succeptance. It finally generates two DC voltages proportional to the size of the passive elements required by the converter. The prototype has been tested with a variety of loads. A comprehensive set of experimental values for each type of load has been presented. The results obtained from the adaptive converter compare well with those using standard RMS equipment.

Chapter 6 explores a completely different approach to the problem of modeling and prototyping. This method is known as "Model-based Design". In the absence of the necessary instruments and other hardware, the Real-Time Simulation has proved extremely effective. In the low frequency applications such as supply harmonic analysis, exact duplicates of the supply voltage or currents have been imported into the MatLab powerful simulation environment. A variety of Fourier analysis and other mathematical manipulations have then been done successfully. In the author's opinion, this is the ultimate prototyping technique and a true eye-opener in the field of design and analysis. Various software such as Mat-lab, Circuit-Maker, Mathematica and Excel have been utilized. All designs and captured results are the author's own work.

Content

Chapter 1

Chapter 2

Chapter 3

Chapter 4

Chapter 5

Chapter 6

Chapter 7

List of figures

Chapter 1

Chapter 2

Chapter 3

Chapter 4

Chapter 5

Chapter 6

Chapter 7

Appendices

List of abbreviations

N_r	shaft speed (RPM)
N_s	synchronous speed (RPM)
S	slip
G	load conductance/phase (S)
B	load succeptance/phase (S)
B_{C1}	first converter succeptance (S)
B_{C2}	second converter succeptance (S)
R	load resistance/phase (Ω)
X	load reactance/phase (Ω)
R_m	motor winding resistance/phase (Ω)
X_m	motor winding reactance/phase (Ω)
L_C	converter inductance (H)
C_C	converter capacitance (uF)
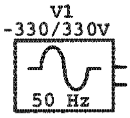	Supply voltage with indicated peak-peak and /or RMS value
μ	permeability (H/m)
A	core cross section area (m^2)
N	number of turns
L	inductance (H)
l	average length of the flux path whithin the core (m)

Chapter 1

Introduction

In the past 30 years, sufficient evidence has emerged that electrification of remote areas is done more economically using single-phase supply. This is mainly due to the high cost of three-phase power distribution such as power lines, transformers, breakers, and other accessories involved. For example the costs quoted by ESKOM (East-London)[13] for 132 kV lines using steel poles and aluminum conductors with steel-reinforcement range from R270, 000 to R300, 000/Km. At 22 kV these costs are reduced to R75, 000. In most cases the end-user power requirement does not justify the installation costs.

Two scenarios can be considered. Case one would be the possibility of converting the supply voltage from single phase to a three-phase at the output of any single-phase distribution transformer. A two or three variable shunt passive-element converter could provide a balanced three-phase supply. The value of each one of such passive elements depends on the load impedance per phase and the only practical way of measuring the load impedance in real time is by using the line currents and voltages. The difficulty in maintaining such balance in the supply would then arise due to the fact that a combination of single and three-phase loads feeding from such transformer is hardly ever balanced. The accurate modeling of these loads through continuous measurement of the line currents and voltages has so far been mathematically impossible.

Second scenario is the allocation of a single to three-phase converter to individual three-phase loads. Today, there are many applications in rural areas, local industries, and domestic appliances where a three-phase induction motor would be a much better choice than a single-phase motor. Unavailability of three-phase power forces the consumer to use his load with a single-phase driving motor. Typical applications are bakeries, woodworking, small machine shops, centrifugal swimming-pool pumps, and general water pumping, all of which would work far more efficiently using three-phase driving motors. It is common knowledge that torque, efficiency, durability, and general performance of three-phase motors are by far superior to single-phase motors.

The conversion of a single to three-phase voltage through different approaches has been available for a long time. For a user with requirements such as speed control, acceleration and deceleration time adjustment and other features in mind, converters with micro-controllers or DSPs as "brain" and fast switches such as IGBTs as "muscles", are available at a high price. However, for a simple application such as a centrifugal pump with the torque characteristics of $(T \propto N^2)$, the demanded torque from the driving motor is usually either for no-load or full-load conditions. Therefore, there is hardly any need for the facilities offered by the modern converters. A simple robust and affordable solution to the single to three-phase conversion would be of great advantage.

In view of the above, the objectives of this thesis are to, primarily design a simple two-element converter specifically for a centrifugal pump of a specific kW rating and then construct a more general controller for pumps and other applications. Furthermore, it is intended to ensure that from the supply power point of view, the injected pollution (harmonics) generated by such converter is kept to a minimum and compliance with the national standards is adhered to.

Literature review

Prior to the commercialization of the solid-state semi-conducting devices around 1975, the conventional methods for the conversion of a single-phase to three-phase voltage were the use of rotary converter or autotransformer converters. A brief review of each method is presented.

Rotary Converters

The construction of a rotary converter is similar to that of a three-phase motor. The three-phase stator winding receives line and neutral between two sets of windings. Additional capacitor is connected across the line and the third set of winding. This introduces a phase shift and hence a starting torque is generated. As the rotor rotates, the emf induced in each rotor coil sets up a field which induces a voltage in the stator winding with 120° phase shift.

The magnitude of the output voltage is limited to the input line to neutral voltage and so it is similar to the static capacitor converter. Phase currents are much less load dependent and hence multi-motor operation is possible.

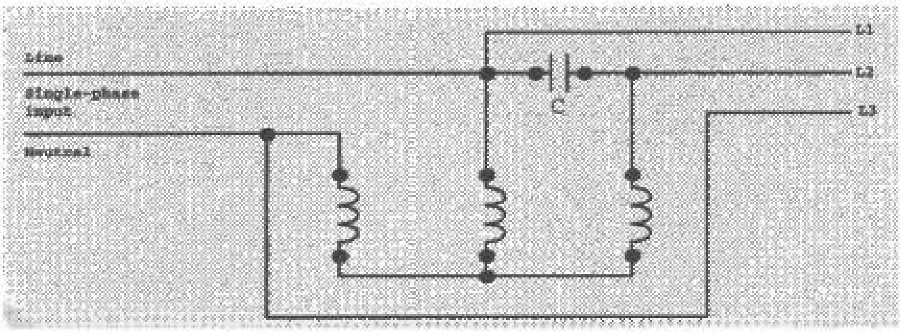

Fig:1.1 Rotary Converter

Static Capacitor Converters

These converters use the 90° phase shift introduced by the capacitor to set up a second magnetic field which interacts with the main field and hence initiates a starting and running torque. Their main drawbacks are:

- The size of the capacitor used is selected in proportion to the current drawn by the load and hence the mechanical load driven by the motor. This is why these converters are not suitable for motors above 1.0 KW. In particular, a motor with variable load will never reach a balanced situation. The smaller motors make use of a starting capacitor, which is disconnected by a centrifugal switch once the motor has reached its rated speed.
- The output line-line voltage cannot exceed the input line to neutral value and hence only the three-phase 240 Volts line-line induction motors can use this type of converter.

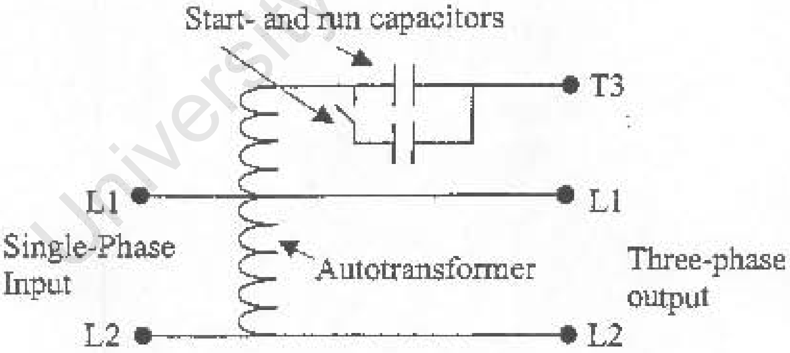

Fig: 1.2 Static capacitor converter

Recent Developments

One of the first attempts to design and construct a two element single to three-phase converter using passive elements was by S.B Dewan[1]. He used phase control and back-to-back thyristors to control the effective value of the converter reactances.

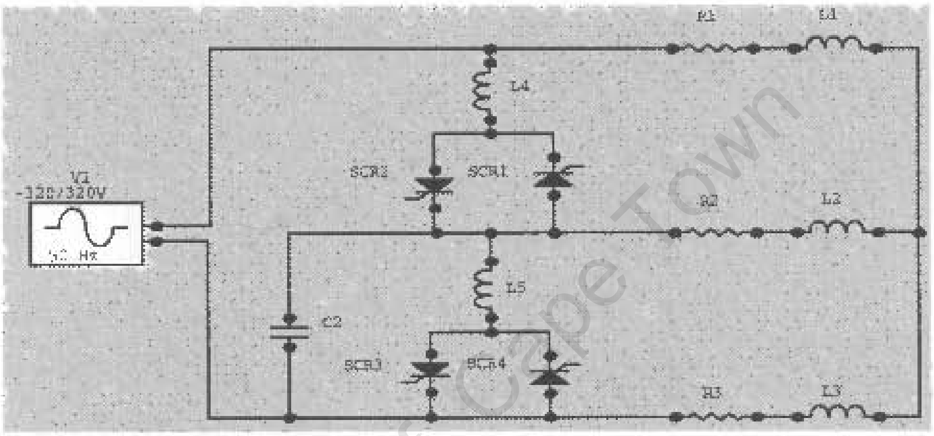

Fig: 1.3 Single to three-phase converter using phase control

A disadvantages of this method is that the design specifications are for star connected static loads only. The design also assumes that the first passive element (L4), is always inductive. This is not always true.

The next converter of interest and commercially supplied of this kind was by P.G.Holmes[2]. His method of varying the passive elements of the converter is similar to that of Dewan with the difference that the load can be connected in delta, which is the case for majority of three-phase induction motors.

The converter is capable of running multiple loads in parallel, taking into account the starting inrush currents. The only disadvantage is that assessing the load parameters and generation of driving signals for the thyristors back-to-back and the chopper transistor (Q_1), is achieved through direct slip measurement. For a single or a group of motors situated far from each other, each motor would have to be equipped with a taco-generator or a shaft encoder which would prove complex and costly.

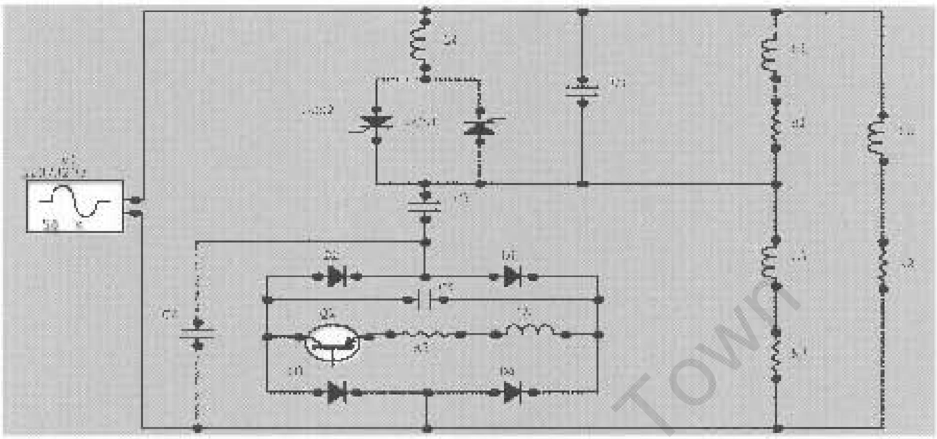

Fig: 1.4 Single to three-phase converter using direct slip measurement

Solid-State digital converters

With the advancement of semi-conducting devices, commercial converters using various power electronic topologies are available and can make various kinds of voltage conversion, including single to three-phase conversion possible. The techniques primarily involve rectifying the input AC voltage and then using different switching methods, half or full-bridge inverters are used to convert the rectified voltage to a single or three-phase AC out put voltage. Following are some of the widely used schemes.

Three-phase full bridge inverters

These inverters like their single-phase counterparts work in switch-mode operation and are applicable to three-phase motors and UPS systems. In the case of AC induction motors, the object is to generate an output AC voltage, which is controllable in magnitude and frequency with a fixed ratio between them. Three-phase motor's efficiency is highly improved using this feature. Depending on the design of the converter and the application, one, two or four quadrant operation is possible. Two types of three-phase inverters are voltage-source and current source inverters. The former is used with small and medium size motors whereas the latter is more suitable for large size AC drives.

Sinusoidal pulse width modulation (SPWM) inverters use uncontrolled rectification for AC-DC conversion. The bus voltage is then switched through a full three-phase "H" bridge to the load. The switching signals are provided by micro-controllers or DSP's, which facilitate a manual or automatic change of frequency ratio and modulation index in order to change the frequency as well as the rms value of the output voltages.

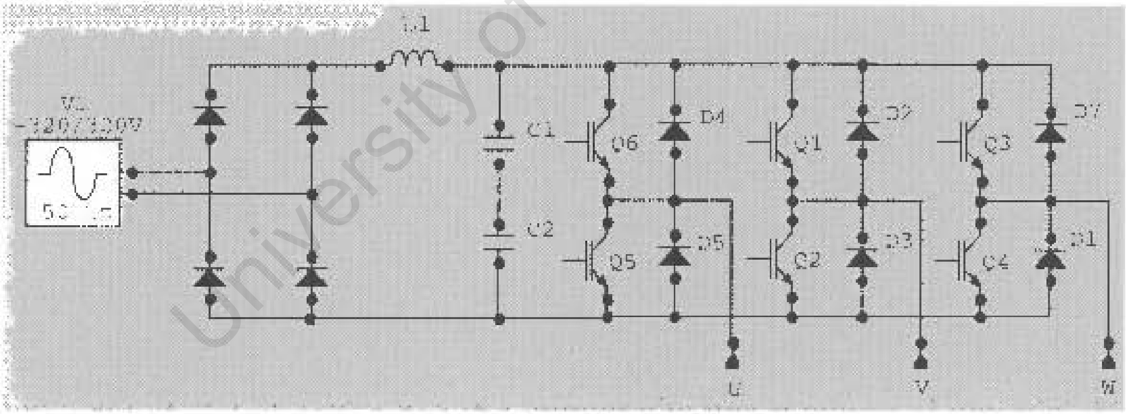

Fig: 1.5 IGBT inverter

Due to non-sinusoidal nature of the current drawn by the rectifier, these inverters work at low power factors and hence demand high currents from the utility. With the new standards on minimum harmonics set by ANSI, NEMA and ICE being enforced, active current shaping or sufficient filtering at the input has become a necessity. Some of the new drives, shown in fig:1.6, have the additional boost switch and a blocking diode.

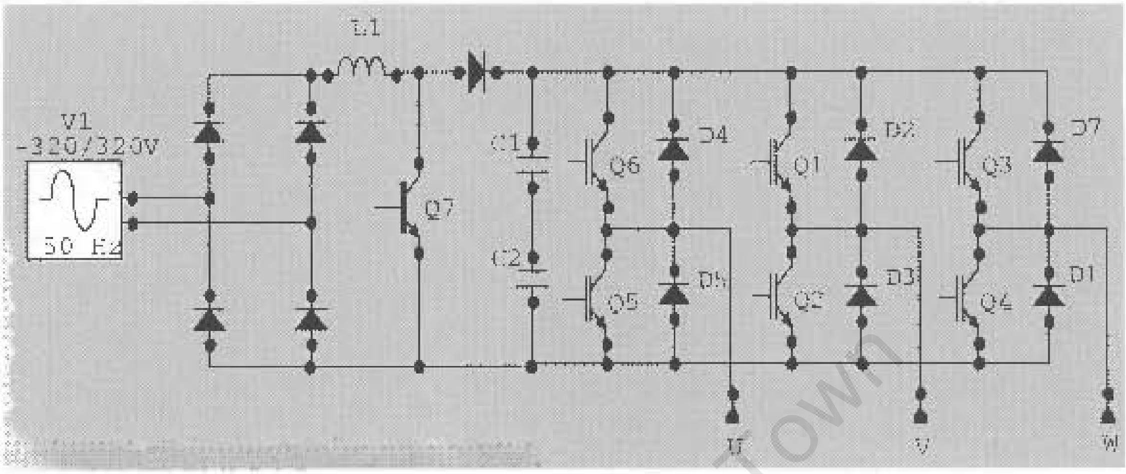

Fig: 1.6 Inverter with current shaping rectifier

Among various other techniques of single to three-phase conversion, standard power configuration is the IGBT, PWM rectifier/inverter system. In this system, the rectifying section of the converter is a two-pulse controlled rectifier, which feeds the bus voltage and then the inversion takes place. The control system is more complex which naturally adds to the cost. See fig: 1.7.

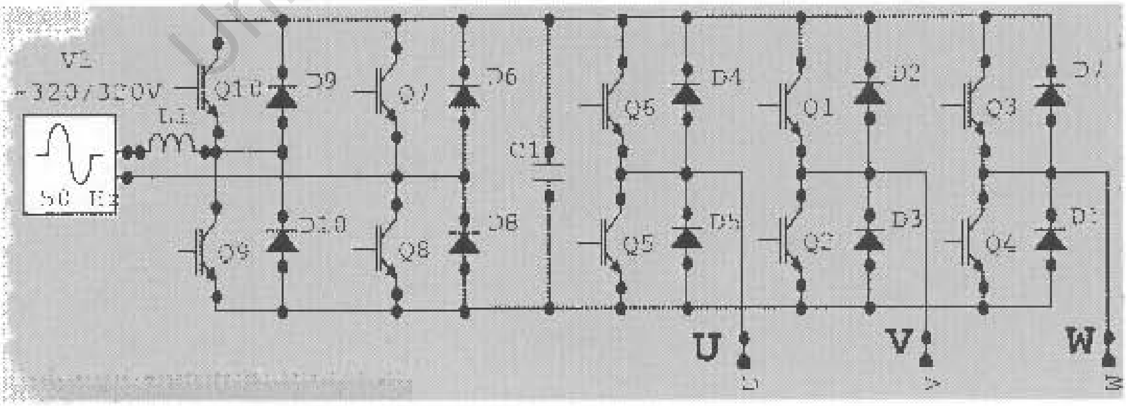

Fig: 1.7 IGBT inverter with PWM rectifier/inverter

Resonant Converters

In switch mode converters, the component used as switch is subjected to high switching stress that increases linearly with the frequency of the PWM. This mode of operation also generates EMI caused by large di/dt and dv/dt at the instant of switching. To minimize these problems, a variety of resonant converter topologies have been introduced. The common denominator for all the topologies and switching strategies is based on some form of LC resonance with zero voltage and/or zero current switching facility. Mohan[3] categorizes these converters into four groups;

a) Load-resonant converters,
b) Resonant-switch converters,
c) Resonant-dc-link converters,
d) High-frequency-link integral-half-cycle converters.

Each of the above converters has it's own merits and forms a separate case of study.

In general the choice between the above modern converters and passive element converters should depend on the following factors,

a) the size of the motor in use,
b) the nature of load, its operating conditions and the torque-slip characteristics,
c) the extra features required from the converter.

Clearly, one would have to pay for extra features offered by modern converters. Some suppliers have quoted R2100.0 for 0.55 kW and R2500.0 for 1.1kW rating drives. It will be shown in this thesis that, for large number of applications, the alternative two-element passive converters will be far more cost effective.

Chapter 2

2.1 Compensation and unbalance voltages

In electrical power engineering, "Compensation" is defined and applied to two types of practical problems. The first is the load compensation where the requirements are usually to cancel or minimize the reactive power demand of large and fluctuating industrial loads, such as electric arc furnaces and rolling mills, etc and to balance the real power drawn from the supply lines. The best location for such compensators is at the load terminals.

The second type of compensation relates to voltage regulation of transmission lines at a given terminal with strong possibility of changes in load conditions, which normally causes voltage level to change up to 15% of the nominal values. In practice, static shunt capacitors and reactors are switched in, to compensate for such under-voltage or over-voltage lines.

By definition, voltage unbalance is a measure of the differences between phase-phase voltages or the displacement angle between phases, or both.

Voltage unbalance is represented as the relationship between the positive and negative sequence set of voltages. By IEC definition:

$$UB = \frac{\text{Negative Phase Sequence Voltages}}{\text{Positive Phase Sequence Voltages}} * 100\% \qquad \text{(Eq:2.1.1)}$$

$$UB = \sqrt{\frac{1-\sqrt{3-6\beta}}{1+\sqrt{3-6\beta}}} \qquad \text{(Eq:2.1.2)}$$

where $$\beta = \frac{V^4_{RY} + V^4_{YB} + V^4_{BR}}{\sqrt{V^2_{RY} + V^2_{YB} + V^2_{BR}}} \qquad \text{(Eq:2.1.3)}$$

Bearing in mind that:

$$\text{Positive phase sequence} = \frac{1}{3}(V_{RY} + a\,V_{YB} + a^2 V_{BR}) \qquad \text{(Eq:2.1.4)}$$

$$\text{Negative phase sequence} = \frac{1}{3}(V_{RY} + a^2 V_{YB} + aV_{BR}) \qquad \text{(Eq:2.1.5)}$$

$$\text{Zero phase sequence} = \frac{1}{3}(V_{RY} + V_{YB} + V_{BR}) \qquad \text{(Eq:2.1.6)}$$

Where "a" operator is $1\angle 120°$.

The main cause of voltage asymmetry is the uneven distribution of the single-phase loads in conjunction with the impedance of the transmission lines. A complete compensation in term of the symmetrical line current components should then include:

a) Elimination of the negative-sequence current components, for voltage balancing,

b) Elimination or minimization of the reactive part of the positive-sequence component, for power factor compensation.

Voltage unbalance shows itself most often in the premature burnout of the 3-phase electric motors. Most manufacturers specify a maximum voltage unbalance of 2%, which is the figure allowed under NRS 048, for a three-phase system. This is relaxed to 3% in areas where the majority of the loads are single phase.

Fig: 2.1.1 shows a Real-Time Simulation model for the measurement of the positive and negative-sequence components of the voltages or currents in a 3-phase system. This model will be discussed and used in chapter 6.

An important observation is that the condition specified in Eq: 2.1.10 does not imply that the actual value of the load phase admittances have to be necessarily the same. It simply implies that for a three-phase balanced voltage to supply a balanced current, the vector sum of the load admittances must be zero.

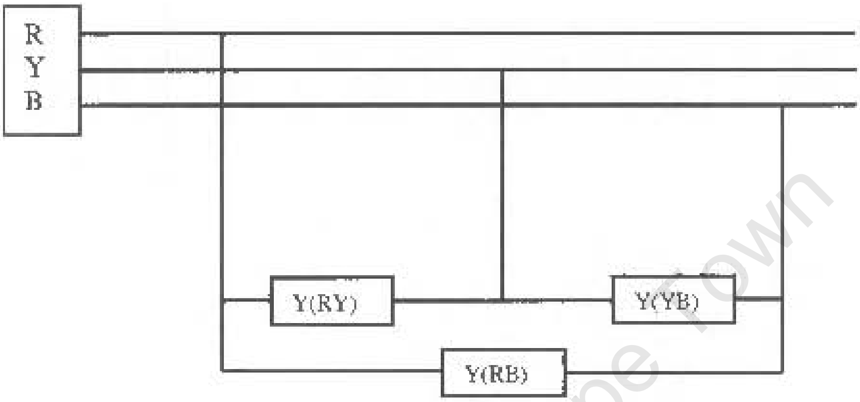

Fig: 2.1.2 Delta connected admittances representing a three-phase load

If the vector sum of the load admittances is not zero, then the load is unbalanced. Addition of at least two parallel admittances (Y_{C1} and Y_{C2}), with two phases of the load can restore the balance. Fig: 2.1.3 shows the balancing effect.

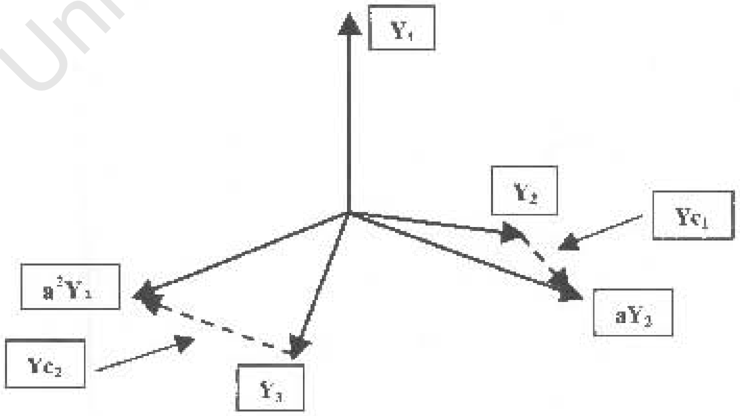

Fig: 2.1.3 Phasor diagram for balancing load admittances

From a three-phase balanced load point of view, provided there is a particular relationship between the load conductance and succeptance, the supply can be "seen" as symmetrical. This can be proved as follows.

In Eq: 2.1.10, if two of the admittances are selected and resolved to their real and imaginarily components,

$$G_1 + jB_1 = (-\frac{1}{2} + j\frac{\sqrt{3}}{2}).(G_2 + jB_2) \qquad \text{(Eq:2.1.11)}$$

equating the real parts:

$$G_1 = -\frac{1}{2}G_2 - \frac{\sqrt{3}}{2}B_2$$
$$B_2 = \frac{-2G_1 - G_2}{\sqrt{3}} \qquad \text{(Eq:2.1.12)}$$

equating the imaginary parts:

$$B_1 = \frac{\sqrt{3}}{2}G_2 - \frac{1}{2}B_2 \qquad \text{(Eq: 2.1.13)}$$

combining Eq:2.12 and 2.13,

$$B_1 = \frac{2G_2 + G_1}{\sqrt{3}} \qquad \text{(Eq: 2.1.14)}$$

For a balanced load such as a three-phase induction motor: $G = G_1 = G_2 = G_3$.

Hence equations 2.1.12 and 2.1.14 can be simplified to:

$$B_1 = +\sqrt{3}\,G$$
$$B_2 = -\sqrt{3}\,G \qquad \text{(Eq:2.1.15)}$$

The above equations are the conditions for a 3-phase balanced load to be seen balanced at the terminals.

Therefore the required succeptances of a two-element converter can be calculated to be,

$$B_{c1} = +\sqrt{3}\,G - B_1$$
$$B_{c2} = -\sqrt{3}\,G - B_2 \qquad \text{(Eq:2.1.16)}$$

where $B = B_1 = B_2$ are the load phase succeptances.

Converting G and B to the equivalent resistance and reactance values:

$$B_{c1} = +j\sqrt{3}\left(\frac{R}{R^2+X^2}\right) + j\left(\frac{X}{R^2+X^2}\right) \qquad \text{(Eq:2.1.17)}$$

$$B_{c2} = -j\sqrt{3}\left(\frac{R}{R^2+X^2}\right) + j\left(\frac{X}{R^2+X^2}\right) \qquad \text{(Eq:2.1.18)}$$

Finally, equations 2.1.17 and 2.1.18 can be summarized to:

$$B_{c1} = j\left(\frac{\sqrt{3}R + X}{R^2+X^2}\right) \qquad \text{(Eq:2.1.19)}$$

$$B_{c2} = j\left(\frac{-\sqrt{3}R + X}{R^2+X^2}\right) \qquad \text{(Eq:2.1.20)}$$

It can be seen from Eq:2.1.20 that as long as the term $(-\sqrt{3}R + X)$ is negative, B_{C2} remains inductive. However, once the term's value is positive, B_{C2} will change sign and therefore becomes capacitive.

The change of sign occurs at $X = \sqrt{3}\,R$, which indicates,

$$\text{Cos ö} = \text{Cos } [\tan^{-1}(\frac{X}{R})] = 0.5 \qquad \text{(Eq:2.1.21)}$$

In general it can be summarized that with the load power factor of 0.5 or less, both converter branches will be capacitive elements.

Next section is an investigation in to a three-phase swimming-pool pump running from a single-phase supply.

2.2 Three-phase water pump

In order to test the principle established previously, a small water pump was used. The whole system consists of a tank, a no-return valve, flow meter and a centrifugal pump driven by a three-phase squirrel cage induction motor. The ratings of the driving motor are:

V = 230/380 V (delta/star), I = 3.3/1.9 A, P = 750 W,

N_r = 2810 rpm, N_S = 3000 rpm, S = 6.33%

The starting point for the assessment of the squirrel-cage motor used with the pump is to establish an equivalent circuit diagram. The IEEE recommended circuit diagram is shown in fig: 2.2.1.

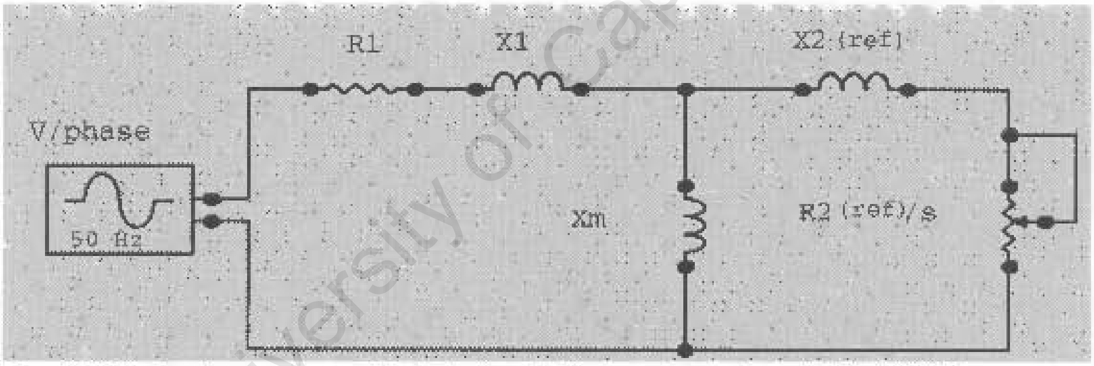

Fig: 2.2.1 Induction motor equivalent circuit diagram recommended by IEEE

The letters R and X have their normal meanings where the subscripts 1 and 2 refer to the stator and rotor windings respectively.

Standard no-load and locked-rotor test is used to calculate the values of the components for the above circuit diagram. These values are,

V/phase = 230.0 V, I_L = 3.10 A, P = 980.0 W

R_1 = 8.6 Ω, X_1 = 7.7 Ω, X_m=198.65 Ω,

$X_{2(ref)}$ = 7.7 Ω, $R_{2(ref)}/S$ = 9.4/S

The equivalent circuit diagram can be further reduced to an equation representing the impedance/phase of the motor as a function of slip.

$$\text{Z/phase} = \frac{-1529.6S + j1867.3}{9.4 + j206.4S} + 8.6 + j7.7 \qquad \text{(Eq: 2.2.1)}$$

It is interesting to see how theoretically the motor parameters vary with the speed. The results are plotted in fig: 2.2.2.

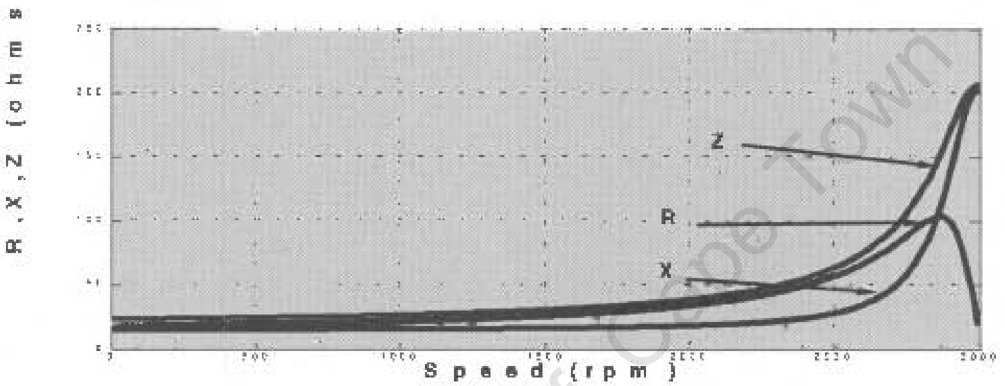

Fig: 2.2.2 Variation of motor parameters/phase with speed

The values of the motor parameters seem to change very slowly up to about 2000 rpm and then change rapidly at speeds close to rated speed. These curves resemble the torque/slip characteristics of the pump ($T \propto N^2$).

In the situation where the full physical load is available, perhaps a more accurate way is to measure the current, voltage and the power per phase at no-load and full-load conditions and calculate the exact values of motor parameters for both conditions. Changes of parameters due to temperature rise are ignored.

The measurements lead to two sets of values for the motor parameters. Fig: 2.2.3(a) and (b), show the equivalent circuit diagrams for start-up and full-load conditions.

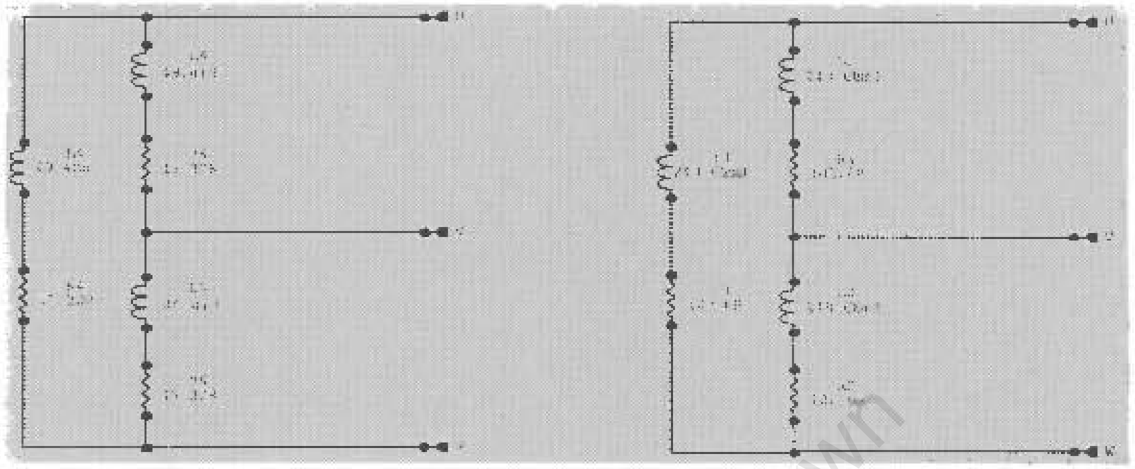

(a) (b)

Fig: 2.2.3 Equivalent circuit diagram for start-up and full-load conditions

These values are then used to determine the range of values for passive converter elements.

Using the inverted version of Eq: 2.1.19 and 2.1.20,

$$L_C = -j\left(\frac{R_m^{\,2} + X_m^{\,2}}{\sqrt{3}R_m + X_m}\right)$$

$$C_C = +j\left(\frac{R_m^{\,2} + X_m^{\,2}}{\sqrt{3}R_m + X_m}\right) \qquad \text{(Eq: 2.2.2)}$$

R_m and X_m refer to the motor reactance and resistance per phase. With the full load speed of 2854 rpm, the range of motor slip is from 1 to 4.87%. Therefore, the converter element values have to change according to the above range of motor slip. A Matlab program shows the following variation of converter capacitive element [appendix 1.1].

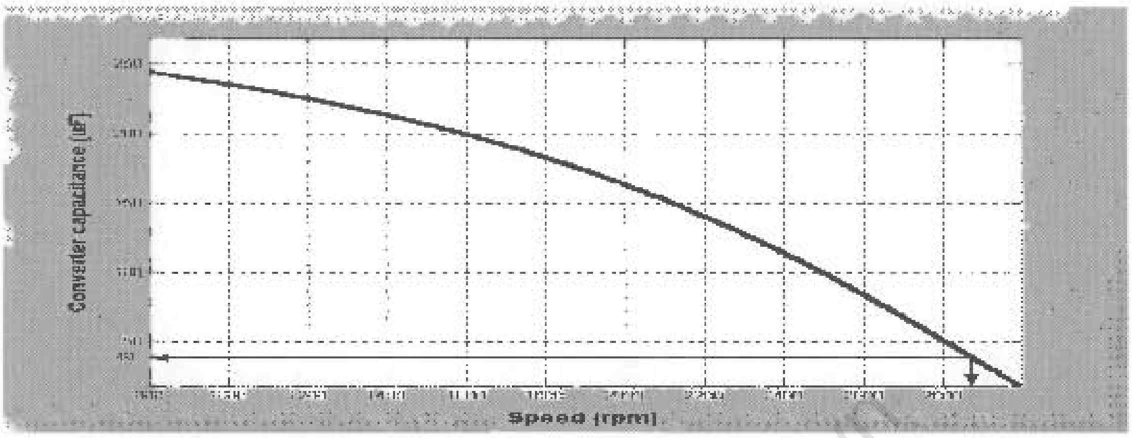

Fig: 2.2.4 Variation of converter capacitive element with speed

Taking the inertia of the motor-pump in to account, the above variation can be assumed to be approximately inversely linear. The range of converter capacitance is 250 uF at start up down to 40 uF at full-load.

The variation of the converter inductive element with speed is quite different and somehow awkward to analyze. Fig: 2.2.5 shows that for a wide range of slip, the inductance of the converter remains almost constant and closer to the rated speed, it rises sharply to a maximum value of 3.0 Henry.

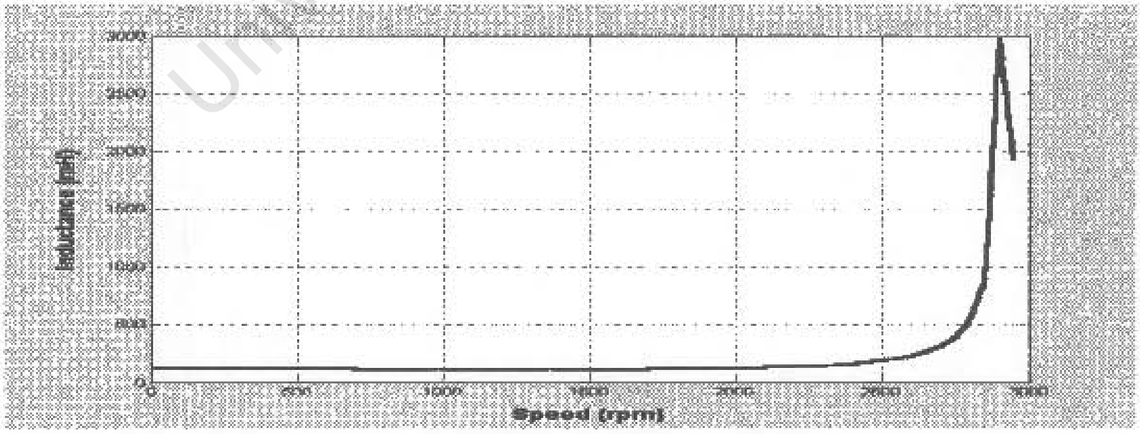

Fig: 2.2.5 Variation of converter inductive element with speed

For the range of speed, a converter inductance from 118 to 533 mH is required to keep a balanced supply voltage across the motor. The first set of simulated values for the motor parameters and the converter succeptances are shown in fig: 2.2.6.

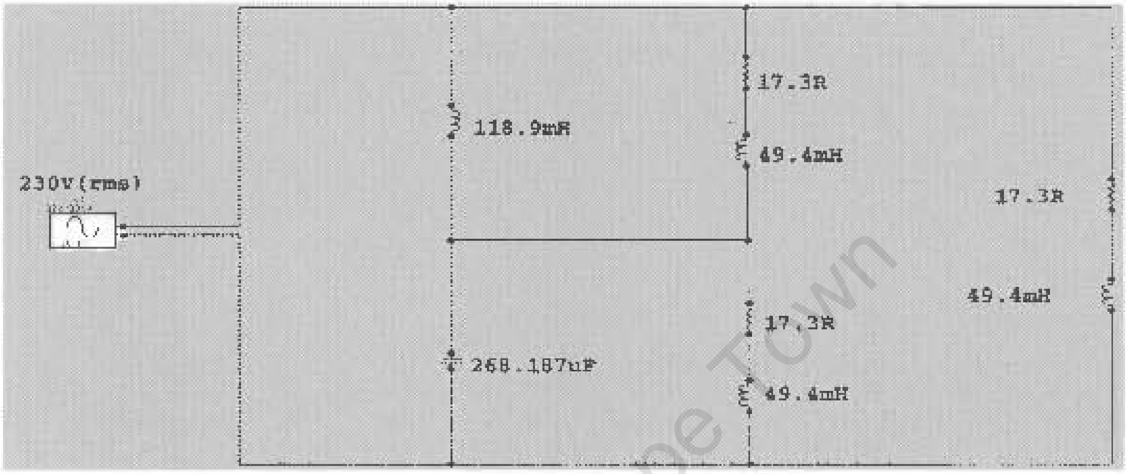

Fig: 2.2.6 Simulated values for the motor and converter elements at startup

The simulated current waveforms are shown in fig: 2.2.7.

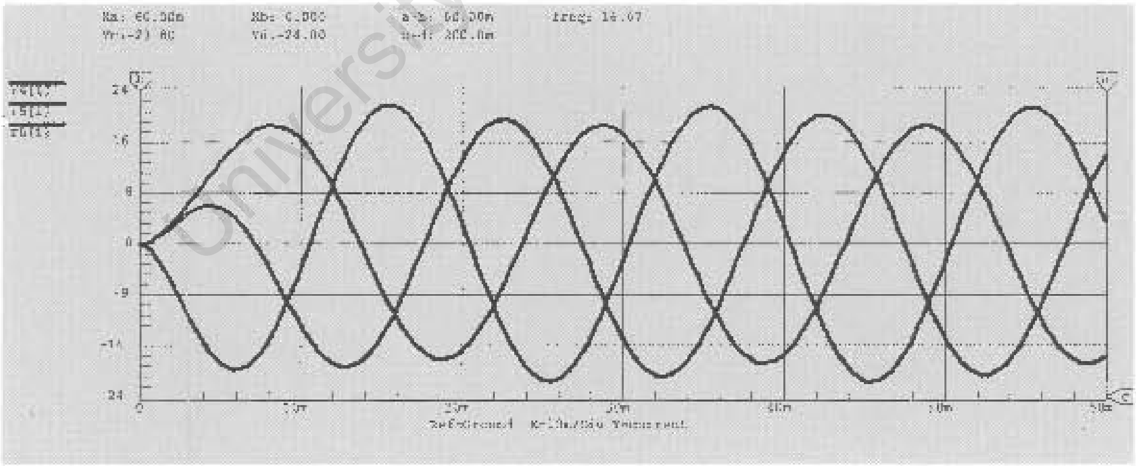

Fig: 2.2.7 Simulated load terminal voltages at start up

The full-load values can also be examined. The simulated values and waveforms are shown in fig: 2.2.8 and 2.2.9.

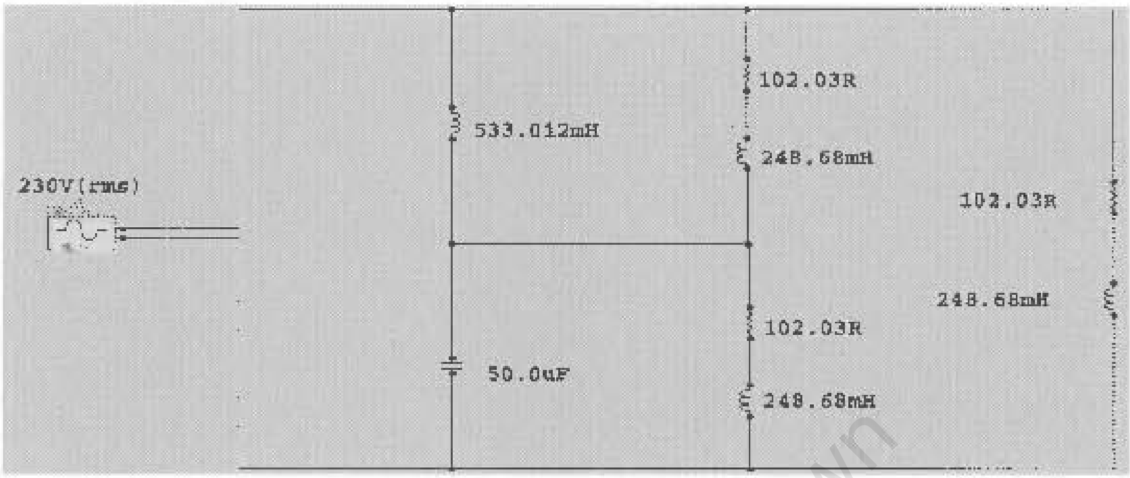

Fig: 2.2.8 Simulated values for the motor and converter elements at full-load

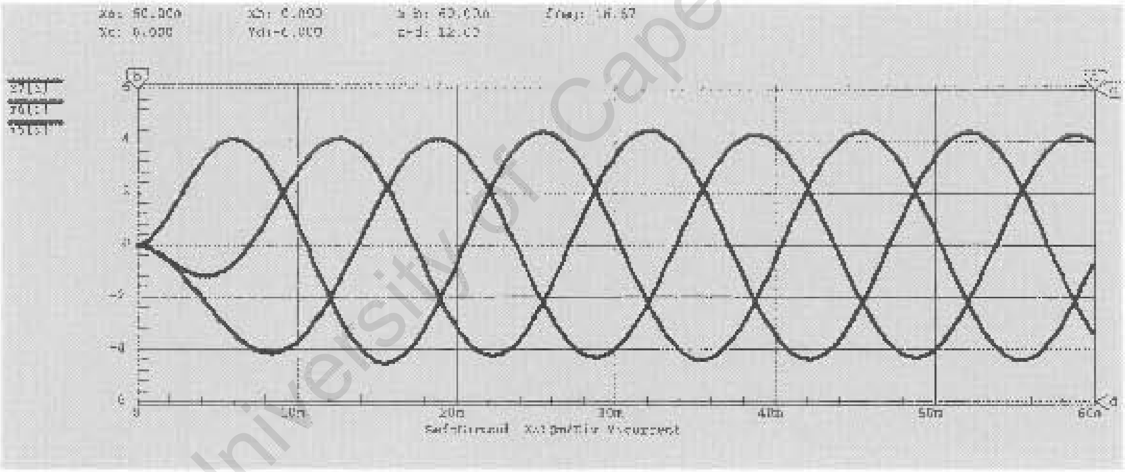

Fig: 2.2.9 Simulated load terminal voltages at full-load

With the range of converter elements for balancing the terminal voltages established, the next chapter will investigate various methods of producing variable sources of succeptance.

2.3 Variable Sources of Succeptance

Power authorities have traditionally used a variety of methods for VAR generation and/or voltage regulation. These are all basically, fixed or variable sources of reactance connected in single shunt, series or in three-phase, connected in star or delta across the main lines to serve one or both purposes mentioned earlier. The more popular techniques are listed in below,

a) Thyristor controlled inductor (TCI),
b) Thyristor controlled reactance (TCR),
c) Thyristor switched capacitor (TSC),
d) DC voltage-controlled choke, also known as saturable reactor,
e) synchronous condenser (phase shifter).

Reactive power compensation with thyristor-controlled inductors and shunt capacitors enable adaptive compensation at the cost of harmonic distortion increase. Harmonic distortions are further increased due to resonance with the supply system reactance.

A partial solution is to connect such reactors across the mains in delta to cancel out the effect of the triplet harmonics. Alternatively, if the thyristors are switched in 60° intervals, the current harmonics of the third order will mutually cancel in the supply current [7].

In three-phase compensation, if a compensator is not only used as a VAR generator, but also to balance the load voltage, it's branches have to be controlled independently and consequently, harmonics of 3rd order at relatively high RMS values are injected into the supply. Studies show that even some harmonics not present at symmetrical conditions, appear in systems with non-linear loads. For the purpose of this report, an extensive study of voltage and current harmonic distortions, generated by independently controlled two-element adaptive compensator, has been pursued.

For a two element adaptive converter to adapt and respond to the changes in load parameters, it's component's value must change accordingly and rapidly with the load parameters. Before considering the options on preferred sources of variable succeptance, a brief study of the supply voltage and it's harmonic content is required.

Generally, the supply voltage on premises with a large number of computers installed is expected to be abnormally flat at positive and negative peaks. This is simply due to the smoothing capacitors used in the power supplies charging up simultaneously and overloading the supply lines during the peak periods of the supply cycles.
The supply voltage at UCT versus the current through a 50.0uF capacitor is shown in fig:2.3.1.

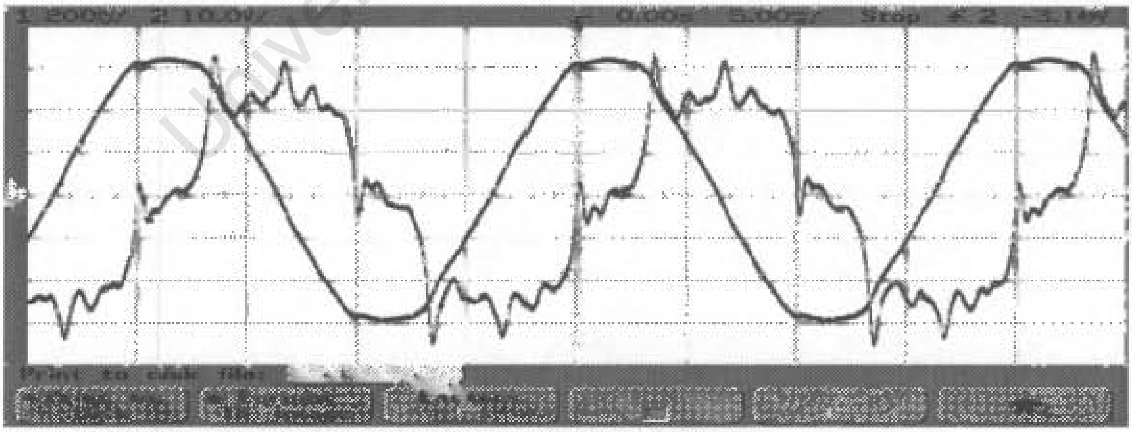

Fig: 2.3.1 Voltage/current waveforms for a 50 uF capacitor

The distortion in the current waveform can be explained as follows,

$$I_{nm}=V_{nm}n\,\omega C \qquad \text{(Eq: 2.3.1)}$$

Hence, for a range of harmonic orders in the supply voltage, the expression for the current waveform is:

$$i(t) = V_{1m}\omega C\sin(\omega t + \pi/2) + V_{2m}2\omega C\sin(2\omega t + \pi/2) + V_{3m}3\omega C\sin(3\omega t + \pi/2) + \ldots\ldots\ldots + V_{nm}n\omega C\sin(n\omega t + \pi/2) \qquad \text{(Eq: 2.3.2)}$$

$$i(t) = I_{1m}\sin(\omega t + \pi/2) + 2\,I_{2m}\sin(2\omega t + \pi/2) + 3\,I_{3m}\sin(3\omega t + \pi/2) + \ldots\ldots\ldots + nI_{nm}\sin(n\omega t + \pi/2) \qquad \text{(Eq:2.3.3)}$$

Eq: 2.3.3 shows clearly that for any specific harmonic present in the voltage waveform across a capacitor, the peak current harmonic of the same order will be n times larger.

In an attempt to start with a cleaner signal, a G-M set is utilized. With direct on line capacitors connected, the generated voltage and the currents are shown in fig: 2.3.2.

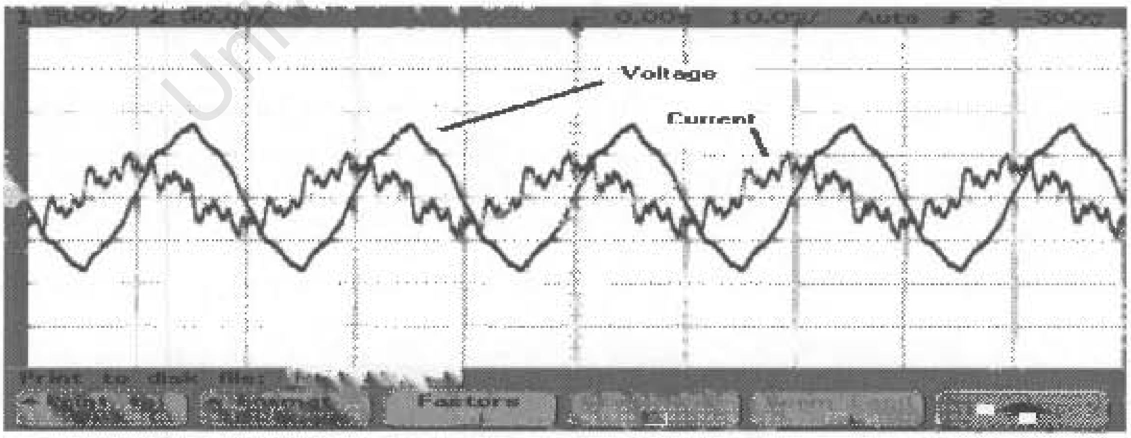

Fig: 2.3.2 Voltage and current waveforms for capacitors using G-M set

Clearly, there is a large order of harmonics present in the generated voltage. Although, by the shape of the current waveform, these harmonics have small magnitudes, there seem to be a wide range present. Possible explanations are, oxidization of the slip rings, un-smoothness of the brushes and uneven spring tension due to age. The field supply of the alternator is from a six-pulse rectifier with minimum ripple, so that the distortion due to field current is unlikely.

A second G-M set was tried out. Unfortunately, due to the absence of voltage and/ or speed feedback, drastic volt-drops were experienced at high load currents. At this point in time, no further experiments were carried out on stand-by generators and thereafter the mains were used for the rest of this report.

2.3.1 Thyristor-Controlled Inductance (TCI)

TCI is used as a variable source of inductive succeptance in the compensating networks either for static VAR compensation or load voltage balancing or both. The following circuit has been built and tested.

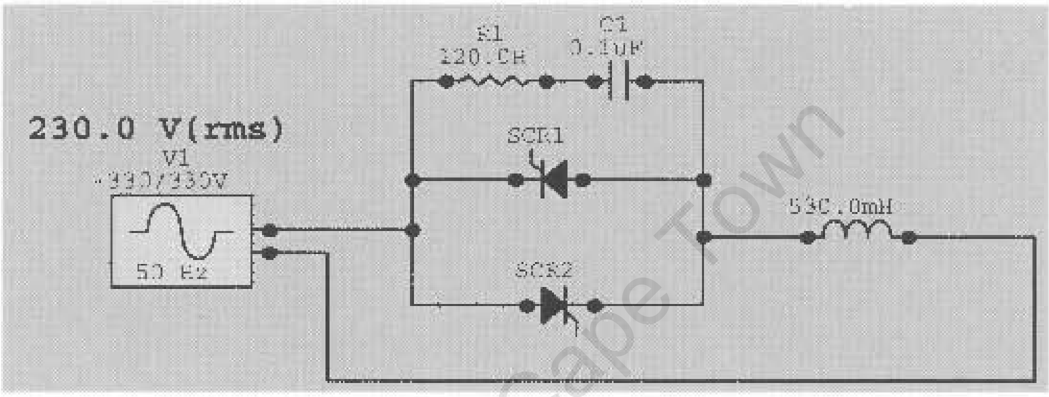

Fig: 2.3.3 Thyristor-Controlled Inductor

Naturally, the fundamental component of the current lags the supply voltage by 90° and hence the control of current and effective value of the load inductance can only start at firing angle of $\pi / 2$ Radians. Snubber circuits are provided to protect the thyristors against the load back emf. Fourier analysis can be used to express the supply current as a function of firing angle:

$$I_{(\alpha)} = \frac{V}{\pi \omega L}(2\pi - 2\alpha + Sin 2\alpha) \qquad \frac{\pi}{2} \leq \alpha \leq \pi \qquad \text{(Eq: 2.3.4)}$$

Typical waveforms of supply voltage, load current, and the firing pulses are shown in Fig: 2.3.4.

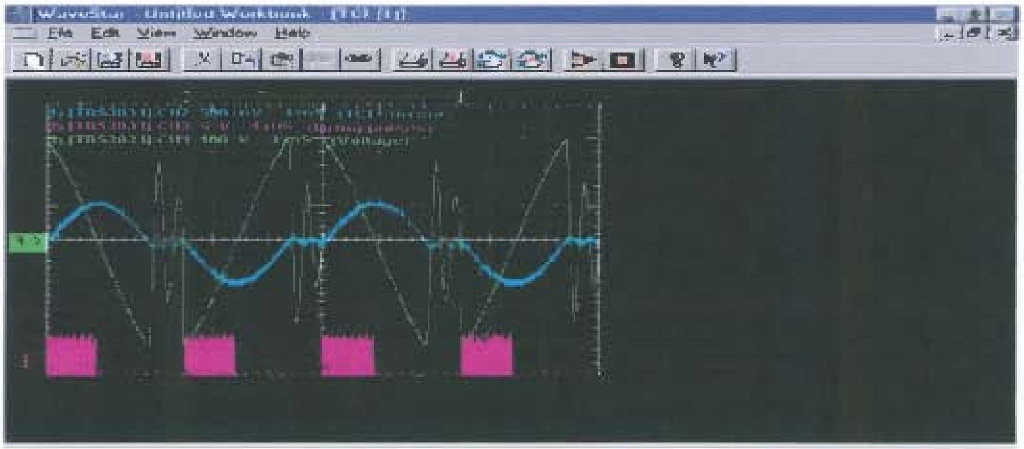

Fig: 2.3.4 TCI waveforms **Applied voltage** **TCI current** **Firing pulses**

By the nature of "phase control", the inductor current cannot be pure sine wave and contains odd harmonics. The magnitude of such harmonics, as a ratio of the fundamental, depend on the firing angle (α). The graph of Fig: 2.3.5 shows the changes of percentage "Current Harmonic Distortion" versus firing angles of 90° to 180° in 10° steps.

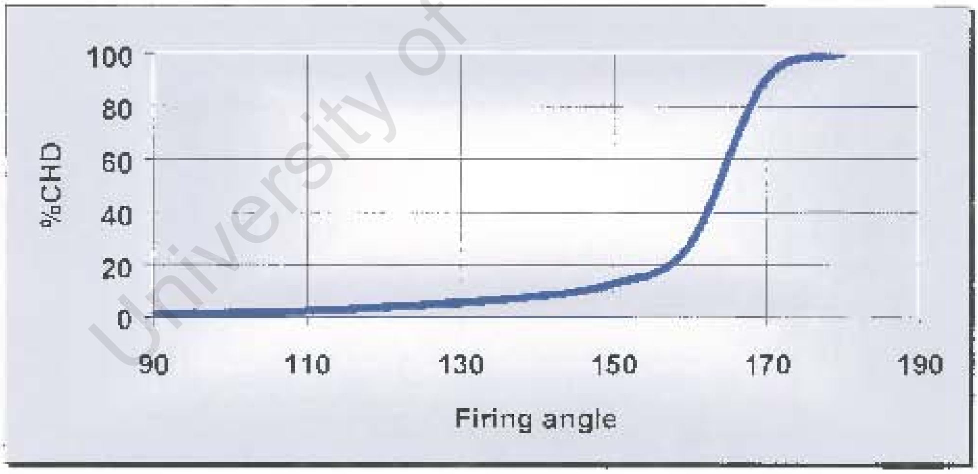

Fig: 2.3.5 Percentage current harmonics distortion in a TCI

Since the current is intentionally interrupted and hence deviates from original sinusoidal shape, the percentages obtained cannot be strictly considered as harmonic content of the current waveform. The graph in this case is a measure of the difference between the TCI current at $\alpha = \pi / 2$ and $\alpha \rangle \pi/2$, expressed as a percentage of current at $\alpha = \pi / 2$.

$$\frac{I(\alpha = \pi/2) - I(\alpha)}{I(\alpha = \pi/2)} * 100\ \% \qquad \text{(Eq: 2.3.5)}$$

Current harmonics are measured using "Real-Time Simulation". The method and it's powerful capabilities are explained thoroughly in chapter 6.

2.3.2 Thyristor-Controlled Succeptance

A TCS comprises a fixed capacitor in parallel with a TCI. Changing the firing angle of the back-to-back pair of thyristors can vary the inductive reactance and hence combined reactance of the system.

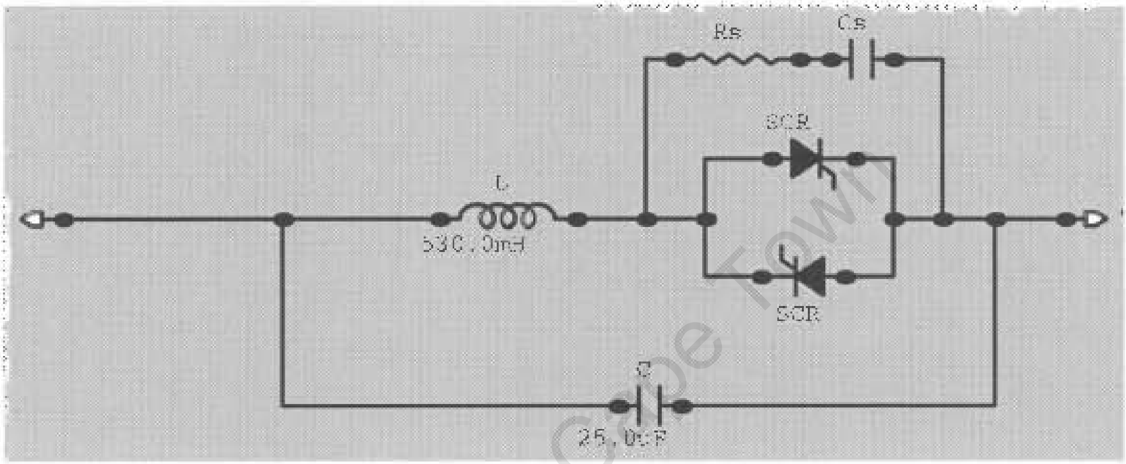

Fig: 2.3.6 Thyristor-Controlled Succeptance

The circuit can act as a variable inductive or capacitive source of reactance, hence the option of using it as a source of variable succeptance has been considered.

For the specific range of succeptance required (B_C and B_L), the values of L and C are calculated using the following equations:

$$C = \frac{B_C}{\omega_1} \quad , \quad L = \frac{\omega_1}{B_L - B_C} \qquad \text{(Eq:2.3.6)}$$

ω_1 represents the angular velocity at the fundamental frequency.

In high voltage applications, due to generated harmonics, the recommendation is to restrict the ratio of X_L to X_C to a maximum of 0.3[5]. Other precaution is that the inductor must be chosen so as to ensure that there is only one resonance frequency in the TCS reactance for the controllable range of α. The total current drawn from the supply is calculated from the following equation:

$$I_S(\alpha) = I_L - I_C = V\left[\frac{1}{\pi\omega L}(2\pi - 2\alpha + \sin 2\alpha) - \omega C\right] \qquad \text{(Eq:2.3.7)}$$

The basic structure of the TCS has two disadvantages. The current harmonics generated by the thyristors may cause resonance between the C and load or supply source inductance. The second disadvantage may appear if the supply voltage is distorted. As a result, resonance may again occur.

For the initial size and the full load requirement of the motor, the capacitive element of the compensator has to be lowered from 250 uF at the start down to 40 uF at full-load. Fine- tuning of the last 20 uF, to cater for changes in the load from no-load to full-load and slip, will be of great advantage.

In the original circuit of fig: 2.3.6, for small values of α beyond π /2 Rad, large percentage odd order harmonics are expected to appear in the current waveform. The worst-case scenario should occur at $\alpha = 90°$. The following graphs show the line and TCI current waveforms for the firing pulses for 90°, 135° and 180°.

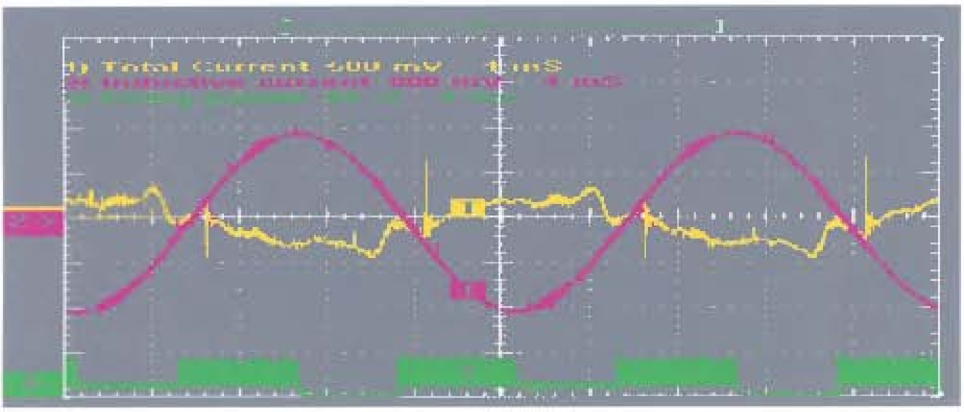

Fig: 2.3.7 TCS currents at 90 degree delay firing angle

Total current TCI Current Firing pulses

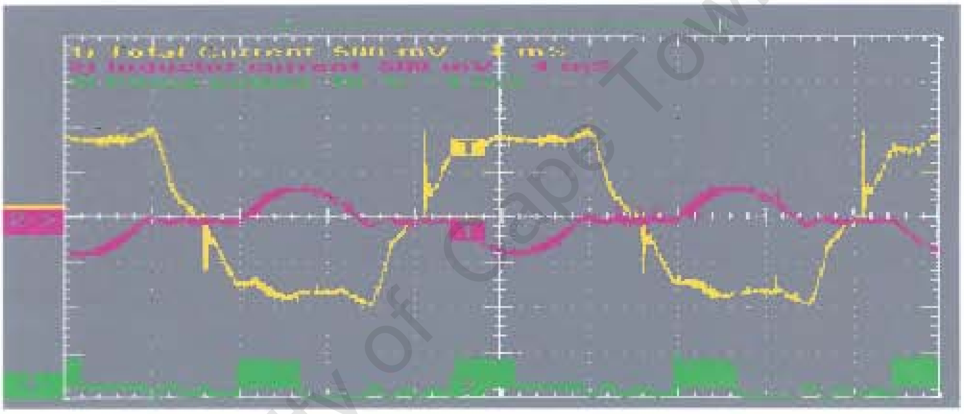

Fig: 2.3.8 TCS currents at 135 degrees delay firing angle

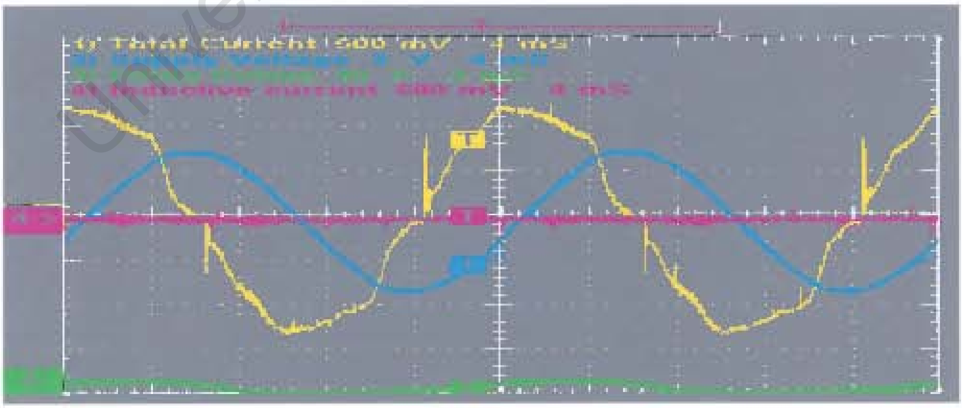

Fig: 2.3.9 TSC currents at 180 degree delay firing angle

Percentage current harmonic distortions versus the firing angle are shown in fig: 2.3.10.

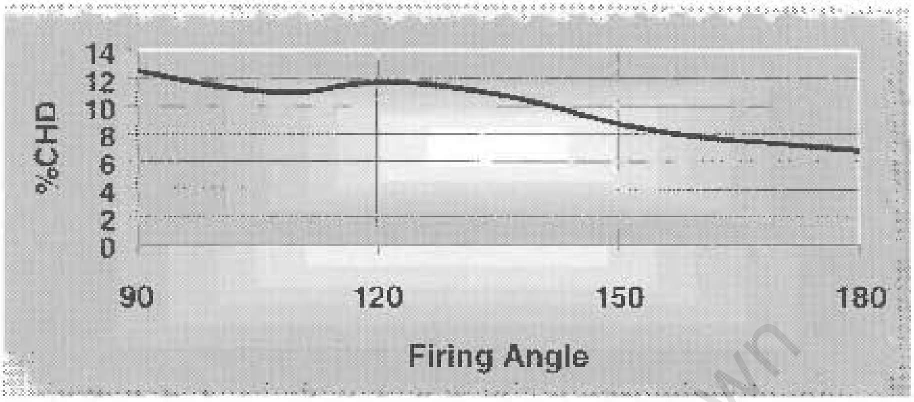

Fig: 2.3.10 Percentage current harmonic distortion versus delay firing angle in TCS

In comparison with other researcher's results in similar experiments [11], the above current distortions are surprisingly low and hence there seem to be no need for any harmonic filtering to be implemented. An additional way to double check the above results is to determine the frequency spectrum of the current drawn for the range of α and calculate the percentage CHD in order to compare with those of fig: 2.3.10.

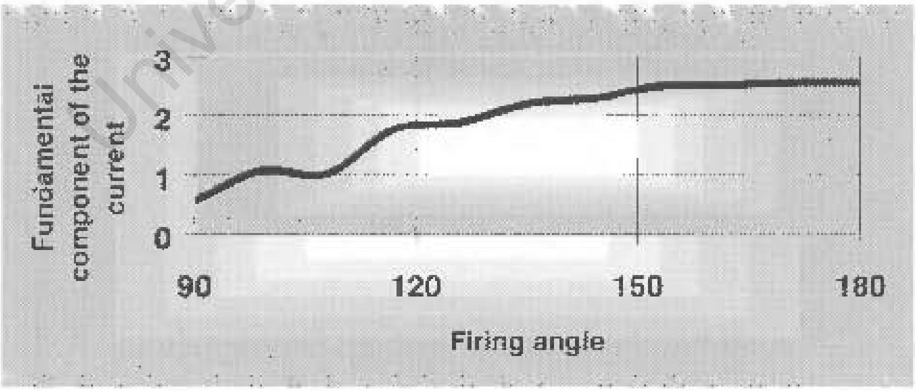

Fig: 2.3.11 Variation of the fundamental component of the current with firing angle

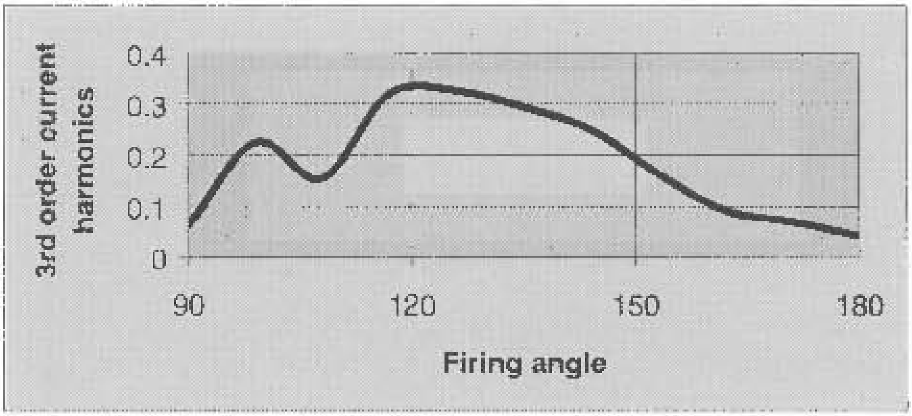

Fig: 2.3.12 Variation of the 3rd order current harmonics with firing angle

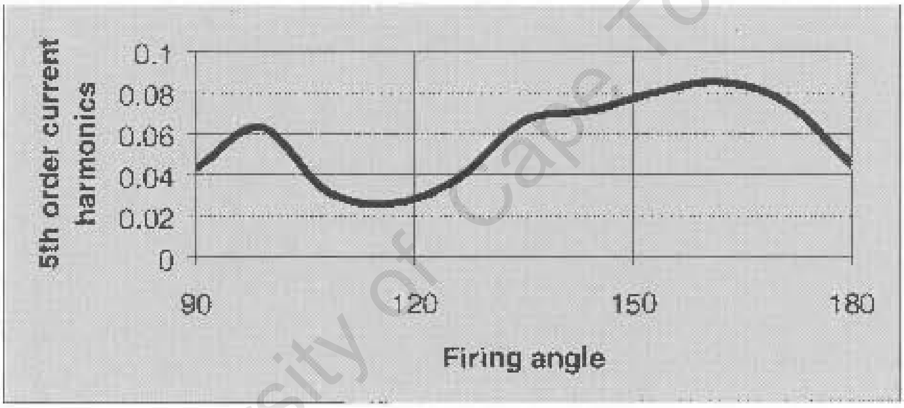

Fig: 2.3.13 Variation of the 5th order current harmonics with firing angle

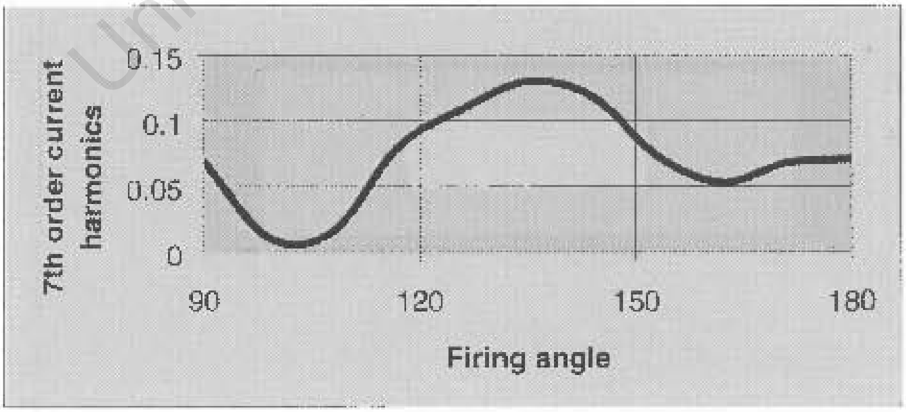

Fig: 2.3.14 Variation of the 7th order current harmonics with firing angle

Using the equation, $\mathrm{CHD} = \frac{\sqrt{{i_3}^2 + {i_5}^2 + {i_7}^2}}{i_1}$, the values of current harmonic distortion for the range of α can be re-plotted. This is shown in fig: 2.3.15.

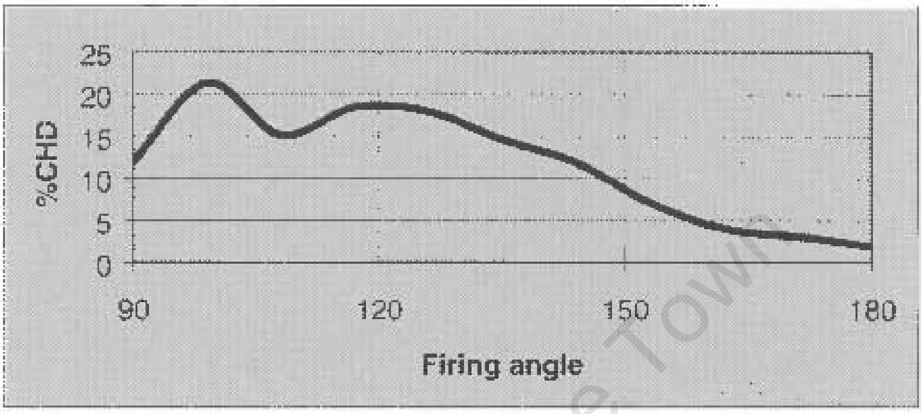

Fig: 2.3.15 Re-evaluated values of current harmonic distortion for the range of firing angle in a TCS

In comparison, certain degree of inconsistency exists between the results of fig: 2.3.10 and 2.3.15. The peak value of CHD of 21% occurring at $\alpha = 100°$ is still within tolerable limits. However, it might after all be worth looking in to a 3^{rd} order harmonic filter to the TCS and modify it as in fig: 2.3.16.

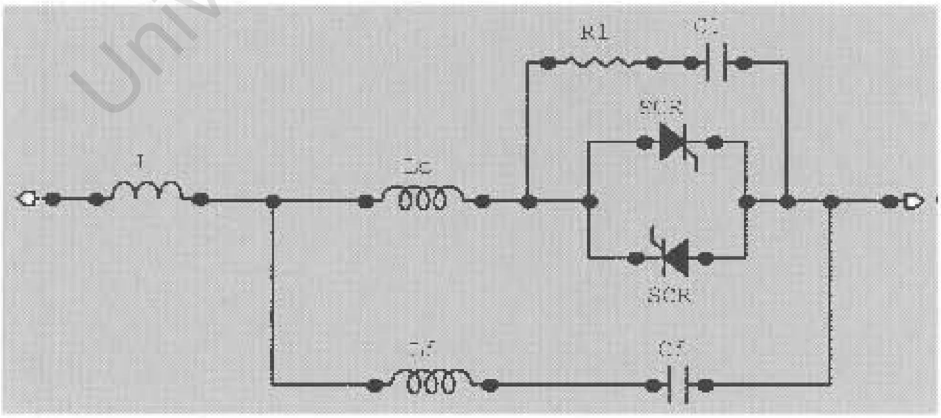

Fig: 2.3.16 Modified TCS

In the modified TCS, a shunt third order harmonic filter is included which provides a low impedance path for the third order current harmonic generated by the TCI . Additionally, a series inductor increases the compensator impedance for the supply voltage harmonics. Two factors need be considered,

a) the range of succeptance required from the TCS and,
b) the possible resonance frequency occurring between the shunt branch and the TCI in on state (f_R).

The range of succeptance ($B_{C1} \rightarrow B_{C2}$) requirement is from 18.064 down to 16.62 (Siemens). The resonance frequency should be selected as far as possible from frequencies of harmonics that could appear in the supply voltage. With the values selected in the original TCS and the range of controllable succeptance, resonance at fundamental frequency cannot occur. The components are calculated using the following equations[11].

$$\begin{aligned}
&a_3 L^3 + a_2 L^2 + a_1 L + a_0 = 0 \\
&a_0 = 9 - f_R^{\,2} \\
&a_1 = (27 - 11 f_R^{\,2}) \omega_1 . B_{C2} \\
&a_2 = [2B_{C2}(9 - 5f_R^{\,2}) + 9B_{C1}(1 - f_R^{\,2})] \omega_1^{\,2} B_{C2} \\
&a_3 = 9B_{C1}(1 - f_R^{\,2}) \omega_1^{\,3} B^2{}_{C2}
\end{aligned}$$

(Eq:2.3.8)

With the initial selection of $f_R = 1.7$, solving the polynomial equation, the values of L, can be plotted as in Fig:2.3.17.

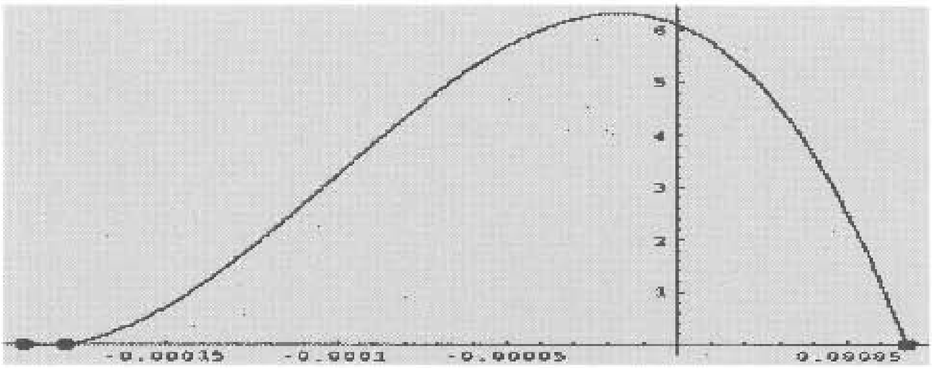

Fig: 2.3.17 Variation of L in the polynomial equation

Three possible symbolic and numerical roots exist:

L_1=-191.826*10^-6, L_2=-179.895*10^-6 L_3=+67.2789*10^-6

There is no clear definition for negative inductance. With L_3 having the only positive value placed in the following equations, the remaining values of the parameters can be calculated.

$$L_f = (\omega_1 L + \frac{1}{B_{C2}})/8$$

$$C_f = \frac{1}{(9\omega_1^2 L_f)}$$

$$L_C = [\omega^2{}_1 L^2 B_{C1} B_{C2} + \omega_1 L(B_{C1} + B_{C2}) + 1]/(B_{C1} - B_{C2})\omega_1$$

(Eq:2.3.9)

$L_f = 10.2\text{mH}$, $C_f = 110.77\text{uF}$ $L_C = 4.1\text{mH}$

Before attempting to implement and modify the TCS, a simulated proof is required to justify the construction.

In the simulation environment, the TCI generated harmonics with the source voltage 3rd order harmonics of (say) 5%, can be viewed in fig: 2.3.18 and 2.3.19.

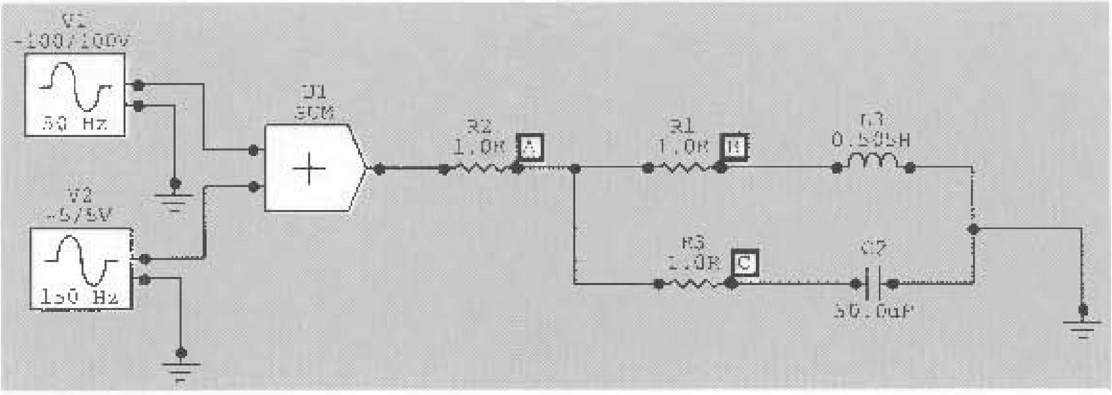

Fig: 2.3.18 Uncompensated TCS simulated with source voltage harmonics

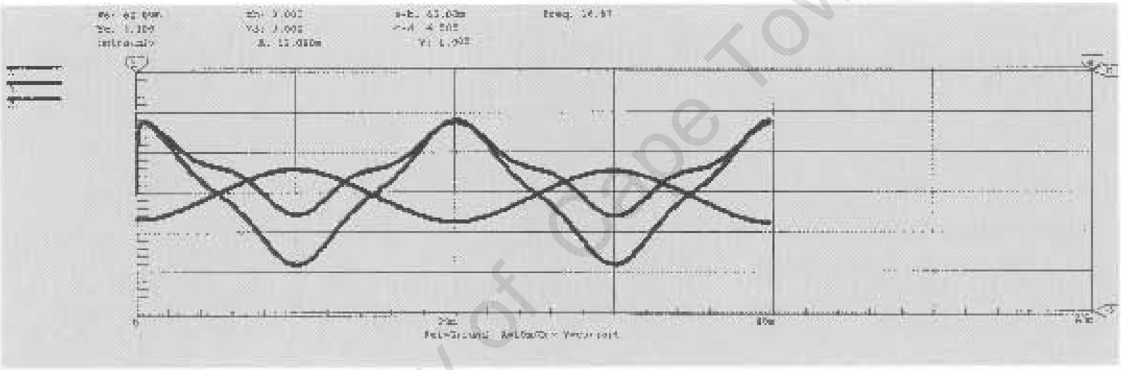

Fig: 2.3.19 Current waveforms for uncompensated TCS

The modified TCS with the appropriate values is shown in fig: 2.3.20.

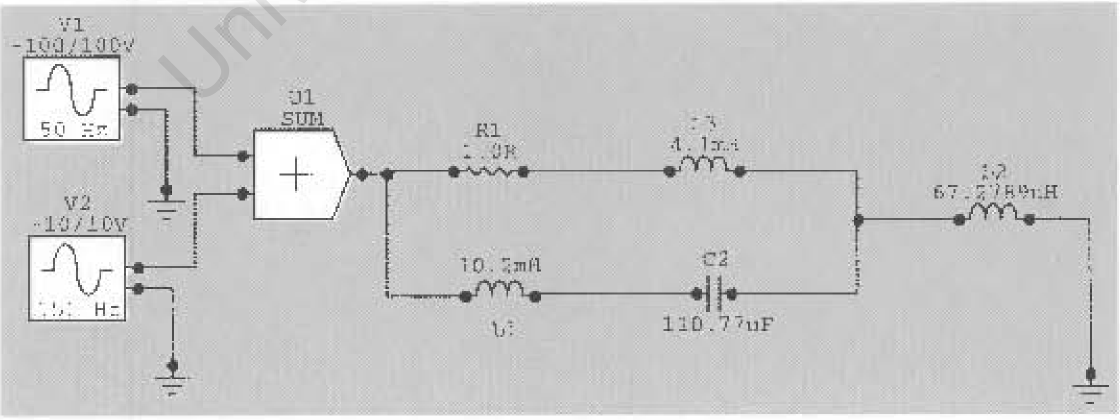

Fig: 2.3.20 Modified TCS with injected source voltage harmonics

Despite all efforts and usage of various simulation techniques, the resulting waveforms with reduced harmonics do not prove satisfactory. Further investigation on this part is required.

2.3.3 Thyristor-Switched capacitors

A commercial technique used by ESKOM and other power authorities is the use of TSC (thyristor-switched capacitors) in static VAR compensators.

Fig:2.7 shows the power diagram. The main capacitor bank is C_1. The auxiliary capacitor bank C_2 is connected in series with a damping reactor and has similar impedance at fundamental frequency.

The parallel damping resistor R1 carries very little fundamental current but provides very effective damping at the important harmonic frequencies (3rd,4th and 5th). The recommended tuning frequency for L1 and C2 is 175 Hz. According to GEC ALSTHOM, the above-mentioned frequency provides a good compromise for the nominal tuning of the TSC circuits, so that the maximum harmonics currents would be limited to about 20% of the fundamental currents in each TSC.

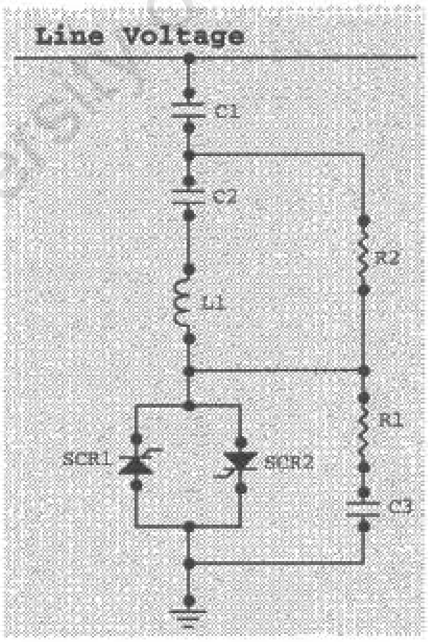

Fig: 2.3.21 Thyristor-switched shunt capacitor

Switching the capacitors at any random point during the input cycle, using back to back pair of thyristors, can generate very large current spikes and damage these switches permanently. This is simply due to i=C.dv/dt . If the capacitors are switched on at the peak of the supply voltage, then the current charging cycle starts at zero amp, which relieves the bi-directional switching components from unnecessary stress.

Unlike the phase-control used in TCIs to vary the effective value of the load inductance, TSC employed uses integral half-cycle control where the capacitor is either fully on or out of the circuit. The circuit diagram of Fig: 2.3.22 uses the voltage across the capacitors as the synchronizing signal to phase lock the firing pulses. The operation of the controller is as follows. A simple supply voltage phase-shift of 90° is followed by zero crossing detectors. The output is ANDed with a stepping control signal and a high frequency train of pulses. Finally, opto-isolators (2500 V) have been incorporated.

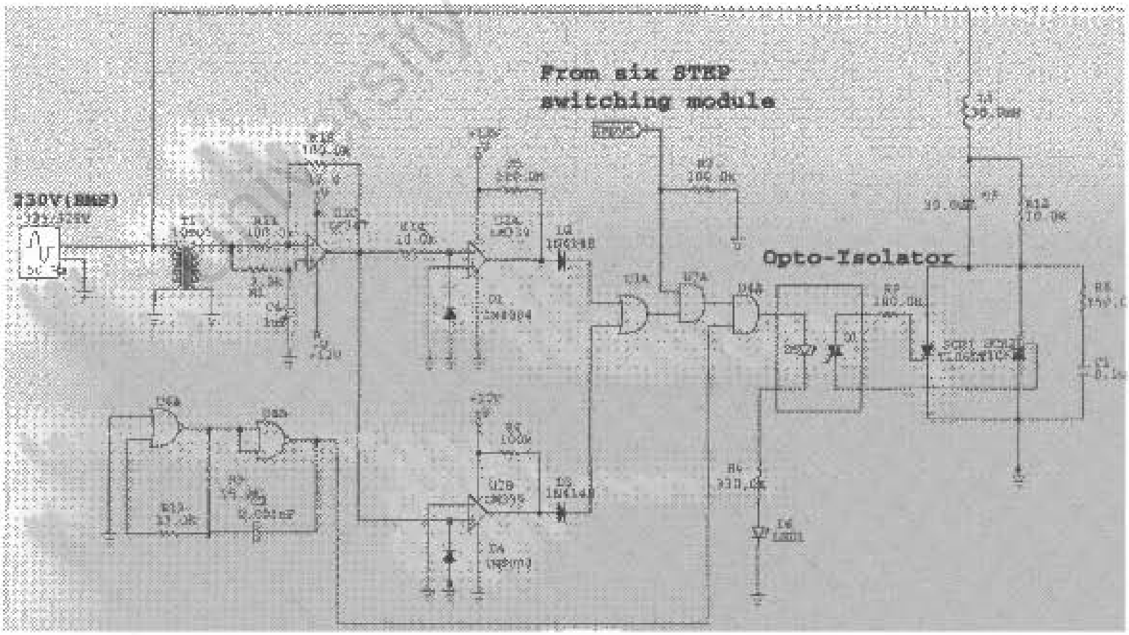

Fig: 2.3.22 Zero current triggering circuit for TSC

As established before, the voltage harmonics across a capacitor are reflected and magnified in the current harmonics. In fig: 2.3.23 the supply voltage fifth order harmonic seems to be the highest one of all.

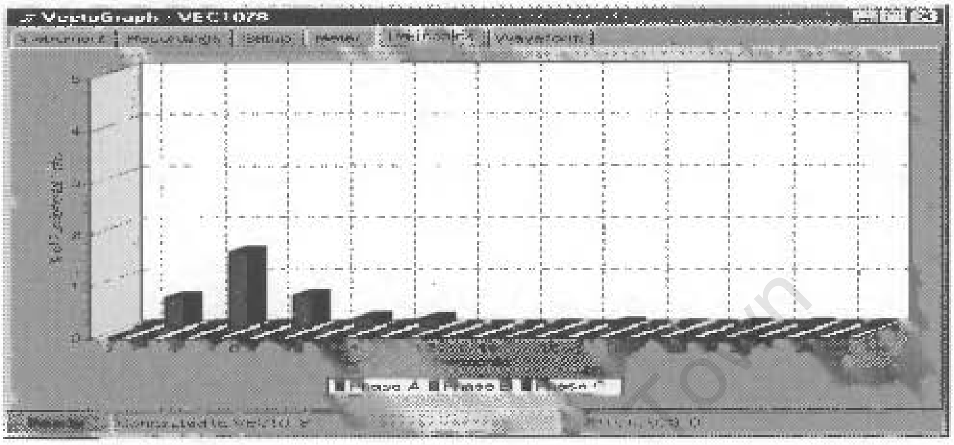

Fig: 2.3.23 Supply voltage harmonics

In fig:2.3.21 and with the absence of R_2 and C_2, current harmonic are measured and shown in Fig: 2.3.24.

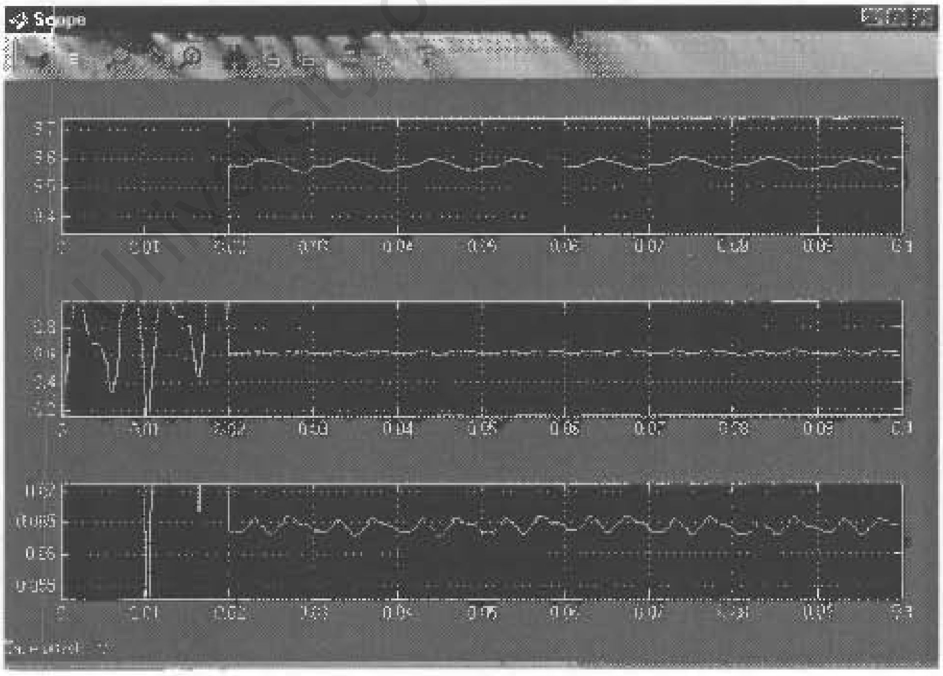

Fig: 2.3.24 5th order current harmonic measured using Real-Time Simulation

In the above measurement, the first, second and the third windows show the magnitude of the fundamental, the 5th order current harmonic and finally the ratio of 5th order to the fundamental component respectively. A consistent current harmonic distortion of nearly 6.5% is recorded for a large range of TSCs. Furthermore the oscilloscope captured voltage and the current waveforms for a 90 uF capacitor are shown in Fig: 2.3.25.

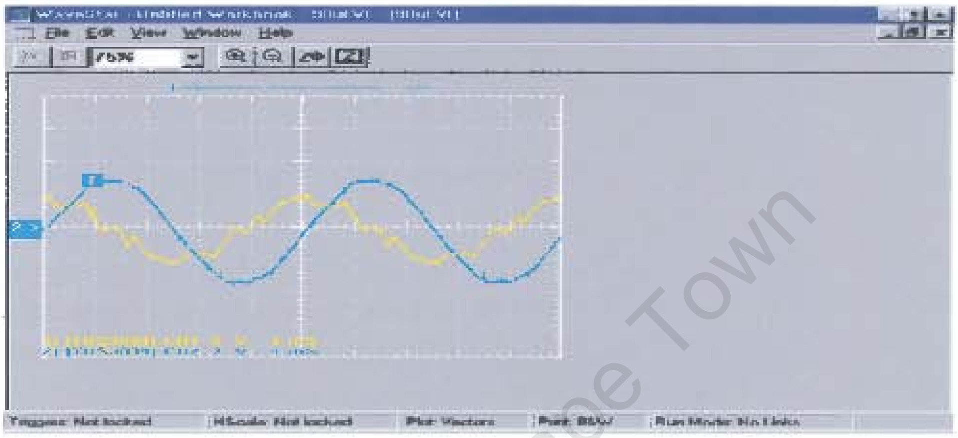

Fig: 2.3.25 Supply voltage and current drawn by 90 uF capacitor

Supply voltage Capacitor current

The harmonics in general seem to be harmless and relatively small, hence no further investigation is required at this stage. A picture of the TSC and related driving electronics is shown in appendix 1.7.

2.3.4 History and operation of magnetic amplifiers

Historically and before the discovery of the semi-conducting devices, magnetic amplifiers used to play an important role in industrial applications such as regulators, relays, starters, amplifiers, servo-systems, DC drives, illumination control and position control systems. Today, very few of them are found in use and the number of articles or even general information about them is very limited.

The terms magnetic amplifier and saturable reactor are often used interchangeably. This is erroneous because although a saturable reactor is the main component of all magnetic amplifiers, the term saturable reactor applies only to one part, the reactor.

The function of the so-called magnetic amplifier, as the name implies and like every other amplifier, is to reproduce an applied signal with an increased amplitude. However the way it is done is quite unique. In these amplifiers, a small DC signal through a separate control winding can vary the magnetic property, or more specifically the permeability of the core material in order to change the inductance and hence the reactance of the AC coils within the unit. This way the impedance and the current on the AC side is controlled.

The DC coil is placed on the joint middle limbs. A variable DC supply is used to feed it. The resulting DC flux is added to the AC flux on the outer limbs in alternating cycles. In other words, in the first half cycle of the supply voltage, the DC flux aids the AC flux produced by one AC coil, while it opposes the flux produced by the other AC coil. This is reversed in the next half cycle of the supply.

For the purpose of this project, the saturable reactor is chosen to function as a variable source of inductance and not as an amplifier. Fig: 2.3.26 shows the basic construction of a saturable reactor.

The basic construction of the saturable reactor is shown in Fig: 2.3.26.

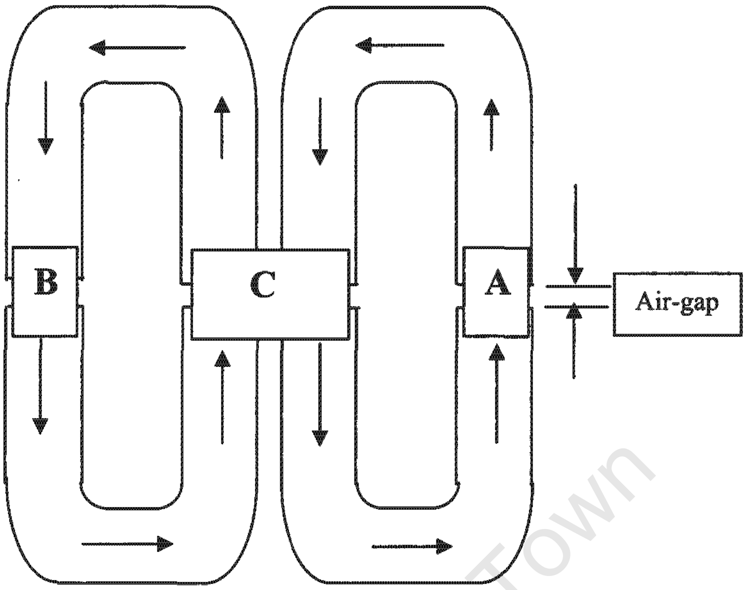

Fig: 2.3.26 Basic construction of the saturable reactor

A and B represent the AC coils on the outside limbs. These coils are wounded in opposite polarity so that the net resulting flux in the joint center limbs is zero. The DC coil is placed on the joint middle limbs (C) and is supplied by a variable DC source. The resulting DC flux is added to the AC flux on the outer limbs in alternating cycles. In other words, in the first half cycle of the supply voltage, the DC flux aids the AC flux produced by one AC coil, while it opposes the flux produced by the other AC coil. This is reversed in the next half cycle of the supply.

If we consider one of the magnetic circuits say the left core, the magnetic flux in that core is a function of both the AC and DC coil that links that particular core.

In the case where no DC ampere-turn current bias is imposed on the mmf of the magnetic circuit, the B-H characteristics will follow those of a normal symmetrical

B-H curve. If a constant AC amplitude voltage is connected to the AC coil, then the B-H curve will operate within the range shown in Fig 2.3.27

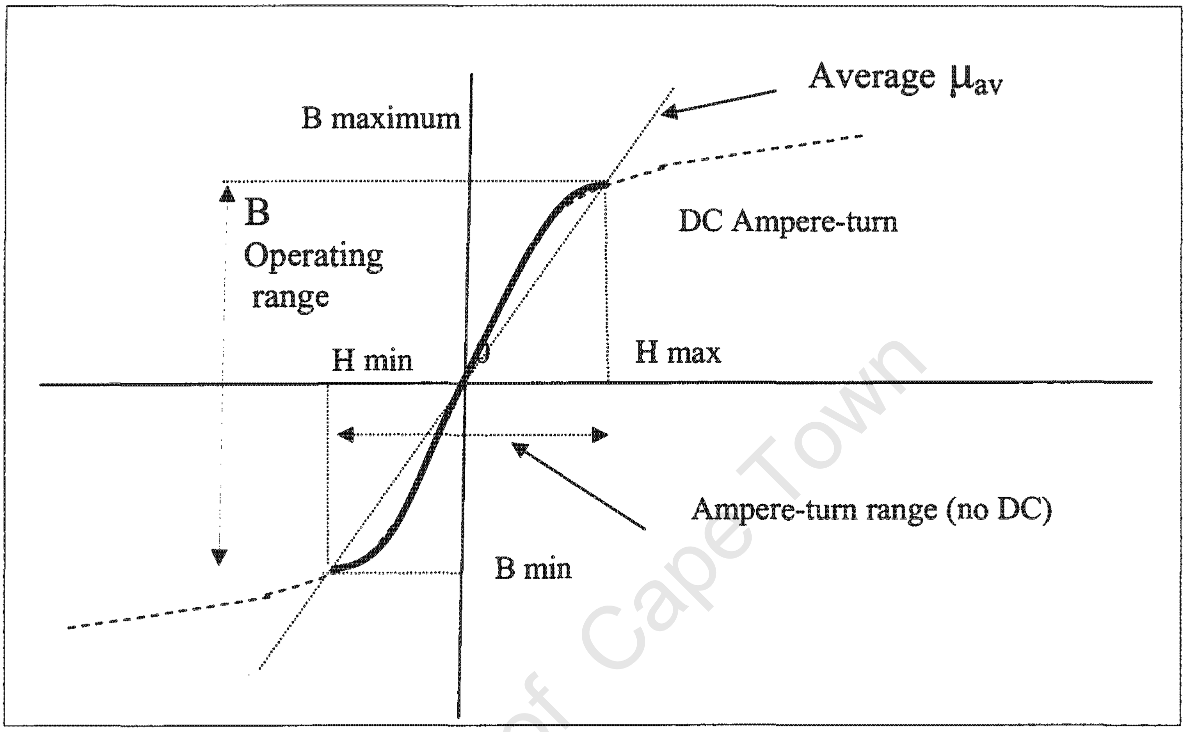

Fig: 2.3.27 B-H characteristic of magnetic circuit of one core showing operating range without the influence of DC biasing

If now a DC ampere-turn from the center coil is added to the mmf, the range of the flux and hence B will have to remain constant as this is a function of the AC voltage only. The operating range of H will be however affected due to the shift of the total Ampere-turn due to the DC coil current. The average permeability of the magnetic circuit will then be affected and hence the effective inductance will change with the DC current see Fig 2.3.28

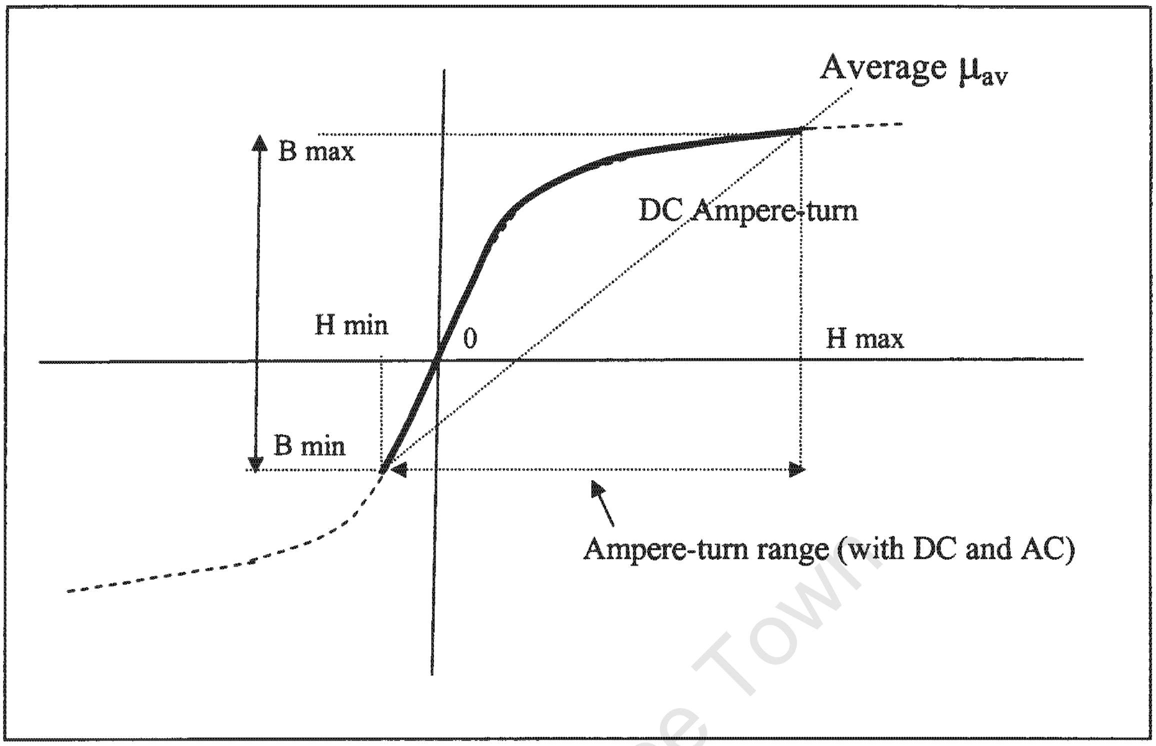

Fig 2.3.28 Effect of DC mmf on B-H curve operating range.

The operation of both magnetic circuits is identical. However the two AC coils are wound so that the AC flux linkage of the DC coil is in opposition. The DC coil should therefore, not be affected by the AC current. This is necessary so that DC current is easily supplied to the DC coil.

The picture of constructed saturable reactor can be seen in appendix 1.7.

These cores are wound from cold rolled GOSS (grain orientated silicon steel), and possess very high degree of magnetic property. For the purpose of constructing a saturable reactor, Grade M5 with the thickness of 0.3 mm was used.

2.3.5 Synchronous Condensers (phase shifter)

Synchronous machines with their power factor improvement abilities do not play any role in the passive element converters and hence are not discussed in this report.

Chapter 3

3.1 Converter for centrifugal pump

This section aims at building a controller card using current and voltage feedback loops to adjust the values of the converter succeptances automatically and in accordance with the motor parameters for the range of slip. An existing motor pump has been used. The acceleration time from standstill to full-load speed is measured to be roughly 3.0 seconds. Furthermore, if the driving motor has the correct power rating for the load flow, it can be safely assumed that it would operate continuously at full-load or at no-load. This raises the question as to what extent does the start up and reaching the full-load speed would depend on the intermediate values of converters elements.

Initially, the following circuit was considered:

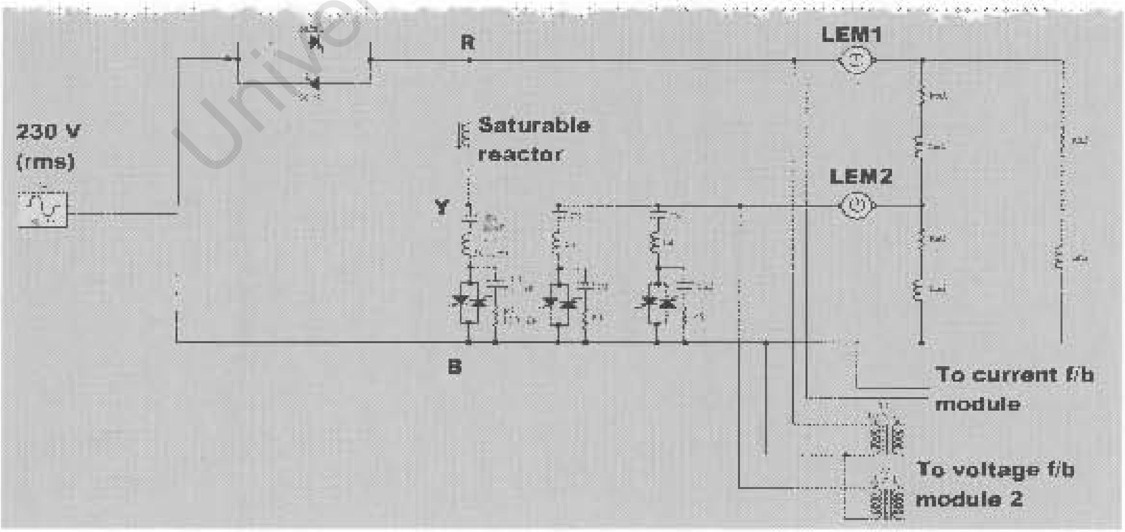

Fig: 3.1 The first proposed converter design

The motor starts initially with no compensation ie with a single-phase supply. Hence, it is expected to draw a large starting current. A back-back thyristor arrangement on the line current can act as a soft starter. For the size of the motor and its short acceleration time and due the fact that pumps only starts up and go off a few times per day, the soft starter may not be included in the final prototype.

The capacitive element of the converter is 270 uF at start up and 40.0 uF for the full-load. This was implemented in six steps of TSCs. Due to lack of space in Fig: 3.1, only three thyristor switched capacitors are shown.

The inductive element of the converter is a saturable reactor. The control technique is based on the full energization of the DC coil to saturate the reactor at start up. Then it produce a low reactance of 118.0 mH. In three seconds, the DC coil is gradually de-energized to reduce the inductance of the reactor to its initial pre energized value of 533 mH required by the motor for the full load conditions. Once the motor starts running, the intermediate values of the converter are adjusted as a function of time.

Before designing any circuitry, manually variable inductors and electro - mechanically switched capacitors were used to confirm the pre calculated values. The outcome shows that, for a smooth startup, the starting values of the converter passive elements are critical. Also for full load conditions, these values have to be accurate. However, during the run up, the intermediate values of the converter elements and the speed of variation are less critical. In other words, without the correct starting values of B_{C1} and B_{C2}, the motor will fail to start. Likewise, at steady state, if the converter elements are more than 5% away from the required values, the voltage balance will not be achieved within acceptable values.

3.2 Control strategy

The experimental control strategy shown in fig: 3.2 uses two line currents and two line-line voltages, as shown in fig: 3.2. A single-phase controlled rectifier provides the DC excitation for the reactor. Current and voltage error amplifiers provide the control signal for the rectifier. Phase or alfa-control is a suitable method to use for highly inductive loads of this nature. TSC switching signal will only depend on the difference in magnitude of the voltages.

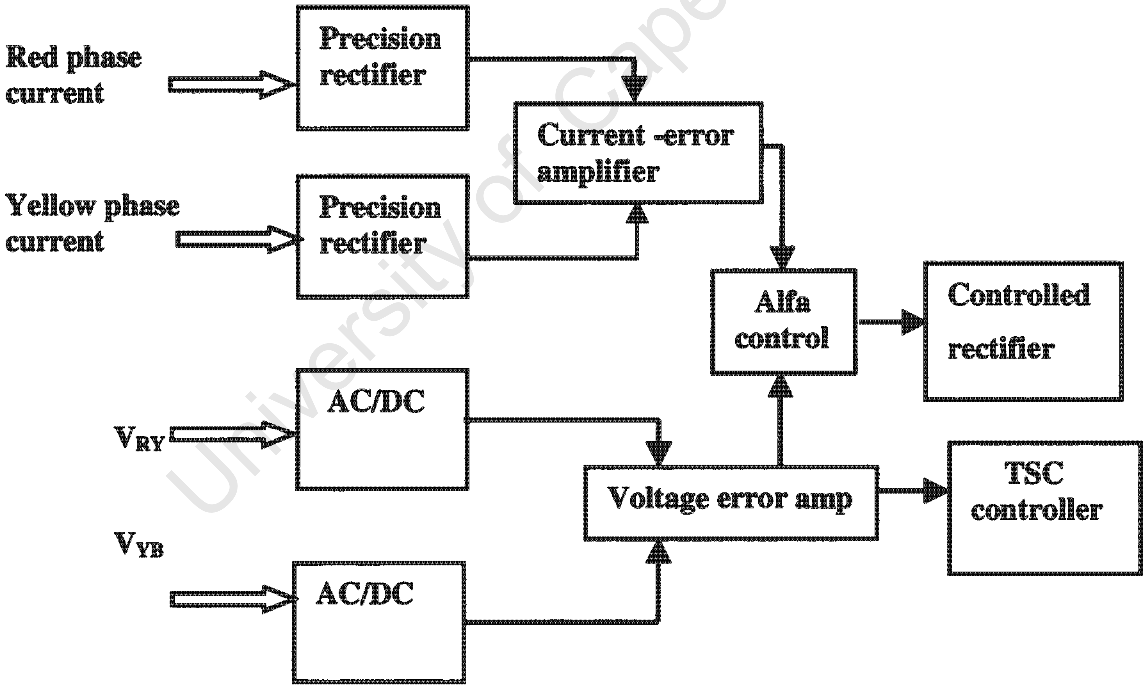

Fig: 3.2 Initial control strategy for the converter

The important blocks of the above strategy are explained next. The detailed circuit diagrams for all blocks are attached in appendix 1.2.

3.2.1 Precision rectifiers

These are used to generate accurate current error signals, which forms part of the feedback loop. Fig: 3.3 shows the circuit diagram for a single-phase precision rectifier.

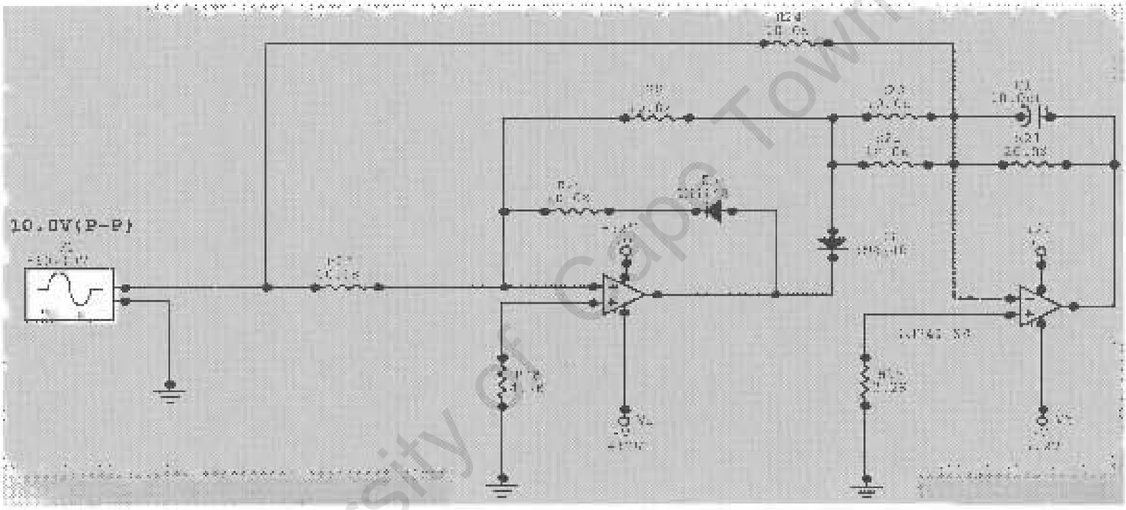

Fig: 3.3 Circuit diagram for a precision rectifier

In a normal four-diode bridge rectifier, two diode volt-drops are subtracted from the output voltage at all times. The above circuit has the advantage of absorbing these volt-drops.

3.2.2 Design of saturable reactor

When designing a saturable reactor, much like a normal transformer, two factors are taken in to consideration. First, the material and dimensions of the winding and secondly the core size and magnetic property which is related to the shape of the B-H curve.

For the windings, copper is the most commonly used material. As for the size, the maximum current in the reactor would be due to the starting inductance of 120 mH. With a negligible winding resistance, the maximum current in the AC coil is calculated from:

$X_L = 2*pi *50*120*10^{-3} = 37.7\ \Omega$,

at $V = 230.0V$, $I = 6.10A$

At rated speed, the inductance requirement rises to 535 mH which draws 1.37 A. According to transformer manufacturers, the current allowance/mm^2 for is 1.55 A/mm^2. This implies a nearly 4 mm^2 wires for the AC coils. Due to the short time for reaching the full load, overheating cannot occur and so a wire size of 1.0 mm^2 (D=1.13 mm) is selected.

The DC circuitry will only serve for the first few seconds after switch on, and is redundant thereafter. Bearing in mind that the AC coils are in series and opposite polarity, the sum of the turns for the reactor's AC coils are calculated using the well-known transformer equation,

$$V=4.44*f*N*B_{max}.A \qquad \text{(Eq: 3.1)}$$

The number of turns also depends on the dimensions of the core. A reasonable size selected is C750, with the property and dimensions of, B_{max} = 2.0 Tesla, Cross section area = A*B = 40*25=1000.0 mm^2 =0.001m^2 and length of the flux path = 333 mm. The values of A and B are shown in data-sheet [App: 1.6]. At supply voltage of 230 V and 50 Hz frequency, the total number of AC coil turns is $N = \dfrac{230}{4.44*50*2*0.001} = 518$ Turns . This means 259 turns on each AC limb. Experiments showed optimum performance at 250 turns per AC limb.

With the core size and number of AC turns per limb decided, it becomes necessary to look into the magnetic property of the reactor.

On the B-H characteristics for C-cores, supplied by the manufacturer (AMC), the knee point on the graph is roughly 1.7 Tesla. The operating range of flux density for the reactor was intended to be between 0.75 and 1.7 Tesla. This range is suitable because the value of permeability at 1.7 T is nearly $1/4.5$ times the permeability at 0.75 T and the reason for selecting it is that at startup the combined AC coils reactances will have to be reduced by this ratio. Data sheets show the values for this range of permeability to be 0.045 to 0.01 H/m {App:1.6].

For the range of permeability, referring to equation 2.3.10,

The above range implies that the DC control signal should inject amper-turns of sufficient size to lower the permeability at start up to μ_1.

3.2.3 Reactor and DC excitation

The DC excitation affects the two AC magnetic loops separately. Hence, the maximum Amper-turn supplied by the DC coil for each AC loop can be calculated as follows,

$$\text{mmf at start up} = I_S.N = 6.1*250 = 1525 \text{ AT}$$

$$\text{mmf at full load} = I_F.N = 1.37*250 = 342.5 \text{ AT}$$

This implies that the DC coil must be able to generate a mmf of,

$$1525 - 342.5 = 1182.5 \text{ AT}$$

$$1525 - 342.5 = 1182.5 \text{ AT}$$

Depending on the wire size of the DC coil and the power available from the DC supply, various combinations are possible. For the required DC current not to exceed 2.5 Amps at start up, a 500-turn DC coil with c.s.a of 1.0 mm^2 is used.

A standard full bridge, half controlled rectifier is used to feed a variable DC voltage to the DC coil. Fig:3.4 shows the power diagram for the DC drive. The supply voltage of 36.0 V and phase control from 0 to 180 degrees fulfills the reactors requirements.

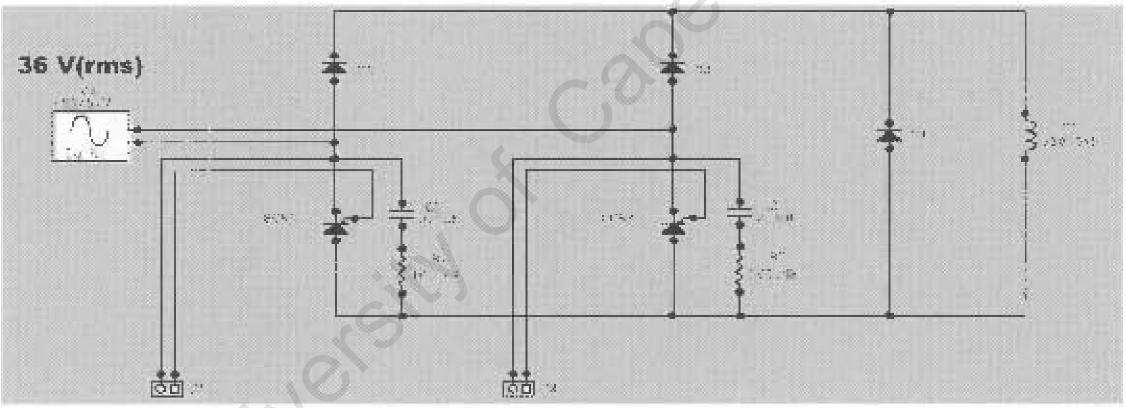

Fig: 3.4 Power diagram for reactor DC excitation

The driving circuit is similar to DC drive circuitry with pulse transformer isolation and facility for current and voltage feedback signals. The circuit diagram is shown in Fig: 3.5.

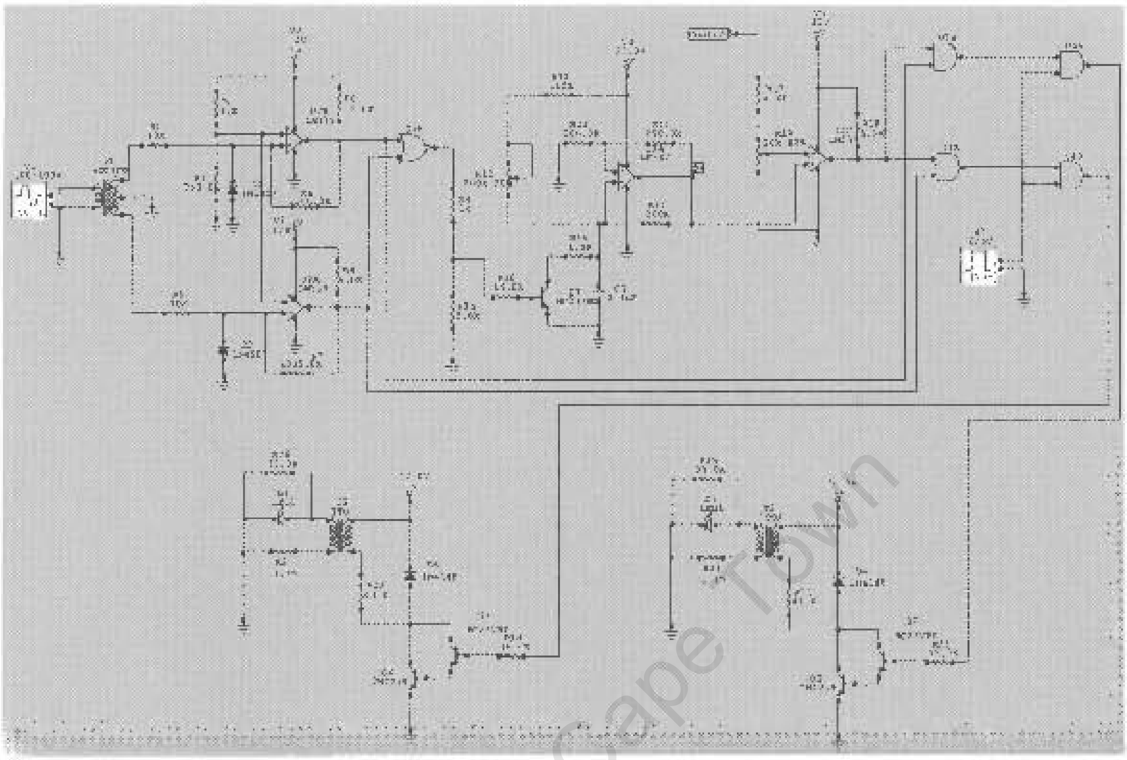

Fig: 3.5 Firing circuit for DC excitation

The control signal drives the DC coil in such way that at start up the reactor's core is highly saturated for minimum inductance, and as the motor runs up, DC excitation is withdrawn to bring the reactor back to its original inductive value.

3.3 Core saturation and air-gaps

Previous studies by engineers and inverter core manufacturers such as "Magnetics" (division of Spang and company), has resulted to standard definition for the term "core saturation".

These studies and the following experiments show that saturation occurs when the peak exciting current is twice the average exciting current. Furthermore, if the applied AC voltage to a transformer winding is unbalanced or in the case of a saturable reactor, additional DC excitation exists, a high residual flux may remain when excitation is removed. Reoccurrence of unbalance or the DC bias may cause deep saturation in the same or opposite direction. As a result an extremely large current spike will appear which is only limited by the source and winding resistance. The result, as experienced several times with the saturable reactor and applied DC biasing, was the failure of the thyristor's of the controlled rectifier.

The problem of minimizing the effect of random and/or forced saturation in the reactor is remedied by introducing an air-gap in to the core assembly which has a powerful demagnetization effect resulting in shearing over of the hysteresis loop and a considerable decrease in permeability of the material. In other words, insertion of air-gap reduces voltage spikes produced by the leakage inductance due to core saturation. In fact, it decreases the DC magnetization and increases the AC magnetization current. The amount of air-gap incorporated has a practical limitation. This is due to the fact it lowers the impedance and increases the magnetizing current. In commercial applications such as spacecraft transformers, extreme care and control is taken when performing gapping operation.
For the purpose of the this study, an air-gap of 0.3 mm was required to adjust the reactor's inductance to 530 mH at full-load condition.

3.4 Experimental results

Primarily, the supply voltage waveforms, harmonic content, THD and the percentage unbalance have been captured in Fig: 3.6.

when excitation is removed. Reoccurrence of unbalance or the DC bias may cause deep saturation in the same or opposite direction. As a result an extremely large current spike will appear which is only limited by the source and winding resistance. The result, as experienced several times with the saturable reactor and applied DC biasing, was the failure of the thyristor's of the controlled rectifier.

The problem of minimizing the effect of random and/or forced saturation in the reactor is remedied by introducing an air-gap in to the core assembly which has a powerful demagnetization effect resulting in shearing over of the hysteresis loop and a considerable decrease in permeability of the material. In other words, insertion of air-gap reduces voltage spikes produced by the leakage inductance due to core saturation. In fact, it decreases the DC magnetization and increases the AC magnetization current. The amount of air-gap incorporated has a practical limitation. This is due to the fact it lowers the impedance and increases the magnetizing current. In commercial applications such as spacecraft transformers, extreme care and control is taken when performing gapping operation.

For the purpose of fine-tuning the saturable reactor, an air-gap of 0.3 mm was used to set the reactor's inductance to 530 mH in the complete absence of DC excitation. Further explanations and detailed calculations on the air-gap can be found in appendix 1.8

3.4 Experimental results

Primarily, the supply voltage waveforms, harmonic content, THD and the percentage unbalance have been captured in Fig: 3.6 using a power quality meter (Vectograph).

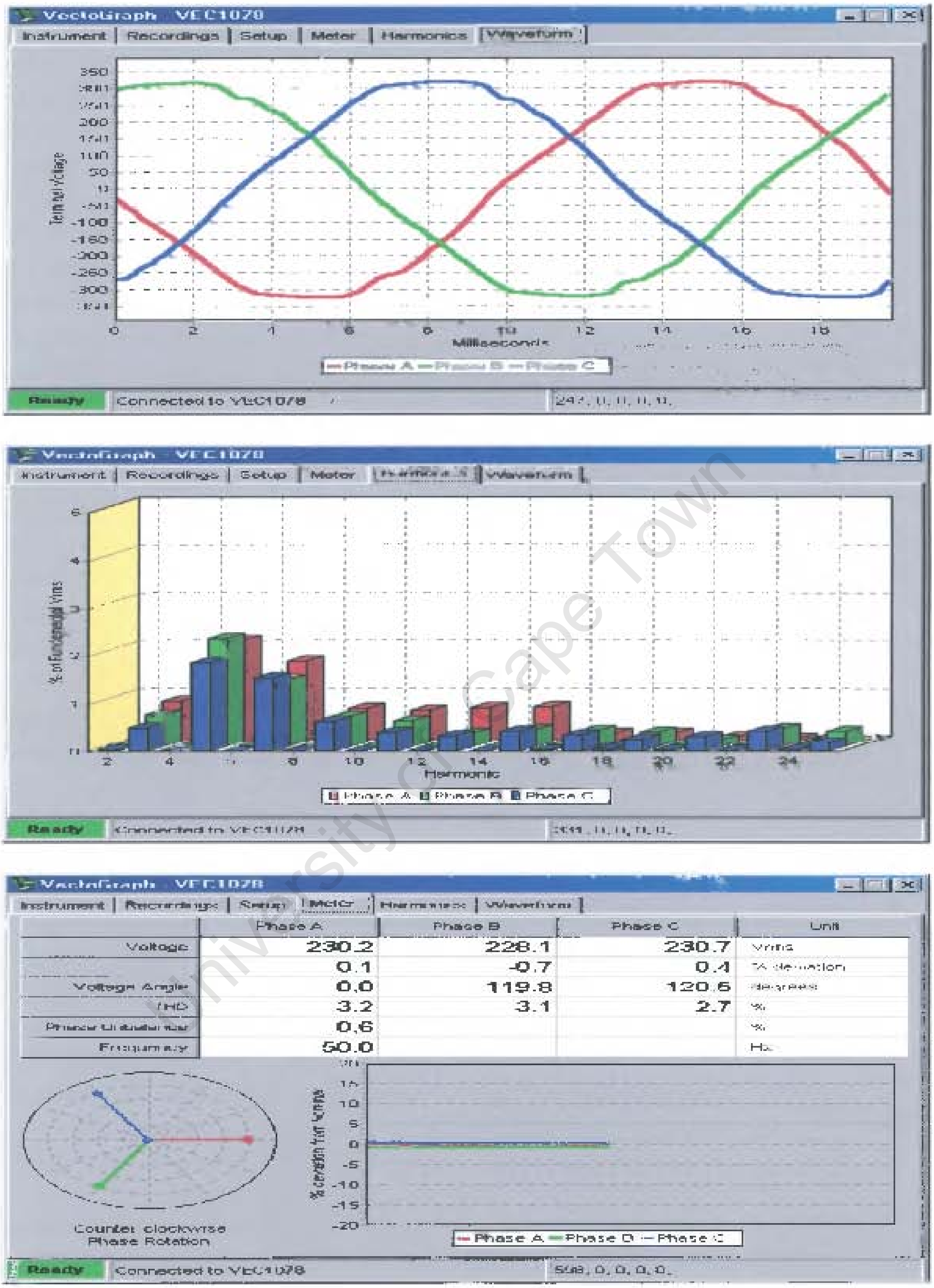

	Phase A	Phase B	Phase C	Unit
Voltage	230.2	228.1	230.7	Vrms
	0.1	-0.7	0.4	% deviation
Voltage Angle	0.0	119.8	120.6	degrees
THD	3.2	3.1	2.7	%
Phase Unbalance	0.6			%
Frequency	50.0			Hz

Fig: 3.6 Measurement of supply voltage harmonic content, phase unbalance and THD

The supply voltage is highly distorted and the figure 3.2% in phase A for THD exceeds the figure set by NRS 048.

The first set of measurements on the reactor is the AC currents versus DC excitation, shown in Fig: 3.7.

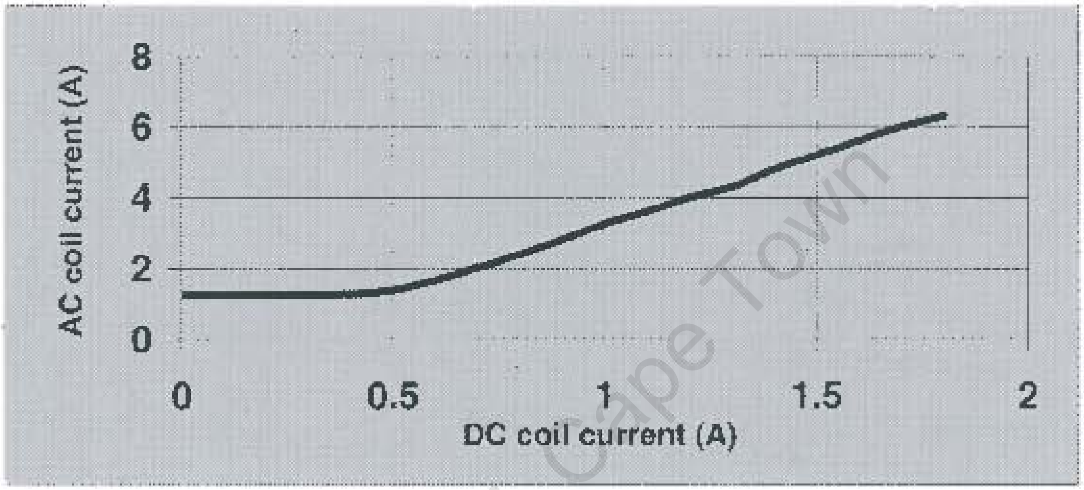

Fig: 3.7 Variation of AC current versus DC excitation

The scope captured AC coil currents for the range of DC excitations from 0.4 up to 1.8 Amps at 0.3 Amp intervals are shown in Fig: 3.8a to 3.8f.

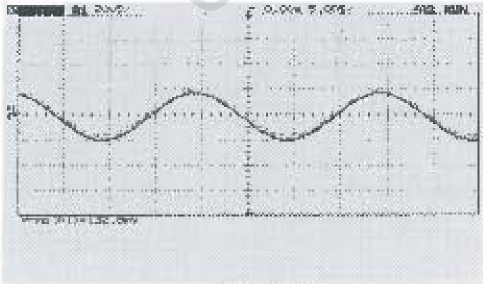

Fig: 3.8a

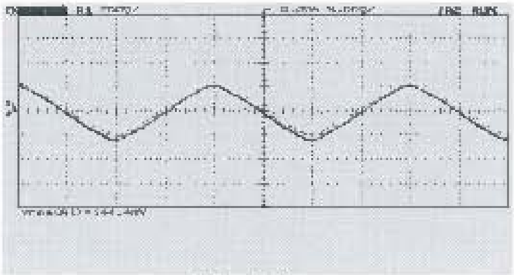

Fig: 3.8b

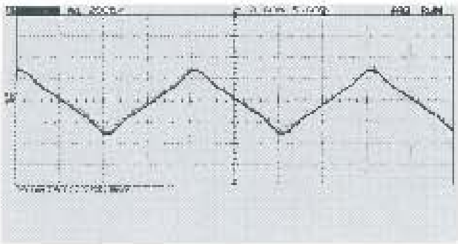

Fig: 3.8c

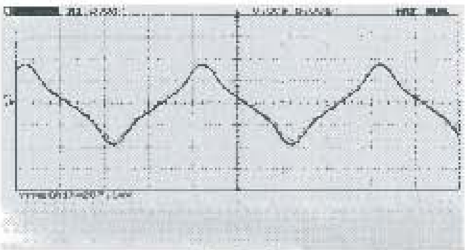

Fig: 3.8d

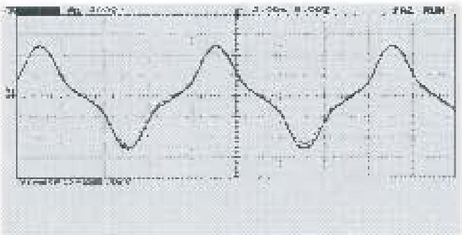

Fig: 3.8e

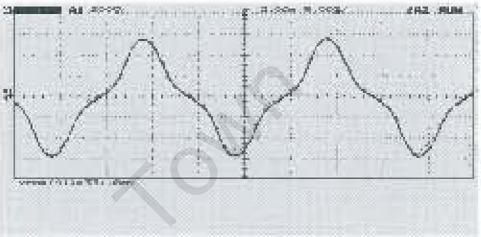

Fig: 3.7f

In the above waveforms it can be observed that as the DC current increases beyond 0.5 Amp, the AC current becomes distorted and harmonics are generated. Standard laboratory equipment such as Vectograph and Fluke power analyzer can be used to measure voltage harmonics, THD and voltage unbalances but current harmonics need more specialized and expensive measuring device. Unfortunately, this was not available at the time of preparation of this report.

For the values of DC current larger than 1.8 A, the core material saturates fully and the AC coil current increases rapidly to dangerously high levels. However, it is convenient to realize that with the parameters selected, there is a linear relationship between the AC and DC coil currents. The minimum and maximum allowable DC excitation current of 0.5 to 1.8 Amps is also a clear indication of the practical limits of the slope of the B-H curve (μ).

The DC current has so far been assumed flat and free of ripples. The Following waveforms show the DC coil current versus DC voltage applied at low and high saturation levels.

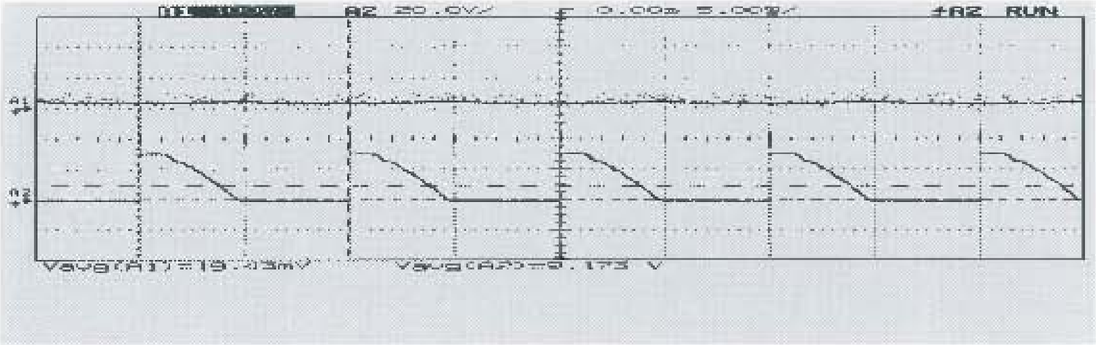

Fig: 3.9 DC coil current and voltage at low saturation level

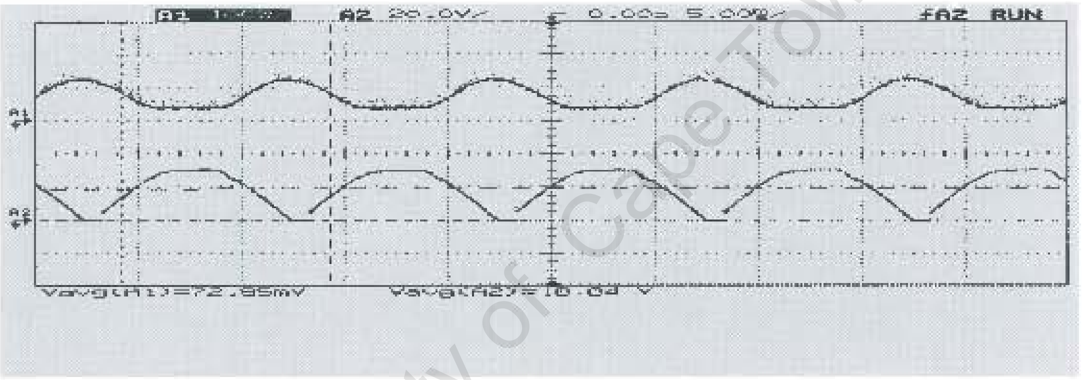

Fig: 3.10 DC coil current and voltage at high saturation level

The AC component in the DC coil current is due to the induced voltage by the AC coil. It cannot really be prevented and since it does not cause any problem, a solution is not applied. A comprehensive set of voltage and current harmonic analysis has been conducted and the results are presented in chapter six.

The objective of this section was only to bring the motor to full-load speed with the converter elements changing simultaneously with the load parameters. During the run up time, the measurement of intermediate values of currents and unbalanced voltages (within a few seconds) are hardly measurable. Therefore, only the final waveforms are examined.

Fig:3.11 shows the oscilloscope image of the generated 3-phase voltage waveforms.

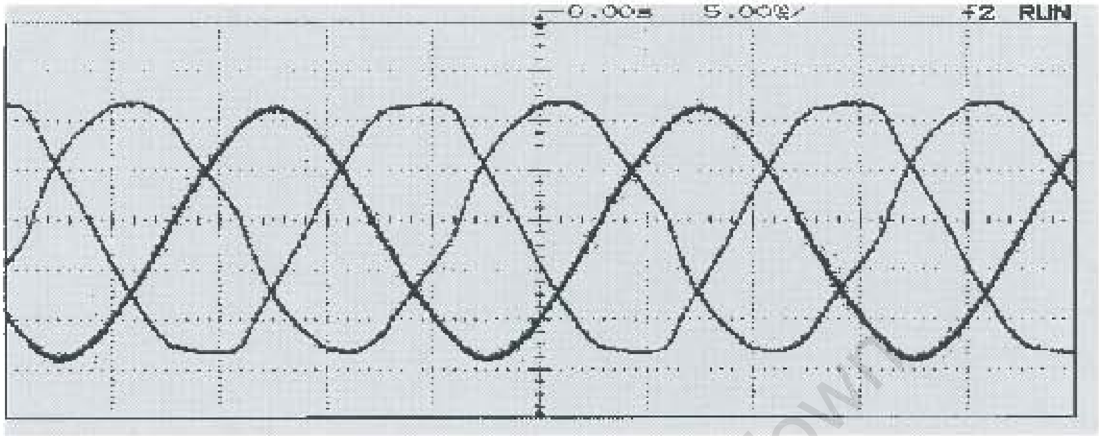

Fig: 3.11 Full-load after compensation waveforms across the motor terminals

3.4.1 Harmonic analysis

In this section, a portable Fluke power analyzer has been used to measure the harmonic content of the system at startup and full load conditions. At start up where the reactor is heavily saturated, voltages are mildly affected by the harmonics generated, whereas the harmonic content in the current waveforms are at highest. For a DC current of 1.0 Amp, phase currents containing 57.5% 3rd, and only 1.0% 5th harmonics were measured.

At rated load with no DC excitation on the reactor, the harmonic content of the voltages and currents were predominantly of 3rd and 5th order. THD for any line current or voltage does not exceed 3%. The phase currents contain 3.8% THD. Measurements are shown in the following figures.

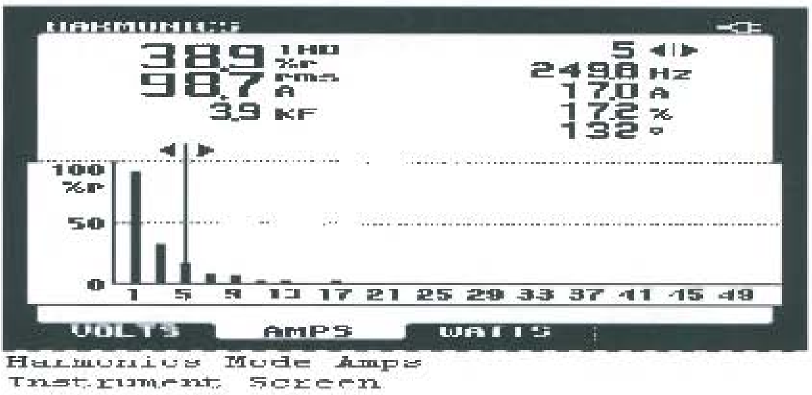

Harmonics Mode Amps
Instrument Screen

Fig: 3.12 Supply current 5th order harmonic content at start up

Fig: 3.13 Supply line voltage 5th order harmonic content at full load

The current harmonics content of the converter passive elements is however, higher. Typical values were measured between 21 to 23%.

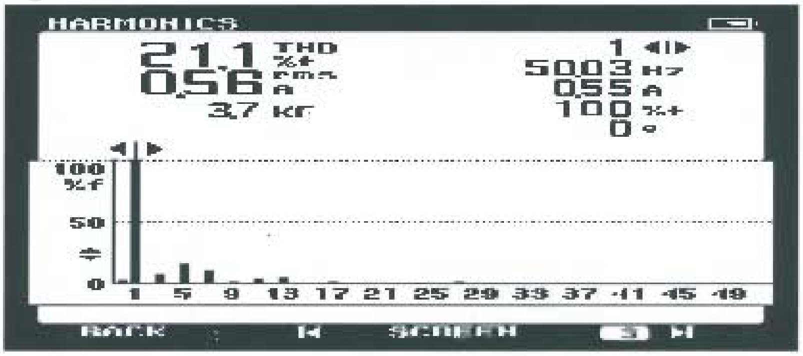

Fig: 3.14 Capacitive element current harmonic content at full load

Apart from start up values, the THD of the line currents and voltages for the full load running conditions are not high. As a matter of exercise two methods of filtering to minimize the dominant third order harmonic has been tried out.

3.4.2 Parallel filtering

Attempts to use a 3rd order parallel harmonic filter did not prove efficient. It changes the parameters of the converter to the point where start up becomes impossible. The arrangement in shown in Fig: 3.15.

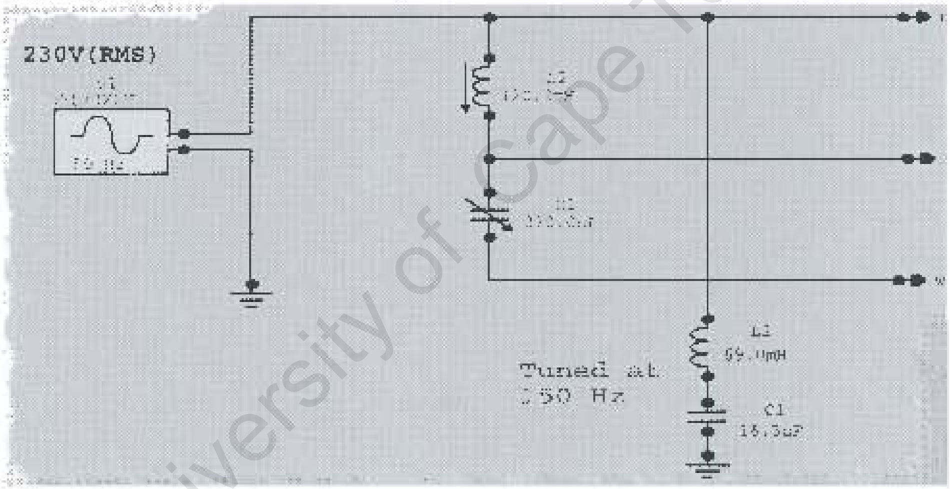

Fig: 3.15 Parallel line 3-rd harmonic filter

For a DC current excitation of 1.0 A at start up, line currents contain 35.8%.

3.4.3 Series filtering

Considering that capacitors are the amplifiers of the current harmonics and that the converter requires maximum capacitance at start up, series inductors of 23.0 mH were placed with each capacitor.

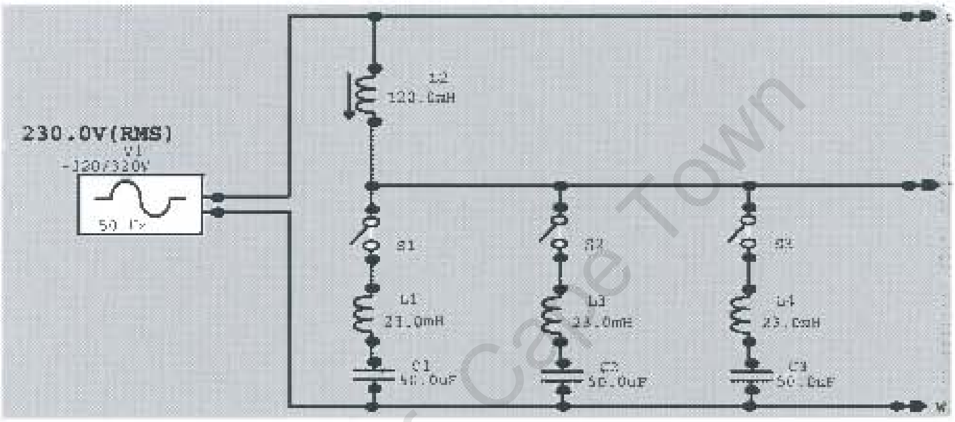

Fig: 3.16 Series filtering

The THD of the line currents improved to 24.1% which is again almost entirely 3rd order. Phase currents contain 28.4% 3rd order harmonics. The 3rd harmonic content of the phase currents are often higher than those in line current harmonics of the same order. This can be justified by the fact that in a delta connected load the 3rd order voltage harmonics sum up to zero but the corresponding currents are in phase and hence circulate a large current in the mesh.

When the series inductor value was increased to 60.0 mH, with the same DC excitation, all the harmonic contents were reduced to nearly half the previous values. The voltage harmonics were reduced to below one percent. These show the best results and hence remained in the system permanently.

3.5 Additional parallel succeptances

It is possible to reduce the maximum values of the converter's passive elements by placing fixed banks of capacitor across each phase of the load. The simulated values of the converter inductive and capacitive elements are shown in Fig: 3.17 and 3.18. See Matlab M-file in Appendix 1.1.

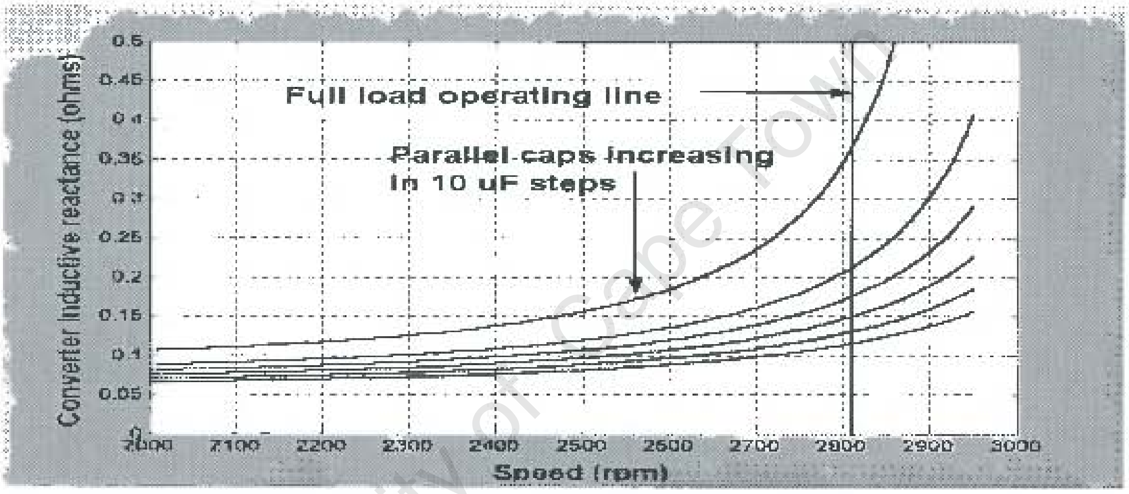

Fig: 3.17 Effect of fixed parallel capacitor banks on the size of the reactor

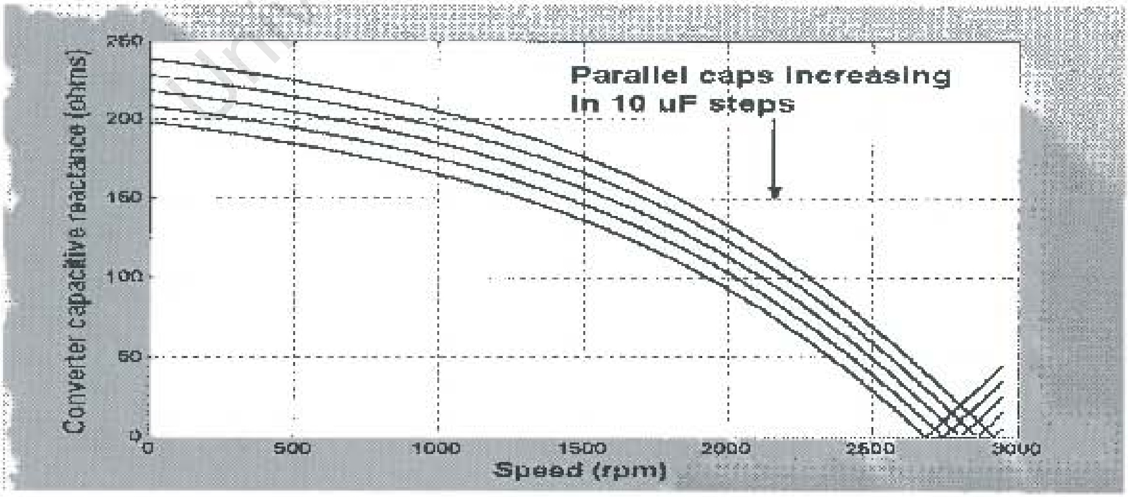

Fig: 3.18 Effect of fixed parallel capacitor banks on the size of the switching capacitors

The circuit diagram and the simulated line current waveforms for rated slip with extra 50 uF capacitor connected in each phase are shown in Fig: 3.19.

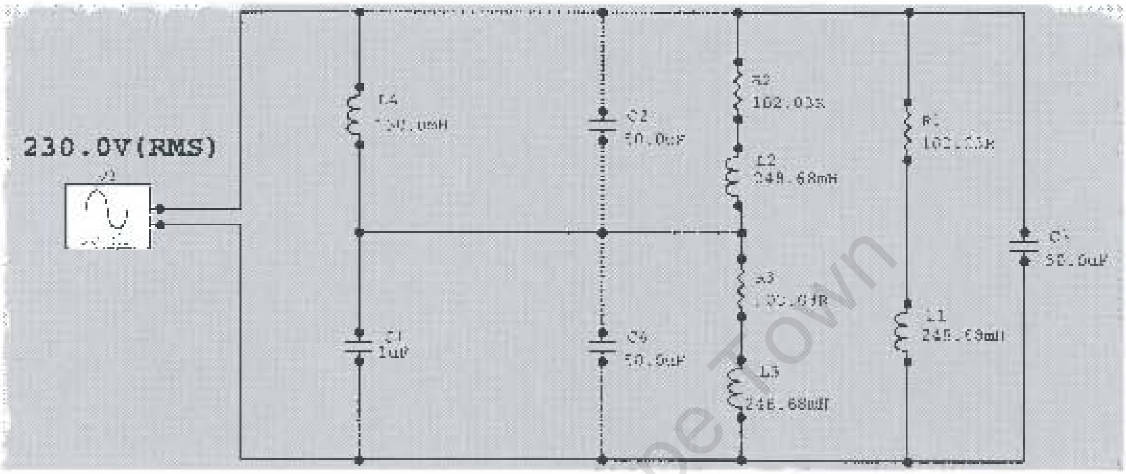

Fig: 3.19 Converter and load at full-load with additional parallel capacitors

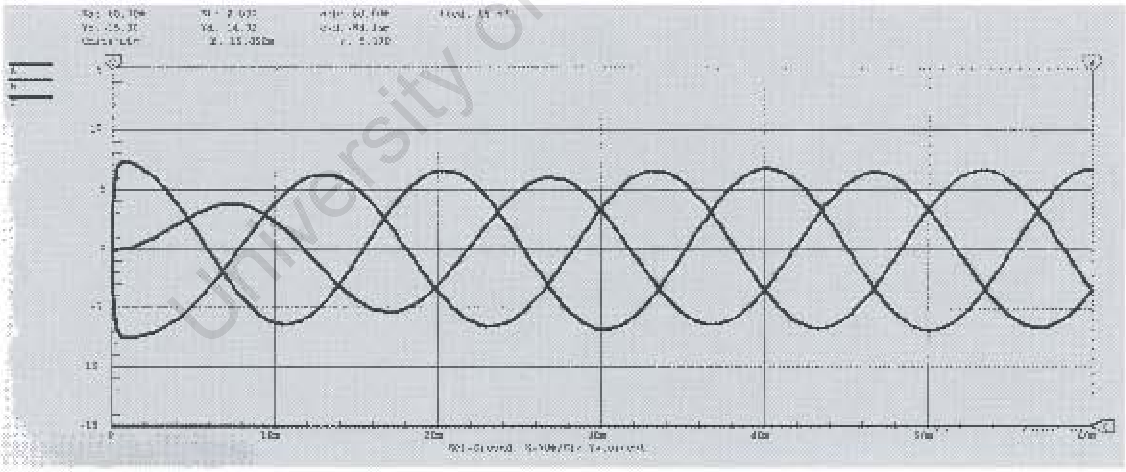

Fig: 3.20 Line current waveforms

Due to unavailability of a variety of different sizes of capacitors and reactors, no further investigation is pursued on this mater.

Some conclusions can be drawn at this stage.

a) For a small motor-pump, the required change of the converter elements with slip is rapid.
b) The worst time occurs at slip values very close to the full-load.
c) The saturation of the reactor is the main cause for the generated harmonics.
d) The capacitors cause large current harmonics. These current harmonics are directly proportional to the frequency.
e) The final tests on the pump prove that, for the specific case of a centrifugal pump-motor assembly of this size and characteristics, varying both converter elements from start up to full-load in direct relationship with the load slip is not necessary.
f) The converter used with a centrifugal pump can be simplified by using only one variable capacitive element in conjunction with a fixed inductive element designed for the full-load conditions. The recommended converter construction can be viewed under "Recommendations" in chapter 7.

Chapter 4

4.1 Development of a general controller

The aim of this chapter is to develop and construct an adaptive converter, which can be used for any three-phase load, supplied with a single-phase voltage. The converter must be able to:

1. sample two line currents and one line to line voltage,
2. derive at least two DC voltages representing the load conductance and succeptance per phase,
3. from the above values calculate and generate two output DC signals proportional to the required values of converter succeptances for voltage balancing.

The simplified diagram for the converter-load connections is shown in Fig:4.1.

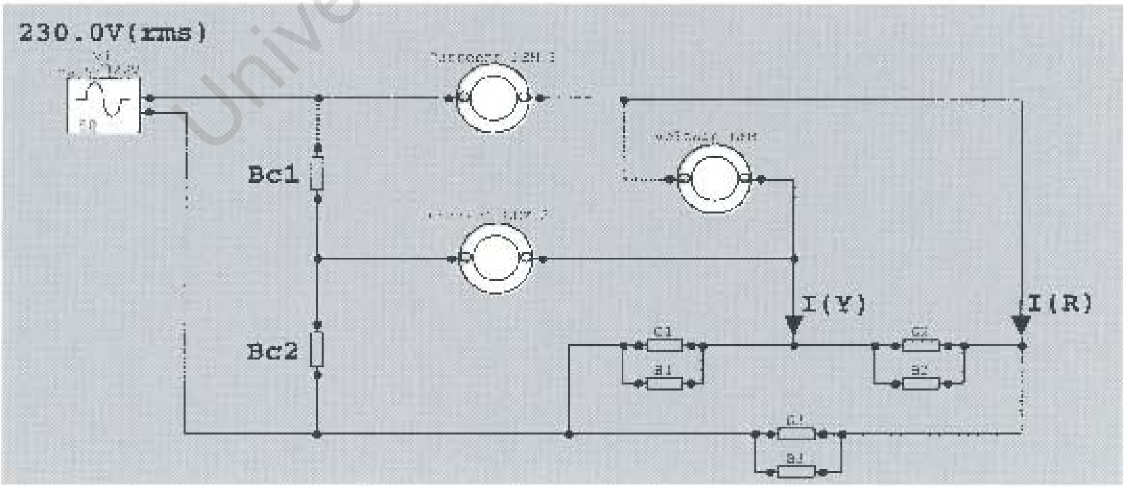

Fig: 4.1 The layout of the three-phase balanced load and line measuring sensors

For a normal 3-phase supply and load connected in delta, the line currents are $\sqrt{3}$ times the phase values. However, with a single-phase supply, one phase current can be sampled using the following relationship.

$$\overline{I_{ph}} = \frac{\overline{I(R)} - \overline{I(Y)}}{3} \qquad \text{(Eq: 4.1)}$$

The simulation in Fig: 4.2, demonstrates how this has been achieved [appendix 1.4]. The mathematical block (M1) subtracts the two line currents. The resulting current is then divided into three equal and parallel resistors.

Fig: 4.3 shows the resulting current waveforms through R_2 and R_4. The 180 degrees phase shift is compensated for in the next stage of modeling.

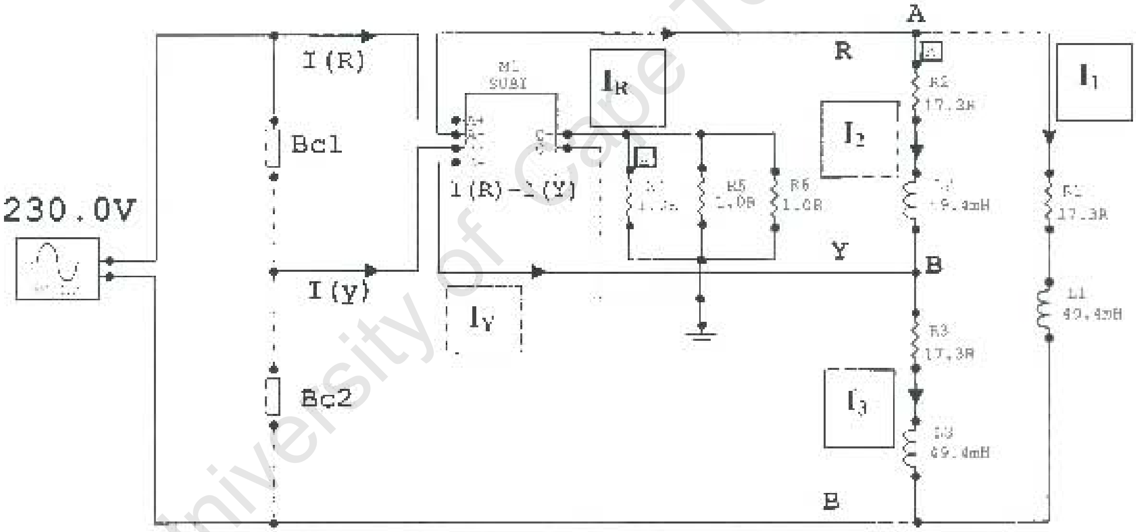

Fig: 4.2 Line and phase current relationship with an unbalanced supply

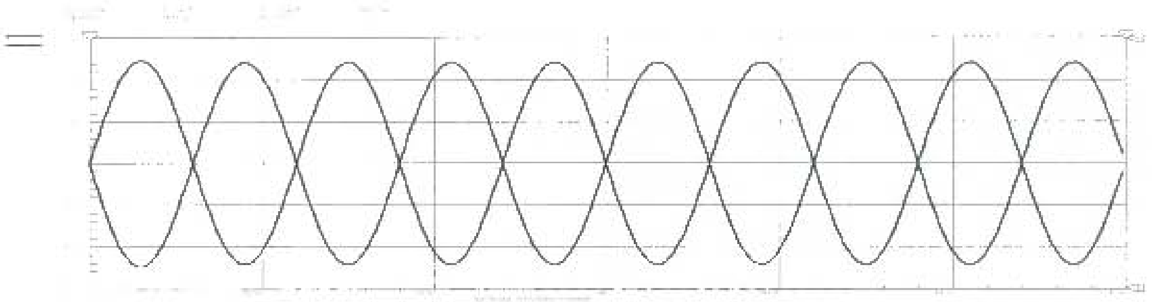

Fig: 4.3 Phase current sampling for unbalanced supply voltage

4.2 Method of calculation

The critical part of the algorithm is the calculation of load admittance. The measurement of load parameters can be done in time domain or frequency domain. Due to easy instrumentation, the time-domain approach is more attractive. However due to some fundamental problems this approach could prove quite ineffective.[7]. The main problem arises due to source voltage harmonics and the values of load succeptance at such harmonics. These harmonic succeptances (B_n) can be calculated, if harmonic reactive power (Q_n) is defined as:

$$Q_n = U_n . I_n . \sin\phi = -B_n . U^2{}_n \qquad \text{(Eq:4.2)}$$

and the voltage spectrum values are known.

Czarnecki [8] proposes a topology for measurement of reactive current rms value meter where each voltage and corresponding current harmonic is measured, generating proportional positive or negative DC values. This is based on the theoretical fact that the reactive current drawn from a voltage source is the sum of reactive current harmonic components shifted by π/2 Radians from the source voltage harmonics. This way the reactive power Q_n and the corresponding succeptances of load at various harmonics can be measured directly. The question arises here that, do the reactive current harmonics in reality always appear π/2 radians later than the corresponding voltage harmonics of the same order? The second problem that need to be addressed is, to what extent would the operation of a reactive current RMS meter would depend on the property of the various filters used?

For the purpose of single to three-phase conversion, the closest method of measuring the same quantities is the method of average values in time domain.
The converter's performance depends primarily on the accuracy of the dynamically measured values of the load parameters. In the following simulations, the following simplifying assumptions have been made,

- the source is a clear sinusoidal waveform which means no supply distortion has been taken in to account and the scattered currents component of the source is assumed zero.
- the reactive components are linear and lossless,
- the converter operates under steady state conditions.

4.3 Power analysis

Calculation of average active and reactive power for a single phase of a balanced three-phase load can be initially done using a Matlab model where a line-line voltage and a phase current are used as inputs. This is shown in fig:4.4.

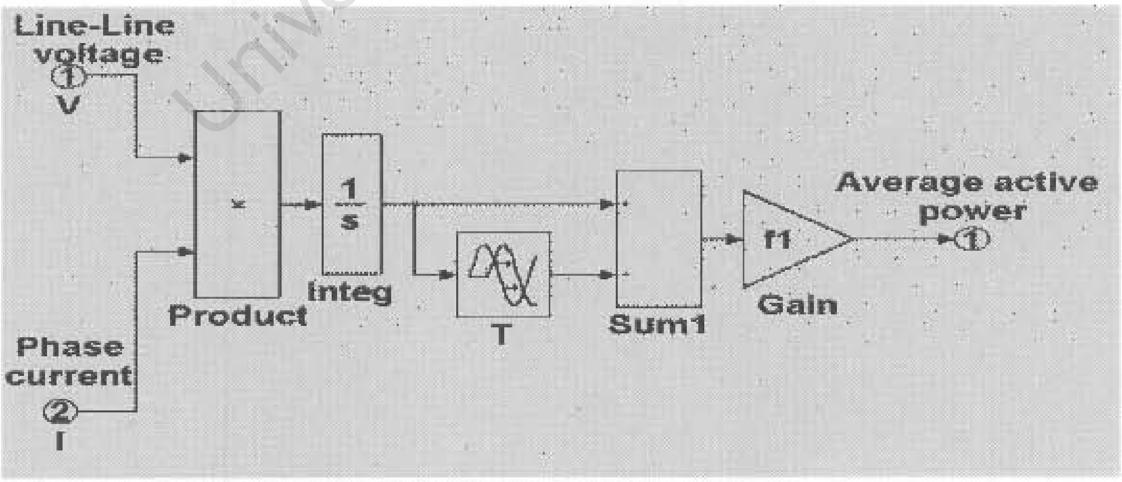

Fig: 4.4 Matlab modeling for average active power measurement

The product of the voltage and current is integrated to find the area under the power curve. T is the phase shift equivalent to one cycle of the power curve frequency in which by subtracting it from the output of the "integ" block, the net average power per cycle of the input is determined. Finally the function of "f1" is to ensure that the output power is calculated for the correct frequency of the power curve. The change in the model for the measurement of average reactive power is based on the voltage being shifted by π/2 radians and then the same steps as before are repeated.

$$Q_{average} = \frac{1}{T}\int^{T}\{v(\omega t - \frac{\pi}{2}).i(\omega t)\}d(\omega t)$$

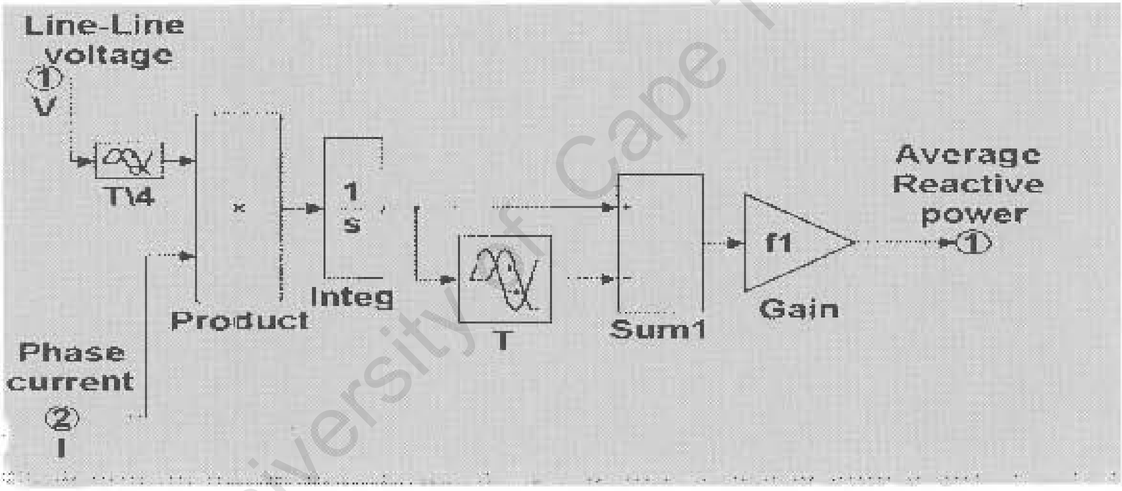

Fig: 4.5 Matlab modeling for average reactive power measurement

The above models can be further developed to calculate the load conductance and succeptance. The block diagram in fig:4.6 shows the layout of the model.

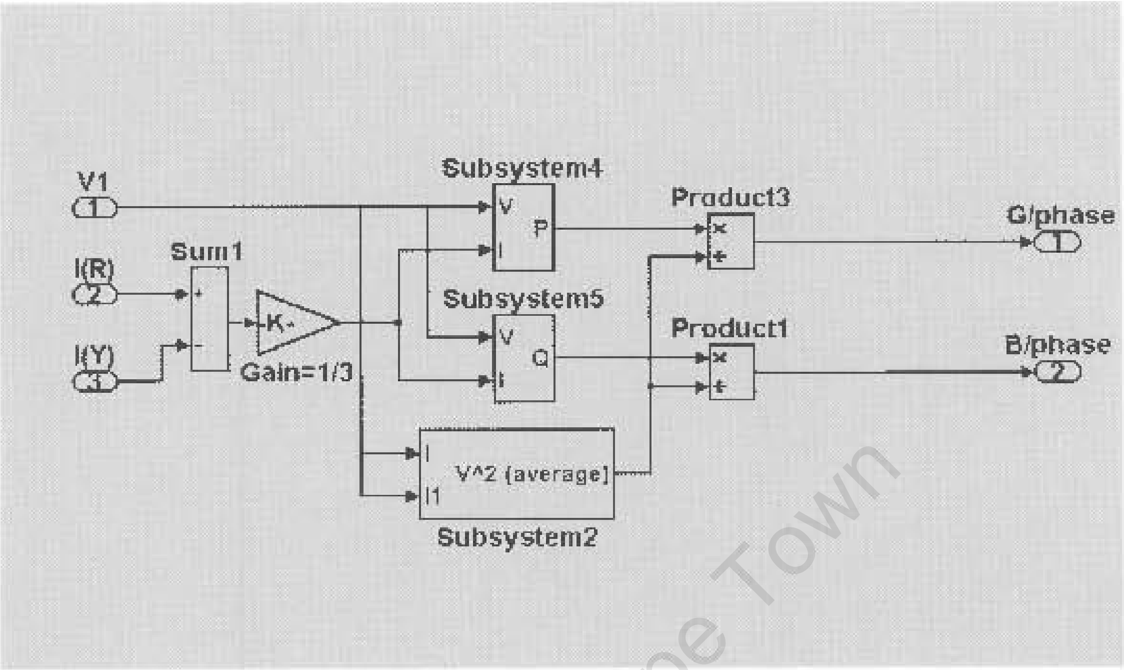

Fig: 4.6 Matlab modeling for three-phase load parameter measurement

The operation of the model in fig:4.6 is based on: $G = \frac{P}{V^2}$ & $B = \frac{Q}{V^2}$. It is possible to extend the model to calculate other load parameters such as power factor and the components of the impedance as well. These are implemented later in this chapter

The final step of this series of modeling is the computation of the passive elements used by the converter. It takes into account the possibility of each converter passive element being capacitive or inductive.

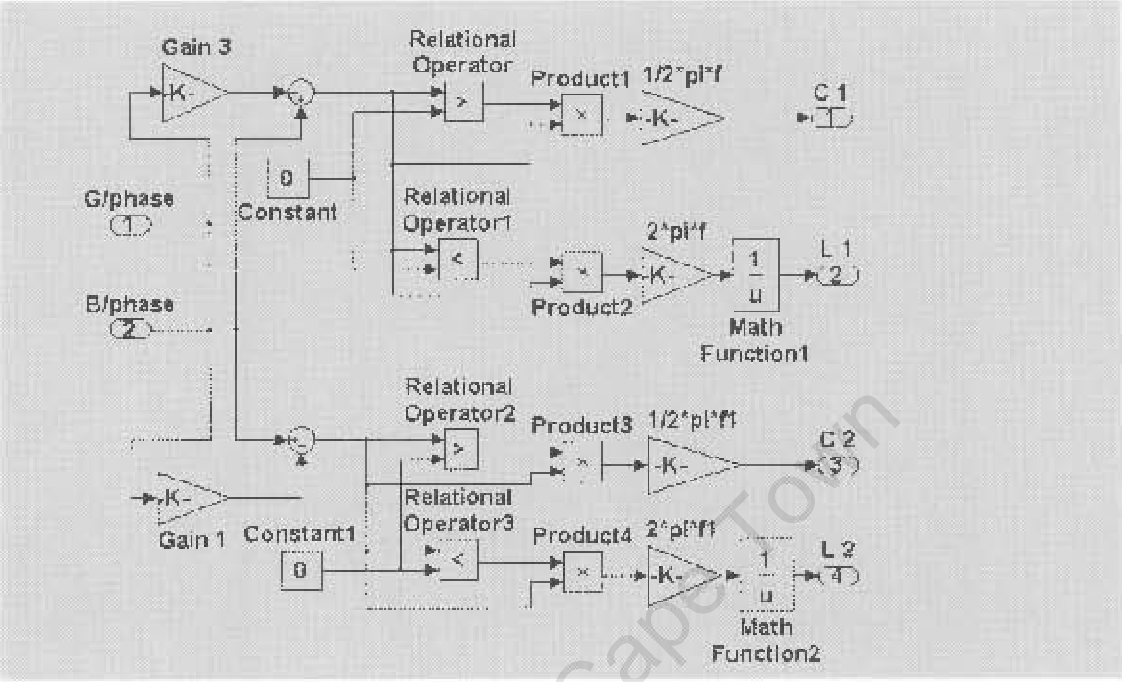

Fig: 4.7 Matlab modeling for calculation of converter elements

The complete model can be tested for two extreme load conditions. Initially, random Bc_1 and B_{C2} are placed across the load. Fig: 4.8 has been used for a balanced 3-phase resistive load of 20 Ω/phase. The model indicates a conductance value of 0.05 Siemens. A small succeptance is calculated which can be ignored. The exact values of the passive elements required, to generate a balanced three-phase voltage across the load terminals are displayed. By replacing the converter's succeptances in the model, the correct phase and line currents can be displayed on scope1and 2.

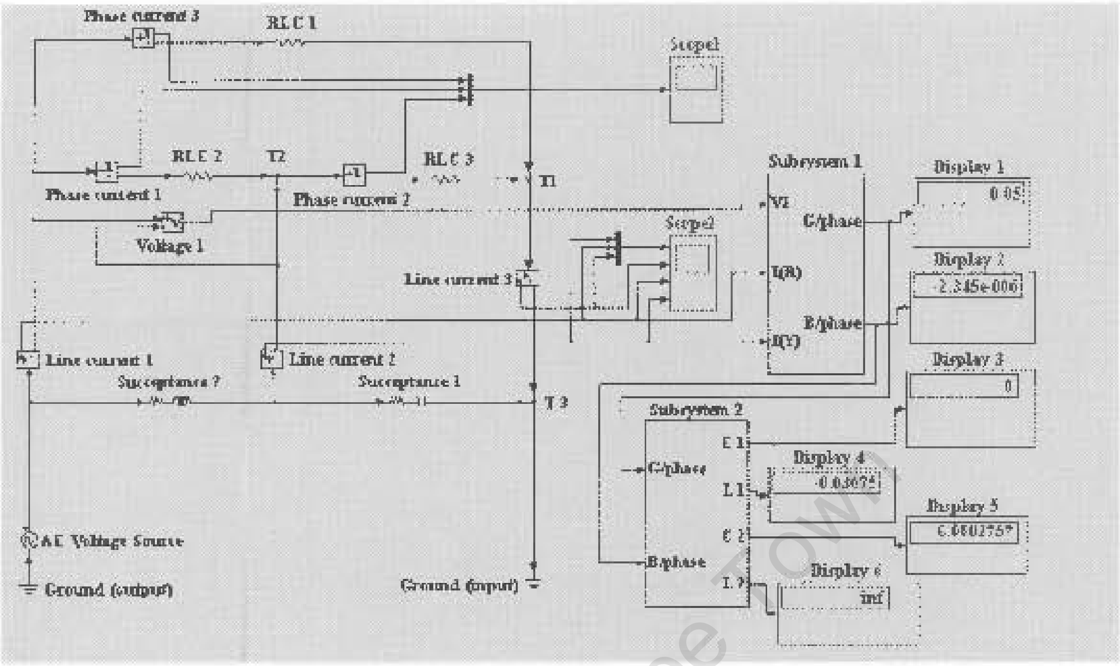

Fig: 4.8 Modeling of 3-phase resistive load and converter element calculation for balancing the supply voltage

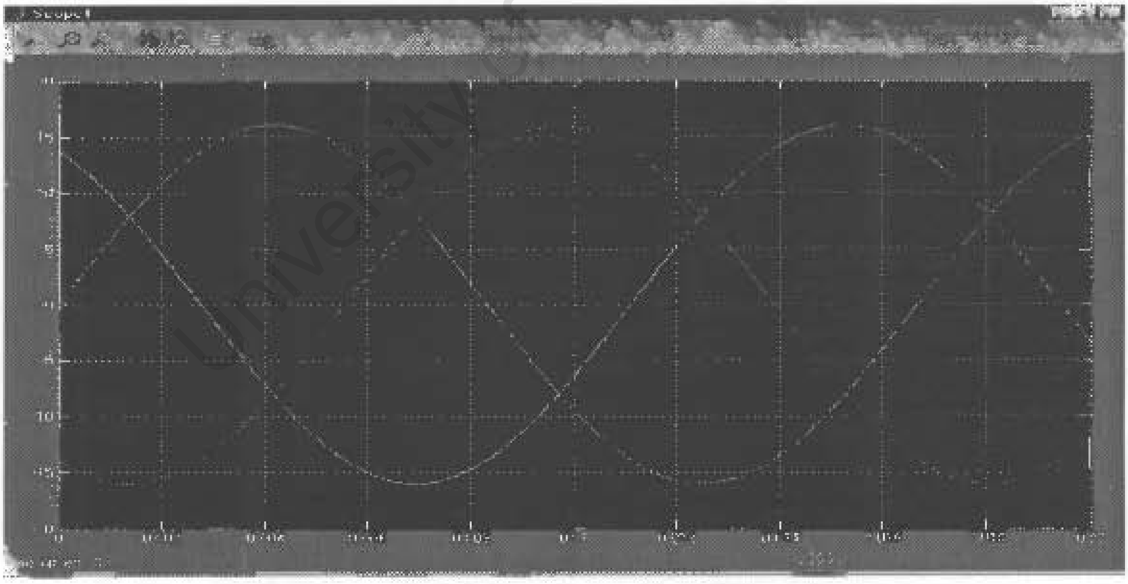

Fig: 4.9 Phase currents for 3-phase resistive load after voltage compensation

Fig: 4.10 shows the operation of the model with a highly inductive load of 20.0Ω in series with a 0.5 Henry inductance. The load power factor of less than 0.5

lagging, both converter elements are capacitive. Phase current waveforms are shown in Fig:4.11.

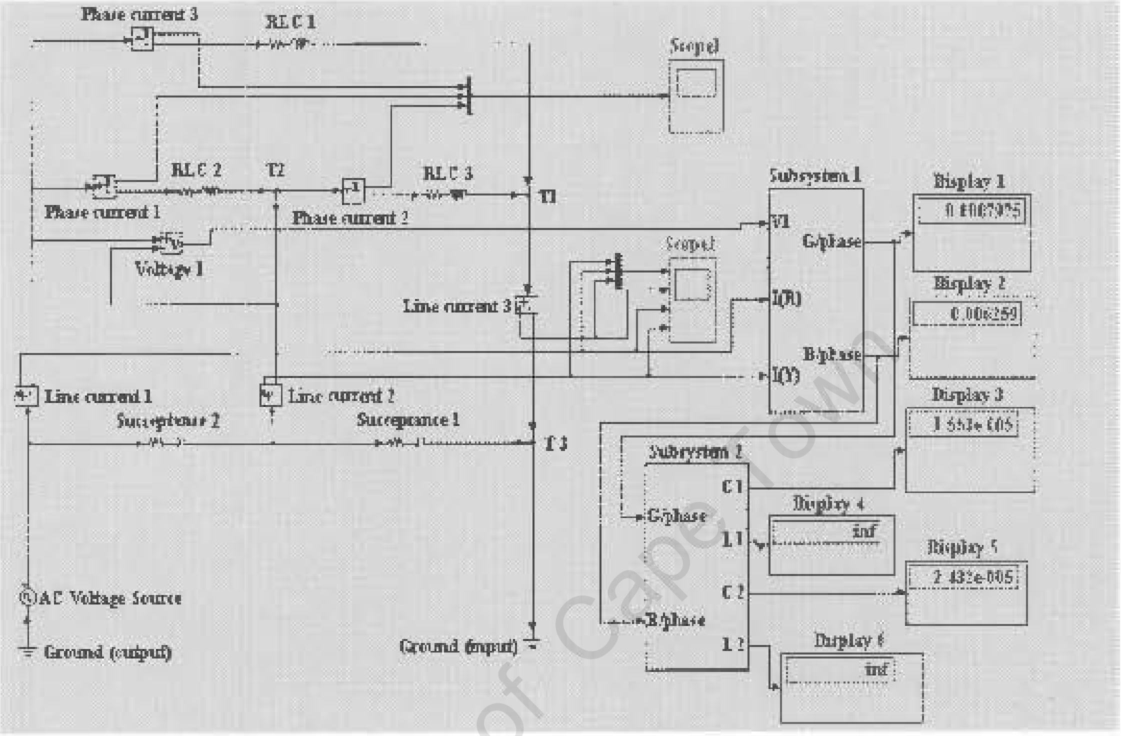

Fig: 4.10 Modeling of 3-phase inductive load and converter element calculation for balancing the supply voltage

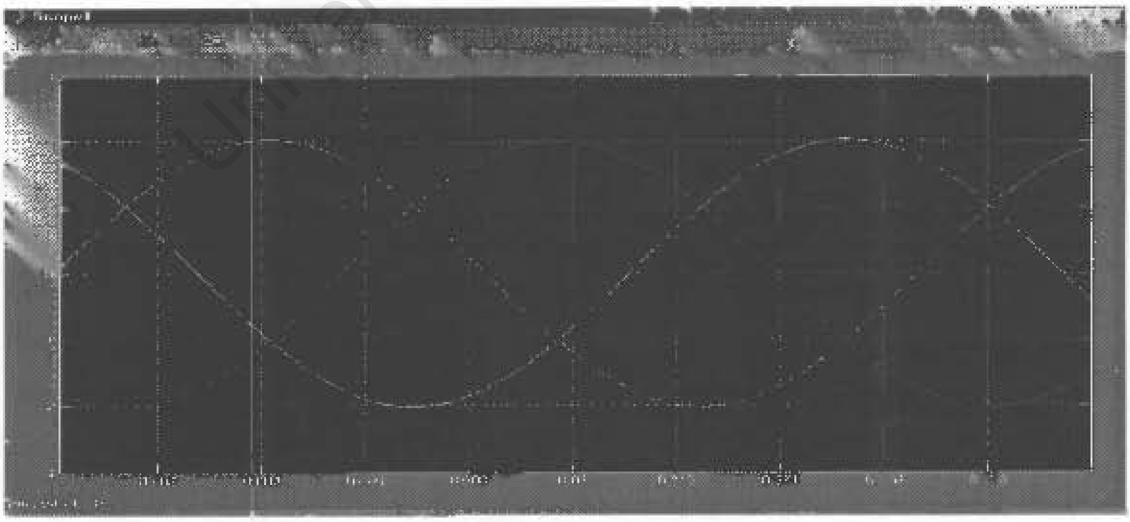

Fig: 4.11 Phase currents for 3-phase inductive load after voltage compensation

With the modeling completed, the construction of a more general controller, using analogue components will start in the following chapter.

Chapter 5

5.1 Adaptive controller

The aim of this chapter is to design an analogue circuit capable of generating at least two positive and/or negative DC signals (-10 to +10 volts), representing the values of the passive elements used in the converter to balance the supply voltage. In the hardware to be developed, there will be a gain factor relating the generated DC values to the actual values of the converter elements.
The power rating of the motors used will depend on the scale-factor reduction selected for the input line voltage and currents. Initially, it is intended to build a controller for three-phase induction motors in the range of one to five kW.

With reference to fig:4.1, the first circuit diagram of these series in fig:5.1 can produce an output voltage of the same magnitude and phase as the phase current of a three-phase balanced delta connected load.

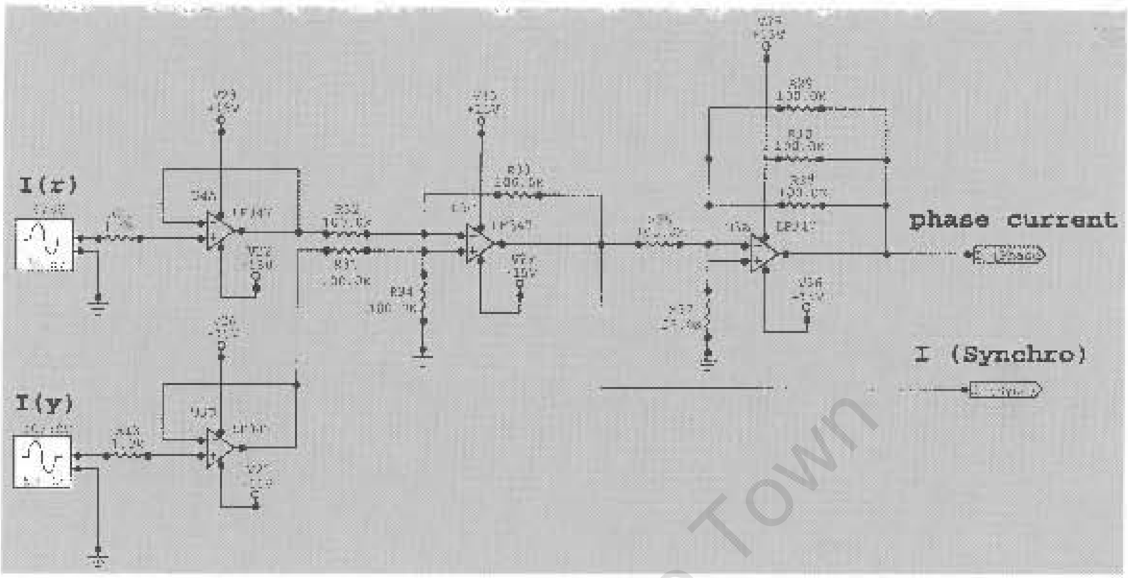

Fig: 5.1 Sampling of phase current from two line currents of a three-phase load

I_r and I_y represent the line currents of any magnitude and phase angle.

The current sensors (LEMS) produce one volt at the output for each amp passing through the input. This limits the input line currents to 8.5 Amps and the maximum power dandling capability of the controller at an average power factor of 0.8 becomes 240*8.5*0.8=1632 Watts. Clearly, by adjusting the current sensors to produce less output voltage for each input amp of current, the VA measuring ability of the controller can be increased. Second part of the controller is the average active and reactive power measurement. In order to calculate various parameters of the converter and the load, a number of multiplications and divisions are implemented using AD633, which performs these functions. Fig: 5.2 on the next page shows the circuit diagram.

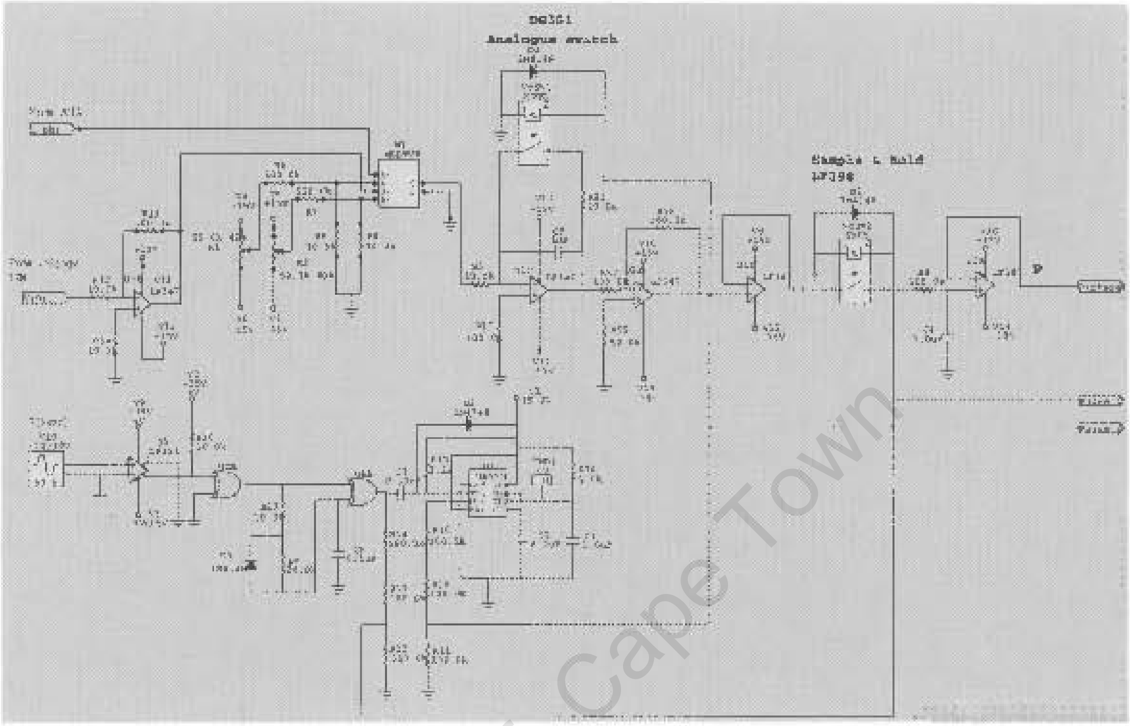

Fig: 5.2 Average active power meter

To obtain an equivalent DC value for average reactive power/phase of the load, the line-line voltage has been shifted using a phase shifter. Then multiplication, integration and sample and holding are the next three steps. The crucial part of these designs is to synchronize two trains of pulses. One set to allow the sample and holder to charge up the output capacitor and a second set, to immediately reset the integrator at every 1/2 cycle of the current signal. Fig: 5.3 demonstrates how this has been achieved.

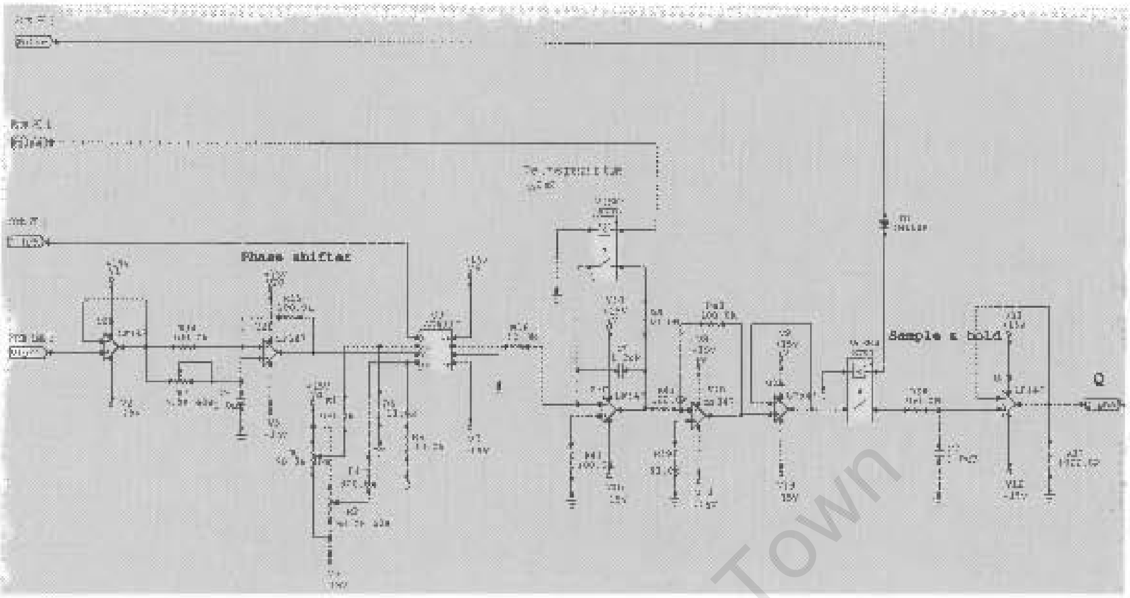

Fig: 5.3 Average reactive power meter

AD633 in different configurations is capable of multiplication, division, square and square rooting of AC and DC signals. Having the values of average P and Q, a line-to-line voltage has to be squared and averaged. Fig: 5.4 shows the circuit diagram.

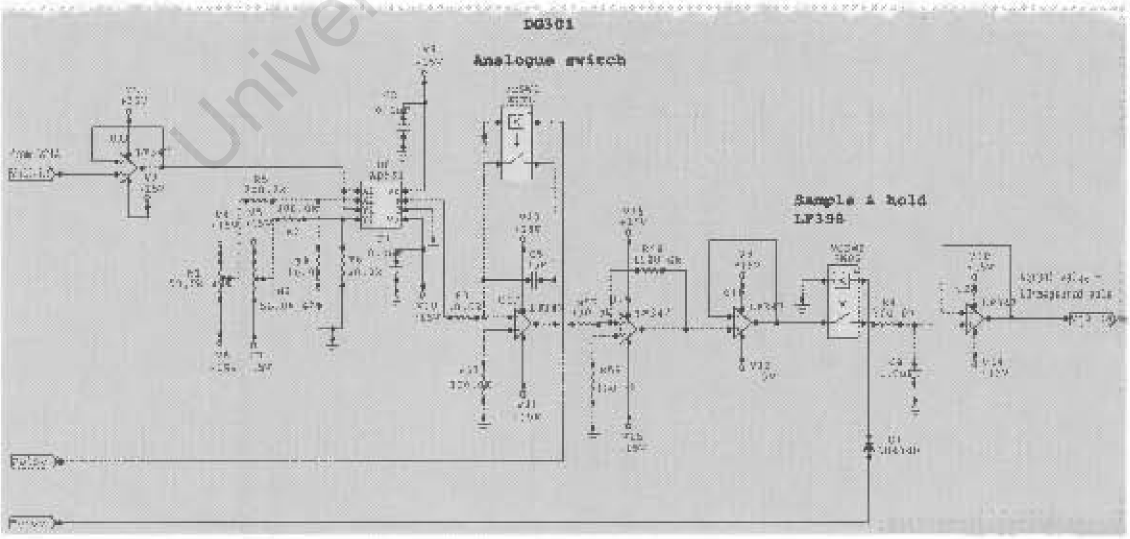

Fig: 5.4 Circuit diagram for the average value of V^2

The fourth stage of the design is two simultaneous divisions to generate positive or negative DC voltages proportional to the load admittance and susceptance per phase. The simplified version of this stage is shown in fig: 5.5.

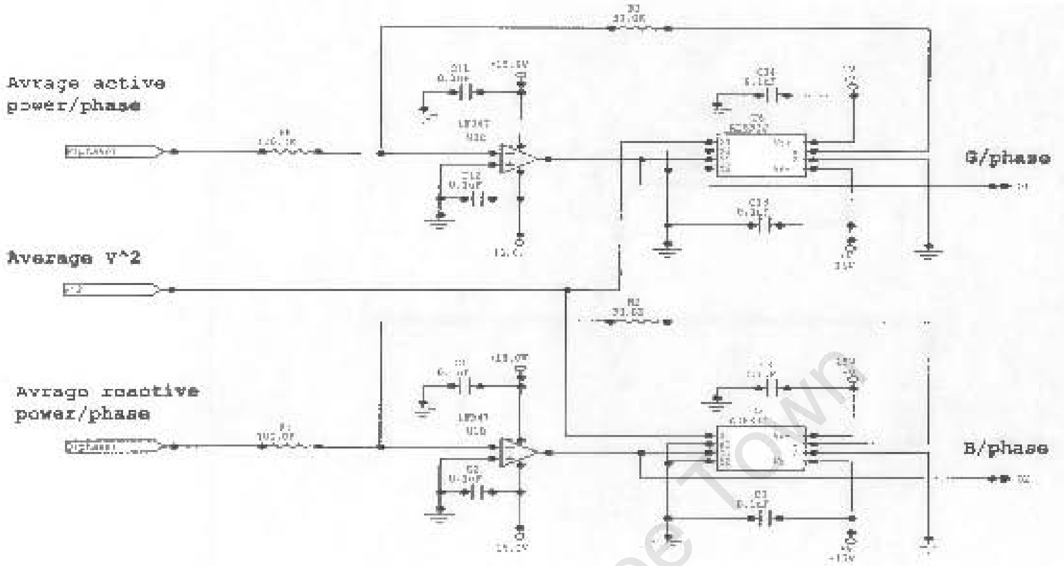

Fig: 5.5 Load admittance and susceptance meter

Next and the final step of the design is to implement the equations in Eq: 2.1.16 and obtain the required DC values proportional to the susceptances for each converter element. This has been illustrated in fig: 5.6.

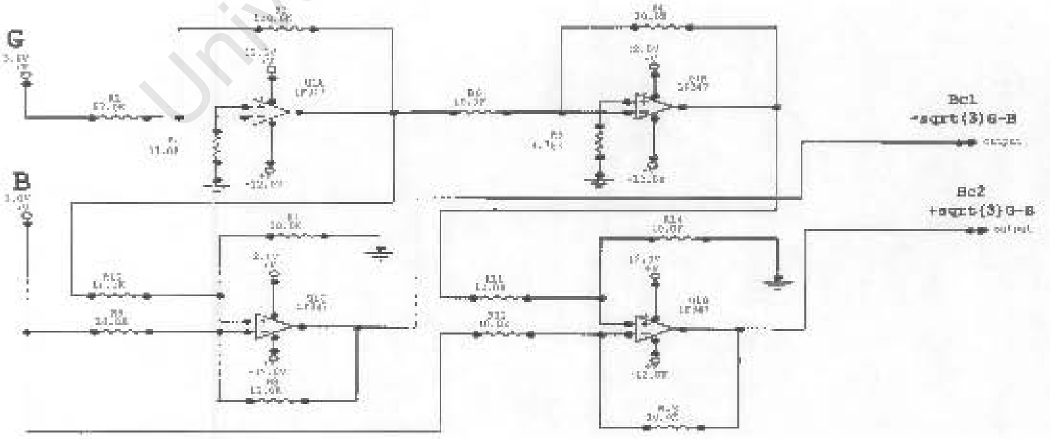

Fig: 5.6 Generation of two DC voltages proportional to converter's susceptances

The forth stage of the design is two simultaneous divisions to generate positive or negative DC voltages proportional to the load admittance and succeptance per phase. The simplified version of this stage is shown in fig: 5.5.

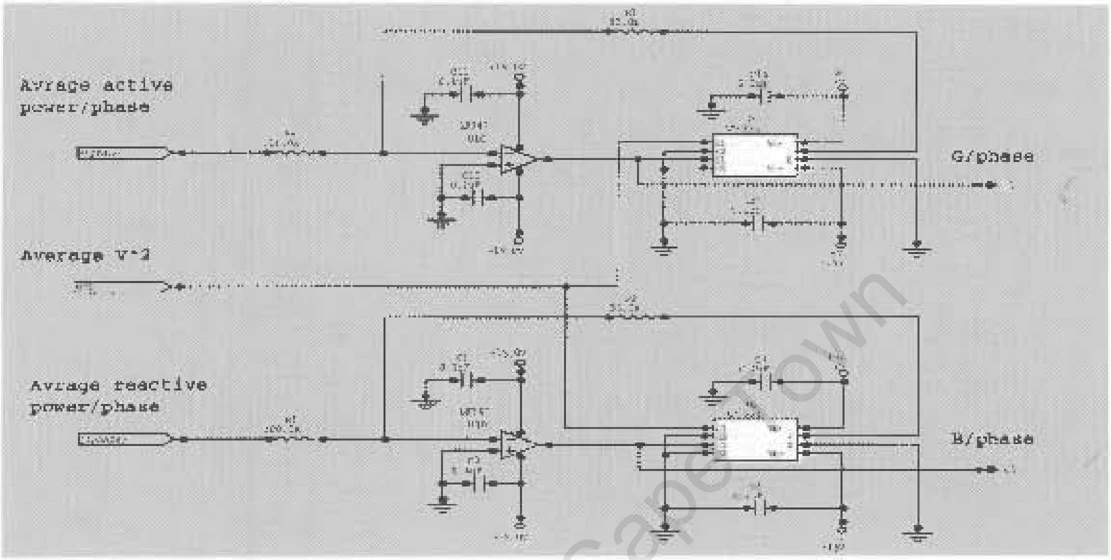

Fig: 5.5 Load admittance and succeptance meter

Next and the final step of the design is to implement the equations in Eq: 2.1.16 and obtain the required DC values proportional to the succeptances for each converter element. This has been illustrated in fig: 5.6.

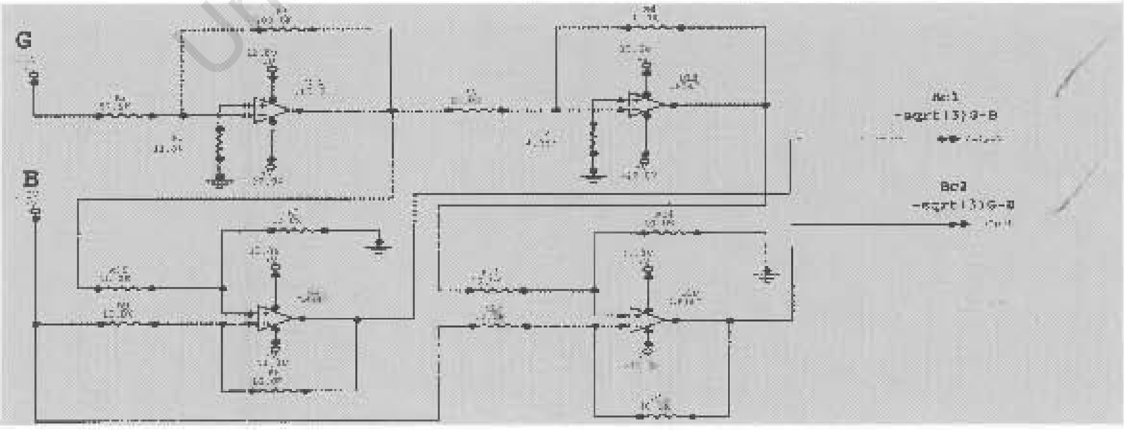

Fig: 5.6 Generation of two DC voltages proportional to converter's succeptances

5.2 Simulated and experimental results

Simulated values have been plotted to produce a guideline on the values of converter values. Fig: 5.7 shows the simulated variation of B_{C1} and B_{C2} versus power factor of a variable resistive load of zero to 100.0 Ω in series with a fixed 350.0 mH inductor.

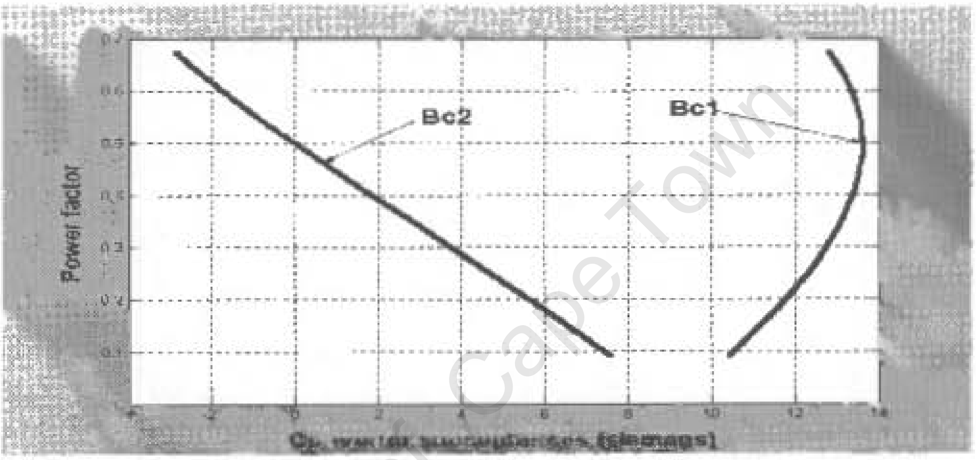

Fig: 5.7 simulated values of converter succeptances versus load PF

As far as cost is concerned, the ratings of the converter elements kVAr in terms of the load kW is shown in fig: 5.8.

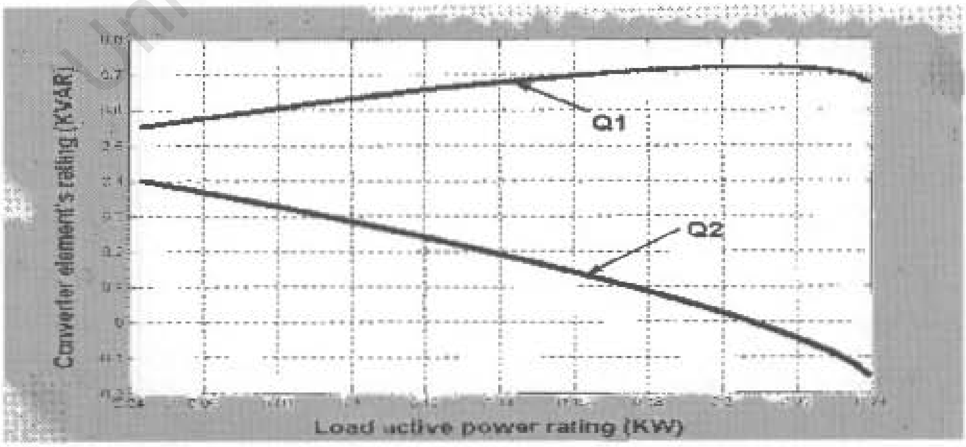

Fig: 5.8 Variation of converter elements kVAr versus load active power (kW)

Experimental results have been obtained in the following manner. First, the adaptive compensator has been tested with a bank of resistive load connected in delta across a 230V line-line voltage. RMS based instruments have been used to measure the relevant voltages, currents and powers. Load stepping of 100.0W has been adapted. The comparison between the actual active power measured through the instrumentation and the average power measured using the adaptive compensator is shown in fig: 5.9.

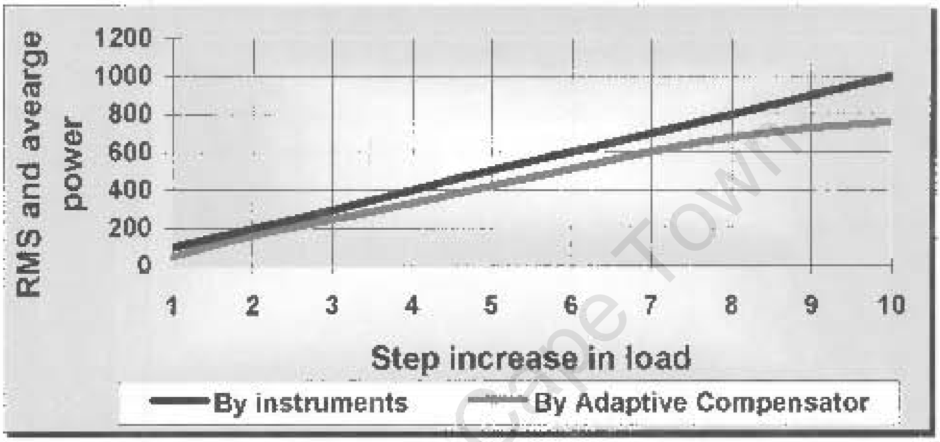

Fig: 5.9 Power measurement using RMS values / average values

Results show that the power readings taken from the instruments are consistently larger than the average power by a factor of nearly 1.2. This can be explained through the term "form factor" of 1.1, which is the ratio of the RMS to average value for a sinusoidal voltage or current.

$$P_{RMS} = 1.1 * V_{average} * 1.1 * I_{average} = 1.21 * P_{average}$$

The oscilloscope captured DC voltages from the adaptive compensator representing the load conductance is compared with the actual values calculated from the instruments. The results are shown in fig: 5.10.

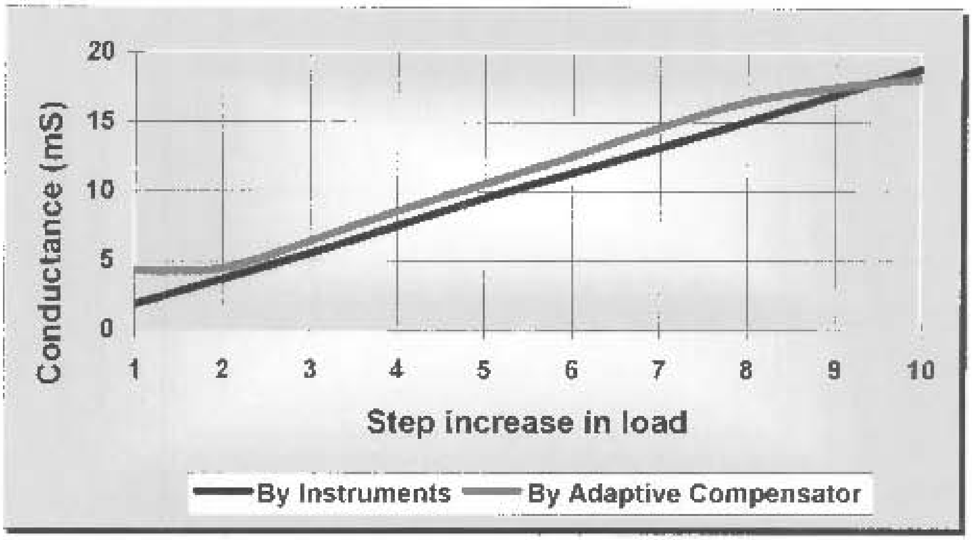

Fig: 5.10 Load conductance measurement using instruments/Adaptive Compensator

The two lines in fig: 5.10 should ideally be superimposed. However, the error margin is small and consistent for a large range of load conductance.

The pattern for the values of converter succeptances are as expected, fig: 5.11 shows the measured values plotted versus the loading steps.

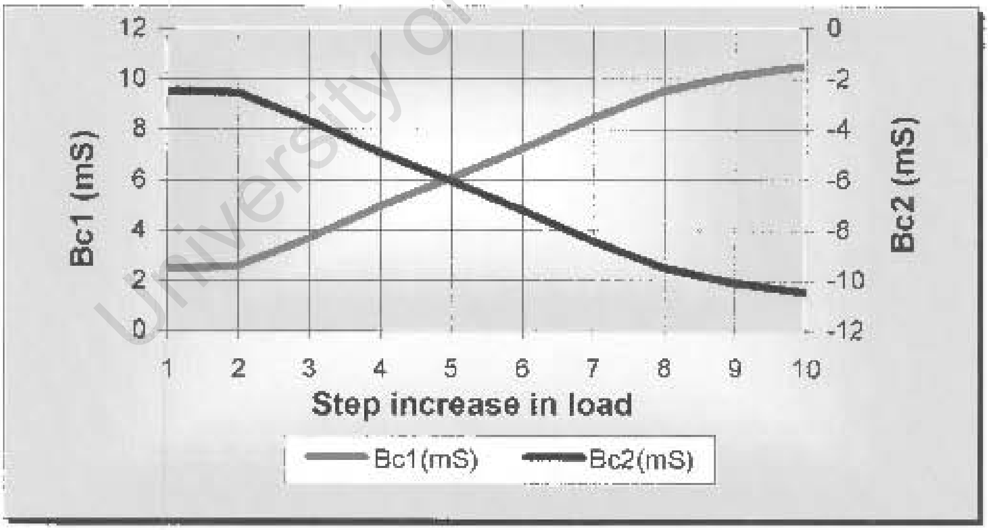

Fig: 5.11 Converter succeptances for resistive loads

It can be seen that the above DC voltages are well within the intended range. For a particular commercial application, initially, the range of converter elements in uF and mH has to be known to the designer. Although the adaptive converter is not required to deliver DC values representing the capacitance or inductance of these elements, the values can be manually calculated and shown in fig: 5.12.

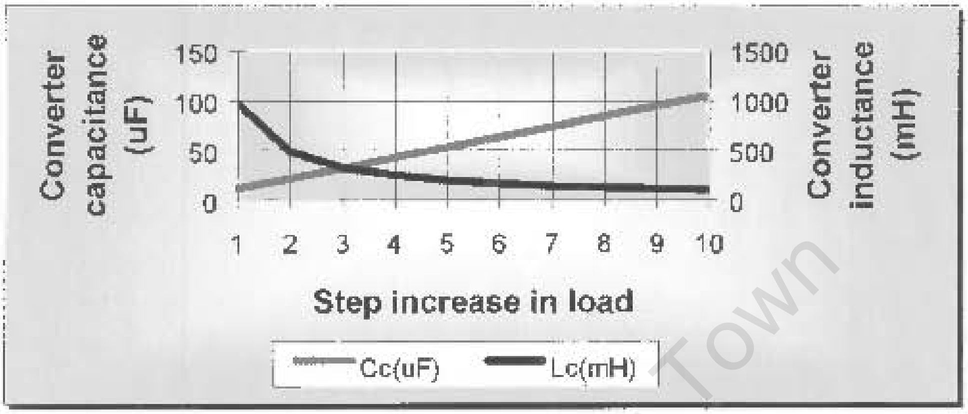

Fig: 5.12 Variation of converter elements values with resistive loading up to 1.0 KW

In fig: 5.13 and 5.14, for a load of 500 W, one set of simulated values is followed by a set of after compensation load voltages.

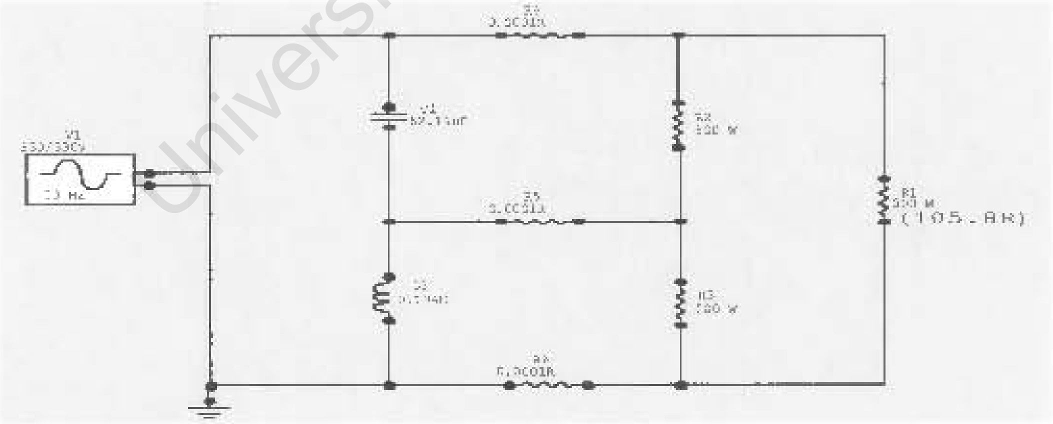

Fig: 5.13 Voltage compensation for a 500 W heating element

It can be seen that the above DC voltages are well within the intended range. For a particular commercial application, initially, the range of converter elements in uF and mH has to be known to the designer. Although the adaptive converter is not required to deliver DC values representing the capacitance or inductance of these elements, the values can be manually calculated and shown in fig: 5.12.

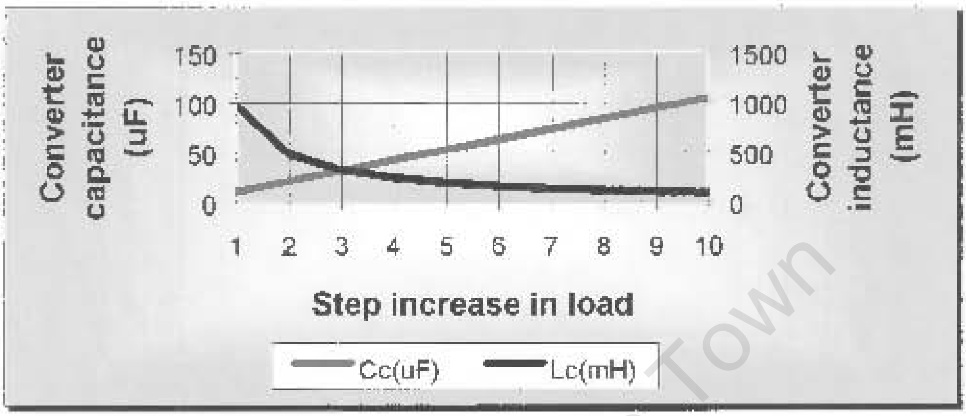

Fig: 5.12 Variation of converter elements values with resistive loading up to 1.0 KW

In fig: 5.13 and 5.14, for a load of 500 W, one set of simulated values is followed by a set of after compensation load voltages.

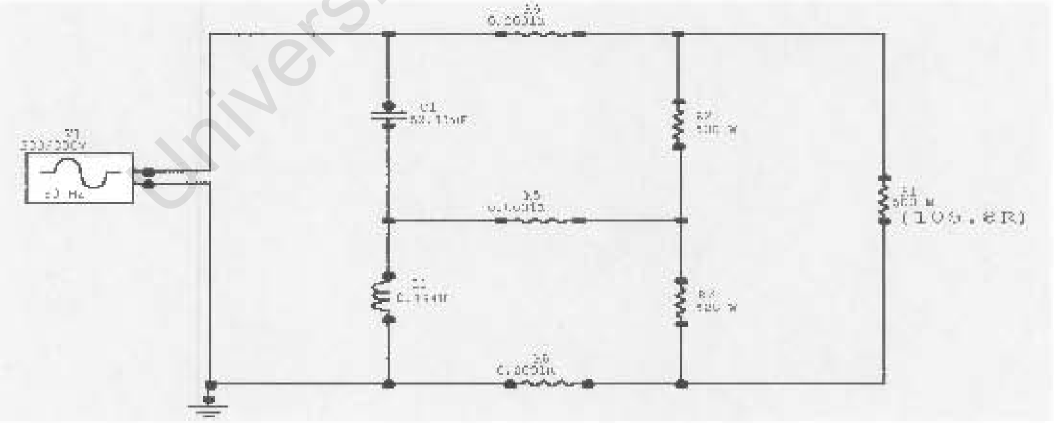

Fig: 5.13 Voltage compensation for a 500 W heating element

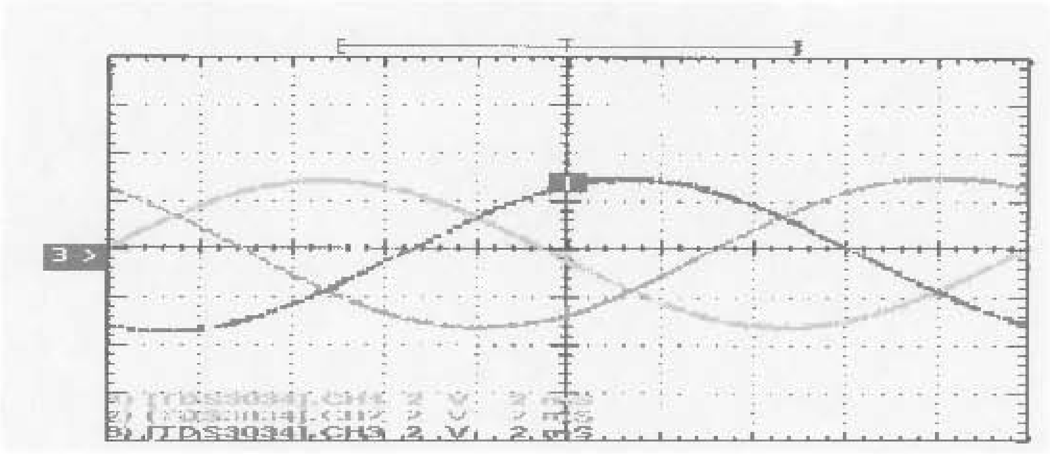

Fig: 5.14 Terminal voltages captured for voltage compensation with 500 W resistive load

The second set of results is for pure inductive loads. In this experiment a range of inductors (0.2-1.5 H) has been tested in five steps. The average reactive power per phase of the load has been measured and compared with those obtained from the instruments. The results are shown in fig: 5.15.

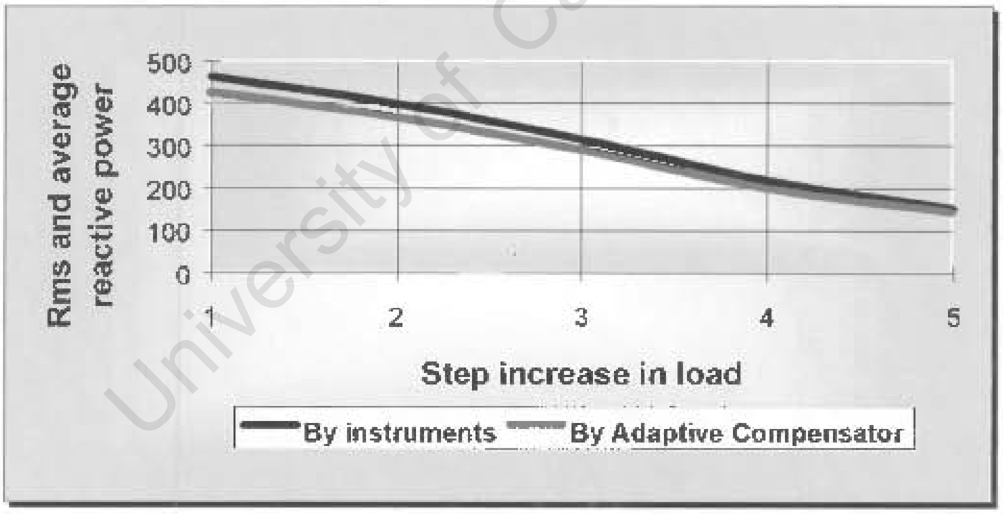

Fig: 5.15 Reactive Power measurement using RMS values / average values

The load succeptance readings using instruments and the compensator have been shown in fig: 5.16.

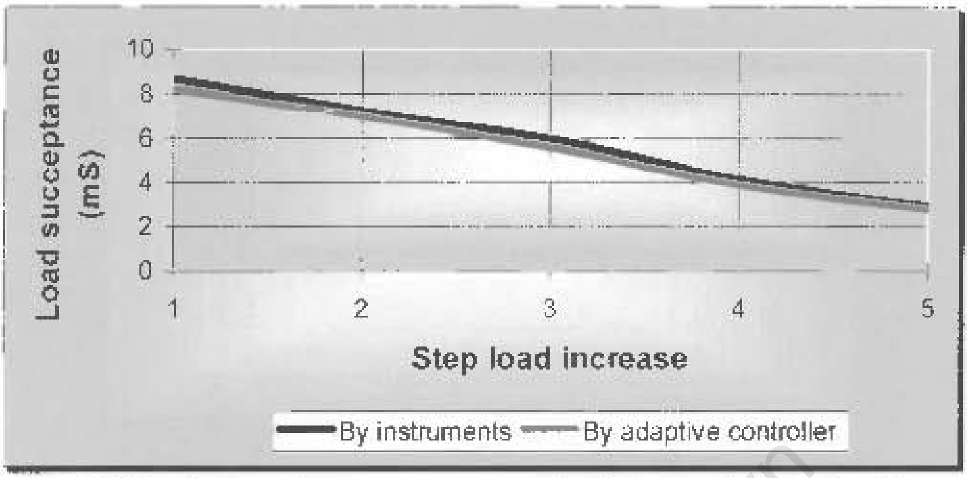

Fig: 5.16 Load succeptance measurement using instruments/Adaptive Compensator

As it is expected, the converter elements have the same value and are both capacitive. Fig:5.17 shows the measured variations versus load inductance/phase.

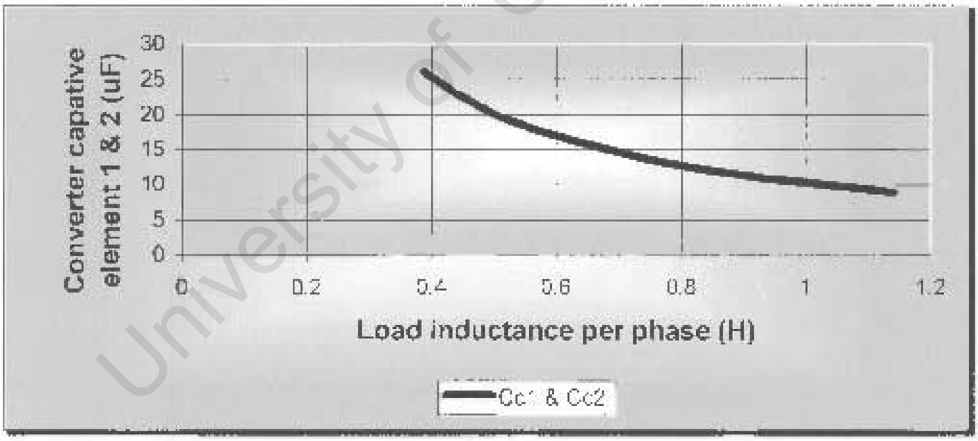

Fig: 5.17 Variations of converter elements for a pure inductive load

Although the values are well within the anticipated range of accuracy, the situation is highly unstable and impractical. The main reason is the load resonating with the converter elements.

With sufficient confidence in the accuracy of the adaptive compensator with individual resistive and inductive load, a combined load can then be tested. The final set of results is collected for a three-phase induction motor of 750 W at 220 V (delta connected). The loading is constant in steps such that the motor line current is increased by 0.1 A. The no-load current is 2.6 A. The maximum available load corresponds to a line current of 3.4A. fig:5.18 shows the variation of load conductance and succeptance with the phase current.

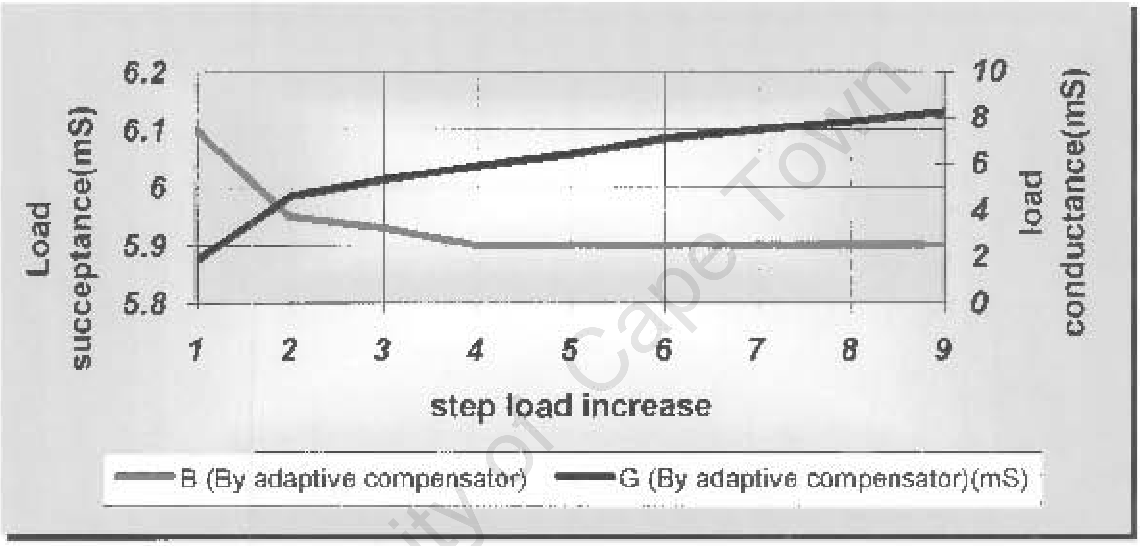

Fig: 5.18 Changes in motor conductance and succeptance with input current

The variation of converter's succeptances versus load current has been demonstrated in fig: 5.19.

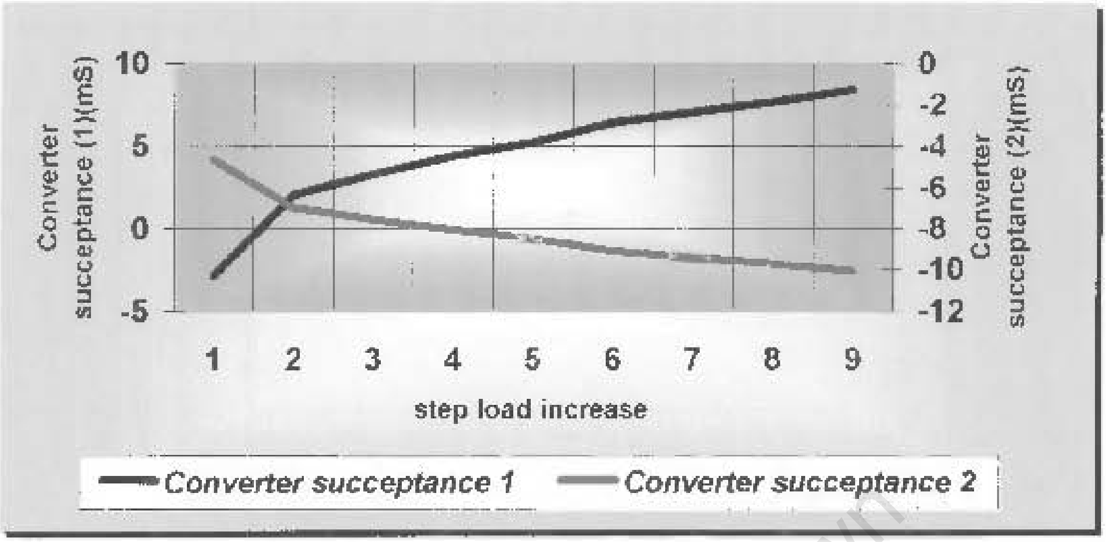

Fig: 5.19 Converter variation of succeptances under various loading conditions

The actual values of converter passive elements are plotted in fig: 5.20.

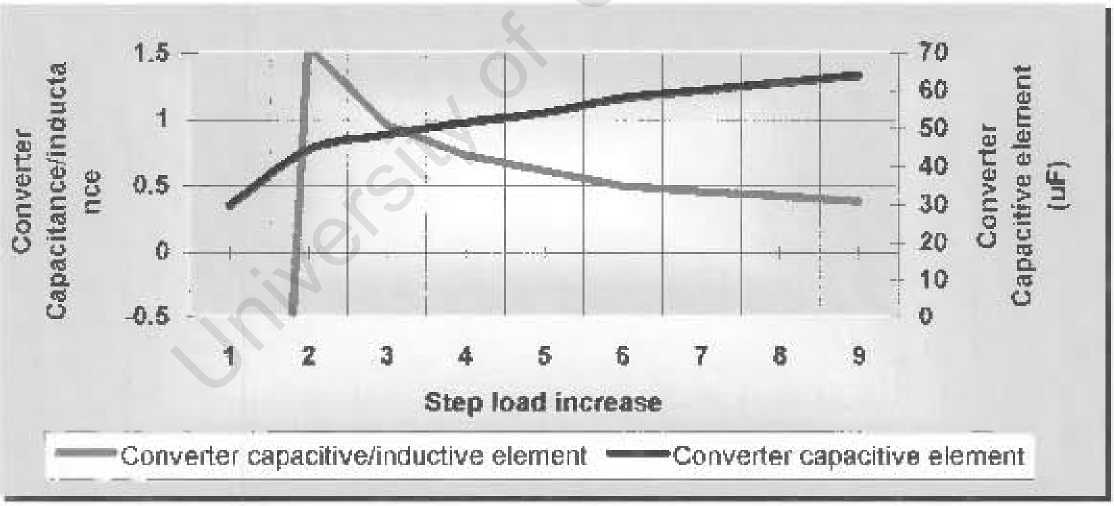

Fig: 5.20 Variation of converter elements with load

Several loading steps have been tested. The actual values of Bc1 and Bc2 have been magnified by a factor of 1000 in order to make useful activating signals. The problems experienced in designs such as in fig: 5.6 are the rapid saturation of the output voltages. Also small output voltages up to one volt are difficult to measure and use as activating signals. For example, small values of load resistance cause the DC equivalent value of B_{C2} which is equal to $-\sqrt{3}G-B$, to saturate almost immediately and an attenuation factor of 1/2, 1/3 or 1/4 has to take over automatically. Various op-amp configurations with automatic variable gain have to be incorporated.

Several loading stages have been setup with the converter appropriate succeptances in place and satisfactory balanced load voltages have been achieved. At the end of this chapter, the scope-captured load-voltages at half-load and full-load have been shown in fig: 5.21 and 5.22.

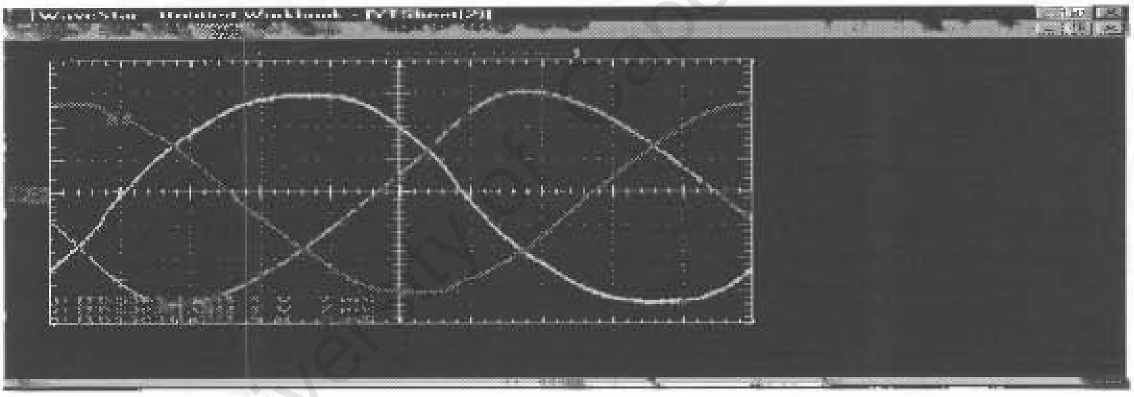

Fig: 5.21 Load voltage at half full-load

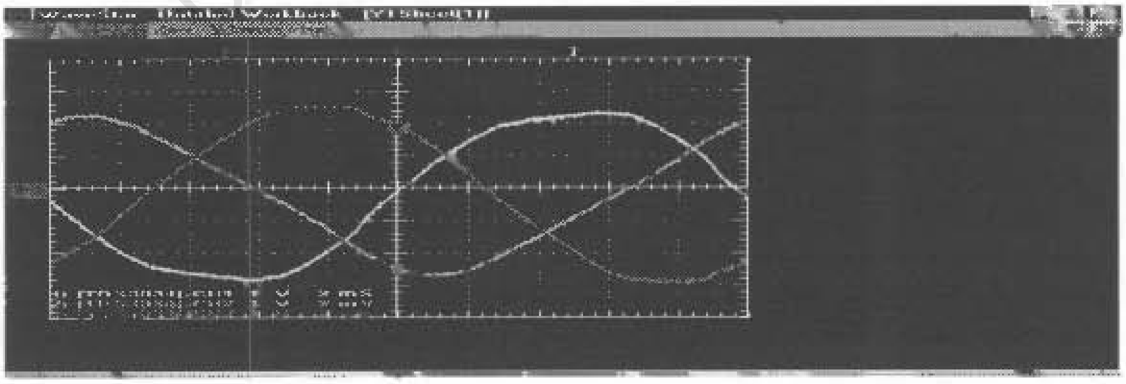

Fig: 5.22 Load voltage at full-load

With the final goals of the thesis accomplished at this point, the next and final chapter of this thesis presents an investigation on the concept of "Real-Time Simulation." The technique came to the author's attention towards the end of this report. Nevertheless, it has been a true eye-opener and well worth the time and effort spent on it.

Chapter 6

6.1 Standard versus Virtual Measurement

The analogue boards previously designed for mathematical calculations of load and converter succeptances, have some drawbacks, which lead to discrepancies between the values of the real and simulated outputs. The main sources of error are attributed to,

1. DC offset voltages and currents from integrated circuits are accumulative and compensation is often inconvenient if not impossible,
2. the output signals from various integrated circuits can saturate. Care must be taken to avoid this, otherwise the measurements become invalid.
3. the main supply voltage is hardly ever a pure siniousoidal waveform. This is due to unevenly distributed single-phase loads, harmonics, dips, sags, etc.

In the non-real time simulation environment, (although to a large extend the inaccuracy of the components can be accounted for), it is impossible to generate accurate signals representing the supply distortions normally encountered. For example this can be seen in the supply voltage on a good day at some parts of Eastern-Cape. Waveforms and harmonic contents are shown in fig: 6.1.

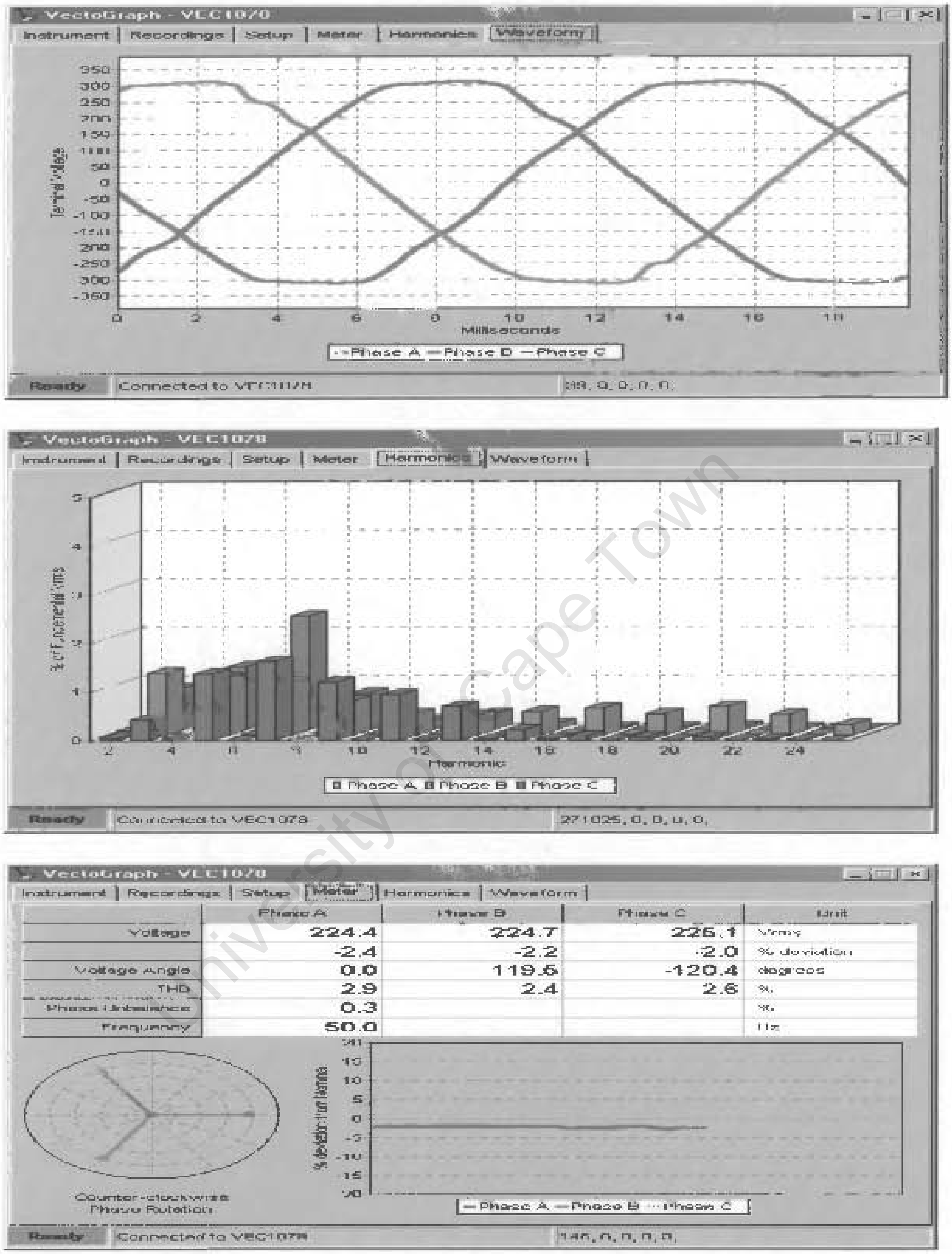

	Phase A	Phase B	Phase C	Unit
Voltage	224.4	224.7	226.1	Vrms
	-2.4	-2.2	-2.0	% deviation
Voltage Angle	0.0	119.6	-120.4	degrees
THD	2.9	2.4	2.6	%
Phase Unbalance	0.3			%
Frequency	50.0			Hz

Fig: 6.1 Waveforms and harmonic content of the mains at Eastern-Cape Technikon, East-London

A different approach to eliminate the above sources of error and prototype a passive-element converter is a PC-target solution. This is a “Model-Based Design” technique in which the load voltages and currents can be fed in to a “Real-Time Simulation” environment through data acquisition cards. A variety of electrical quantities such as currents, voltages, active and reactive powers, Fourier analysis, and THD can then be measured. Therefore, such powerful tool also eliminates the need for the actual measuring equipment during the prototyping stage. Based on the model’s structure, real output signals can be generated and be used to control external hardware such as TCI, TSC and saturable reactors.

The concept and architecture of “Real-Time simulation” in conjunction with “Virtual Instrumentation” and their powerful functionality is explained in details in appendix 1.5a.

6.1.1 Preliminary tests

In order to demonstrate the usefulness of this approach, a simple test is conducted to determine the accuracy of signal processing through the input compared with the signal at the output. Due to the speed of the computer processor, the highest possible sampling time is of 0.2 ms (5.0 KHz). This is shown in fig: 6.2.

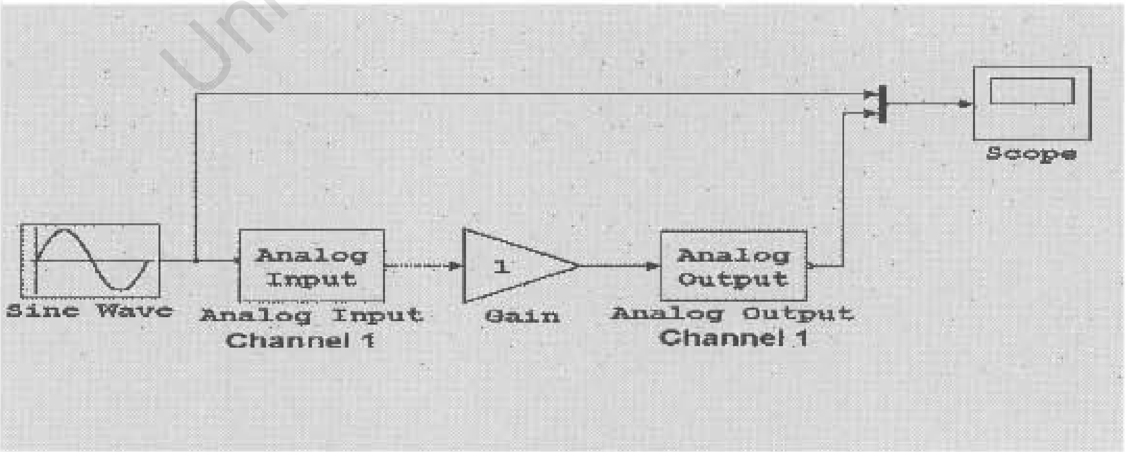

Fig: 6.2 Accuracy test for the CIO-DAS 1600 data acquisition card

The signals are captured before entering the "analog input channel" of the data acquisition card and at the output of the "analog output cannel." The two traces are identical and shown in fig:6.3. For clarity in comparison, a phase shift has been added.

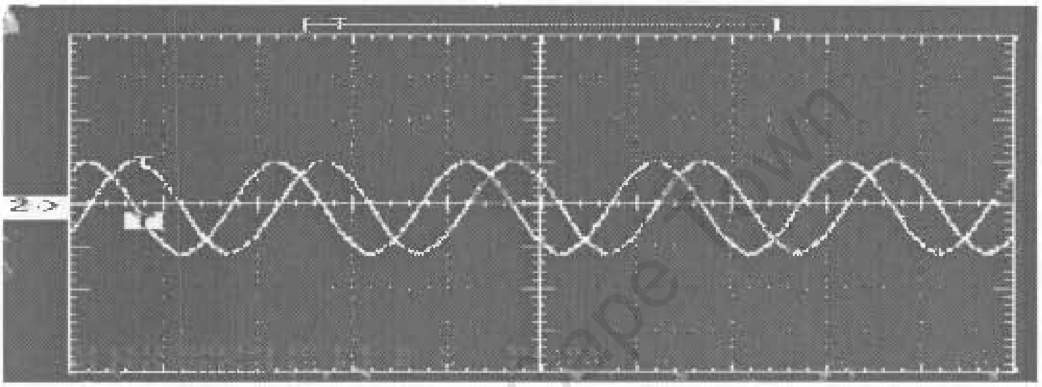

Fig: 6.3 Signal processing and accuracy of data capturing in Virtual Instrumentation

Second test aims at Virtual Measurement of current harmonics. With reference to chapter 4 section two on page 70, a model based on Fourier analysis is used to measure the current harmonic content of the reactor's AC current in real-time and compare them with the corresponding voltage harmonics. This will possibly bring out some verification in to the theory of harmonic succeptances and can demonstrate weather the harmonic reactive power and the corresponding succeptances of the load at various harmonic frequencies can be measured directly and accurately in the frequency domain, or the time domain and average values are the only possible approach.

Fig:6.4 shows the layout of the model. It can be set to odd multiples of the supply frequency and measure the magnitude and phase angle of the individual harmonics of the current and voltage waveforms. For the purpose of this experiment, the saturable reactor and the related hardware used previously have been used again. Although the mains harmonics are not constant throughout the day, the changes are small and can be neglected. The reactor has been driven in to saturation and for different AC currents the magnitude and phase angle of odd current harmonics have been captured and compared with those of the supply voltage.

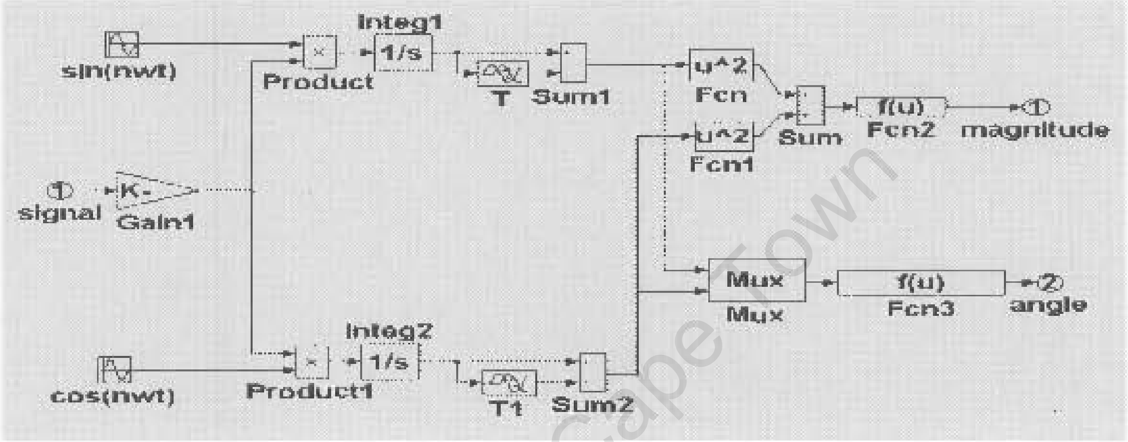

Fig: 6.4 Virtual Measurement of individual voltage or current harmonics

The above model can be expanded to measure the most dominant odd harmonics of the supply voltage at the same time. The expanded model is shown in fig: 6.5.

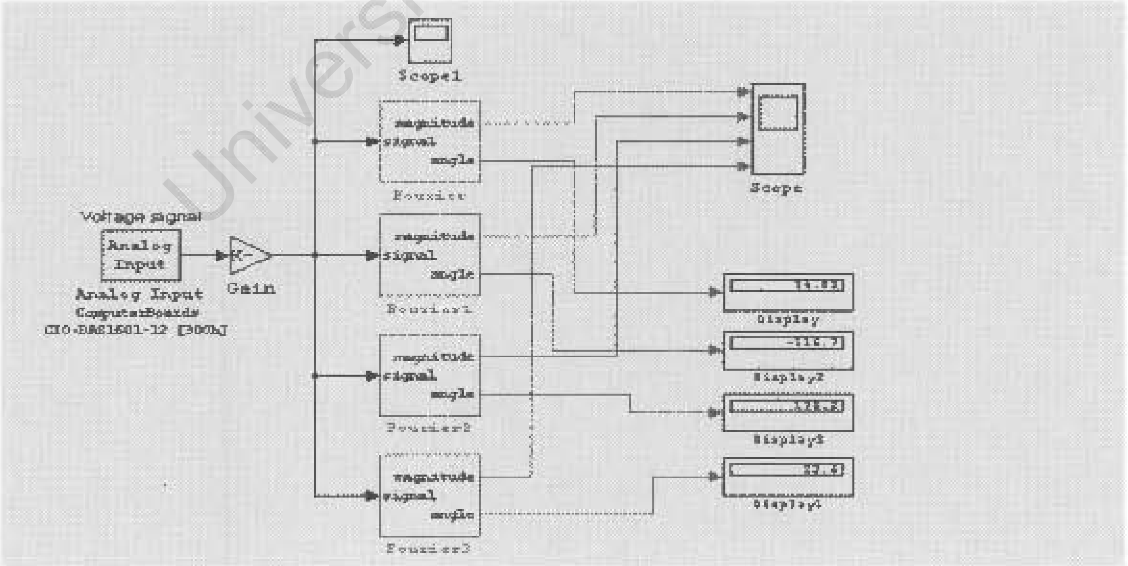

Fig: 6.5 Virtual measurement of odd order harmonics of supply voltage

Magnitude of the fundamental, 3rd, 5th and 7th harmonics are plotted in fig: 6.6.

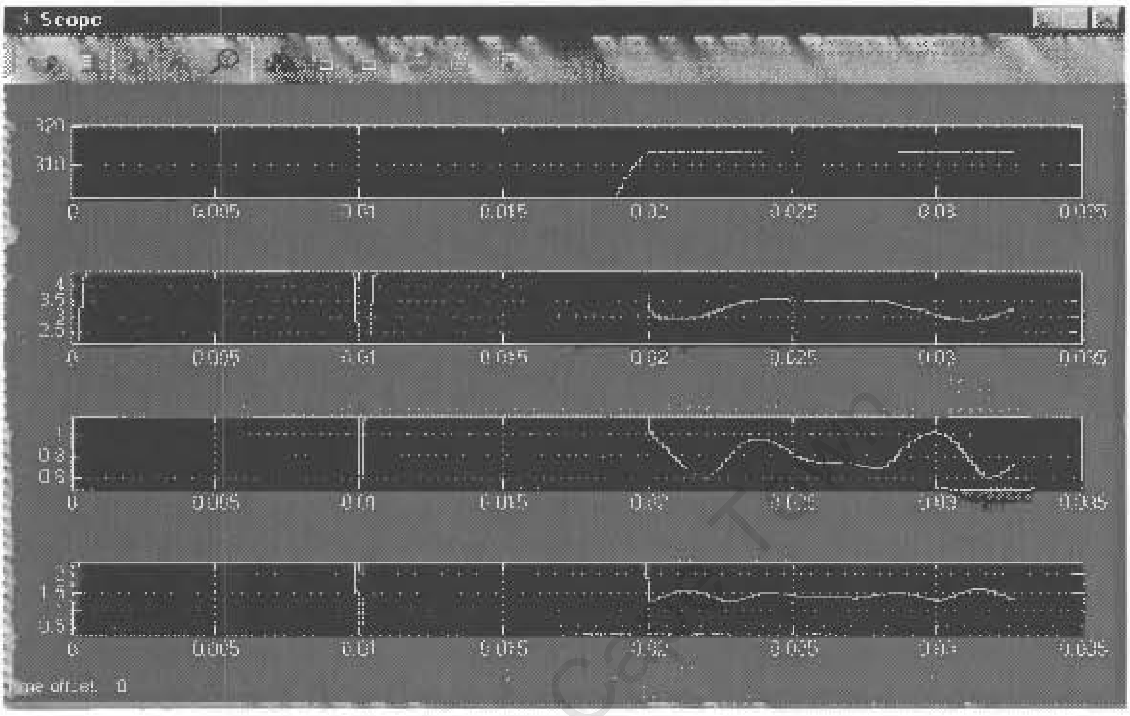

Fig: 6.6 Fundamental and odd harmonic content of the supply voltage

By using $\frac{V_n}{V_1}$, the calculated percentages of the first three odd harmonics are 1.1%, 0.25% and 0.48%. These are in complete agreement with the measurement using Vectograph in fig:6.7.

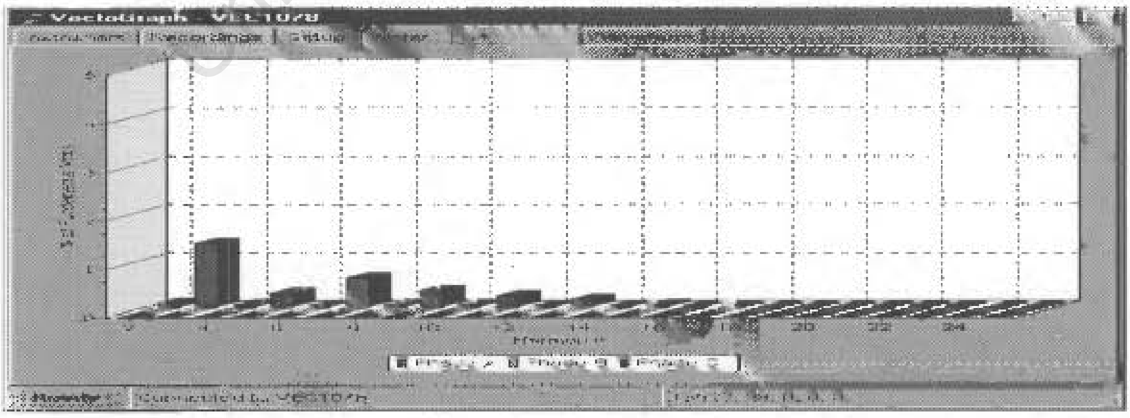

Fig: 6.7 The mains voltage harmonic measurement with a Vectograph

Generally, there is no ruling on the phase shift of the voltage harmonics in relation with the fundamental component. If reactive power measurement is taken in the frequency domain the harmonic succeptances can be measured provided a phase shift of π/2 Radians exists between the reactive current harmonics and the corresponding voltage harmonics.

The assessment of current harmonics and their phase angles is initially not an easy task due to the fact that there are no alternative ways for such measurements to be compared with. The following model is used to compare the current harmonic of any order with the corresponding source voltage harmonic.

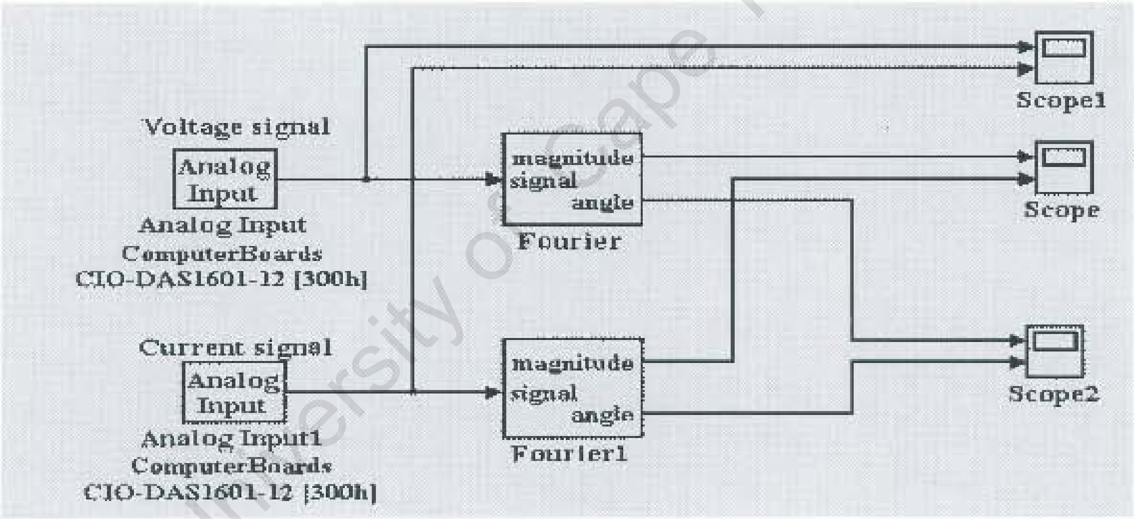

Fig: 6.8 Comparison between the voltage and current harmonics

Initially, in the absence of DC excitation, the source voltage and current waveforms in fig:6.9 show that the reactor forms a pure inductive load.

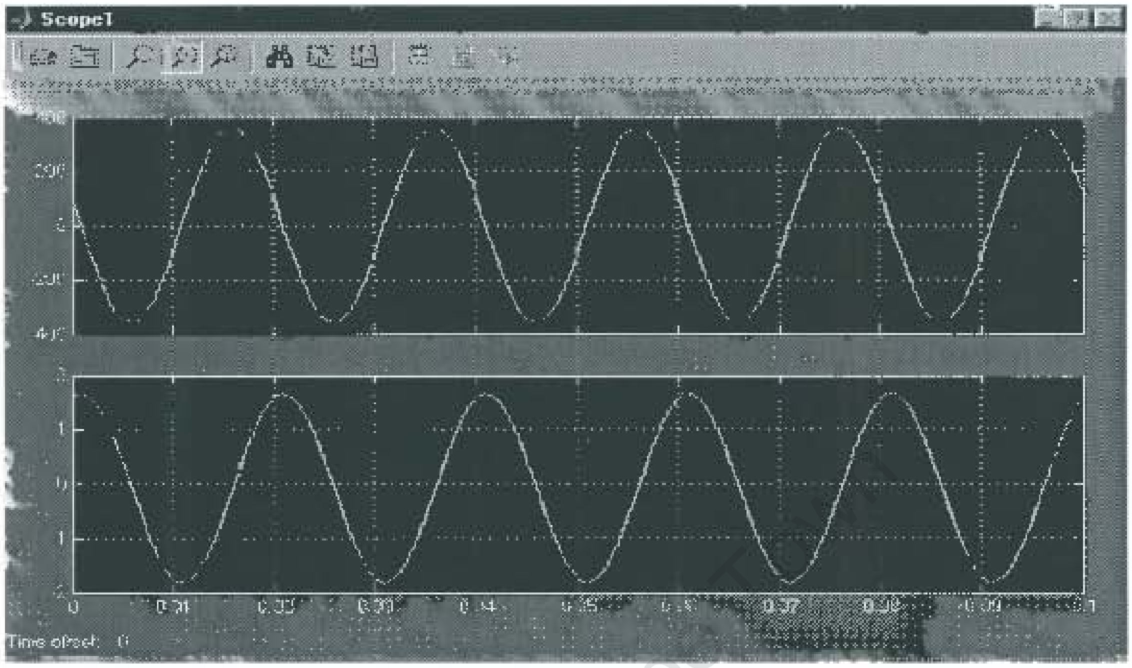

Fig: 6.9 Supply voltage and reactor current with no DC excitation.

The first test is carried out for the third order harmonic values. All the magnitudes are reduced by a factor of 100.

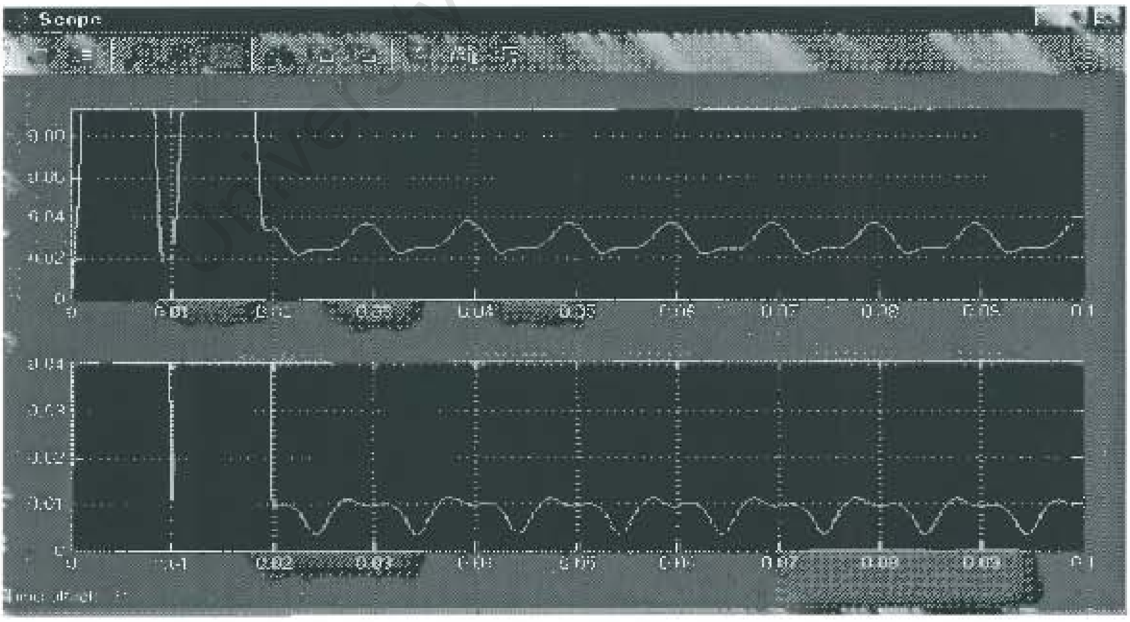

Fig: 6.10 Magnitude of the 3rd order voltage and current harmonics

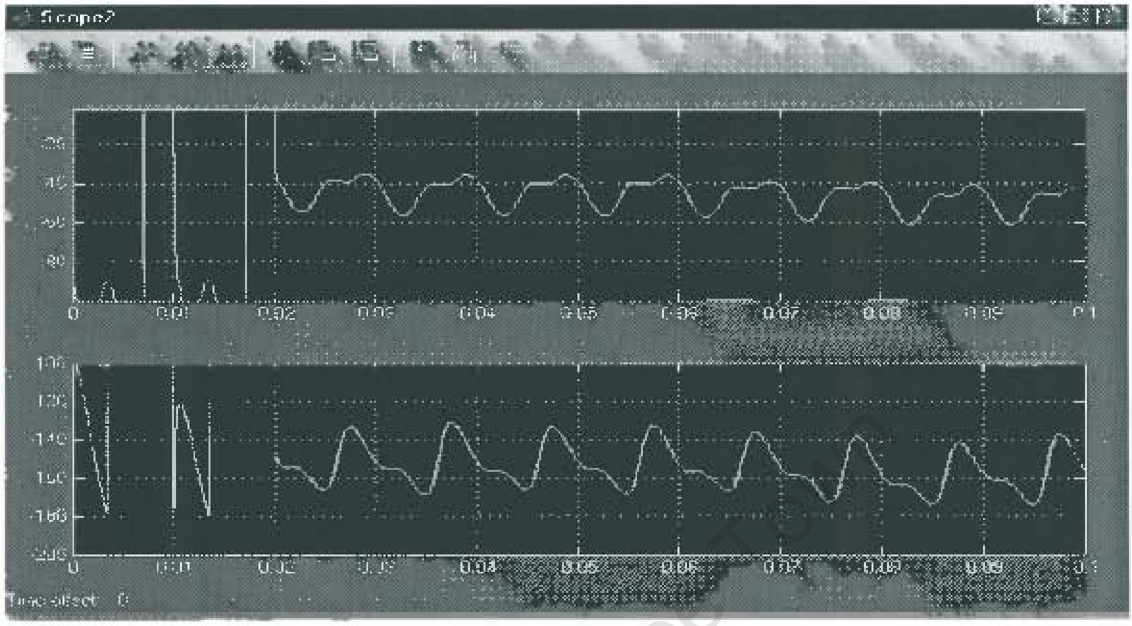

Fig: 6.11 Phase angles of the 3rd order voltage and current harmonics

In fig:6.10, the magnitude of the current harmonic is nearly 1/3 of that of voltage harmonic and in fig: 6.11, a phase difference of nearly 90 degrees exists between the voltage and current harmonics.

The measurements for the 5th and 7th order voltage and current harmonics can be found in appendix 1.5b.

It can be anticipated that the worst-case scenario would be in a saturated core. In fig: 6.12, a specific DC excitation has halved the saturable reactor's AC coil reactance. This automatically doubles the AC current. The magnitude of the current harmonics naturally and by far exceeds those of the voltage harmonics. Additionally, the 90 degrees phase shift between the voltage harmonics and the corresponding current harmonics does not apply any longer.

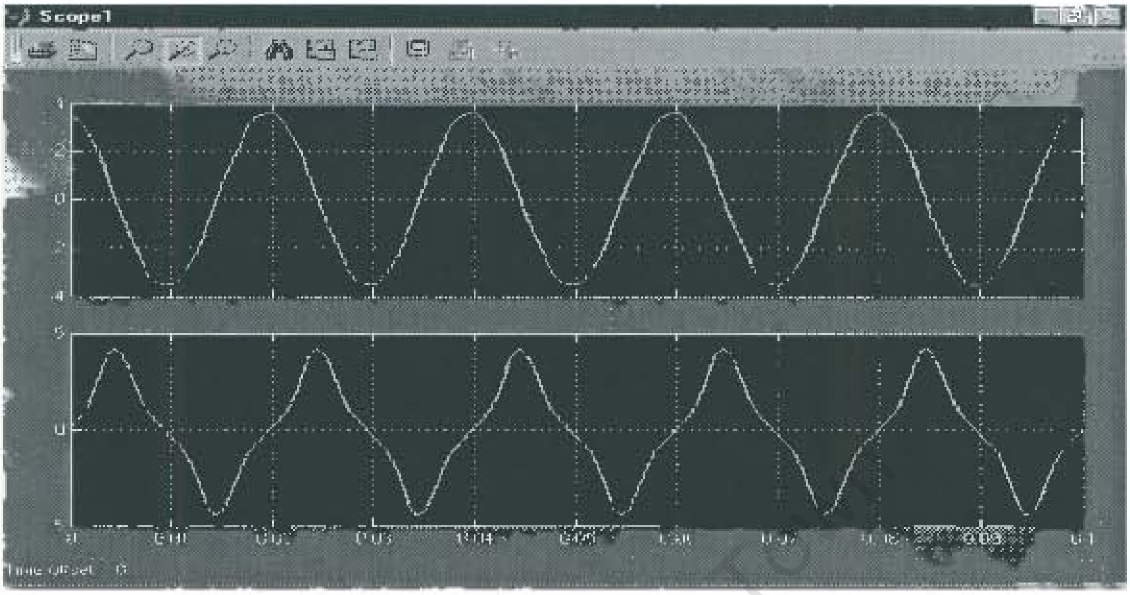

Fig: 6.12 The supply voltage and the AC current for saturated core

The captured results for the 3rd, 5th and 7th order harmonic content of the supply voltage and line current are attached in appendix 1.5c.

Other saturation levels and harmonic orders have been tested. The results show consistently and conclusively that for highly inductive loads such as reactors, any slight saturation in the core material causes the reactive current harmonics to be shifted from their position and hence any measurement on harmonic succeptance of the load at a specific frequency will become invalid.

A final model can be used to measure the complete THD of the reactor's AC current. The model is shown in fig: 6.13.

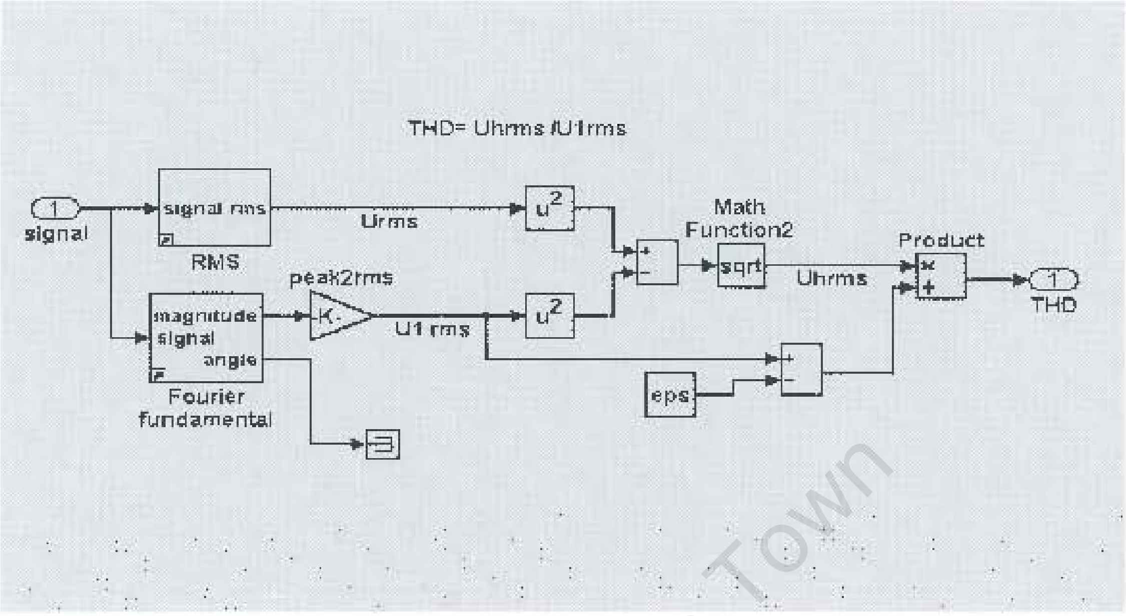

Fig: 6.13 Measurement of THD for reactor AC current

The above model can be used for single-phase measurement or cascaded for three-phase measurement. The only limitation is the capability of the running computer processor. The THD of the AC current through a saturated reactor with a DC excitation of 1.0A is measured at 24% and shown in fig:6.14.

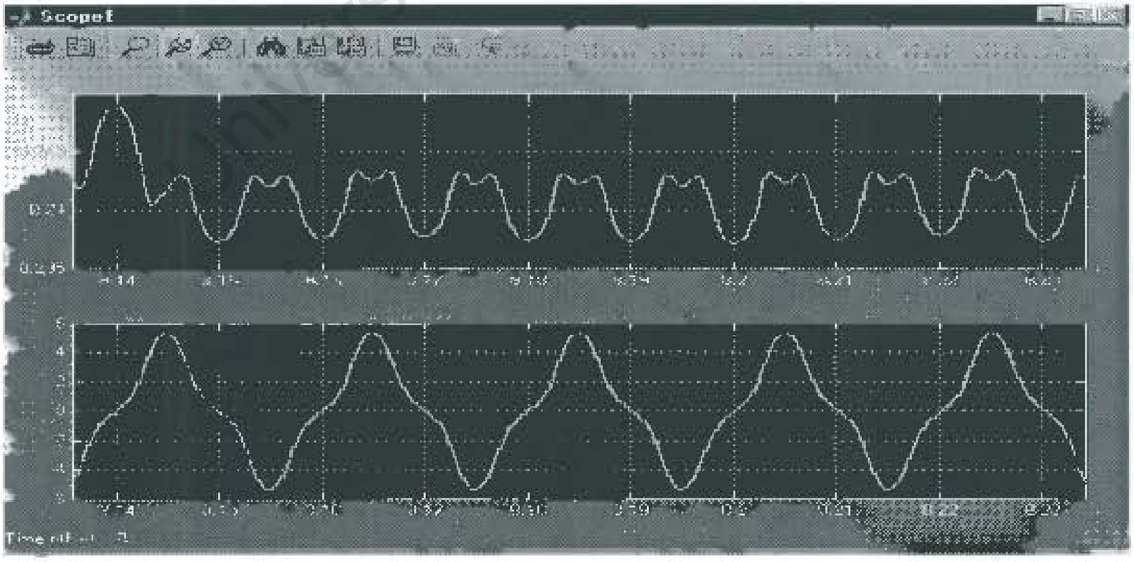

Fig: 6.14 The THD and AC current

Fig: 6.15 shows the variation of the THD versus AC coil current.

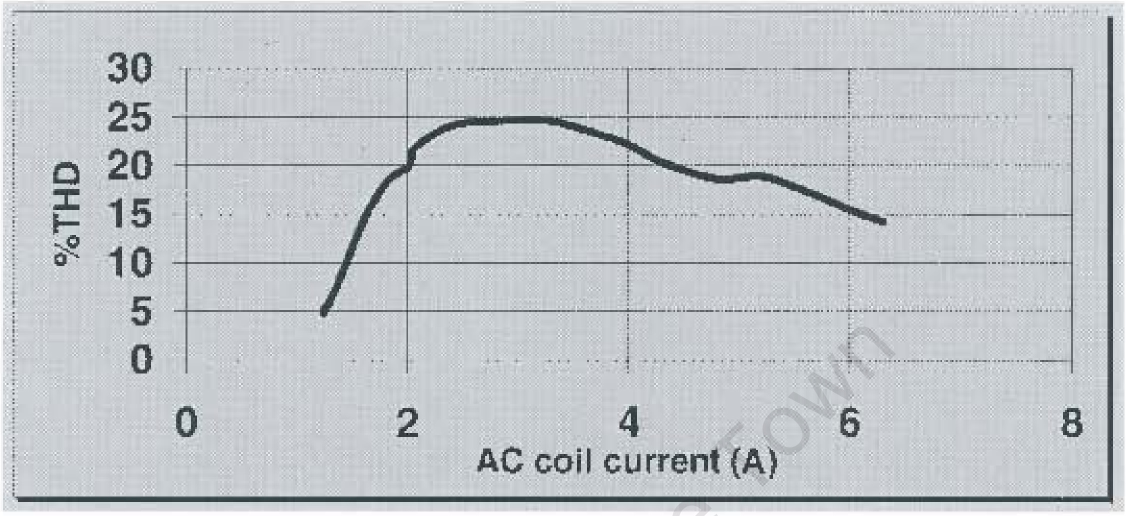

Fig: 6.15 Variation of %THD for AC coil current

The harmonics generated in the line currents are directly the results of the core saturation. It is interesting to notice that the THD increases up to a maximum of 25% and then starts decreasing towards lower values.

In the next section of this chapter, the "Real-Time Simulation" is used to model and test an adaptive compensator.

6.2 Adaptive converter and Real-Time Simulation

Modeling of three-phase balanced loads and calculation of the required parallel susceptances to generate and maintain a balanced three-phase supply can be achieved using "Real-Time Simulation" with all the hardware in the loop.

The investigations carried out in previous chapters proved that in applications such as small water pump, the use of a saturable reactor in the adaptive converter is neither necessary nor economical. However, not all loads have the same characteristics as water pumps. There are many applications such as mixers in the bakeries and woodworking machinery where the required torque by the load changes continuously. Hence, the slip varies and consequently the converter susceptances have to be adjusted accordingly. This chapter aims at modelling the above category of loads. The saturable reactor is brought back to the following designs and used as a variable source of inductive susceptance.

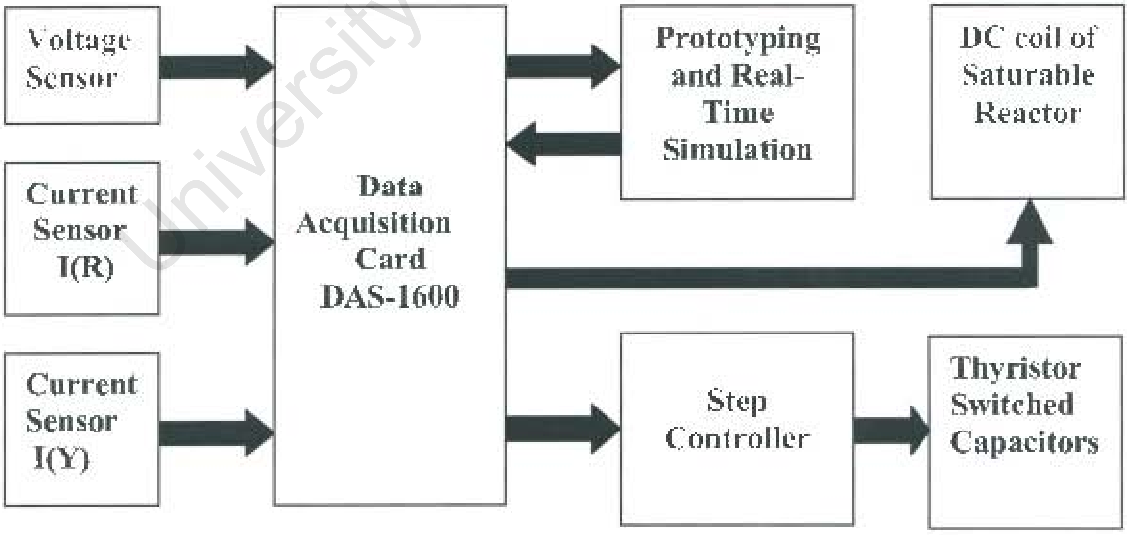

Fig: 6.16 Prototyping with Real-Time Simulation and hardware in the loop

The model of fig: 4.10 on page 76, has been expanded to measure the rms values of the active and reactive power. Additionally, the load power factor can be monitored.

For the purpose of this section, first a series of three-phase delta-connected resistive loads, and then two different sizes of three-phase induction motor with different kind and size loadings have been utilized. For all cases the oscilloscope captured signals have been presented.

The simplified version of the model is shown in fig:6.17.

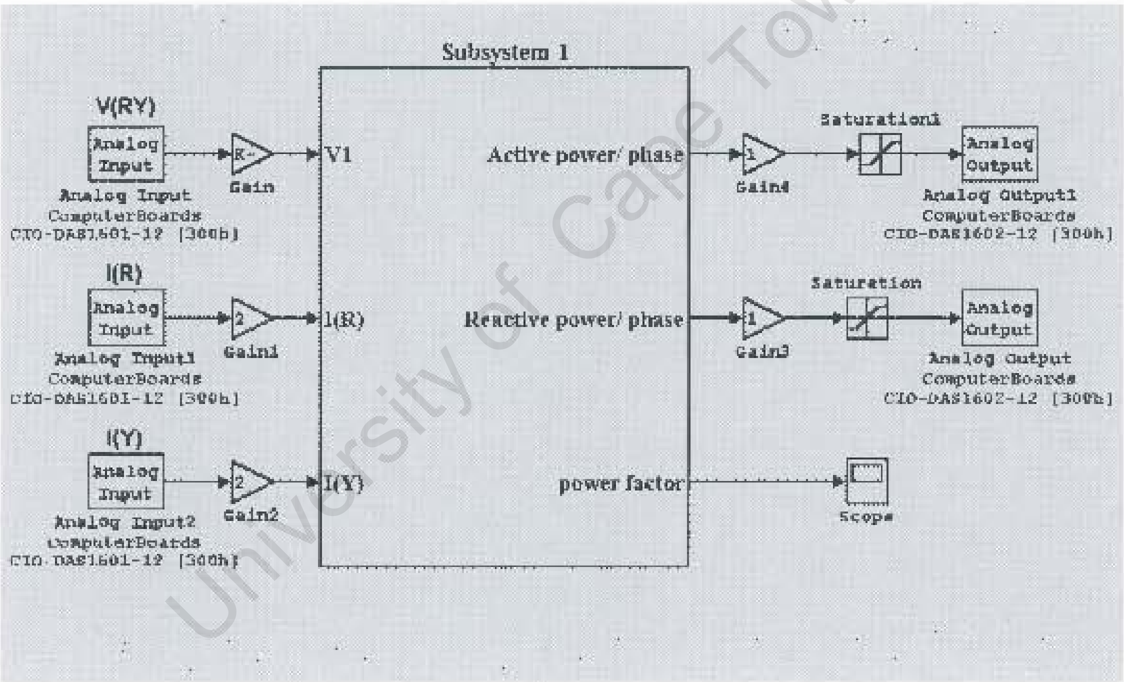

Fig: 6.17 Modeling of a three-phase load using Real-Time Simulation

The additional gain and saturation blocks protect the input and output A/D and D/A channels. The complete expanded prototype can be seen in appendix 1.5d.

The output range of D/As are scaled for 1.0 V to be equivalent to 0.1Henrys and 10.0 uF for the respective converter elements.

The first set of DC equivalent output voltages versus load power for resistive loads are presented in the following graphs.

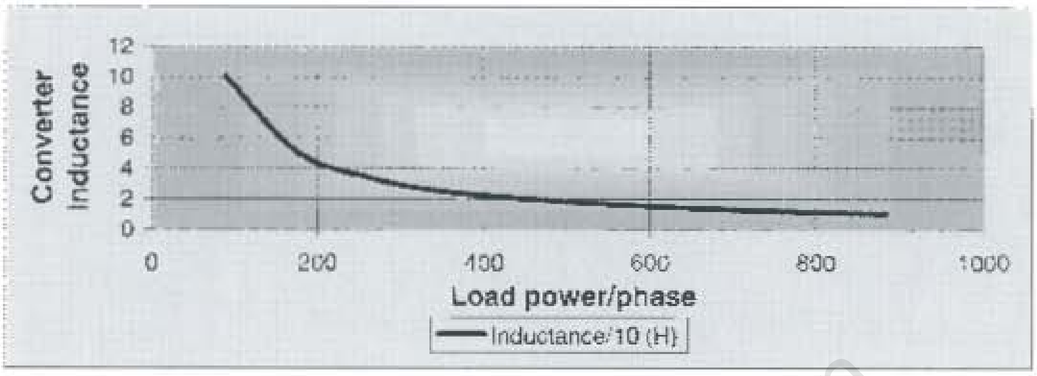

Fig: 6.18 Variation of converter inductive element with load active power for resistive loads

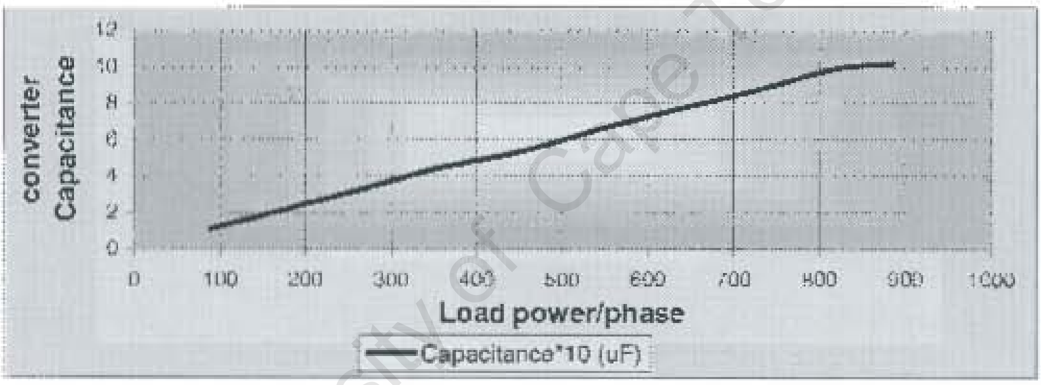

Fig: 6.19 Variation of converter capacitive element with load active power for resistive load

Evidently, low kW resistive loading requires high inductive reactance from the compensator. The capacitive reactance requirement is linear and increases with the load power. Since capacitors are cheaper and more easily available, this type of compensation for resistive loads would be more economical for high load kW ratings.

The following results are captured for a resistive load of 200 W/phase. Similar results for 500 and 900 W/phase are shown in appendix 1.5e.

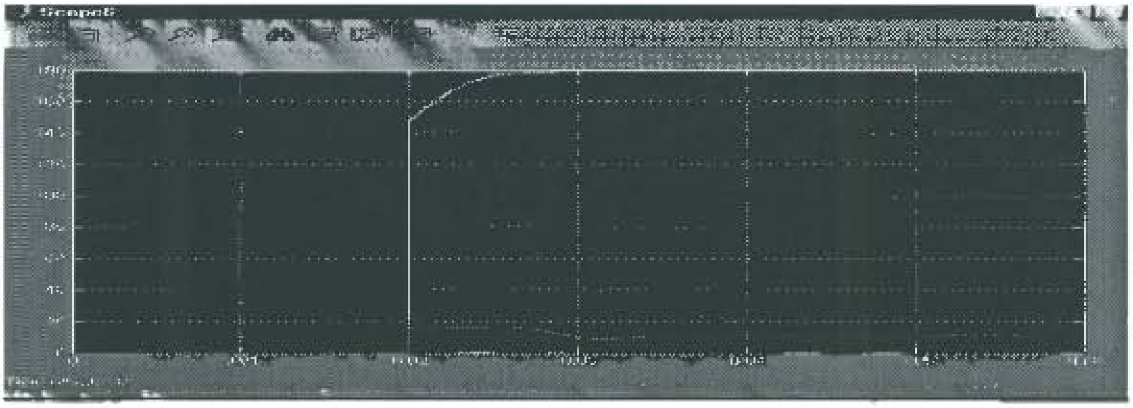

Fig: 6.20 Real-Time measurement of active and reactive power of a 200 Watts load

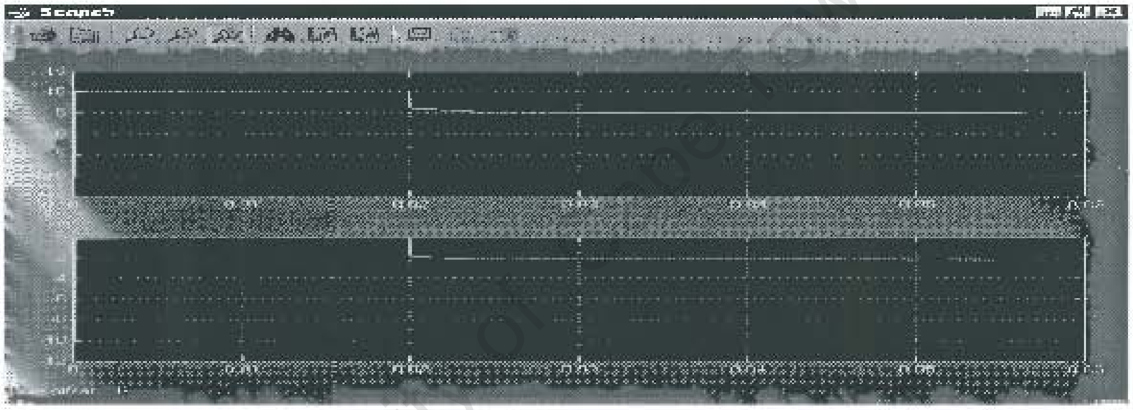

Fig: 6.21 Real-Time DC equivalents of the converter elements at 200 W load

The actual output oscilloscope captured values are shown in fig:6.22.

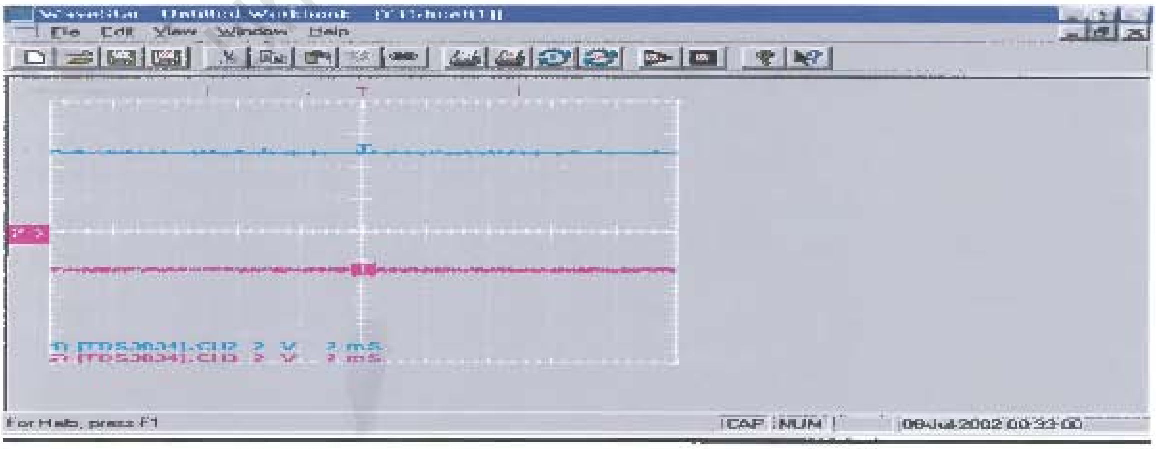

Fig: 6.22 Oscilloscope captured DC equivalents of the converter elements for a 200 W load

Finally, the after compensation line voltages can be seen in fig;6.23.

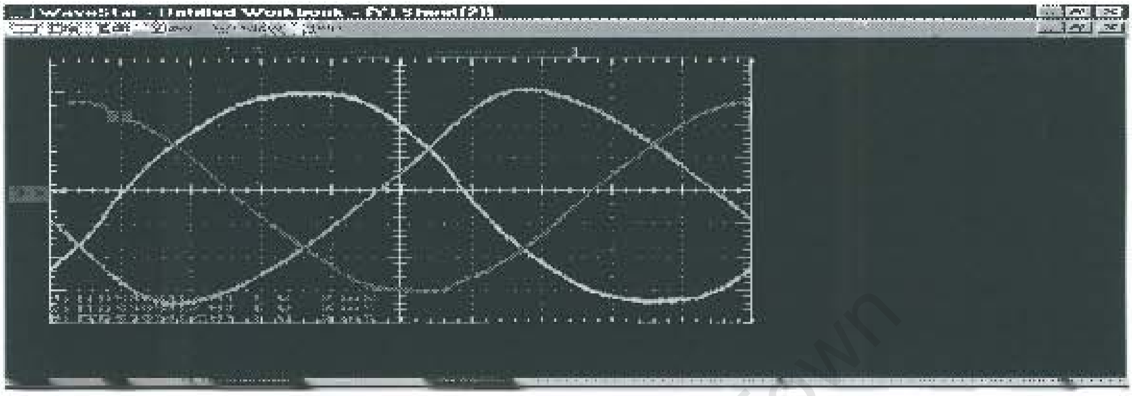

Fig: 6.23 After compensation load voltages for 200 W load

With satisfactory results on resistive loads, the performance of the prototype for a dynamic load such as a three-phase induction motor can now be investigated. Initially and once only, the motor has to be operated with a three-phase supply at no-load and full-load so that the range of the values of converter elements is determined. This eliminates the need for open circuit and locked rotor tests on the motor.

First motor is 1.1 kW and is tested with an eddy-current breaker as load in fixed step loadings. The followings are the results of the no-load up to full-load values for the motor parameters and the converter elements.

No-load conditions

The active and reactive power of 40 W and 260 VArs represent the true and accurate per phase powers of the motor. Traces are shown in fig:6.24 and 6.25.

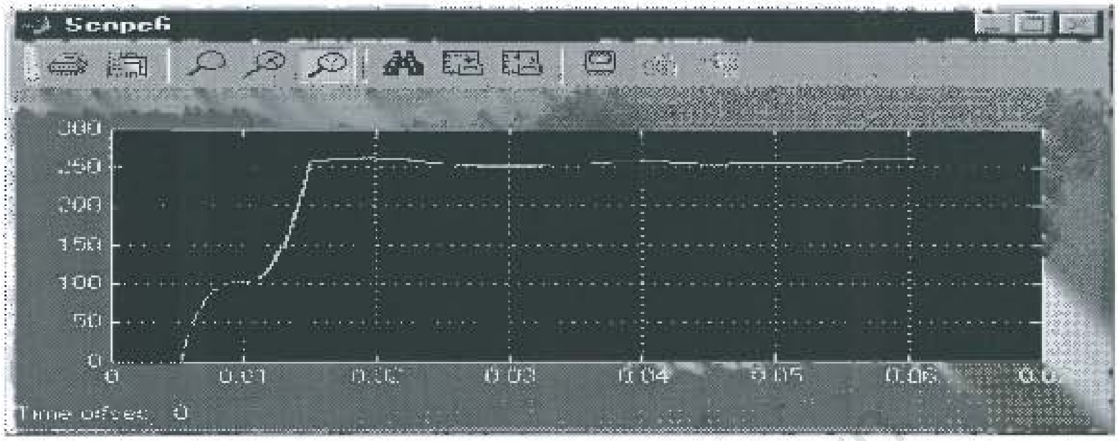

Fig: 6.24 Load reactive power measurement at no-load conditions

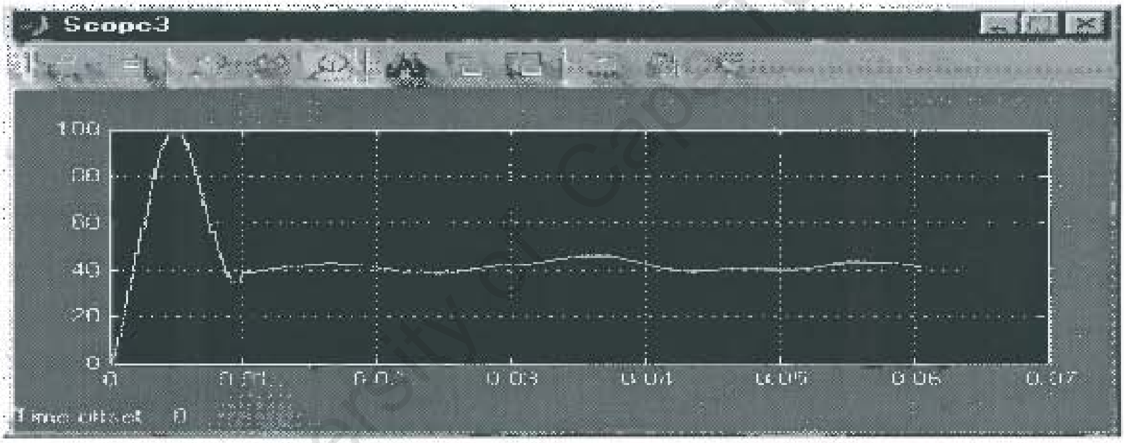

Fig: 6.25 Load active power measurement at no-load conditions

Using standard digital meters, measurements lead to the following calculation.

$$P = \frac{\sqrt{3}.V.I.\cos\phi}{3} = \frac{\sqrt{3}*220*1.6*0.2}{3} = 40.65\ \text{W}$$

The answer confirms the reading of fig:6.25.

The proportional DC values for the compensator inductive and capacitive elements are shown in fig:6.26. As previously explained, for load power factors lower than

0.5 (lagging), both elements are capacitive. The negative values in fig:6.26 indicate capacitive elements.

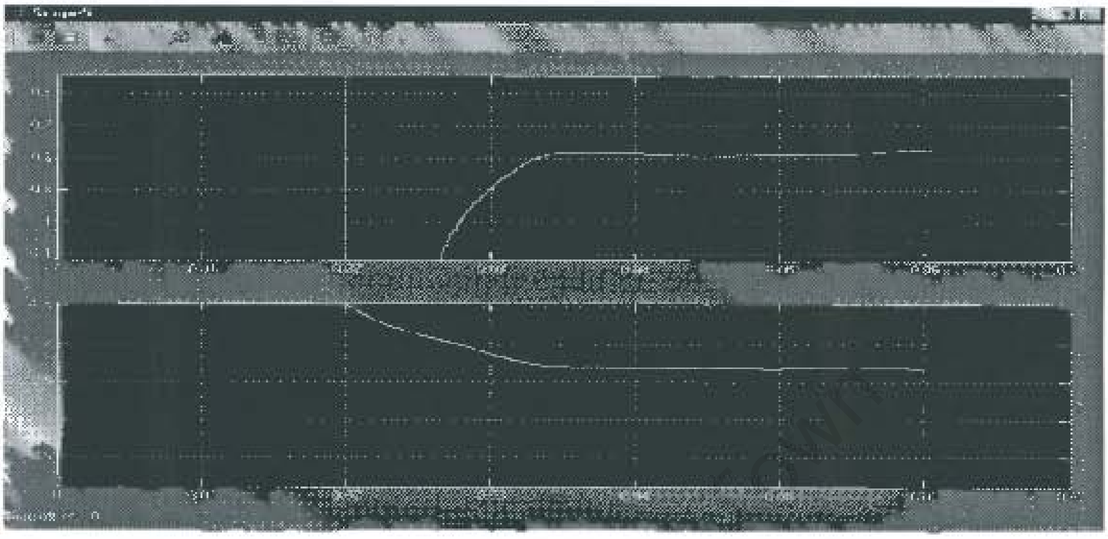

Fig: 6.26 Real-Time simulated proportional DC values for the compensator elements at no-load conditions

The scales are selected so that each 1.0V represents 100.0mH and 10.0 uF. Hence from Fig: 6.26, voltages of 0.8 and 2.3 V should activate 8.0 and 23.0 uF. The actual oscilloscope traces of the output signals are shown in fig:6.27.

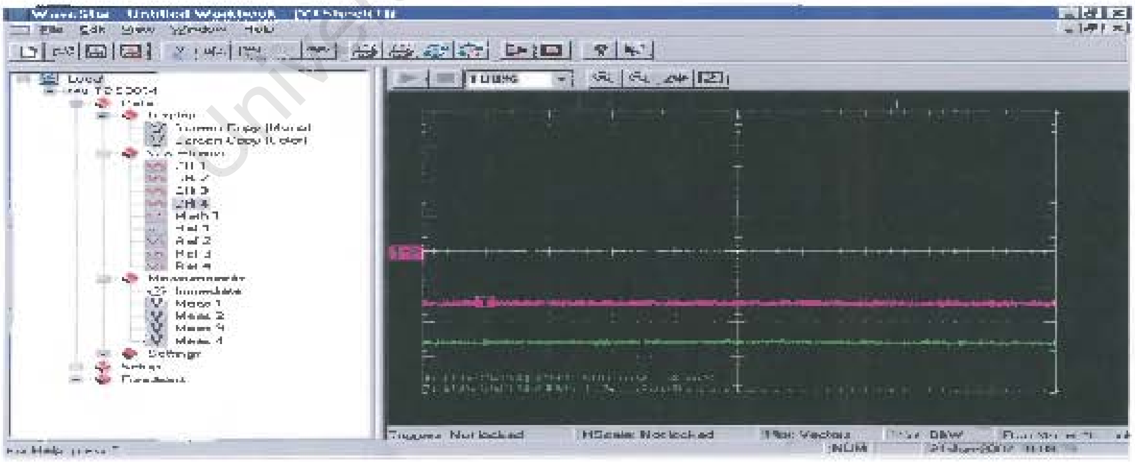

Fig: 6.27 Oscilloscope captured DC voltages proportional to the compensator elements under no-load conditions

The circuit diagram of fig:6.28 is the motor equivalent at no-load with the converter elements connected to it. After compensation line currents are captured in fig:6.29.

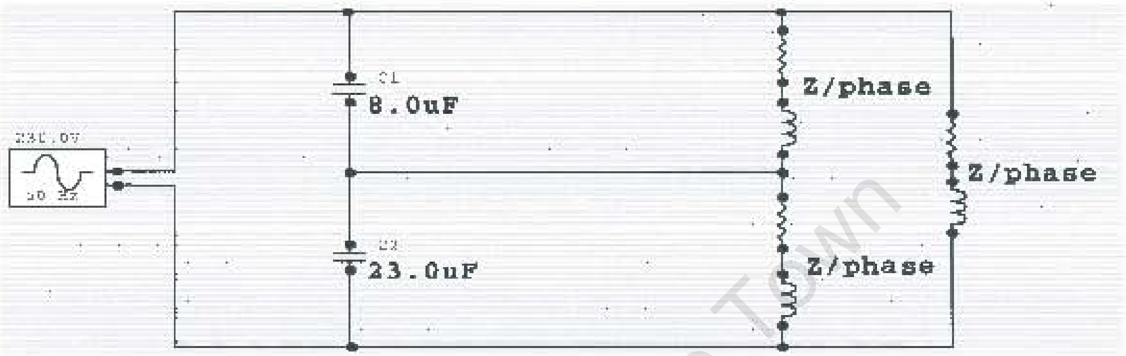

Fig: 6.28 **Motor equivalent and the compensator values at no-load conditions**

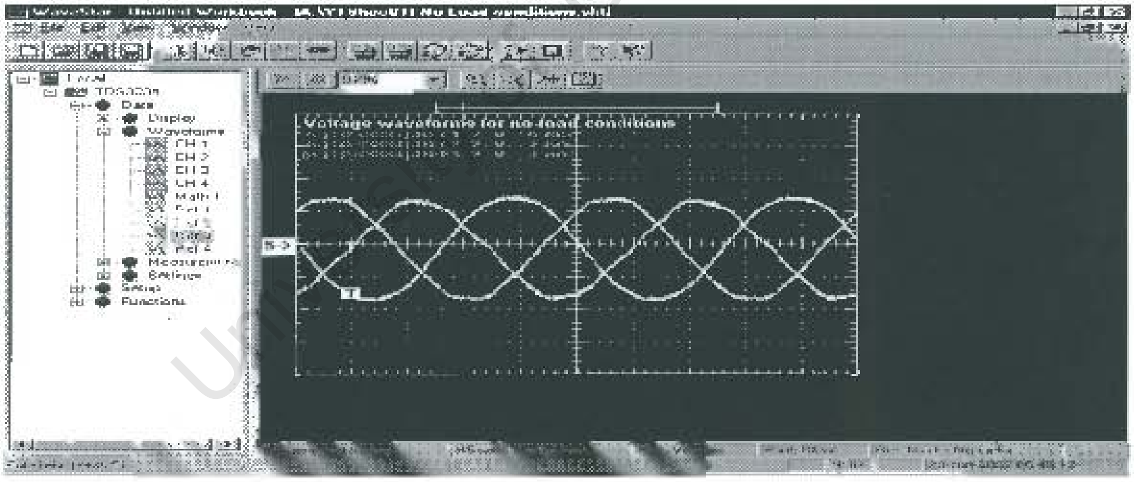

Fig: 6.29 **After compensation line currents at no-load conditions**

The loading is increased in 0.2 A steps. The variation of the converter's elements with the load power factor is of particular interest. These are shown in fig:6.30 and 6.31.

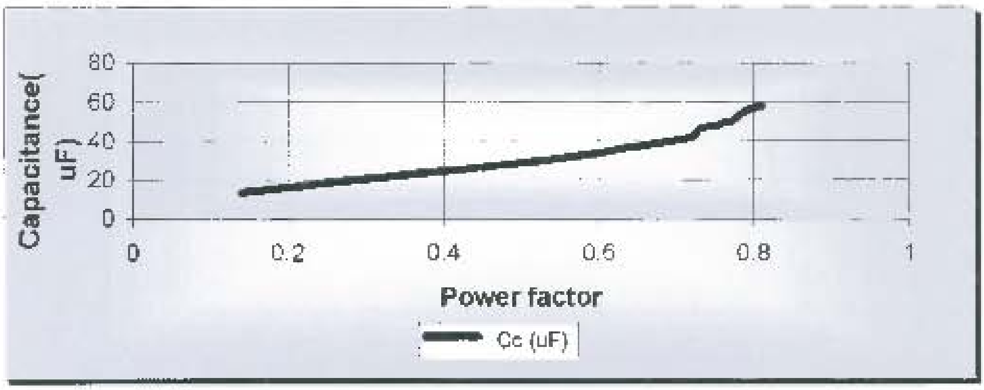

Fig: 6.30 Variation of compensator capacitive element with load power factor

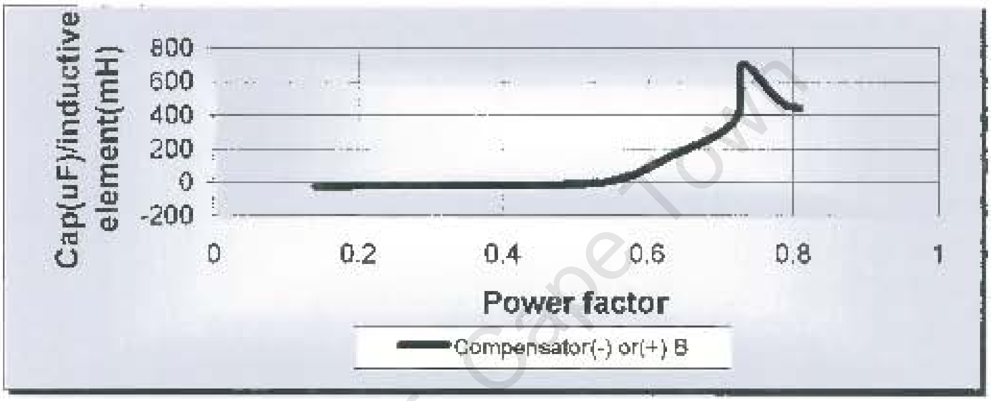

Fig: 6.31 Variation of compensator capacitive/inductive element with load power factor

Finally The variation of these elements with line current can be seen in fig: 6.32.

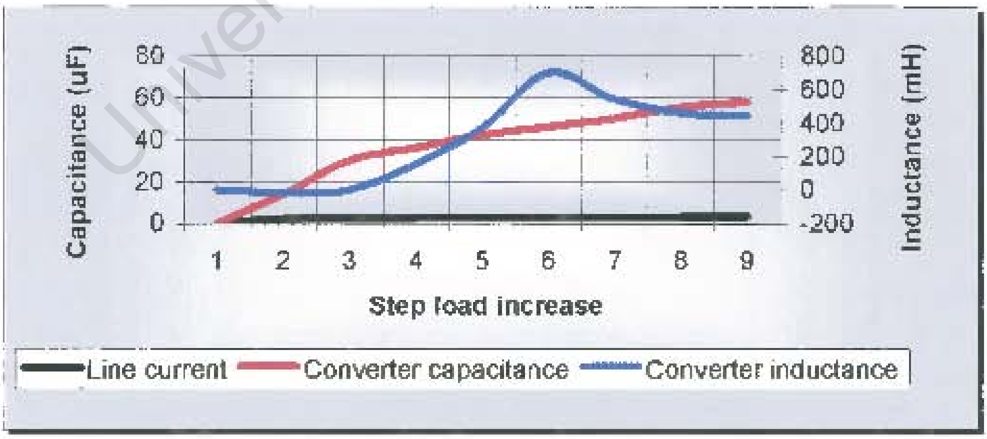

Fig: 6.32 Variation of converter elements with line current

The patterns of the above graphs are similar to those of fig: 5.20.

The second motor tested is a 750 W induction motor coupled to a DC generator. The generator is loaded with 100 Watts light bulbs. Increasing the load causes relatively large terminal volt-drops. This is due to armature resistance and ultimately the small size of the generator. Nevertheless, the loading of the generator is considered to be at 100W steps. Fig: 6.33, 6.34 and 6.35 show the variation of the compensator's elements with the motor's power factor and variation of converter elements with load steps respectively.

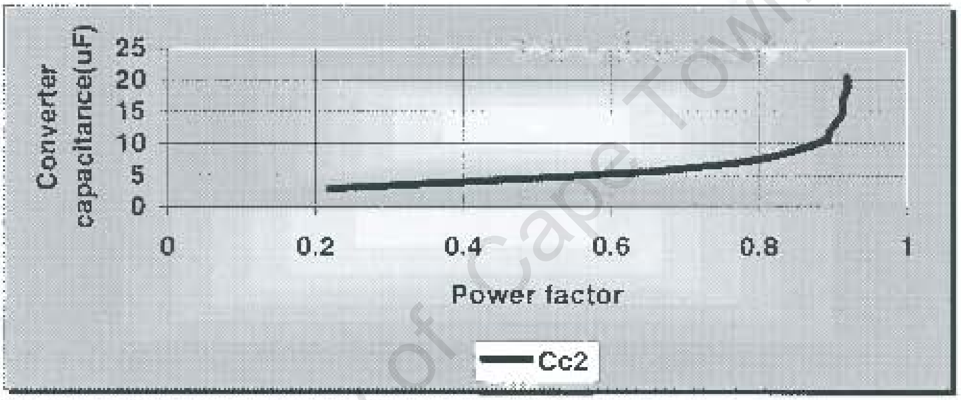

Fig: 6.33 Variation of compensator capacitive element with load power factor

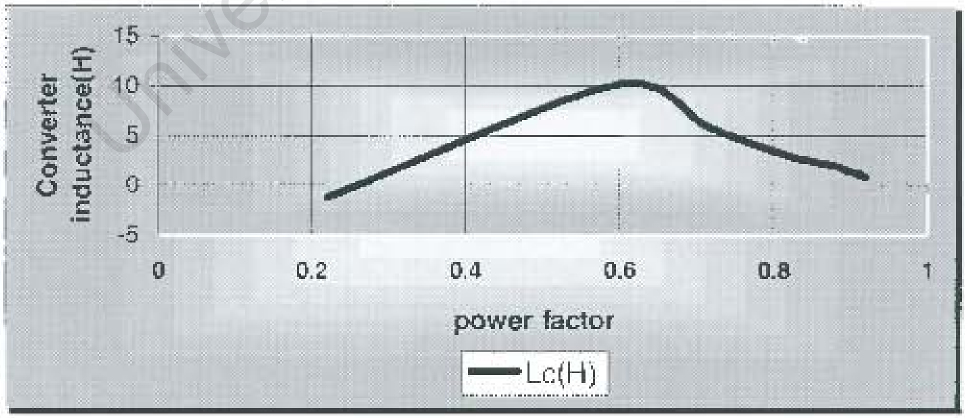

Fig: 6.34 Variation of compensator capacitive/inductive element with load current

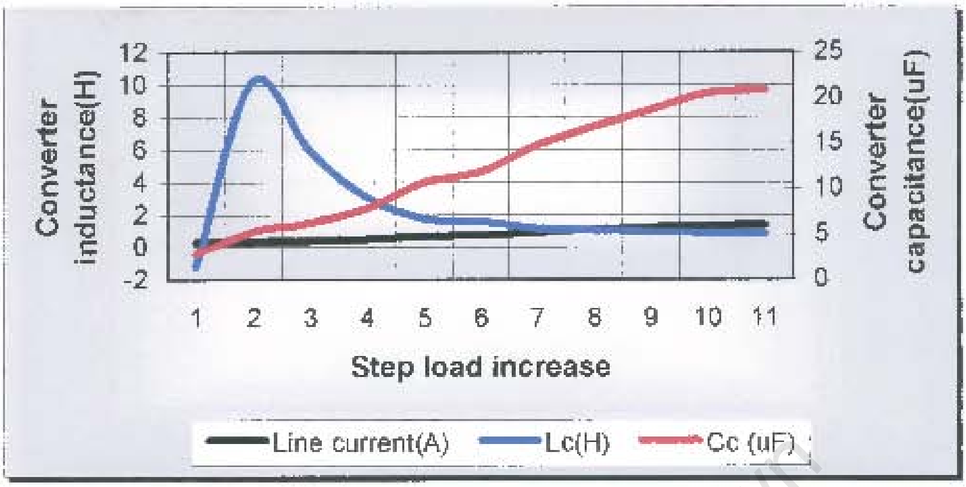

Fig: 6.35 Variation of converter elements with line current

Several points on the above set of values have been set up and tested. The "Real-Time simulated" values of average active and reactive powers, converter elements DC equivalents and finally the after compensation terminal voltages for the corresponding loads have been captured. Fig: 6.36, 6.37 and 6.38 show such values at no-load conditions.

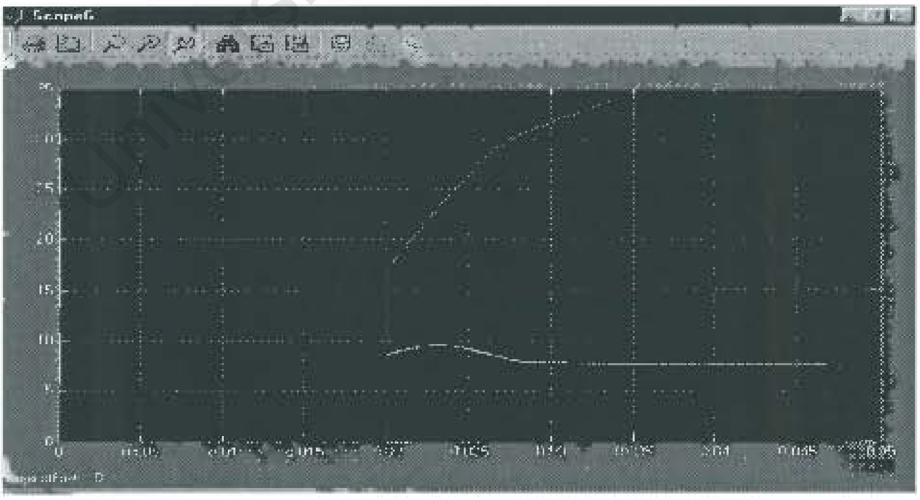

Fig: 6.36 Average active and reactive power at no-load conditions

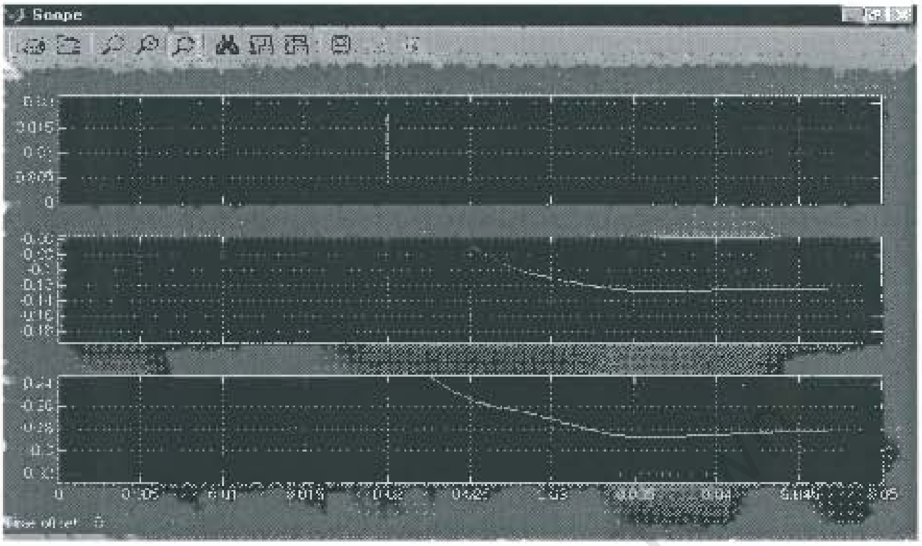

Fig: 6.37 Converter element DC equivalent values at no-load conditions (1.25 uF and 2.8uF)

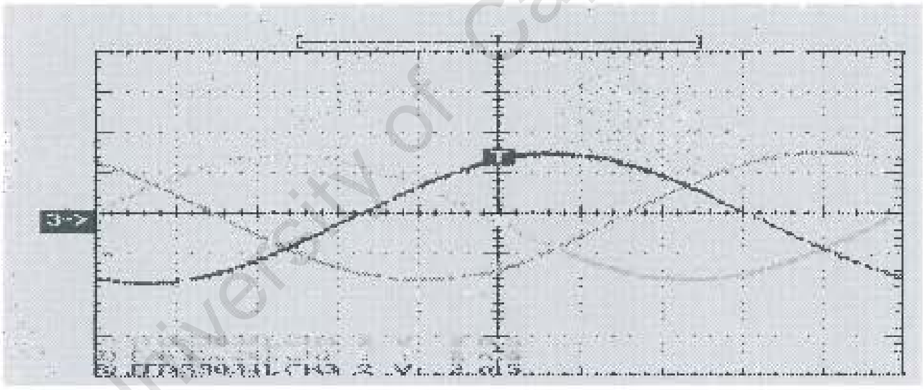

Fig: 6.38 Driving motor terminal voltages at no-load

The rest of the captured loading values can be found in appendix 1.5f. The percentage unbalance can be measured using the modified version of fig:2.1.1 on page 12.

After introducing the appropriate phase shifts, the model calculates the rms values of the positive and negative phase sequence voltages and produces an accurate value of the percentage unbalance in the line voltages. See fig: 6.39

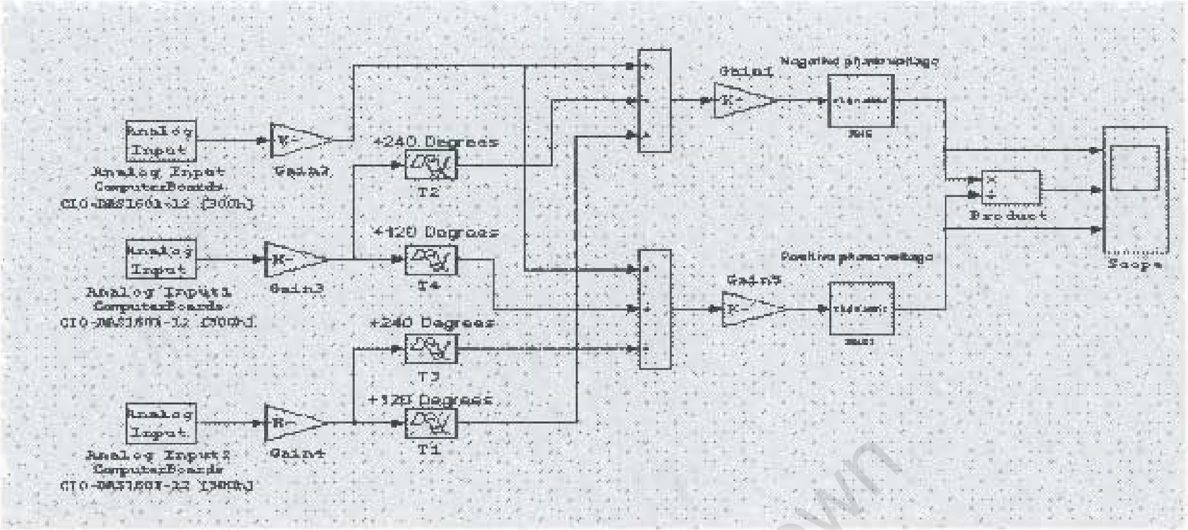

Fig: 6.39 Modified version of the model for measurement of positive and negative phase sequence voltages

As an example, fig: 6.40 shows the measurement for the loading of 800 Watts on the generator set.

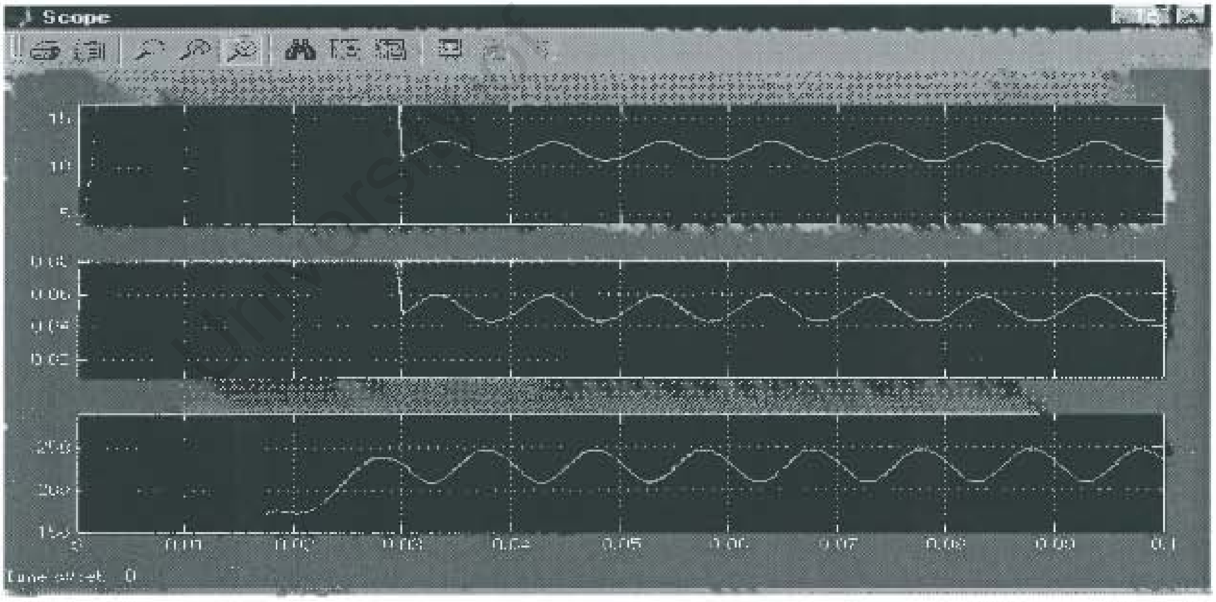

Fig: 6.40 Real-Time captured values for phase sequence and voltage unbalances

A voltage unbalance of 5% is measured in the middle window, which is within the acceptable limits.

In the “Real-Time Simulation” environment many other types of measurements can be taken and any concept or theory related to this report can be prototyped. As for adaptive passive-element converters, this chapter is now completed.

Chapter 7

Conclusions

The successful operation of a passive element adaptive converter depends on two main factors. Firstly, accurate modeling of the load and dynamic measurement of its parameters and secondly, rapid adjustment of the converter elements to suit the above load parameters.

The type and size of these passive elements used for voltage compensation must be determined first in order to establish the cost. For a single or a group of resistive loads, passive-element voltage compensation is most economical. It is interesting to know that for dynamic loads with poor power factor, voltage compensation of this nature is well-worth considering. For the most common category of dynamic loads (three-phase motors), the nature and the size of such passive elements depend highly on the load torque-slip characteristics.

The results on two types of motor loadings (centrifugal pump and M-G set with variable static loads on the generator) have shown clearly the differences between these load requirements for voltage compensating elements. In the case of a centrifugal pump, the converter elements have to be of correct value at startup and full-load conditions. However, the rate of change of intermediate values of the converter elements is not critical.

For the loads with constant torque demand increasing or decreasing in steps, the change of motor parameters falls into a narrower range. It has been experimentally proven that in such cases, even if the driving motor starts from standstill, it only requires parallel succeptances corresponding to a specific load condition. One would assume that with a large size motor of perhaps 10 KW or more and due to a much larger inertia and longer acceleration time, this might not necessarily apply.

With a better understanding on the influence of different load categories on the nature and size of the compensator, it is unfortunate that building a general compensator for a wide range of three-phase dynamic loads would prove bulky, expensive, and hence impractical. However, for a specific size motor and loads of different characteristics attached to it, prototyping with "Real-Time Simulation" can be used to directly measure the load parameters and evaluate the range of values for the converter elements. This way a tailor-made compensator with large reduction in cost and volume can be constructed.

With the use of a fast computer and an appropriate data acquisition card equipped with four or six analogue output channels, any other load parameter such as active and reactive power, power factor or other parameters can be conveniently measured in real-time.

Recommendations

In the first load application reviewed, (centrifugal pump), the most economically viable way of replacing a single-phase driving motor with a three-phase motor, would be to use the method shown in fig: 7.1. A fixed inductor for the final no-load or full-load speed (which are very close to each other) can be used as the first element. The second succeptance should consists of capacitors being switched on or off in two or three-steps. The number of steps depends on the size of the pump.

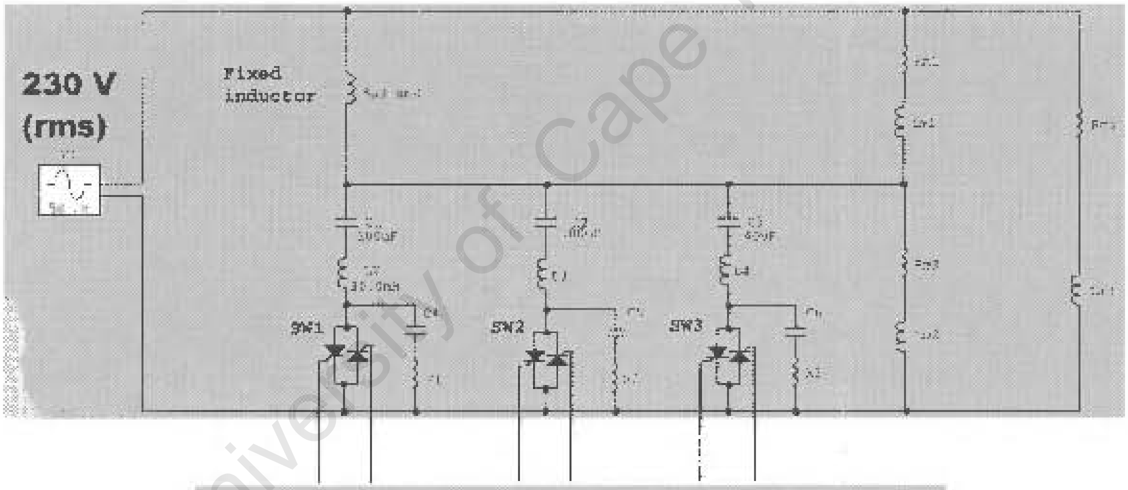

On activation, this controller would deactivate SW1 and SW2 in a few seconds.

Fig: 7.1 Recommended converter layout for small size centrifugal pumps

In the hardware constructed for the centrifugal pump the back-back thyristor blocks were deactivated in six steps of 30.0 uF each. For a small pump of 1.0 kW or less, the number of deactivation steps can be reduced from six to three with no major effect on the motor start up performance.

For other types of load with constant torque requirement, the two-element passive converter can be suitably tailor-made for a specific kW rating motor. Referring to fig: 5.20, 6.51 and 6.54, it is recommended that for the converter to stay small in size and cost effective (for commercial applications), it should be applied to motors with loads that change only a few percent from full-load. The converter would then consist of a fixed inductor (L1), and three TSCs (SW1, SW2, SW3) for full-load conditions. Fine- tuning can be done for small load fluctuations through SW4 and SW5. Furthermore, by connecting additional parallel capacitors (C_1, C_2 and C_3) across all three phases, the overall size of both elements would be reduced. The proposed layout in shown in the following diagram.

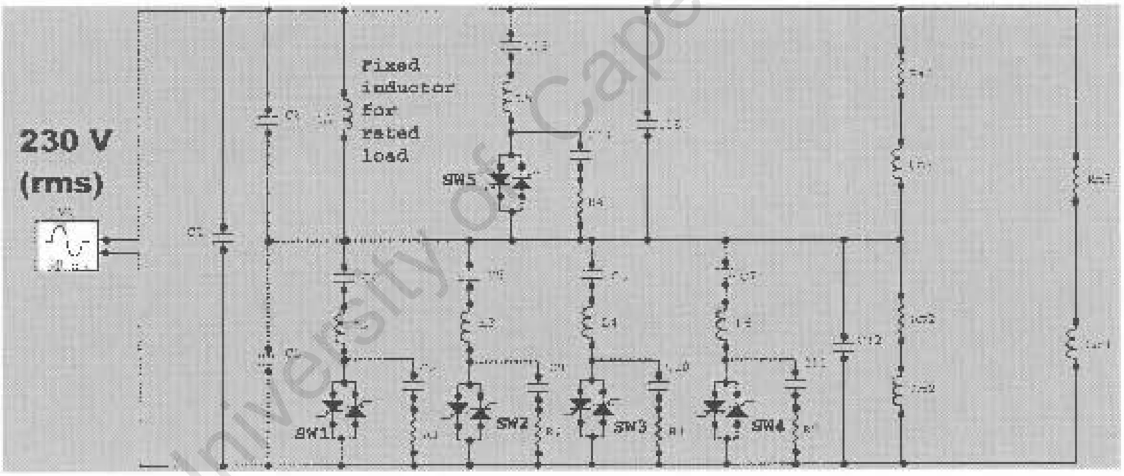

Fig: 7.2 Recommended converter layout for loads with small degree of fluctuations from full-load

References

1. S.B Dewan, " A novel static single to three-phase converter" Transactions on magnetics Vol. Mag-17, No. 6, November 1981.

2. P.G Holmes, " Single to three-phase transient phase conversion in induction motor drives." IEEE proceedings, Vol. 132, pt. B, No.5. September 1985.

3. Mohan, Underland, Robbins power electronics, second edition, John Wiley and sons, Inc. ISBN 0-471-58408-8 (cloth).

4. Enjeti, " An active line conditioner to balance voltages in three-phase system" IEEE transactions in industrial applications, Vol.32 No. 2, March/April 1996.

5. B.S Rigby, " Design of a three-phase thyristor controlled series capacitor." SAUPEC 2001.

6. S. Marino~~u~~Es, "Single to three-phase converters using passive elements," UCT, MSc thesis 1999.

7. L.S Czarnecki, " Considerations on the reactive power in a non-sinusoidal situations." IEEE transactions on instrumentations and measurements, Vol.IM-34, No.1, Sep 1985.

8. L.S Czarnecki, " Measurement principle of the reactive current RMS value and the load succeptance for harmonic frequency meter," IEEE transaction on instrumentation and measurement. Vol. IM-34, No 1, March 1985.

9. M. Malengret preliminary PHD research at UCT.

10. N.G. Hingorani, L.Gyugyi: " understanding FACTS " IEEE press, Piscataway NJ, 1999, ISBN 0-7803-3455-8.

11. L.S Czarnecki "Adaptive balancing compensator", IEEE Transaction on power delivery, Vol. 10, No.3, July 1995.

12. N. G Hingorani, L. Gyugyi: "Understanding FACTS", IEEE press, Piscataway NJ,1999, ISBN 0-7803-3455-8

13. L.Pitterin, Power quality and distribution, ESKOM, East-London.

Appendices

Appendix 1.1

Matlab programs

1) Calculation of pumps motor parameters for the range of speed

```
clear;
f=50;                                          (Frequency of supply)
p=2;                                           (Pole pair number)
ns=(120*f)/p;                                  (Synchronous speed)
nr=1:10:3000;                                  (Range of shaft speed)
s=[ns-nr]./ns;                                 (Slip)
Zm=[(-1529.6*s+1867.31*i)./(9.4+206.35*s*i)]
    +(8.6+7.7*i);                     (Motor impedance as a function of s)
Lm=(imag(Zm))./(2*pi*50);                      (Inductance per phase)

Rm= real(Zm);                                  (Resistance per phase)
p.f=cos(Rm./abs(Zm));                          (Power factor)
x1=-[real(Zm).^2+(imag(Zm).^2)]*i./[(imag(Zm)
    -sqrt(3)*(real(Zm)))];                     (Reactance of the first
                                                compensative element)
x2=[real(Zm).^2+(imag(Zm).^2)]*i./[(imag(Zm)
    +sqrt(3)*(real(Zm)))];                     (Reactance of the second
                                               compensative element)
Lc=1000*(imag(x1))./(2*pi*50);                 (Inductance of the   first
                                               compensative element)
Cc=1000000./(2*pi*50*imag(x2));                (Capacitance of the second
                                               compensative element)

plot(nr,Lm)
Plot(nr,Rm)
plot(nr, Zm)
```

2) Calculation of converter elements with extra parallel capacitors connected with each phase of the load.

```
clear;
nr=10:10:2950;                                          (Range of speed)
f=50;                                                   (Frequency of supply)
p=2;                                                    (Pole pair number)
ns=(120*f)/p;                                           (Synchronous speed)
s=[ns-nr]./ns;                                          (Slip)
Zm=[(-1529.6*s+1867.31*i)./(9.4+206.35*s*i)]+(8.6+7.7*i); (Motor impedance)
Lm=(imag(Zm))./(2*pi*50);                                     (Inductance/phase)
Rm= real(Zm);                                                 (Resistance/phase)
p.f=cos(Rm./abs(Zm));                                         (Power factor)
C1=0.1e-4;                                                    (10 uF in parallel)
Xc1=-[1./(2*pi*50*C1)]*i;                                     Capacitive reactance
Zt1=[(Zm*Xc1)./(Zm+Xc1)];                                     (Total
                                                              impedance/phase)
x1=-[real(Zt1).^2+(imag(Zt1).^2)]*i./[(imag(Zt1)-sqrt(3)*(real(Zt1)))];
                                                        (Reactance of the first
                                                        compensative element)
x2=-[real(Zt1).^2+(imag(Zt1).^2)]*i./[(imag(Zt1)+sqrt(3)*(real(Zt1)))];
                                                        (Reactance of the second
                                                        compensative element)
Lc1=(imag(x1))./(2*pi*50);                              (Inductance of the first
                                                        compensative element)
Cc1=1000000./(2*pi*50*imag(x2));                        (Capacitance of the second
                                                        compensative element)
C2=0.2e-4;                                                    (20 uF in parallel)
Xc2=-[1./(2*pi*50*C2)]*i;                                The cycle repeats itself.
Zt2=[(Zm*Xc2)./(Zm+Xc2)];
x3=-[real(Zt2).^2+(imag(Zt2).^2)]*i./[(imag(Zt2)-sqrt(3)*(real(Zt2)))];
x4=-[real(Zt2).^2+(imag(Zt2).^2)]*i./[(imag(Zt2)+sqrt(3)*(real(Zt2)))];
Lc2=(abs(x3))./(2*pi*50);
Cc2=1000000./(2*pi*50*abs(x4));
C3=0.3e-4;
Xc3=-[1./(2*pi*50*C3)]*i;
Zt3=[(Zm*Xc3)./(Zm+Xc3)];
x5=-[real(Zt3).^2+(imag(Zt3).^2)]*i./[(imag(Zt3)-sqrt(3)*(real(Zt3)))];
x6=-[real(Zt3).^2+(imag(Zt3).^2)]*i./[(imag(Zt3)+sqrt(3)*(real(Zt3)))];
Lc3=(abs(x5))./(2*pi*50);
Cc3=1000000./(2*pi*50*abs(x6));
```

```
C4=0.4e-4;
Xc4=-[1./(2*pi*50*C4)]*i;
Zt4=[(Zm*Xc4)./(Zm+Xc4)];
x7=-[real(Zt4).^2+(imag(Zt4).^2)]*i./[(imag(Zt4)-sqrt(3)*(real(Zt4)))];
x8=-[real(Zt4).^2+(imag(Zt4).^2)]*i./[(imag(Zt4)+sqrt(3)*(real(Zt4)))];
Lc4=(abs(x7))./(2*pi*50);
Cc4=1000000./(2*pi*50*abs(x8));
C5=0.5e-4;
Xc5=-[1./(2*pi*50*C5)]*i;
Zt5=[(Zm*Xc5)./(Zm+Xc5)];
x9=-[real(Zt5).^2+(imag(Zt5).^2)]*i./[(imag(Zt5)-sqrt(3)*(real(Zt5)))];
x10=-[real(Zt5).^2+(imag(Zt5).^2)]*i./[(imag(Zt5)+sqrt(3)*(real(Zt5)))];
Lc5=(abs(x9))./(2*pi*50);
Cc5=1000000./(2*pi*50*abs(x10));
C6=0.6e-4;
Xc6=-[1./(2*pi*50*C6)]*i;
Zt6=[(Zm*Xc6)./(Zm+Xc6)];
x11=-[real(Zt6).^2+(imag(Zt6).^2)]*i./[(imag(Zt6)-sqrt(3)*(real(Zt6)))];
x12=-[real(Zt6).^2+(imag(Zt6).^2)]*i./[(imag(Zt6)+sqrt(3)*(real(Zt6)))];
Lc6=(abs(x11))./(2*pi*50);
Cc6=1000000./(2*pi*50*abs(x12));
C7=0.7e-4;
Xc7=-[1./(2*pi*50*C7)]*i;
Zt7=[(Zm*Xc7)./(Zm+Xc7)];
x13=-[real(Zt7).^2+(imag(Zt7).^2)]*i./[(imag(Zt7)-sqrt(3)*(real(Zt7)))];
x14=-[real(Zt7).^2+(imag(Zt7).^2)]*i./[(imag(Zt7)+sqrt(3)*(real(Zt7)))];
Lc7=(abs(x13))./(2*pi*50);
Cc7=1000000./(2*pi*50*abs(x14));
plot(ns,Cc2)
hold on
plot(nr,Cc3)
hold on
plot(nr,Cc4)
hold on
plot(nr,Cc5)
hold on
plot(nr,Cc6)
hold on
plot(nr,Cc7)
```

Appendix 1.2

Circuit diagrams for centrifugal pump

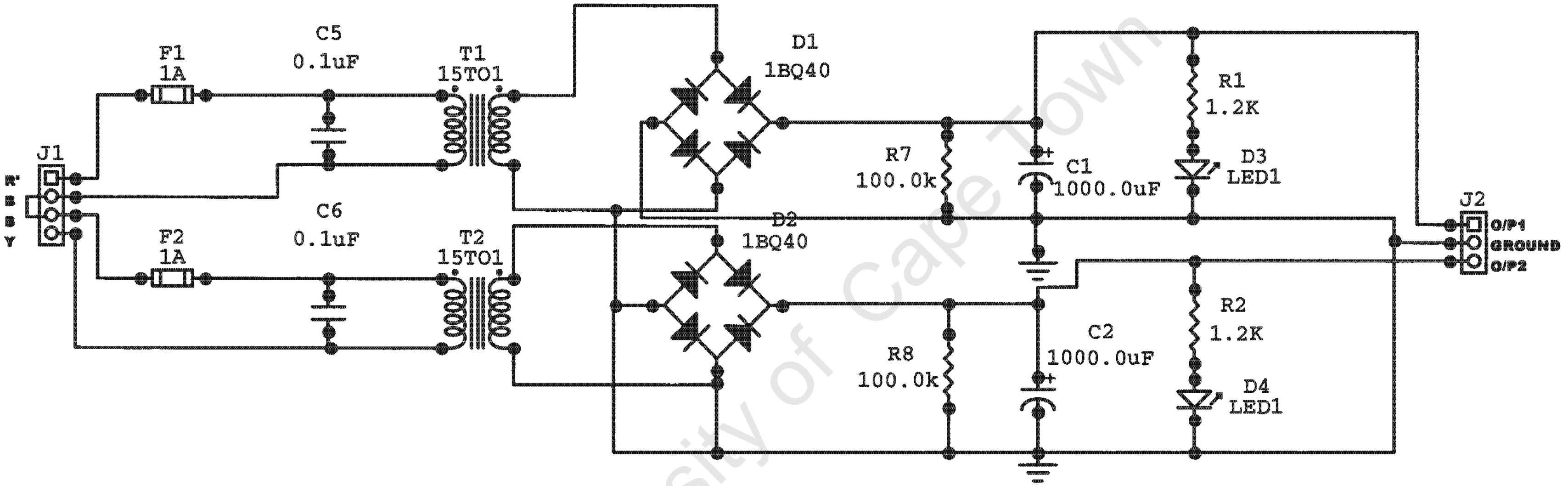

To caps drive diagram 1

Name: Voltage feedback

Title: Adaptive compensator

Rev
ID
Fig: 7.3

Date: 9.1.2001
Page: 1 of 1

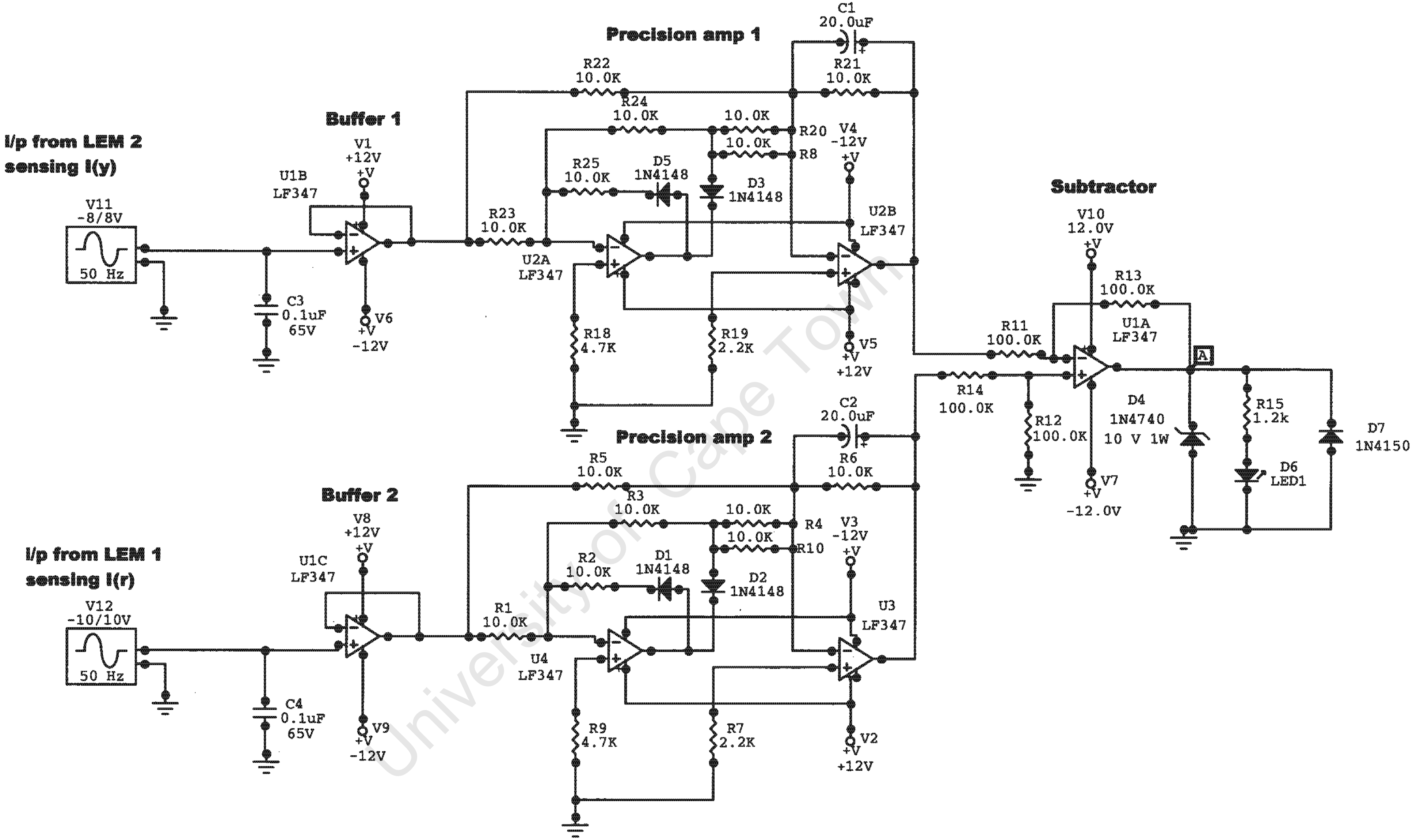

Name: Currnet feed-back amplifiers

Title: Adaptive compensator

Rev ID

Fig: 7.4

Date: Page: 1 of 1

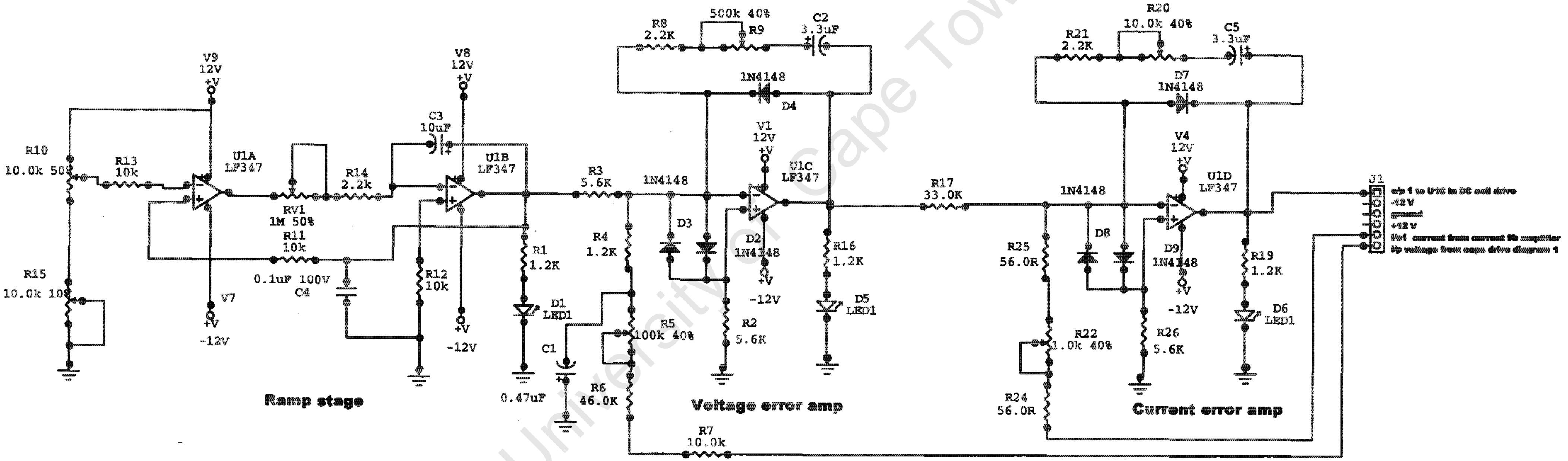

Name: Voltage and current error amplifier

Title: Adaptive compensator

Rev ID

Fig: 7.5

Date:

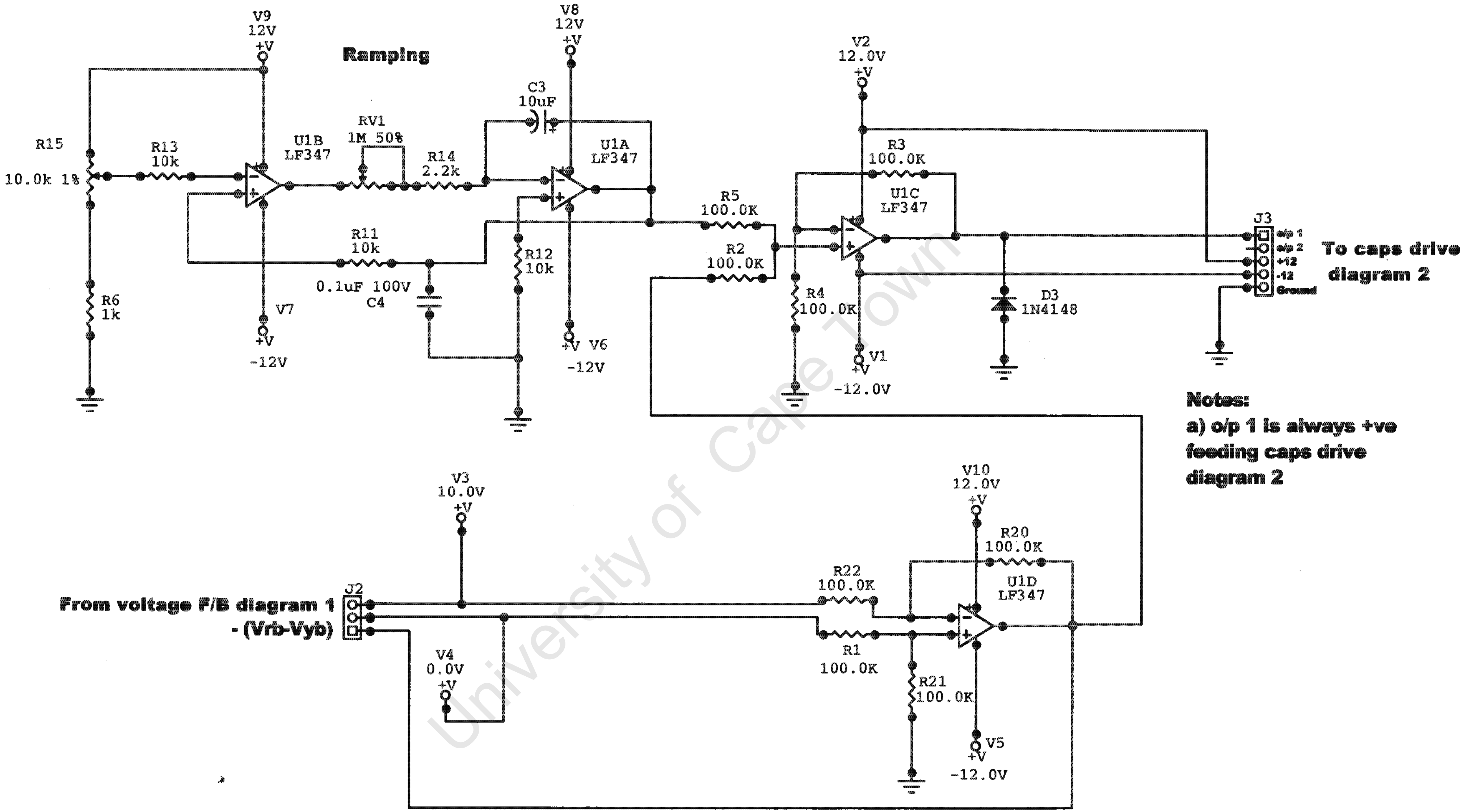

Notes:
a) o/p 1 is always +ve feeding caps drive diagram 2

Name: Caps drive 1

Title: Adaptive compensator

Rev ID
Fig:7.6

Date: 9.1.2001 Page: 1 of 1

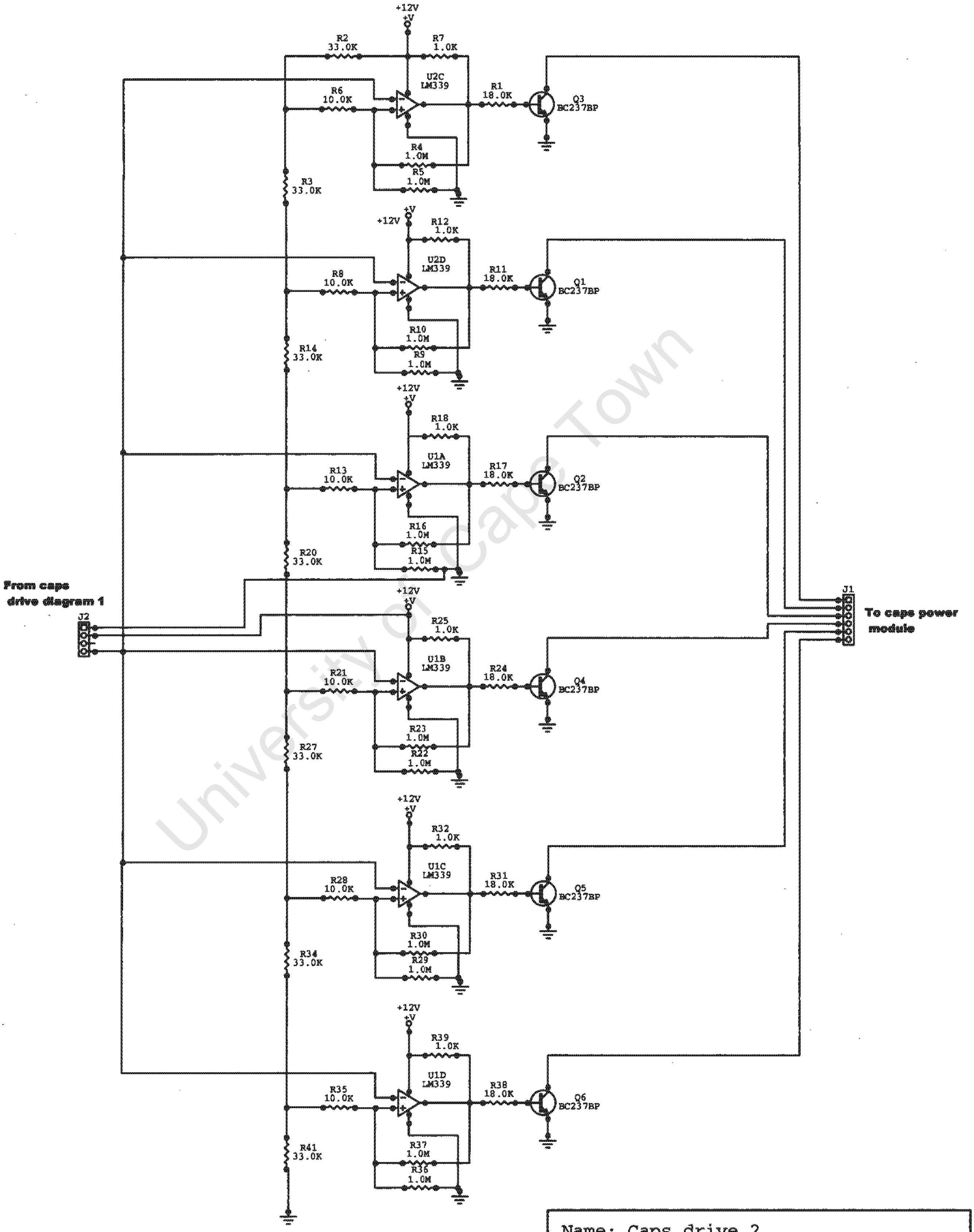

Name: Caps drive 2

Title: Adaptive compensator

Rev ID

Fig:7.7

Date:

Page: 1 of 1

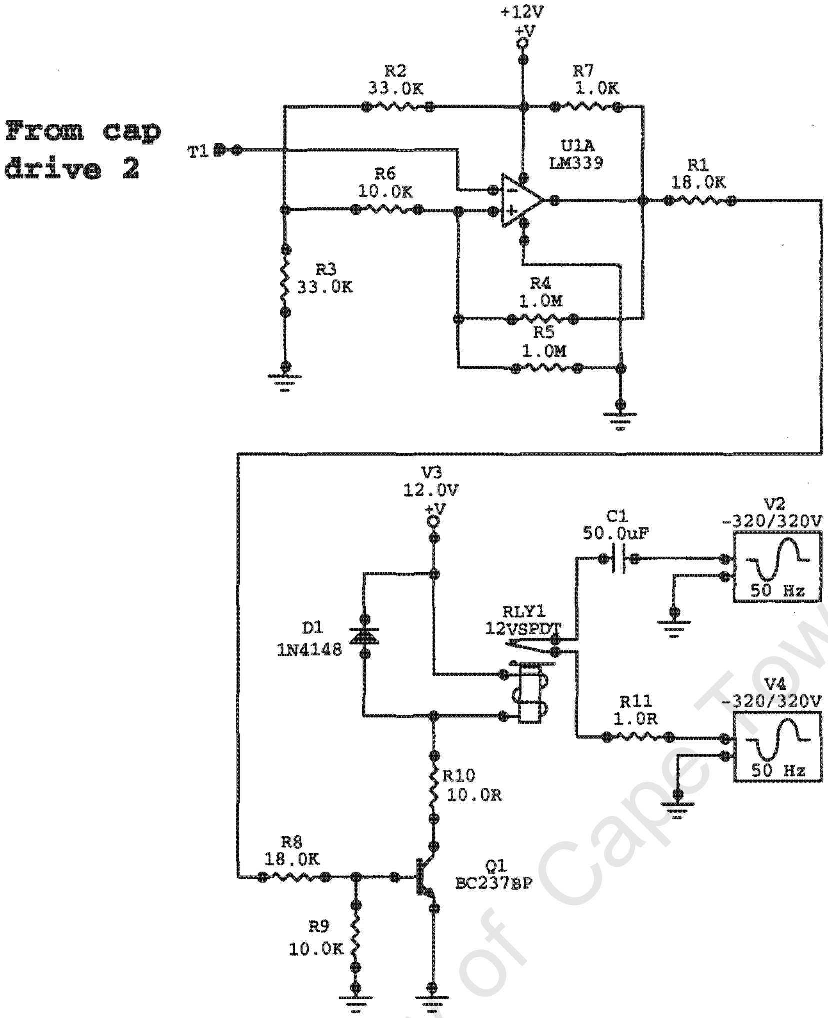

Name: Caps drive 3	
Title: Adaptive compensator	
Rev	ID Fig: 7.8
Date:	Page: 1 of 1

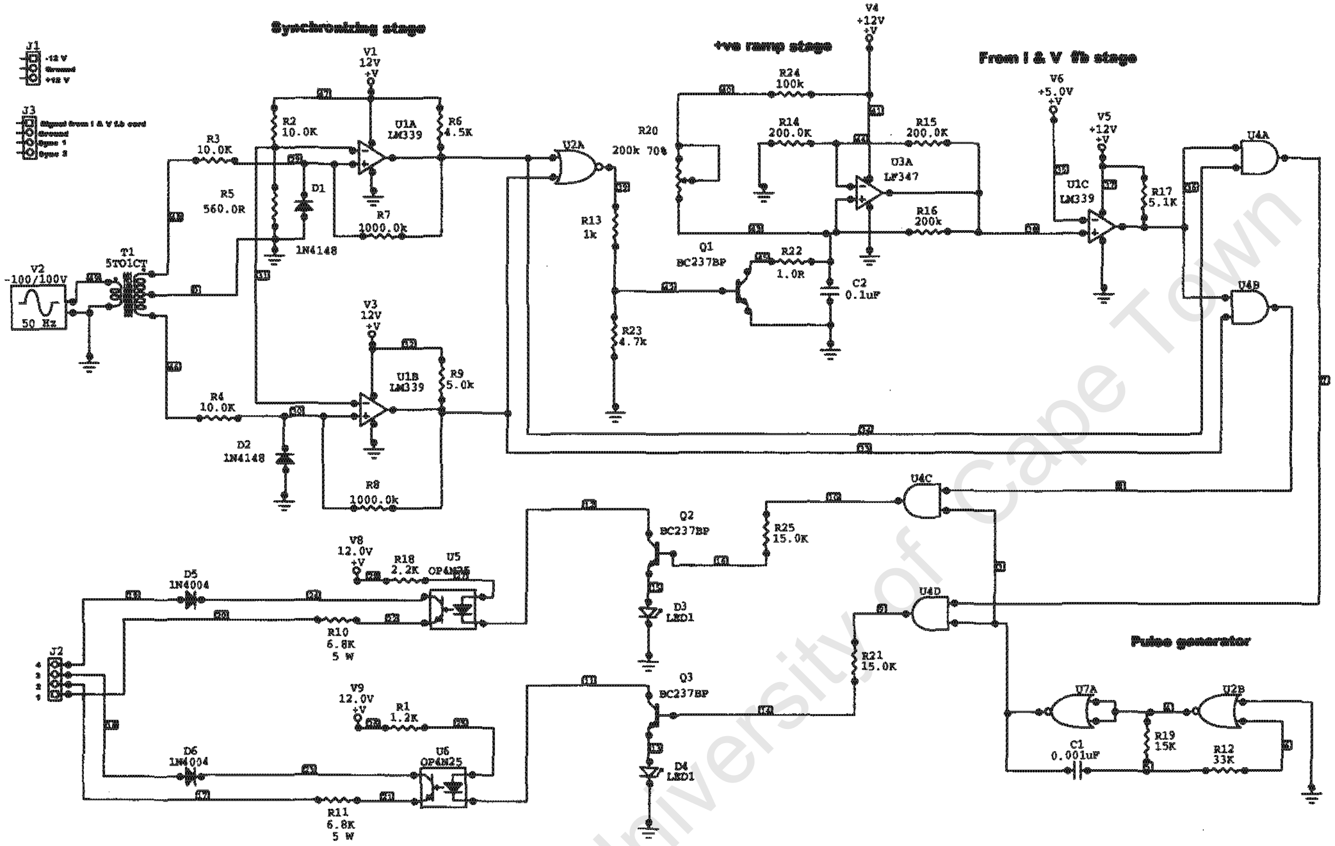

Name: Saturable reactor DC coil drive

Title: Adaptive compensator

Rev ID
Fig:7.9

Date: Page: 1 of 1

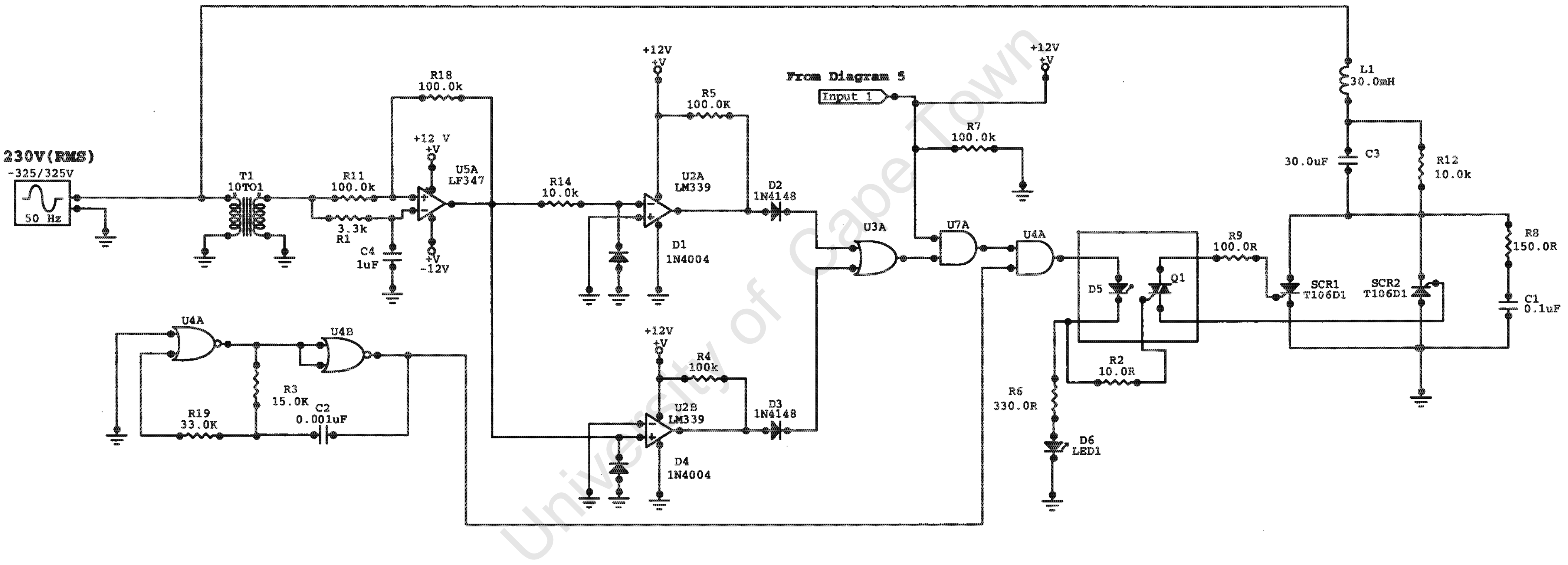

Name: Thyristor-switched caps triggering circuit	
Title: Adaptive compensator	
Rev	ID Fig:7.10
Date:	Page: 1 of 1

Appendix 1.3

Circuit diagrams for adaptive compensator

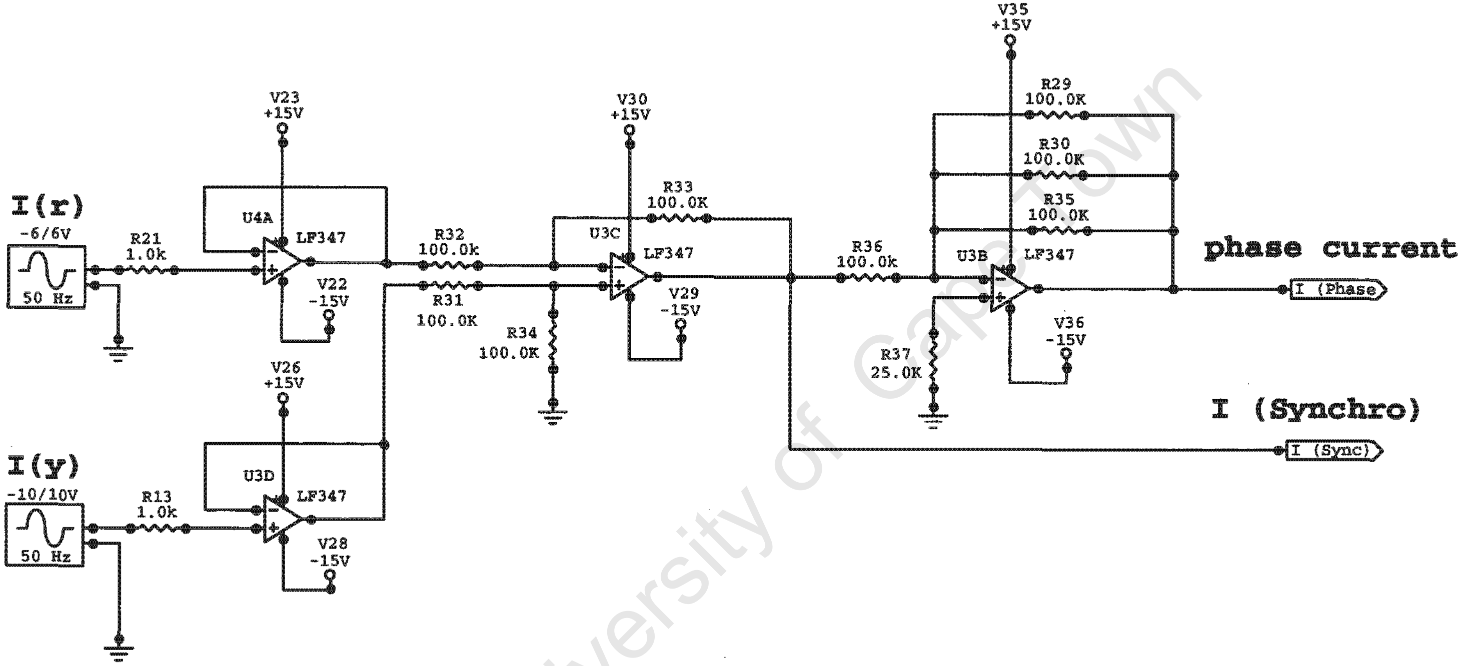

Name: Phase current sampling circuit	
Title: Adaptive compensator	
Rev	ID Fig:7.11
Date:	Page: 1 of 1

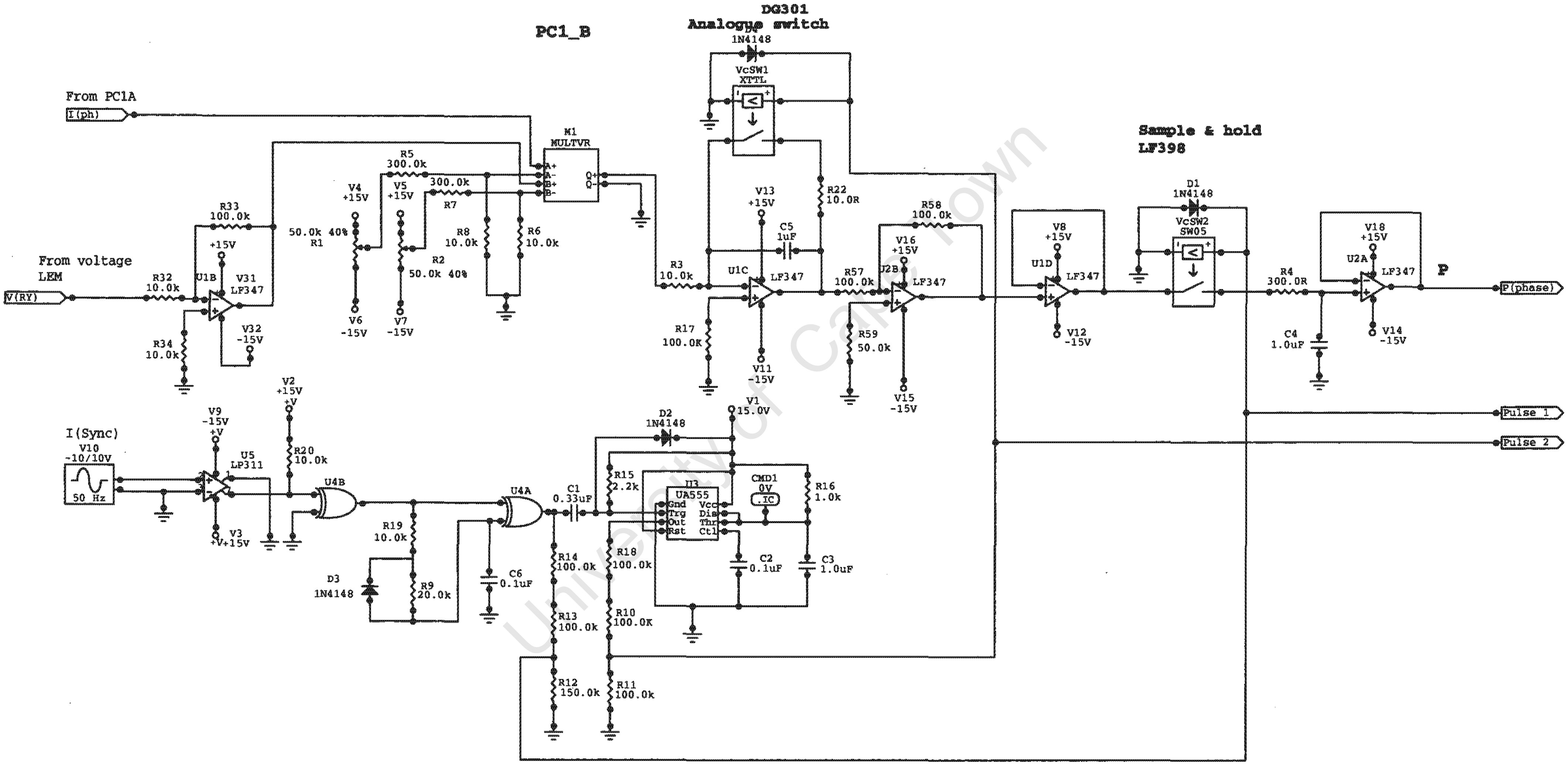

Name: Phase average active power meter

Title: Adaptive compensator

Rev | ID

Fig:7.12

Date:

Page: 1 of 1

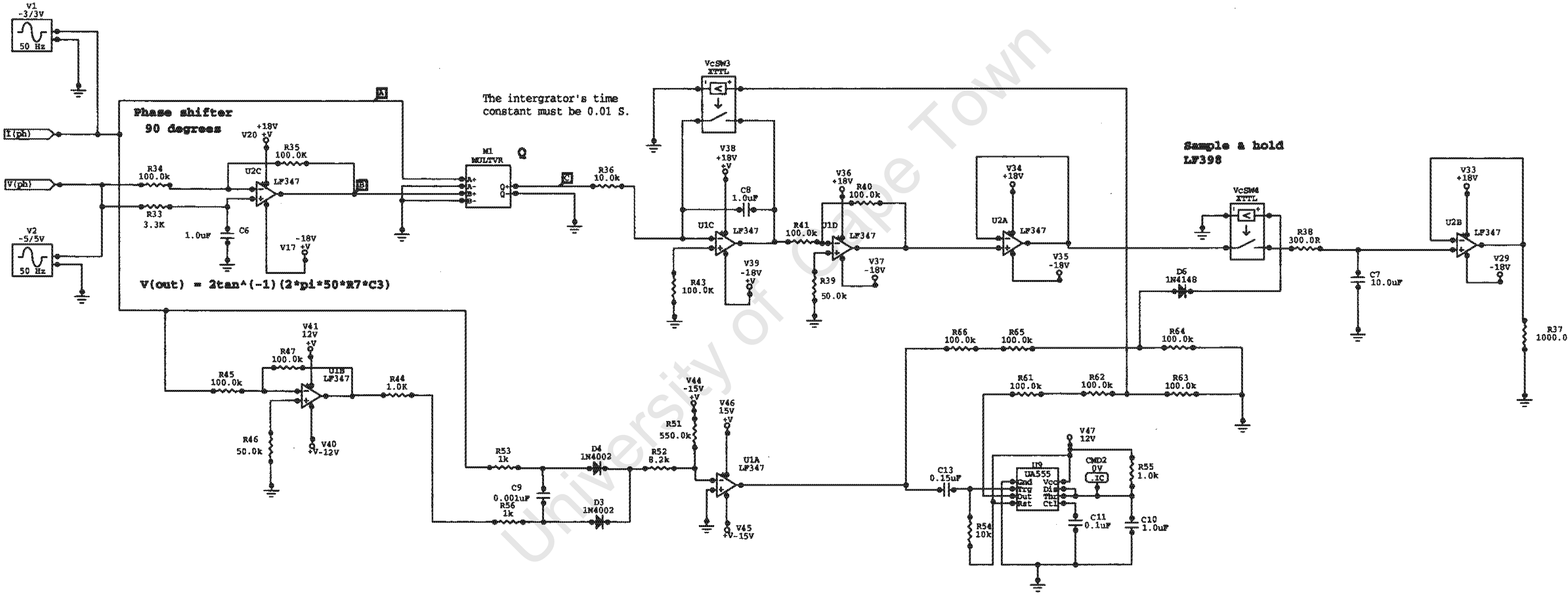

Name: Phase average reactive power meter

Title: Adaptive compensator

Rev ID

Fig:7.13

Date: Page: 1 of 1

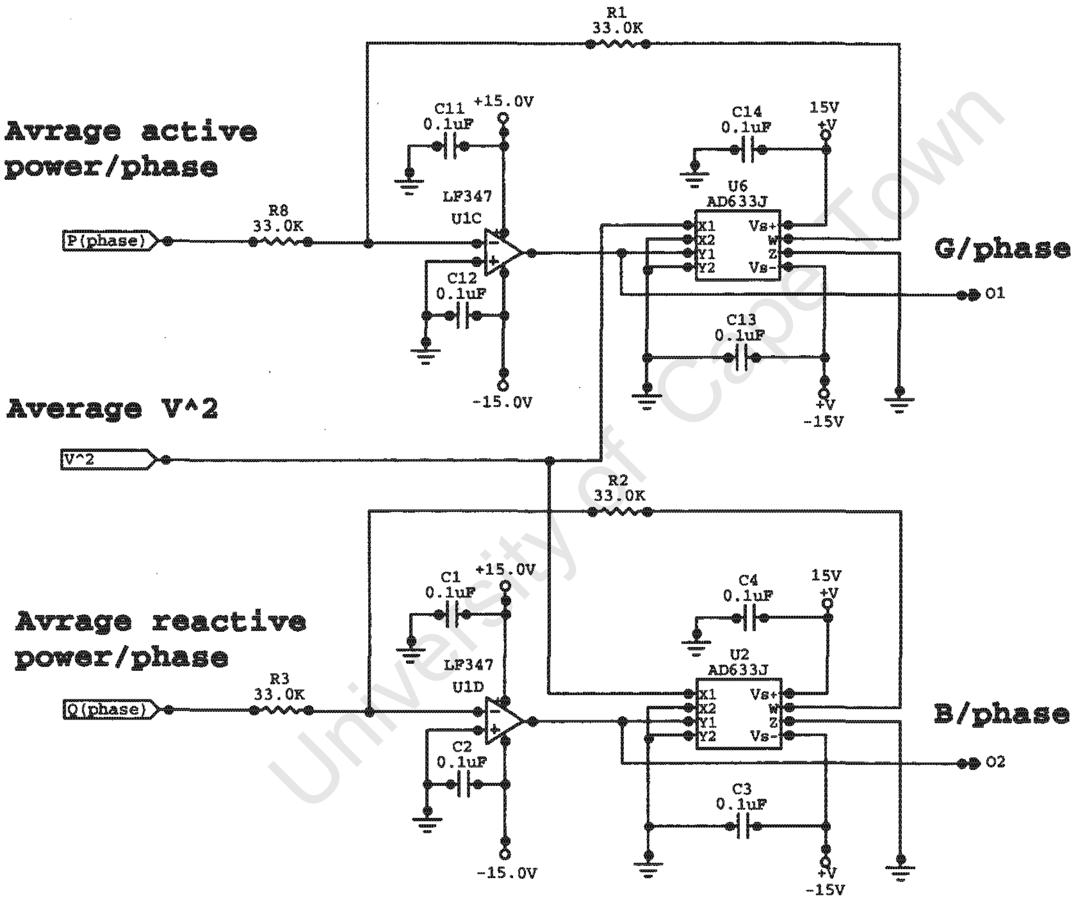

Name: Load conductance and succeptance meter

Title: Adaptive compensator

Rev	ID Fig:7.14
Date:	Page: 1 of 1

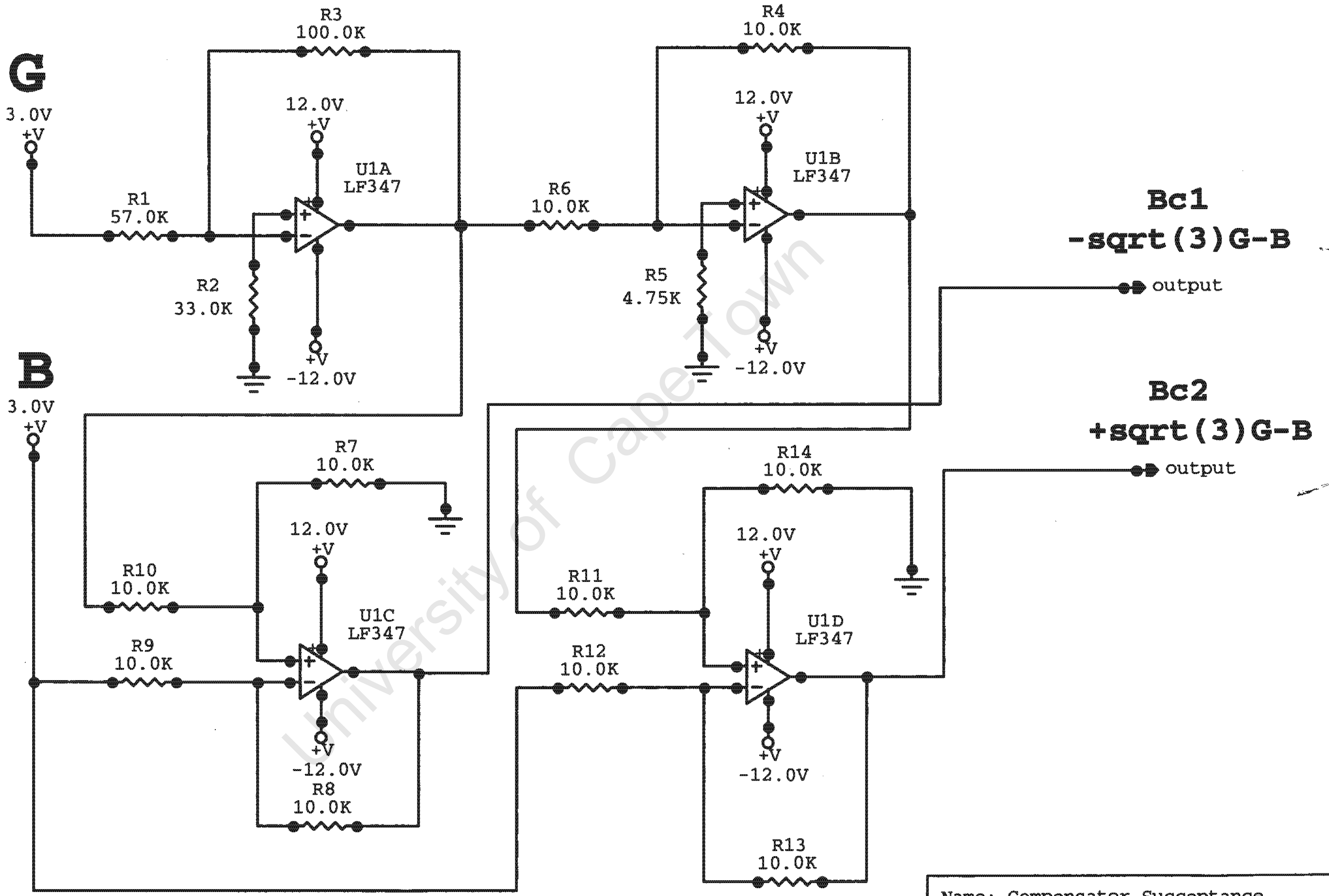

Name: Compensator Succeptance	
Title: Adaptive compensator	
Rev	ID Fig:7.15
Date:	Page: 1 of 1

Appendix 1.4

Derivation of phase current for unbalanced supply voltage

Derivation of phase current in a three-phase balanced load supplied with a single-phase voltage.

With reference to Fig: 4.2,

$$V_R - V_Y = V_{RY} = I_2.Z_2 \tag{1}$$

also $$V_{YB} = I_3.Z_3 \quad \text{and} \quad V_{RB} = I_1.Z_1 \tag{2}$$

The voltages around the load phases are: $$V_{RB} = V_{RY} + V_{YB} \tag{3}$$

At node A, $$I_R = I_2 + I_1 \tag{4}$$

At node B, $$I_Y = I_3 - I_2 \tag{5}$$

Putting (1) and (2) into (3),

$$I_1.Z_1 = I_2.Z_2 + I_3.Z_3 \tag{6}$$

Since, $Z_1 = Z_2 = Z_3$, equation (6) can be divided through by Z,

$$I_1 = I_2 + I_3 \tag{7}$$

Using equations (4) and (5) into (7),

$$I_R - I_2 = I_2 + I_Y + I_2 \tag{8}$$

$$I_R - I_Y = 3 * I_2 \tag{9}$$

$$I_2 = \frac{I_R - I_Y}{3} \tag{10}$$

Legend

I_1, I_2, I_3	Phase currents
Z_1, Z_2, Z_3	Corresponding phase impedances
I_R, I_Y, I_B	Line currents

All the above terms are vector quantities, ie the phase angles are included.

Appendix 1.5a

Concept and architecture of Real-Time Simulation

Matlab 6.1, Real-Time Workshop, and the accompanying third party software offer a real time development environment in which prototyping with hardware-in the loop and simulation in real-time becomes possible. Attractive features of this method of prototyping are:

- **Data acquisition** I/O cards are used to import the signals from the real external hardware. For a low frequency application e.g. 50 Hz fundamental and 1.0 KHz for the highest order of harmonic content, a typical sampling rate of 5 to 10 KHz, provides an excellent miniature duplication of the real signal.
- **Real-Time measurement and control** by using Simulink models that mimic system dynamics, real-life measurement and actuation signals. In the absence of expensive digital scopes and power analyzers, virtual instrumentation of this kind is extremely useful.
- **Interactive Real-Time parameter tuning** allows the change of parameters while the program is executing.
- **The conversion of the model to C or ADA codes** is done automatically by the Real-Time workshop. These codes can also be exported to other simulation programs.

Due to the above advantages, this technique can be applied to a variety of applications such as, signal visualization, parameter tuning, real-time control and real-time hardware in the loop simulation.

System Architecture

The general architecture of the modelling system is shown in the next page.

Before testing and applying the system to the converter, a clear understanding of the various parts of the structure is required.

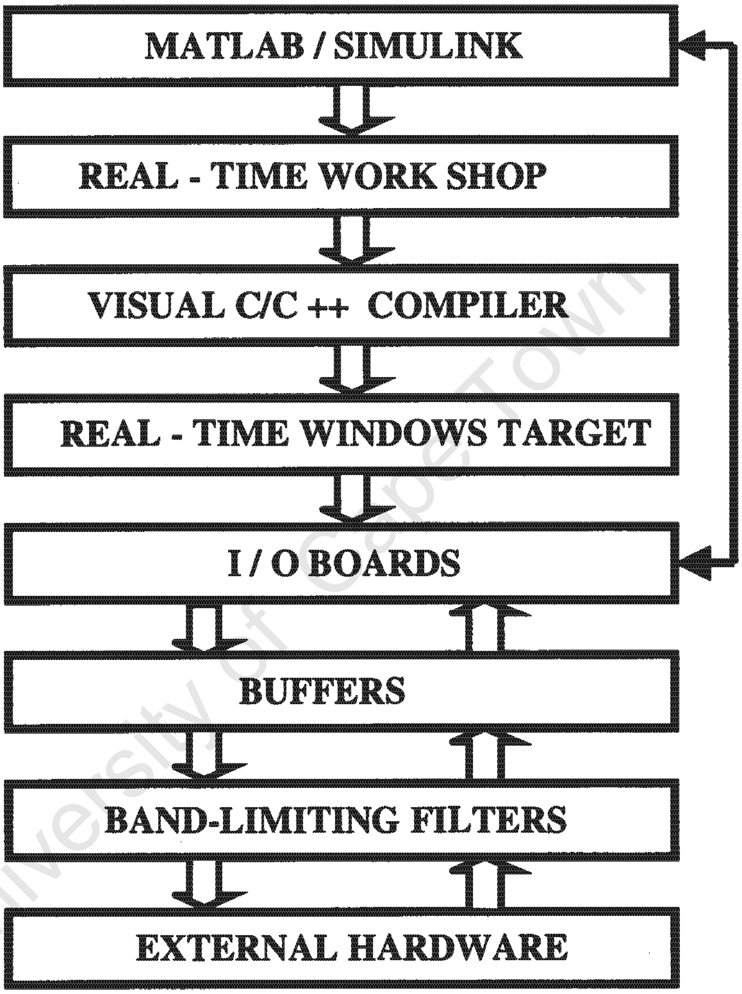

Fig : 7.16 Architecture of the prototyping system

Matlab/Simulink is used as the front-end to design any electrical/electronics system by using block diagrams to develop models.

Real-Time workshop is activated with Simulink external mode of operation and is responsible for generating C codes for models representing discrete-time, continuous-time and hybrid systems. In essence this is a direct path from system design to hardware implementation.

Third-party product i.e. a C-compiler is required to create executable code from the C code generated by the Real-Time Workshop. Microsoft Visual C/C++ professional version 5.0 is recommended.

Real-Time Windows Target is an add-on product that extends the functionality of the Real-Time Workshop. Integration between Simulink external mode and Real-Time Windows Target allows the usage of any simulink model as a graphical user interface.
In addition, this product provides support/drivers for nearly 100 different I/O boards. A small real time Kernel is used with the Real-Time Windows Target to ensure the real-time application runs in real time. The real-time Kernel runs at CPU ring zero and uses the built-in PC clock, as it's primary source of time.

Data Acquisition cards with D/A and A/D channels, have to be used to convert the executable C codes to real signals available at the output terminals. The available card for this project was CIO-DAS1600 from Computer-Boards with16 single-ended analogue inputs and two analogue outputs. The full specifications are attached in appendix 1.6.

Buffers are used for every input and output analog signal to reduce possible heavy currents drawn from the input isolating current and voltage transducers and/or from the I/O card.

Anti-Aliasing filters are used to band-limit the input signals and suppress any possible spikes entering the card.

Appendix 1.5b

Voltage and current harmonics in an unsaturated reactor

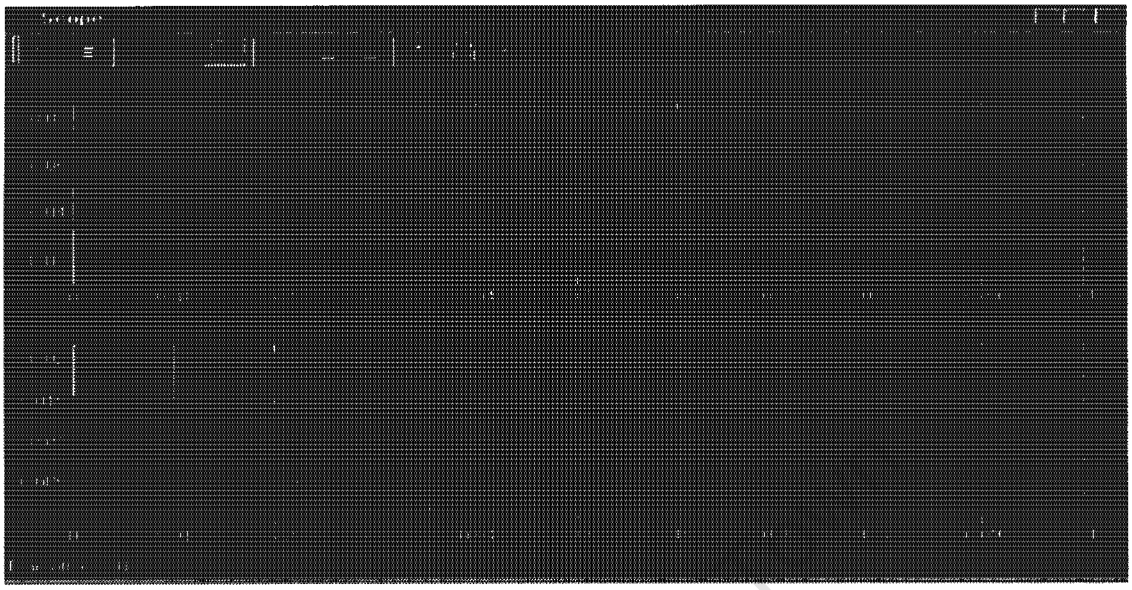

Fig: 7.17 Magnitudes of the 5^{th} order voltage and current harmonics

For a pure inductive load, the n^{th} harmonic currents must be of 1/n value of the corresponding voltage harmonics. This is clearly shown in the above figure.

The phase angles for the same order are shown in the following diagram.

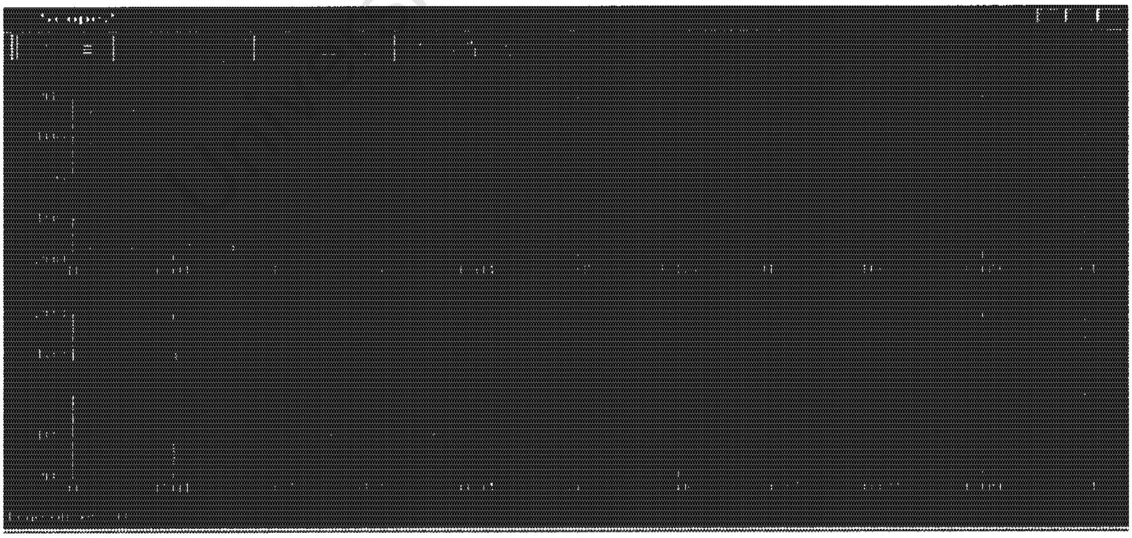

Fig: 7.18 Phase angles of the 5th order voltage and current harmonics

The phase difference is shown to be nearly 90 degrees.

Final test is for the 7^{th} order harmonics. The voltage harmonic has roughly seven time the magnitude the corresponding current harmonics and the phase difference between the two components is $\pi/2$ Radians.

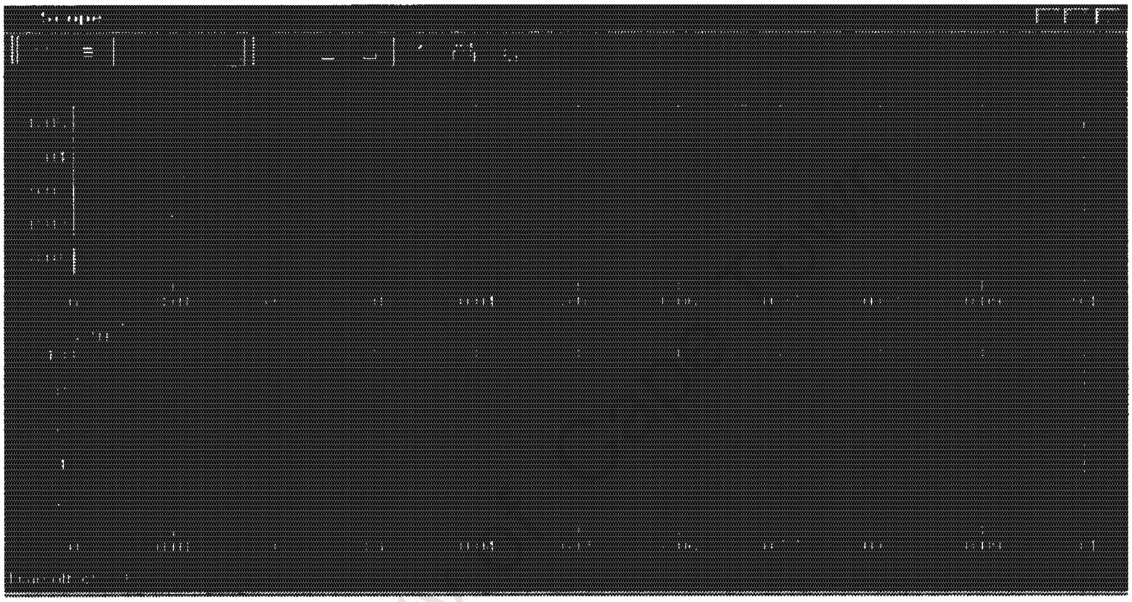

Fig: 7.19 Magnitude of the 7th order voltage and current harmonics

Fig: 7.20 Phase angles of the 7th order voltage and current harmonics

Appendix 1.5c

Voltage and current harmonics in a saturated reactor

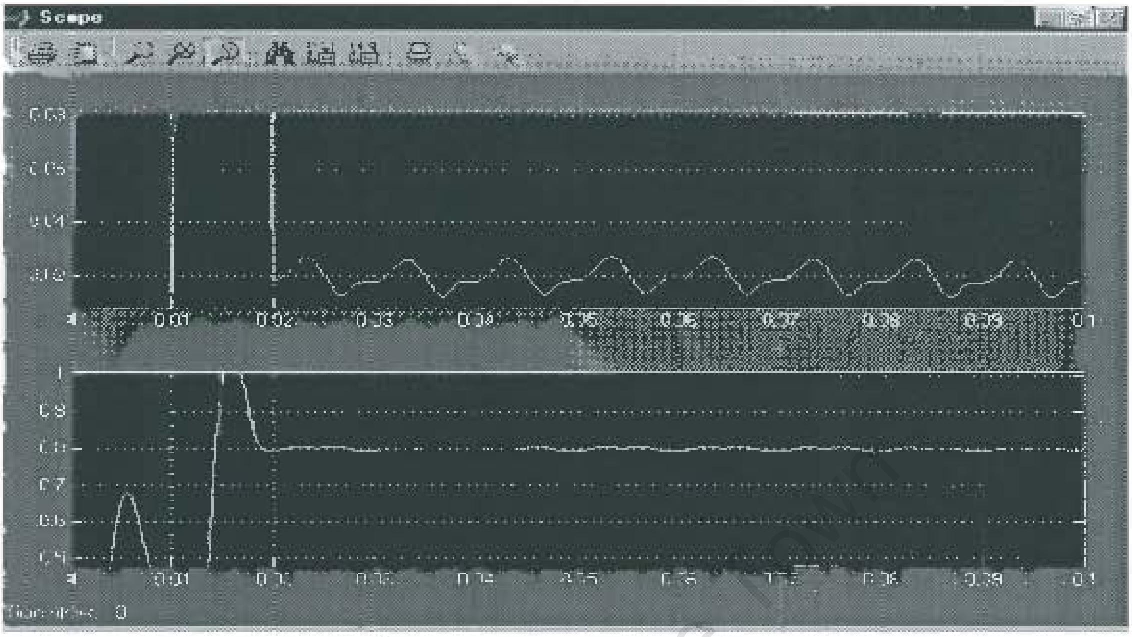

Fig: 7.21 Magnitude of the 3rd order voltage and current harmonics for a saturated core

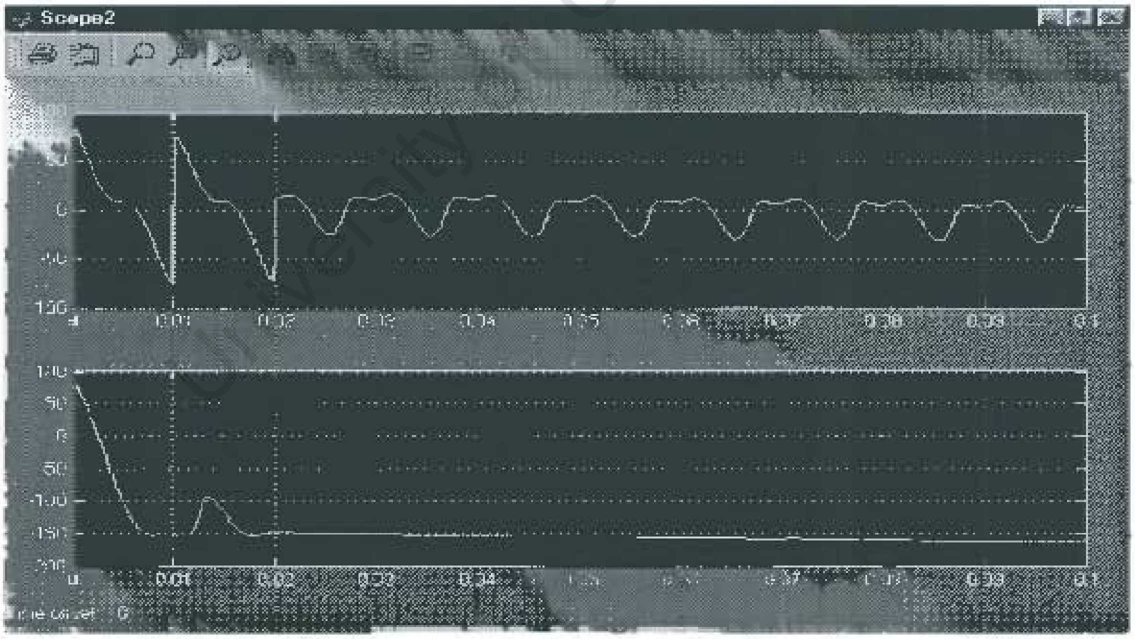

Fig: 7.22 Phase angles of the 3rd order voltage and current harmonics

Fig: 7.23 Magnitude of the 5th order voltage and current harmonics in a saturated core

Fig: 7.24 Phase angles of the 5th order voltage and current harmonics

Fig: 7.25 Magnitude of the 7th order voltage and current harmonics in a saturated core

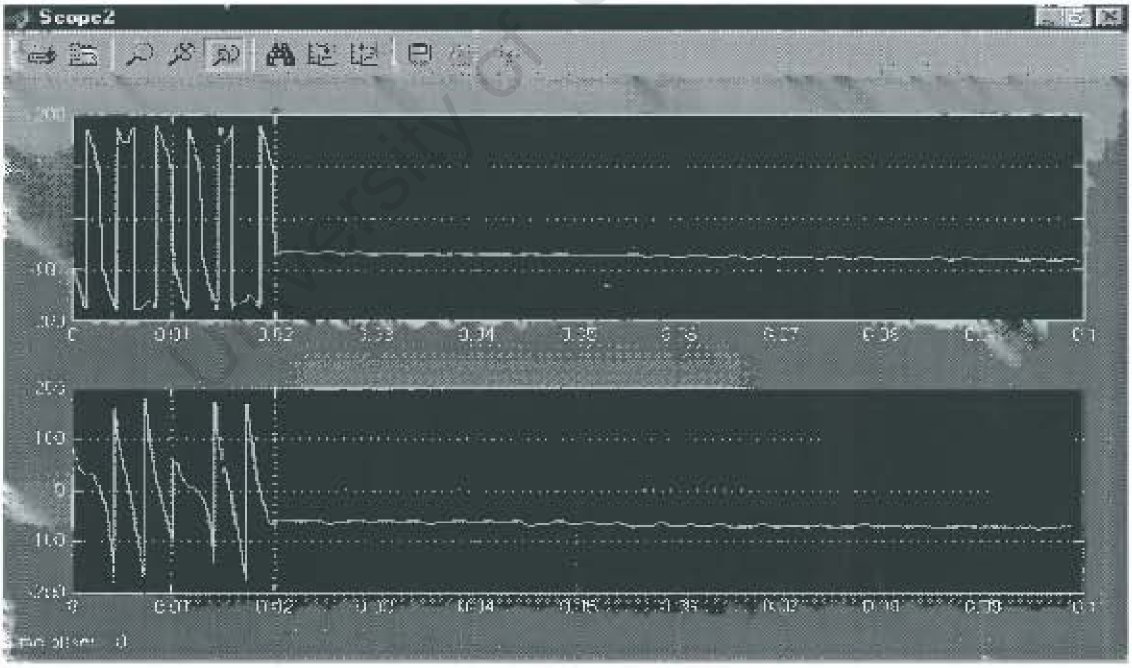

Fig: 7.26 Phase angles of the 7th order voltage and current harmonics

Appendix 1.5d

Expanded model for Adaptive Passive Element Converter

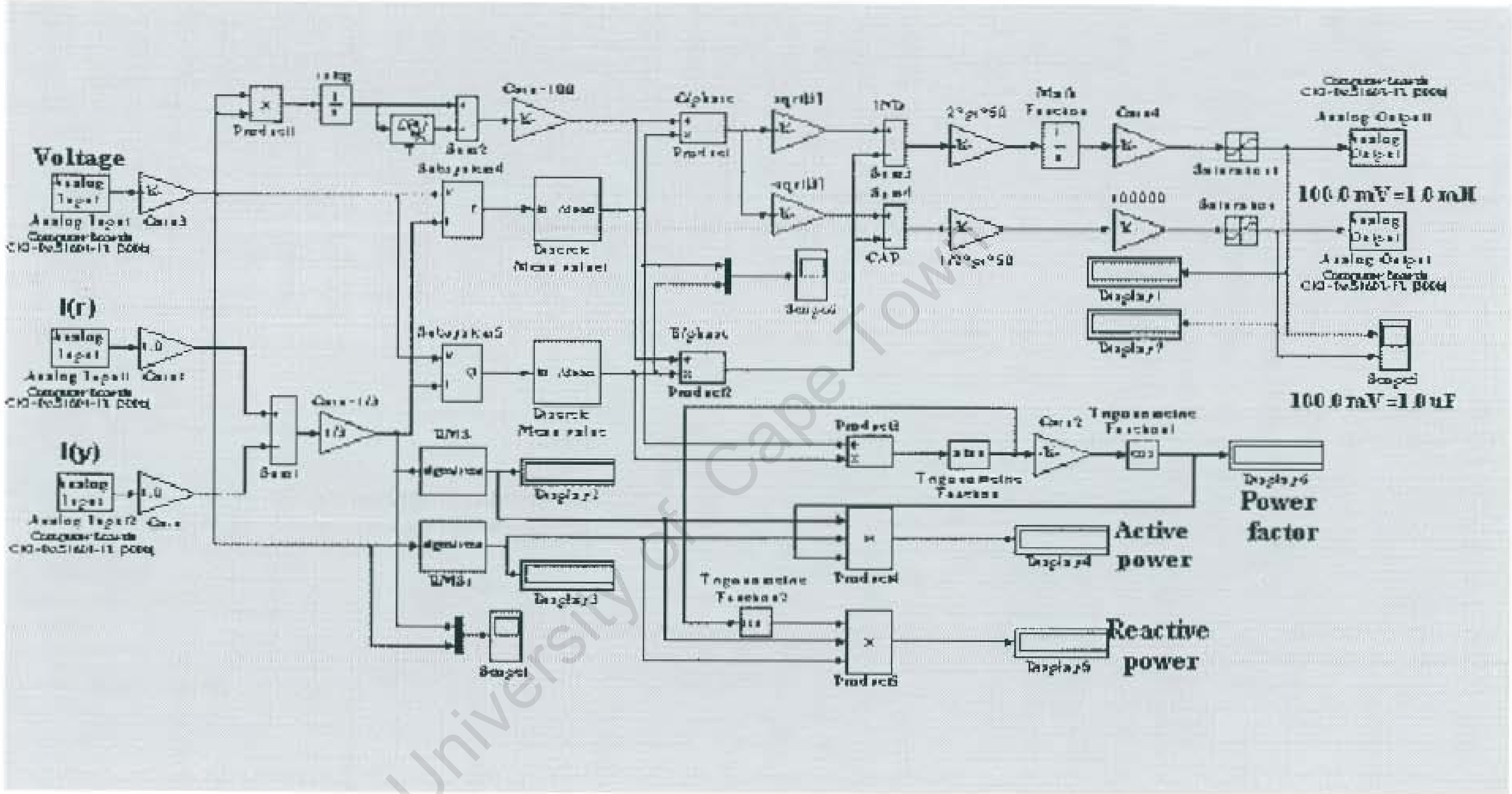

Fig: 7.27 Expanded model for three-phase voltage compensation

Appendix 1.5e

Real-Time simulated results for resistive loads

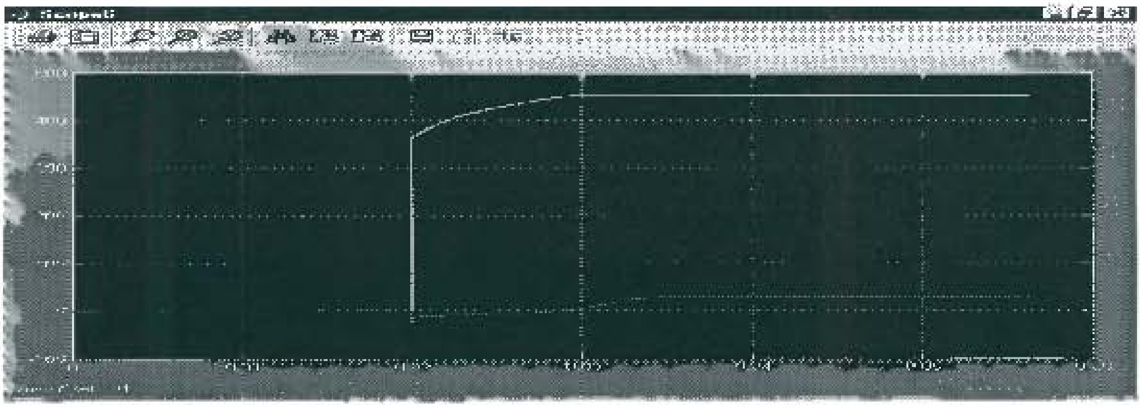

Fig: 7.28 Real-Time measurement of active and reactive power of a 500 W resistive load

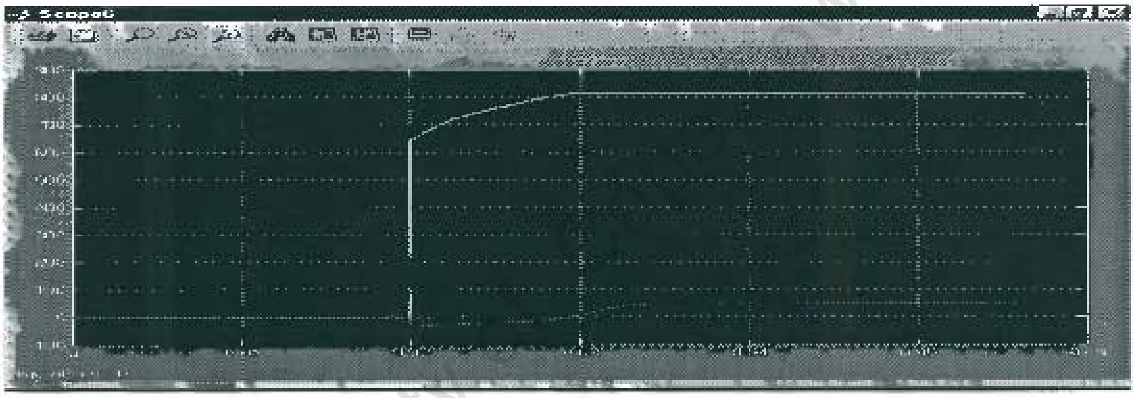

Fig: 7.29 Real-Time measurement of active and reactive power of a 900 W resistive load

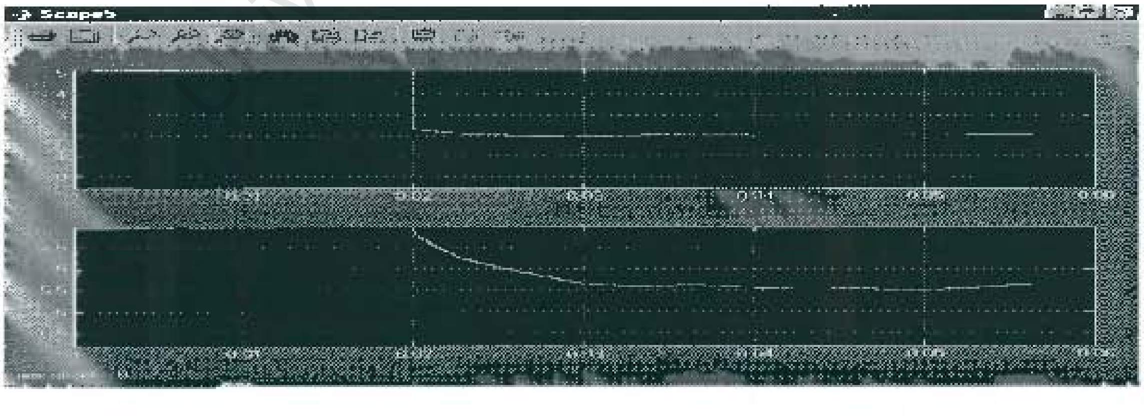

Fig: 7.30 Real-Time DC equivalent of the converter elements at 500 W load

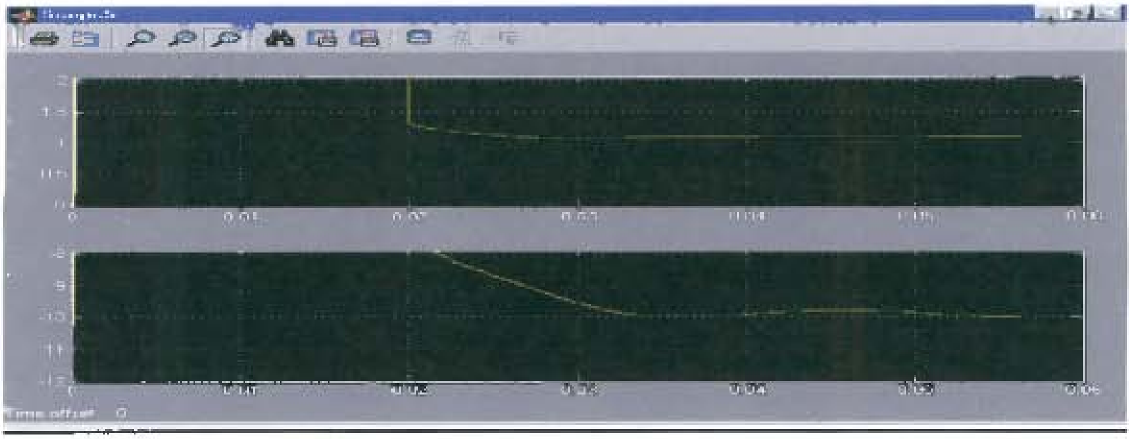

Fig: 7.31 Real-Time DC equivalents of the converter elements at 900 W load

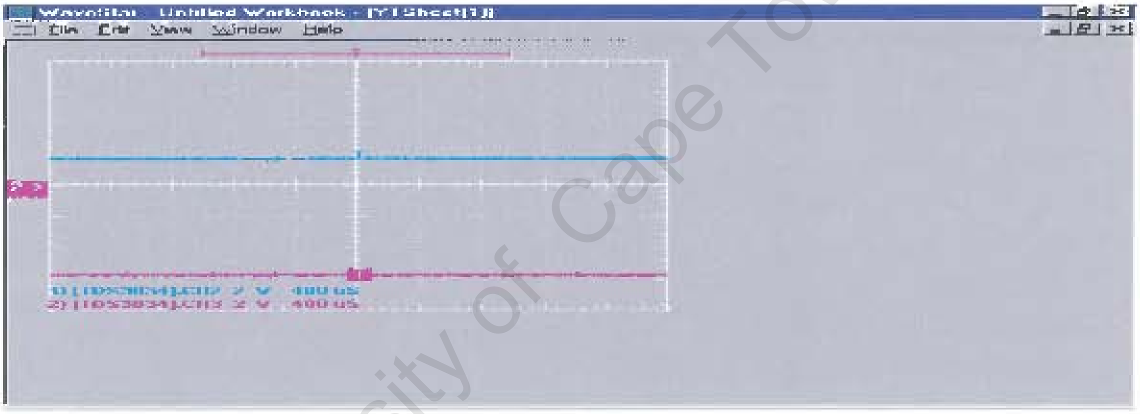

Fig: 7.32 Oscilloscope captured DC equivalents of the converter elements for a 500 W load

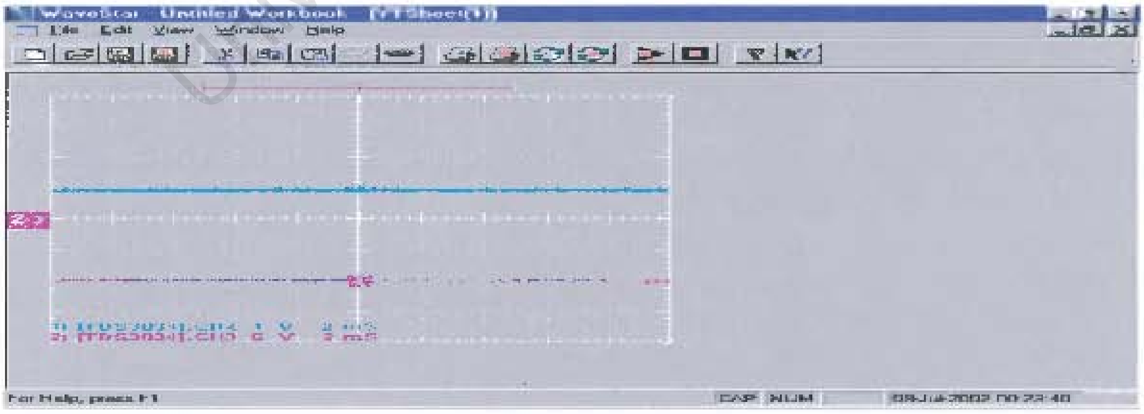

Fig: 7.33 Oscilloscope captured DC equivalents of the converter elements for a 900 W load

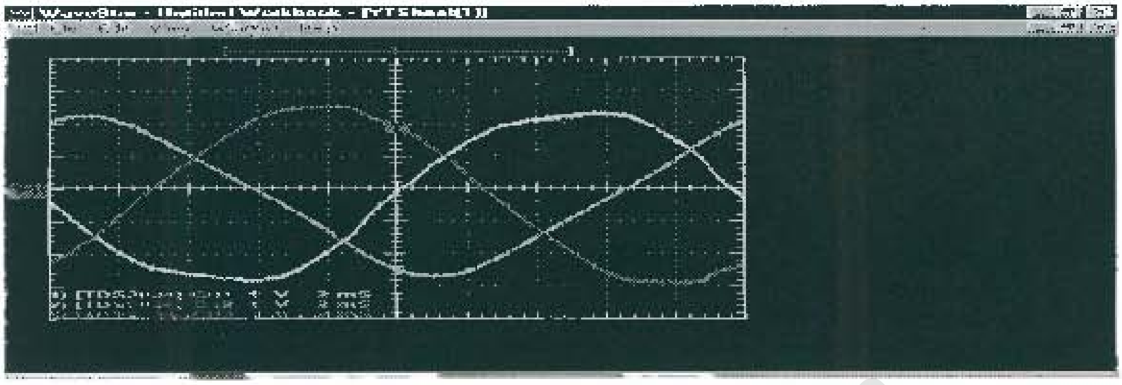

Fig: 7.34 Line voltages after compensation for 500 W load

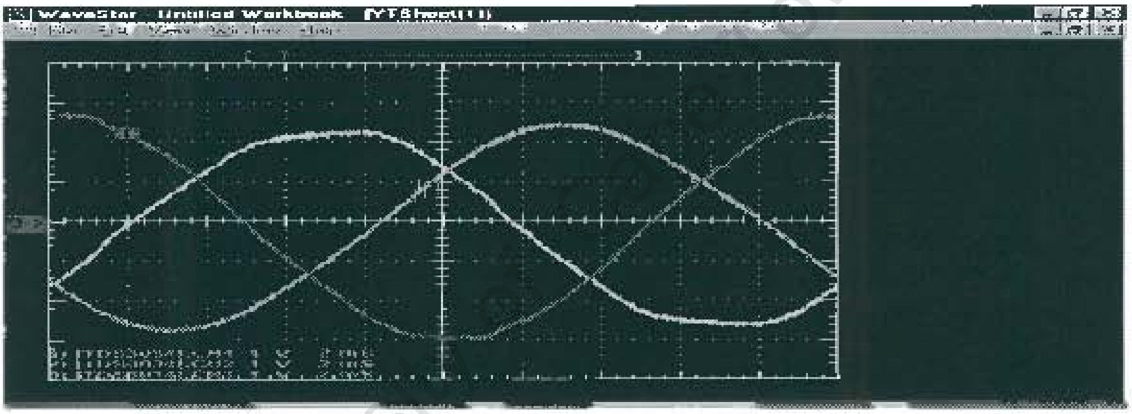

Fig: 7.35 Line voltages after compensation for 900 W load

Appendix 1.5f

M-G Real-Time Simulated results

300 W load on the generator

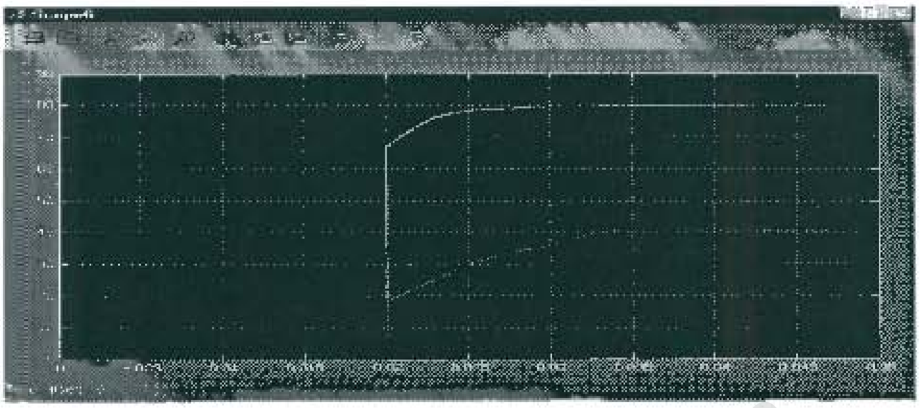

Fig: 7.36 Average active and reactive power

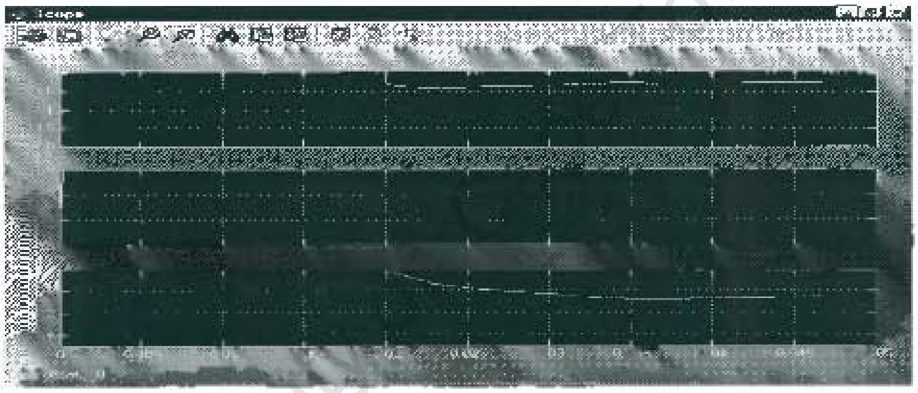

Fig: 7.37 Converter element DC equivalent values at 300W load (1.75H and 10.6uF)

500 W load on the generator

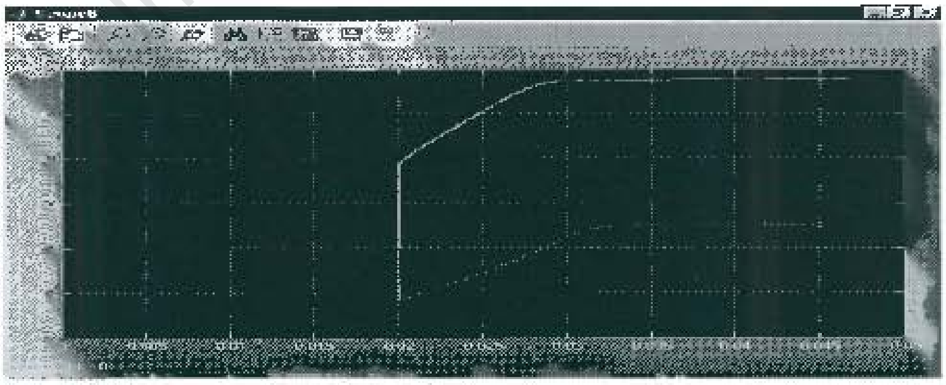

Fig: 7.38 Average active and reactive power

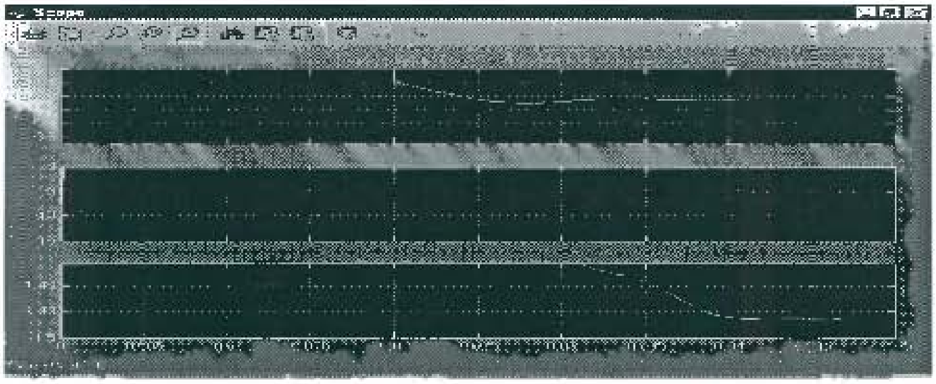

Fig: 7.39 Converter element DC equivalent values at 500W load (1.15H and 15.0uF)

800W load on the generator

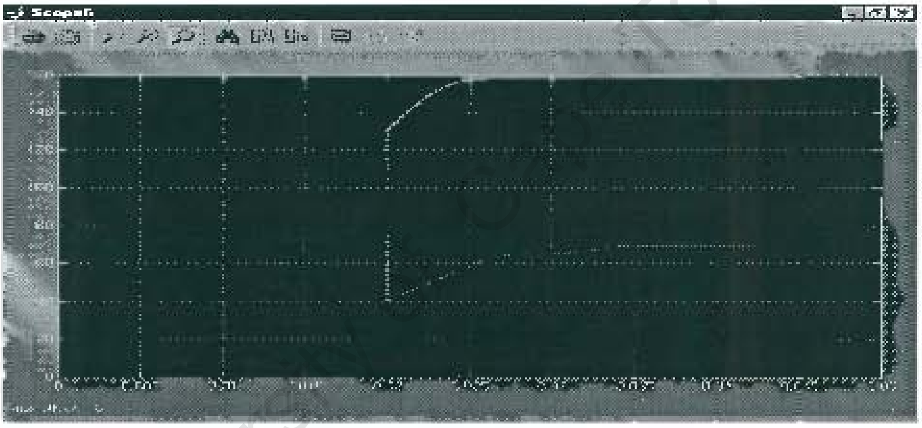

Fig: 7.40 Average active and reactive power

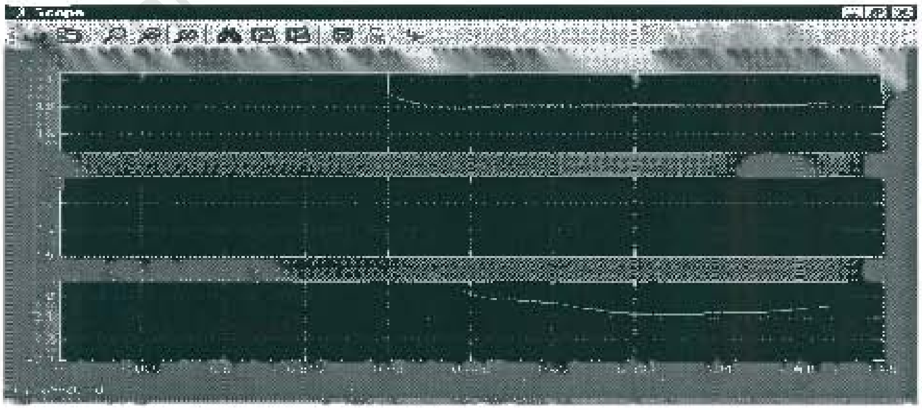

Fig: 7.41 Converter element DC equivalent values at 800W load (0.825H and 20.0uF)

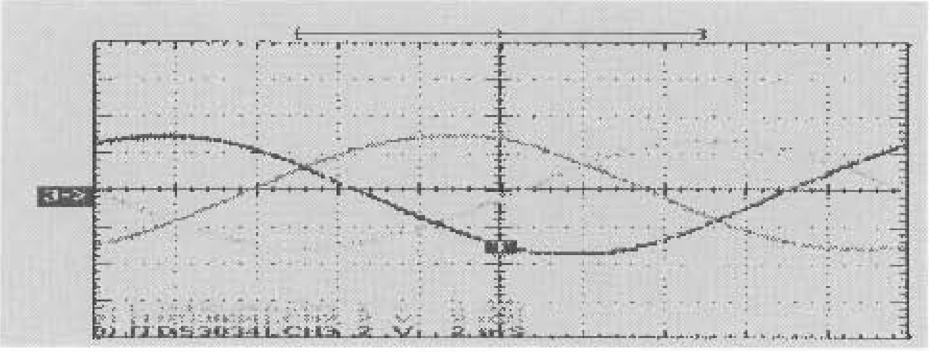

Fig: 7.42 After compensated load voltage waveforms for 300W load

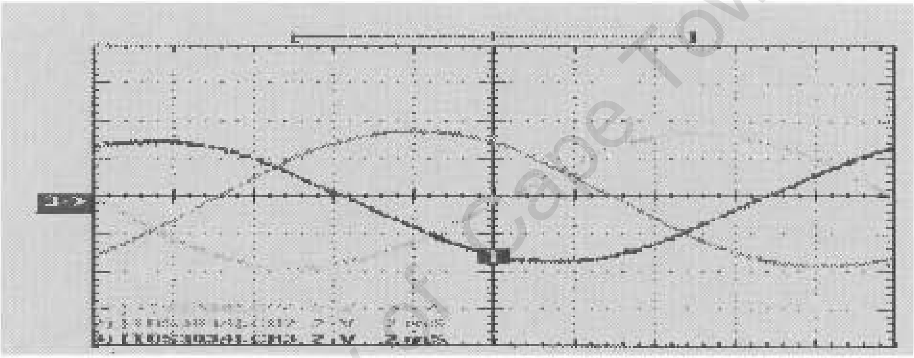

Fig: 7.43 After compensated load voltage waveforms for 500W load

The rest of the loading with appropriate converter values attached produce similar waveforms.

Appendix 1.6

Data sheets on CIO-DAS1600 data acquisition card from "Measurement Computing", voltage and current transducers (LEMS) from "Denver technical products" and saturable core material by "Alloy Magnetic" Cores.

9 SPECIFICATIONS

9.1 CIO-DAS1601/12 & CIO-DAS1602/12

Power consumption	
+5	1.4 A typical, 2.1 A max
Analog input section	
A/D converter type	ADS7800 successive approximation
Resolution	12 bits
Programmable ranges	
CIO-DAS1601/12	±10V, ±1V, ±0.1V, ±0.01V, 0 to 10V, 0 to 1V, 0 to 0.1V, 0 to 0.01V
CIO-DAS1602/12	±10V, ±5V, ±2.5V, ±1.25V, 0 to 10V, 0 to 5V, 0 to 2.5V, 0 to 1.25V
A/D pacing	Programmable: external source (DIn0, positive edge) or internal counter (positive or negative edge, jumper-select able) or software-polled
Burstmode	4 µs
Data transfer	From 512 sample FIFO via interrupt, DMA, DT-Connect to external memory board or software polled
Polarity	Unipolar/Bipolar, switch selectable
Number of channels	8 differential or 16 single-ended, switch selectable
Interrupts	2 to 7
Interrupt enable	Programmable
Interrupt sources	End-of-conversion, terminal count (DMA)
DMA	Channel 1 or 3
Trigger sources	External hardware/software (DIn0)
A/D conversion time	3.3 µs
Throughput	
DMA	160 kHz
DT-Connect (multi-channel)	250 kHz
DT-Connect (single-channel)	330 kHz
Differential Linearity error	±1 LSB
Integral Linearity error	±1 LSB
No missing codes guaranteed	12 bits
Gain drift	±60 ppm/°C
Zero drift	±160 ppm/°C
Input leakage current (@25 Deg C)	200 nA
Input impedance	Min 10 Megohms
Absolute maximum input voltage	±35V

Analog Output:

Resolution	12 bits
Number of channels	2
D/A type	MX7548
Voltage Ranges	±10V, ±5V, 0 to 5V, 0 to 10V or user defined range between 0 and 10V. Each channel independently configurable by jumpers.
Offset error	Trimmable to 0 by potentiometer
Gain error	Trimmable to 0 by potentiometer
Differential nonlinearity	±1 LSB max
Integral nonlinearity	±1 LSB max
Monotonicity	Guaranteed monotonic
D/A pacing	Software paced
Data transfer	Double buffered software transfer, update on write to MSB register.
Throughput	System dependent, software paced.
Slew Rate	0.3V/µs
Current Drive (OP07)	±5 mA min
Output short-circuit duration	Indefinite
Output coupling	DC
Output impedance	0.1 Ohms max
Miscellaneous	Double-buffered output latches

Digital Input / Output

Digital Type (Digital I/O connector)	82C55 (not applicable on -P5 versions)
Configuration	2 banks of 8, 2 banks of 4, programmable by bank as input or output
Number of channels	24 I/O
Output High	3.0 volts min @ –2.5 mA
Output Low	0.4 volts max @ 2.5 mA
Input High	2.0 volts min, 5.5 volts absolute max
Input Low	0.8 volts max, –0.5 volts absolute min

Digital Type (Main analog connector)	
Output	74LS197
Input	74LS244
Configuration	4 fixed input, 4 fixed output
Number of channels	8
Output High	2.7 volts min @ –0.4 mA
Output Low	0.5 volts max @ 8 mA
Input High	2.0 volts min, 7 volts absolute max
Input Low	0.8 volts max, –0.5 volts absolute min

Counter section

Counter type	82C54
Configuration	3 down-counters, 16 bits each

- Counter 0 - Independent, user configurable
  - Source: Programmable - Internal 100 kHz or external (CTR0 Clock In)
  - Gate: External (DIn2)
  - Output: Available at user connector (CTR0 Out)
- Counter 1 - ADC Pacer Lower Divider
  - Source: 1 or 10 MHz oscillator (jumper selectable)
  - Gate: Tied to Counter 2 gate, programmable source.
  - Output: Chained to Counter 2 Clock.
- Counter 2 - ADC Pacer Upper Divider
  - Source: Counter 1 Output.
  - Gate: Tied to Counter 1 gate, programmable source.
  - Output: ADC Pacer clock

Clock input frequency	10 MHz max
High pulse width (clock input)	30 ns min
Low pulse width (clock input)	50 ns min
Gate width high	50 ns min
Gate width low	50 ns min
Input low voltage	0.8V max
Input high voltage	2.0V min
Output low voltage	0.4V max
Output high voltage	3.0V min

Environmental

Operating temperature range	0 to 50°C
Storage temperature range	−20 to 70°C
Humidity	0 to 90% non-condensing
Weight	11.2 oz. (320g)

9.2 CIO-DAS1602/16

Power consumption

+5	1.4 A typical, 2.1 A max

Analog input section

A/D converter type	ADS7805 successive approximation
Resolution	16 bits
Programmable ranges	±10V, ±5V, ±2.5V, ±1.25V, 0 to 10V, 0 to 5V, 0 to 2.5V, 0 to 1.25V
A/D pacing	Programmable: external source (Din0, positive edge) or internal counter (positive or negative edge, jumper-selectable) or software-polled
Burstmode	13.3 µs
Data transfer	From 512-sample FIFO via interrupt, DMA, DT-Connect to external memory board or software polled
Polarity	Unipolar/Bipolar, switch selectable

Current Transducer LA 55-P/SP1

I_{PN} = 50 A

For the electronic measurement of currents : DC, AC, pulsed..., with a galvanic isolation between the primary circuit (high power) and the secondary circuit (electronic circuit).

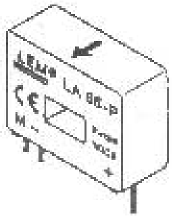

Electrical data

I_{PN}	Primary nominal r.m.s. current	50	A
I_P	Primary current, measuring range	0 .. ± 100	A

R_M	Measuring resistance @		T_A = 70°C		T_A = 85°C		
			$R_{M\,min}$	$R_{M\,max}$	$R_{M\,min}$	$R_{M\,max}$	
	with ± 12 V	@ ± 50 A_{max}	0	215	0	210	Ω
		@ ± 100 A_{max}	0	35	0	30	Ω
	with ± 15 V	@ ± 50 A_{max}	0	335	30	330	Ω
		@ ± 100 A_{max}	0	95	30	90	Ω

I_{SN}	Secondary nominal r.m.s. current	25	mA
K_N	Conversion ratio	1 : 2000	
V_C	Supply voltage (± 5 %)	± 12 .. 15	V
I_C	Current consumption	10 (@ ± 15V) + I_S	mA
V_d	R.m.s. voltage for AC isolation test, 50 Hz, 1 mn	2.5	kV

Accuracy - Dynamic performance data

X	Accuracy @ I_{PN} , T_A = 25°C	@ ± 15 V (± 5 %)	± 0.65	%
		@ ± 12 .. 15 V (± 5 %)	± 0.90	%
ε_L	Linearity		< 0.15	%

			Typ	Max	
I_O	Offset current @ I_P = 0, T_A = 25°C			± 0.10	mA
I_{OM}	Residual current [1] @ I_P = 0, after an overload of 3 x I_{PN}			± 0.15	mA
I_{OT}	Thermal drift of I_O	0°C .. + 70°C	± 0.05	± 0.25	mA
		- 25°C .. + 85°C	± 0.05	± 0.30	mA

t_{ra}	Reaction time @ 10 % of $I_{P\,max}$	< 500	ns
t_r	Response time [2] @ 90 % of $I_{P\,max}$	< 1	μs
di/dt	di/dt accurately followed	> 200	A/μs
f	Frequency bandwidth (- 1 dB)	DC .. 200	kHz

General data

T_A	Ambient operating temperature		- 25 .. + 85	°C
T_S	Ambient storage temperature		- 40 .. + 90	°C
R_S	Secondary coil resistance @	T_A = 70°C	145	Ω
		T_A = 85°C	150	Ω
m	Mass		18	g
	Standards [3]		EN 50178	

Features

- Closed loop (compensated) current transducer using the Hall effect
- Printed circuit board mounting
- Insulated plastic case recognized according to UL 94-V0.

Special features

- I_P = 0 .. ± 100 A
- K_N = 1 : 2000.

Advantages

- Excellent accuracy
- Very good linearity
- Low temperature drift
- Optimized response time
- Wide frequency bandwidth
- No insertion losses
- High immunity to external interference
- Current overload capability.

Applications

- AC variable speed drives and servo motor drives
- Static converters for DC motor drives
- Battery supplied applications
- Uninterruptible Power Supplies (UPS)
- Switched Mode Power Supplies (SMPS)
- Power supplies for welding applications.

Notes :
[1] Result of the coercive field of the magnetic circuit
[2] With a di/dt of 100 A/μs
[3] A list of corresponding tests is available

981130/9

DENVER TECHNICAL
PRODUCTS (PTY) LTD
P.O. Box 75910, Garden View 2047
Tel. (011) 828-2023
Fax (011) 828-2005

LEM

Voltage Transducer LV 20-P

I_{PN} = 10 mA
V_{PN} = 10 .. 500 V

For the electronic measurement of voltages : DC, AC, pulsed..., with a galvanic isolation between the primary circuit (high voltage) and the secondary circuit (electronic circuit).

5 YEARS WARRANTY

CE

Electrical data

I_{PN}	Primary nominal r.m.s. current		10		mA
I_P	Primary current, measuring range		0 .. ± 14		mA
R_M	Measuring resistance		$R_{M\,min}$	$R_{M\,max}$	
	with ± 12 V	@ ± 10 mA $_{max}$	30	190	Ω
		@ ± 14 mA $_{max}$	30	100	Ω
	with ± 15 V	@ ± 10 mA $_{max}$	100	350	Ω
		@ ± 14 mA $_{max}$	100	190	Ω
I_{SN}	Secondary nominal r.m.s. current		25		mA
K_N	Conversion ratio		2500 : 1000		
V_C	Supply voltage (± 5 %)		± 12 .. 15		V
I_C	Current consumption		10 (@±15V)+I_S		mA
V_d	R.m.s. voltage for AC isolation test[1], 50 Hz, 1 mn		2.5		kV

Accuracy - Dynamic performance data

X_G	Overall Accuracy @ I_{PN}, T_A = 25°C	@ ± 12 .. 15 V	± 1.1		%
		@ ± 15 V (± 5 %)	± 1.0		%
C_L	Linearity		< 0.2		%
			Typ	Max	
I_O	Offset current @ I_P = 0, T_A = 25°C			± 0.20	mA
I_{OT}	Thermal drift of I_O	0°C .. + 25°C	± 0.10	± 0.30	mA
		+ 25°C .. + 70°C	± 0.14	± 0.40	mA
t_r	Response time[2] @ 90 % of $V_{P\,max}$		40		µs

General data

T_A	Ambient operating temperature	0 .. + 70	°C
T_S	Ambient storage temperature	- 25 .. + 85	°C
R_P	Primary coil resistance @ T_A = 70°C	250	Ω
R_S	Secondary coil resistance @ T_A = 70°C	110	Ω
m	Mass	22	g
	Standards[3]	EN 50178	

Features

- Closed loop (compensated) voltage transducer using the Hall effect
- Insulated plastic case recognized according to UL 94 V0
- Optimized.

Principle of use

- For voltage measurements, a current proportional to the measured voltage must be passed through an external resistor R_1 which is selected by the user and installed in series with the primary circuit of the transducer.

Advantages

- Excellent accuracy
- Very good linearity
- Low thermal drift
- Low response time
- High bandwidth
- High immunity to external interference
- Low disturbance in common mode

Applications

- AC variable speed drives and servo motor drives
- Static converters for DC motor drives
- Battery supplied applications
- Uninterruptible Power Supplies (UPS)
- Power supplies for welding applications

Notes : [1] Between primary and secondary
[2] R_1 = 25 kΩ (L/R constant, produced by the resistance and inductance of the primary circuit)
[3] A list of corresponding tests is available

010802/0

Dimensions LV 20-P (in mm. 1 mm = 0.0394 inch)

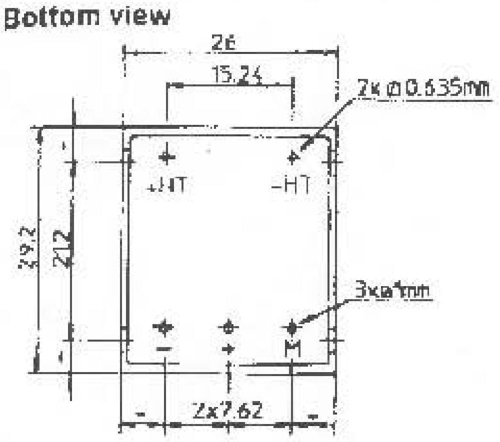
Bottom view

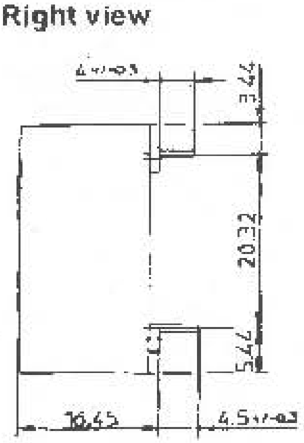
Right view


Top view

Secondary terminals

Terminal + : supply voltage + 12 .. 15 V
Terminal M : measure
Terminal - : supply voltage - 12 .. 15 V

Connection

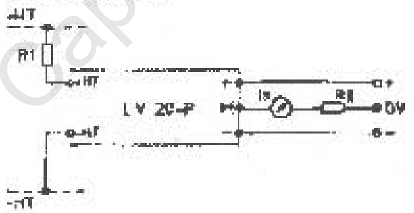

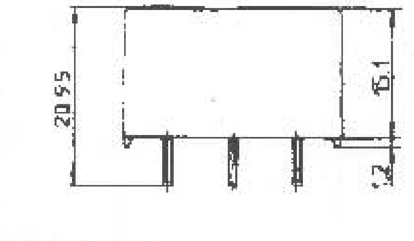

Back view

Mechanical characteristics

• General tolerance	± 0.2 mm
• Fastening & connection of primary	2 pins 0.635 x 0.635 mm
• Fastening & connection of secondary	3 pins Ø 1 mm
• Recommended PCB hole	1.2 mm

Remarks

- I_S is positive when V_P is applied on terminal +HT
- This is a standard model. For different versions (supply voltages, turns ratios, unidirectional measurements ...), please contact us.

Instructions for use of the voltage transducer model LV 20-P

Primary resistor R_1: the transducer's optimum accuracy is obtained at the nominal primary current. As much as possible, R_1 should be calculated so that the nominal voltage to be measured corresponds to a primary current of 10 mA.

Example: Voltage to be measured V_{PN} = 250 V
a) R_1 = 25 kΩ / 2.5 W, I_P = 10 mA Accuracy = ± 1 % of V_{PN} (@ T_A = + 25°C)
b) R_1 = 50 kΩ / 1.25 W, I_P = 5 mA Accuracy = ± 2 % of V_{PN} (@ T_A = + 25°C)

Operating range (recommended): taking into account the resistance of the primary windings (which must remain low compared to R_1, in order to keep thermal deviation as low as possible) and the isolation, this transducer is suitable for measuring nominal voltages from 10 to 500 V.

DENVER TECHNICAL
PRODUCTS (PTY) LTD
P.O. Box 75810, Garden View 2047
Tel. (011) 626-2023
Fax (011) 626 2009

3.1 Table of Physical Sizes: Single phase cores for shell type transformers in GOSS

3.1 Tabelle physikalischer Groessen: Einphasige Kerne fuer Manteltransformator in GOSS

3.1 Tabla de Dimensiones Físicas: Núcleos de una-fase para transformadores de tipo revestido en ASGO (GOSS)

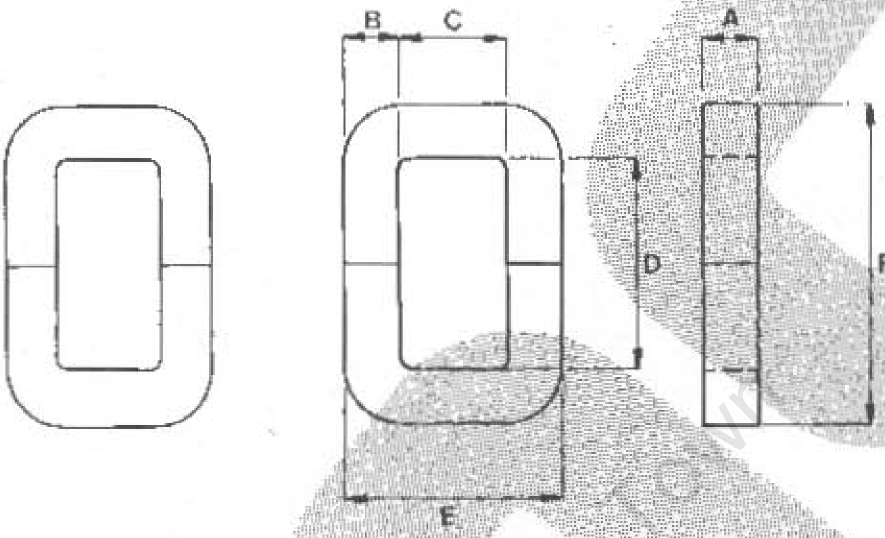

Code or VA/ Set Code oder VA/ Set Código o VA/ Set	V/T at 1.7 Tesla V/T bei 1.7 Tesla V/T a 1.7 Tesla	Nominal Dimensions (mm) Nennabmessungen (mm) Dimensiones Nominales (mm)						Length of Flux Path (cm) Laenge des Kraftflusswegea (cm) Longitud de camino de Flujo (cm)	Nett Area/ Set (cm²) Netto-flaeche/ Set (cm²) Area Neta/ Set (cm²)	Nominal Weight/ Set (kg) Nenn-gewicht/ Set (kg) Peso Nominal/ Set (kg)
		A	B	C	D	E	F			
C 50	0.258	40	9	13	38	33	59	12.4	6.84	0.72
C 100	0.344	40	12	19	54	46	83	17.7	9 12	1,36
C 250	0,430	40	15	26	64	59	100	22.1	11,40	2.10
C 350	0.537	50	15	26	64	59	100	22.1	14.25	2.61
C 500	0.645	60	15	26	64	59	100	22.1	17.10	3.14
C 750	0.716	40	25	30	102	83	158	33.3	19.00	5.29
C 1000	0.895	50	25	30	102	83	158	33.3	23.75	6.61
C 1250	1.074	60	25	30	102	83	158	33.3	28.50	7.94
C 1500	1.343	75	25	30	102	83	158	33.3	35.62	9.93
C 2000	1.656	75	29	30	127	91	193	40.0	41.32	13.60
C 3000	1.719	75	32	40	130	108	204	43.9	45.60	16.32
C 4000	2.041	75	38	40	165	120	252	53.0	54.15	23.27
C 5000	2.450	90	38	40	165	120	252	53.0	64.98	27.94
C 7500	2.450	90	38	42	229	122	317	64.8	64.98	34.50
C10000	3.288	90	51	42	229	148	343	69.8	87.21	49.77
C12000	3.674	90	57	50	270	168	396	82.4	97.47	64.72
C15000	3.997	90	62	50	250	178	386	79.6	106.02	68.78
C20000	4.126	90	64	57	273	189	414	86.3	109.44	76.69

For Bobbins see section 8.1.2

3.2 Economy Range: 0,5 mm NOSS Single Phase C-Cores

It is possible to manufacture cores from non-grain oriented silicon steels for applications where superior magnetic properties are not required e.g. welding transformers. In these cases, the use of NOSS in strip wound cores affords competitive prices to lamination packages, while offering savings in handling and assembly time and improved electric performance. These C-Cores have been designed to suite bobbins used in laminations.

3.2 Preisguenstige Bauserie: Einphasige NOSS C-Kerne, 0,5 mm

Kerne koennen auch aus nicht-kornorientiertem Silizlumstahl hergestellt werden. Diese finden Anwendung in Gebieten, in denen keine hochwertigen magnetischen Eigenschaften noetig sind, z.B. fuer Schweisstransformatoren. NOSS in bandgewickelten Kernen ist preiswert im Vergleich zu Laminierungen; NOSS ist leichter zu behandeln und montieren, und bietet verbesserte elektische Leistung. Diese C-Kerne sind geeignet fuer Spulen, die in Laminierungen verwendet werden.

3.2 Gama Economica: Núcleos "C" Monofásicos: 0,5 mm ANSO* (NOSS)*

Es posible manufacturar núcleos de Acero al Silicio que no poseen Granc Orientado para aplicaciones en dond propiedades magnéticas superiores r son requeridas, por Ej: Transformadores para soldaduras. E estos casos, el úso de acero del tipo ASNO (NOSS) en núcleos laminado de sección cortada permite precios competitivos para laminacion en cantidades, así le ofrece la oportunidad de ahorrar en el tiempo manejo y montaje mejorando el rendimiento eléctrico. Estos núcleos "C" han sido diseñados para la adaptación de bobinas úsadas en laminaciones.

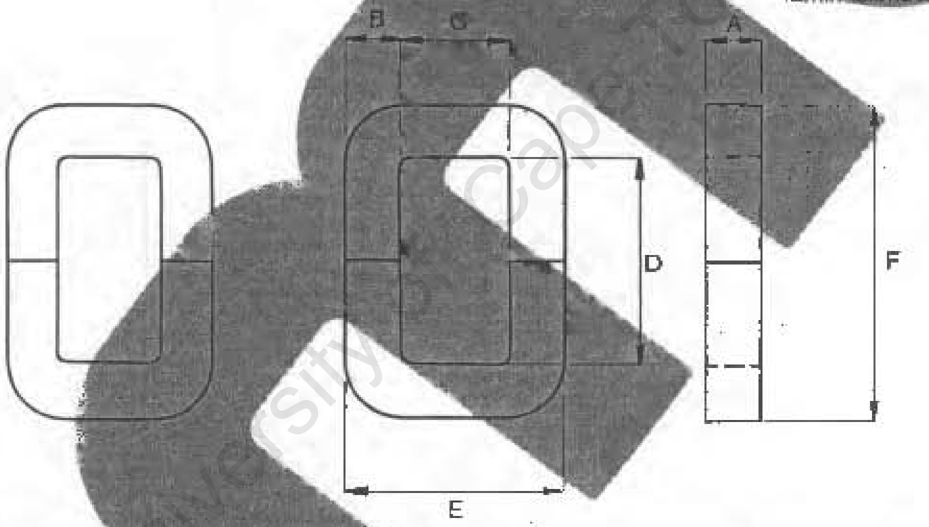

Code or VA/Set Code oder VA/Set Codigo [illegible]	V/T at 1.4 Tesla V/T bei 1.4 Tesla V/T a 1.4 Tesla	Nominal Dimensions (mm) Nennabmessungen (mm) Dimensiones Nominales (mm)						Flux Path (cm) Kraftflussweg (cm) Camino de Flujo (cm)	Area/Set (cm²) Flaeche/Set (cm²) Area/Set (cm²)	Weight/Set (kg) Gewicht/Set (kg) Peso/Set (kg)
		A	B	C	D	E	F			
[illegible]	0.579	40	24.5	35.0	114	87	169	37.5	18.62	5.64
CH1000	[illegible]	50	24.5	35.0	114	87	169	37.5	23.28	7.05
CH1250	0.796	55	24.5	35.0	114	87	169	37.5	25.60	7.75
CH1500	[illegible]	60	24.5	35.0	114	87	169	37.5	27.93	8.46
CH2000	[illegible]	[illegible]	31.0	44.5	121	111	191	42.8	35.34	12.30
CH2500	[illegible]	75	31.0	44.5	121	111	191	42.8	44.18	15.38
CH3000	[illegible]	85	31.0	44.5	121	111	191	42.8	50.07	17.43
CH4000	1.661	[illegible]	37.5	44.5	165	123	250	44.6	53.44	23.27
CH4500	1.882	85	37.5	44.5	165	123	250	44.6	60.56	26.36
CH5000	2.103	95	37.5	44.5	165	123	250	44.6	67.69	29.47

* For Bobbins see P 8 - 5 under code 246

9.0 Performance Curves

9.1 GOSS

Magnetic Properties according to Specifications conforming to AISI* standards.

GOSS is guaranteed in terms of its maximum core loss at either 1.5 T or 1.7 T and at 50 Hz. Induction is guaranteed at 800 A/m.

* American Iron and Steel Institute.

9.0 Leistungsdiagramme

9.1 GOSS

Magnetische Eignenschaften laut Spezifikationen sind conform mit AISA* Normen.

Max. Eisenverlustwerte von GOSS sind auf 1.5 T oder 1.7 T und 50 Hz fixiert. Wir garantieren Induktion bei 800 A/m.

* American Iron and Steel Institute.

9.0 Rendimiento de Curvas

9.1 ASGO* (GOSS)

Propiedades Magnéticas de acuerdo las especificaciones en conformidad con AISI.*

ASGO es garántizado en términos de su pérdida máxima de núcleo a 1,5 T 1,7 T y a 50 Hz. La inducción es garantizada a 800 A/m. A menos que se haya especificado de otra manera ASGO (GOSS) es suministrado con e valor de su pérdida de núcleo a 1,5 T 50 Hz y su valor de inducción a 800 A/m.

* ASGO = Acero al Silicio de Grano Orientado

* GOSS = Grain Oriented Silicon Stee

* AISI = American Iron and Steel Institute.
IAHA = Instituto Americano del Hierro al Acero.

Grade Grad Grado	Thickness (mm) Dicke (mm) Espesor (mm)	Density (g/cm^3) Dicke (g/cm^3) Densidad (g/cm^3)	Max Core Loss at 50 Hz (Watt/kg) Maximaler Kernplattenverlust bei (Watt/kg) Pérdida Maxima de Núcleo (Vátio/kg)		Min Induction at 800 A/m, T Minimale Induktion bei 800 A/m, T Inducción A/M, T a 800 A/m, T
			1.5 T	1.7 T	
M0H	0.3	7.65	0.76	1.05	1.88
M2H	0.3	7.65	0.84	1.17	1.88
M4	0.3	7.65	0.90	1.32	1.80
M5	0.3	7.65	0.97	1.39	1.80

NOTE:
Tests are conducted in accordance with JIS C 2550 - 1986 methods which are practically the same as ASTM A 34 using specimens taken longitudinal to he rolling direction and then annealed o develop full magnetic properties.

ANMERKUNG:
Pruefungen laut JIS C 2250- 1986 Methoden; diese sind fast ASTM A34 gleich. Proben werden aus der Laengsrollrichtung genommen, dann ausgeglueht, um max. magnetische Eigenschaften zu entwickeln.

NOTA:
Los experimentos son llevados a cabo de acuerdo a los métodos JIS C 2550 - 1986, los cuáles son prácticamente los mismos que en ASTM A 34 usando muestras que han sido tomadas longitudinalmente a la dirección del láminador para luego se recocidas desarrollando sus propiedades magnéticas al máximo.

Core Loss (Iron Losses) - 0.3 mm GOSS - Tested at 50Hz

Kern Verlust (Eisenverlust) - 0,3 mm GOSS - Getestet bei 50Hz

Pérdidas de núcleo (Pérdidas de Hierro) - 0.3 mm ASGO (GOSS) Copelado a 50Hz

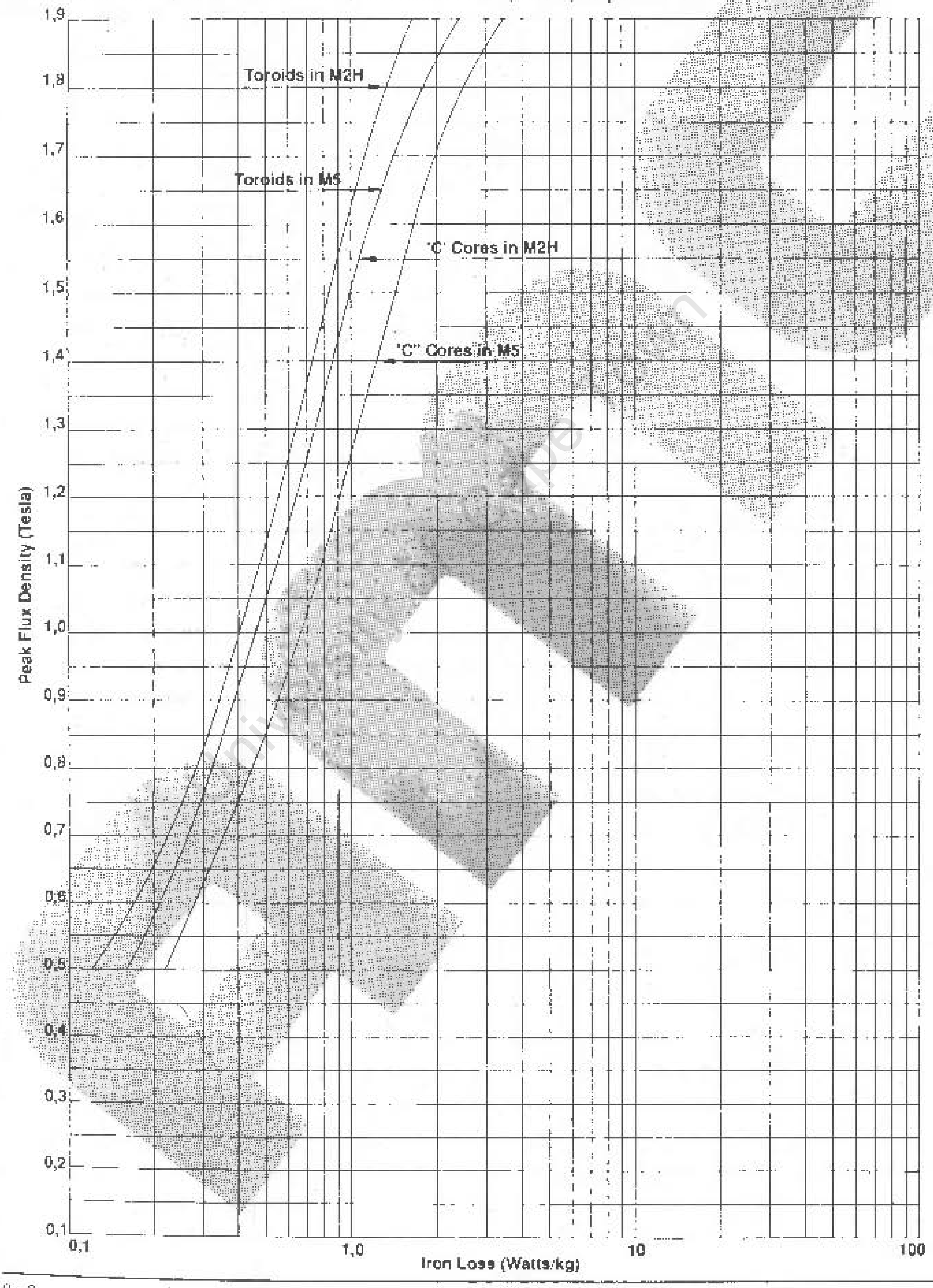

Magnetising Characteristics - Toroids in 0.3 mm GOSS - Tested at 50Hz

Magnetisierung Eigenschaften - Ringkerne mit 0,3 mm GOSS - Getestet bei 50Hz

Caracteristicas Magnétizantes - Toroidales en 0,3 mm ASGO (GOSS) - Copelado a 50Hz

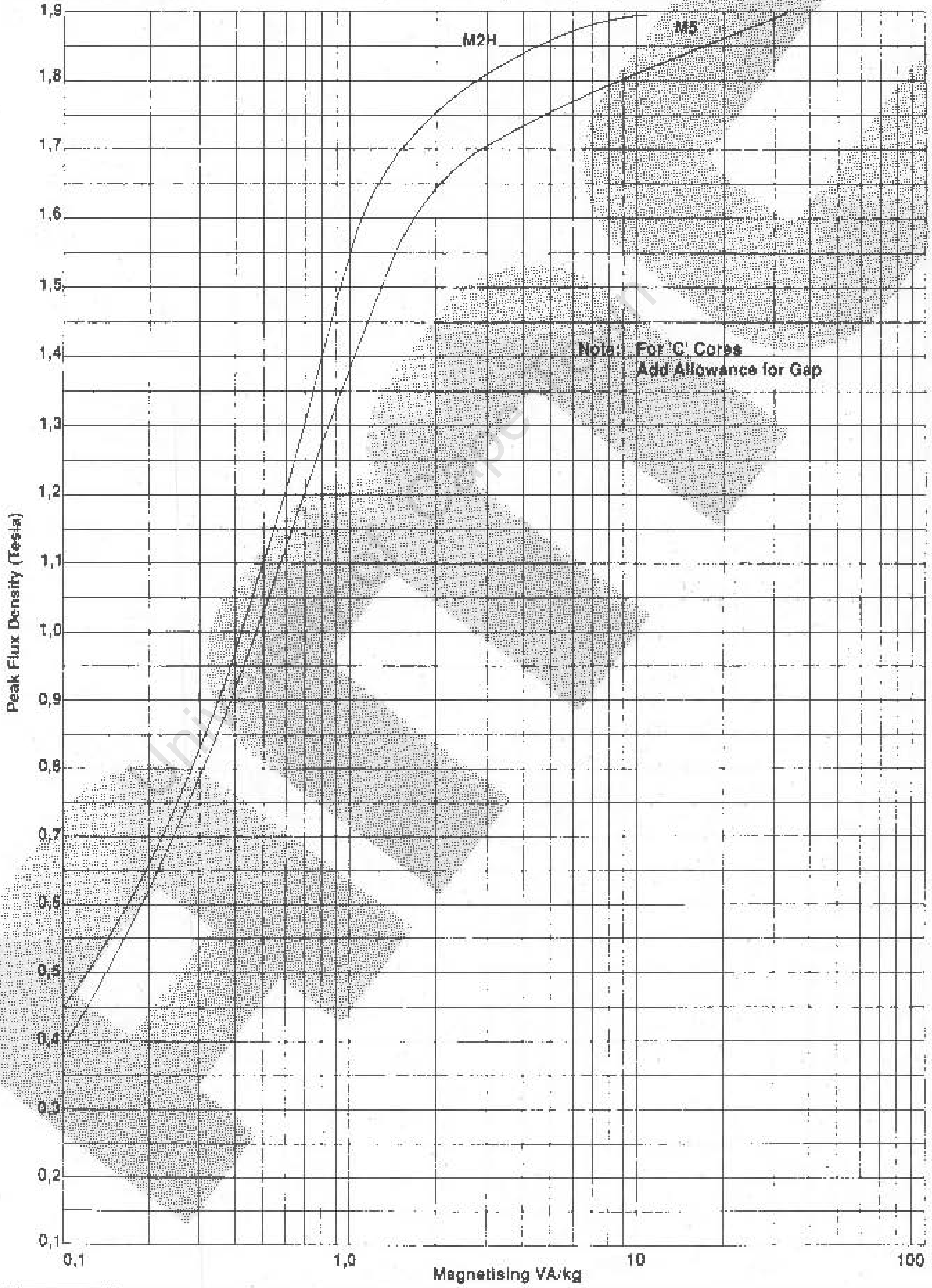

Note: For 'C' Cores
Add Allowance for Gap

Appendix 1.7

Selected photographs

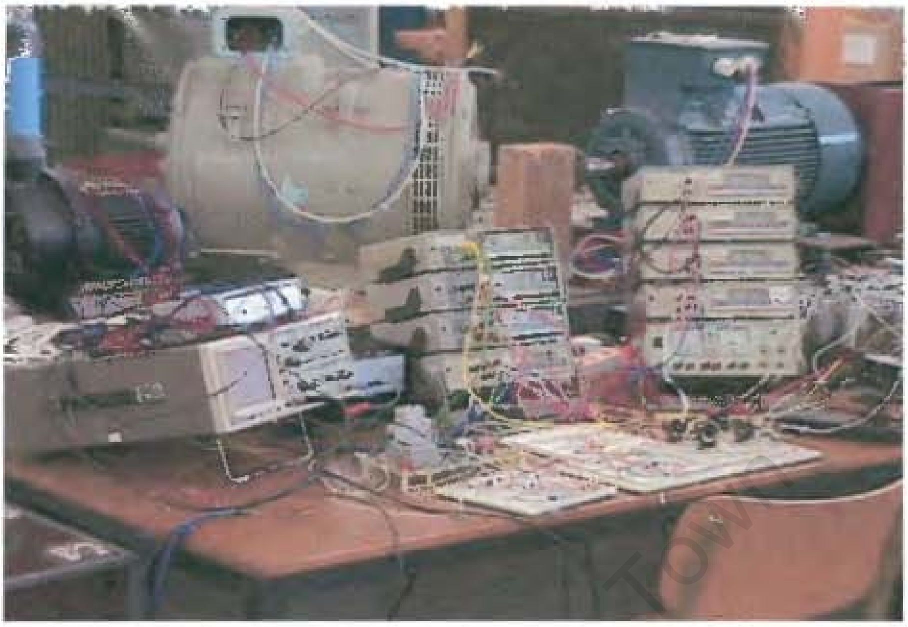

Fig: 7.44 Set up at UCT

Fig: 7.45 Thyristor switched capacitors

Fig: 7.46 Various parts of the Adaptive Converter

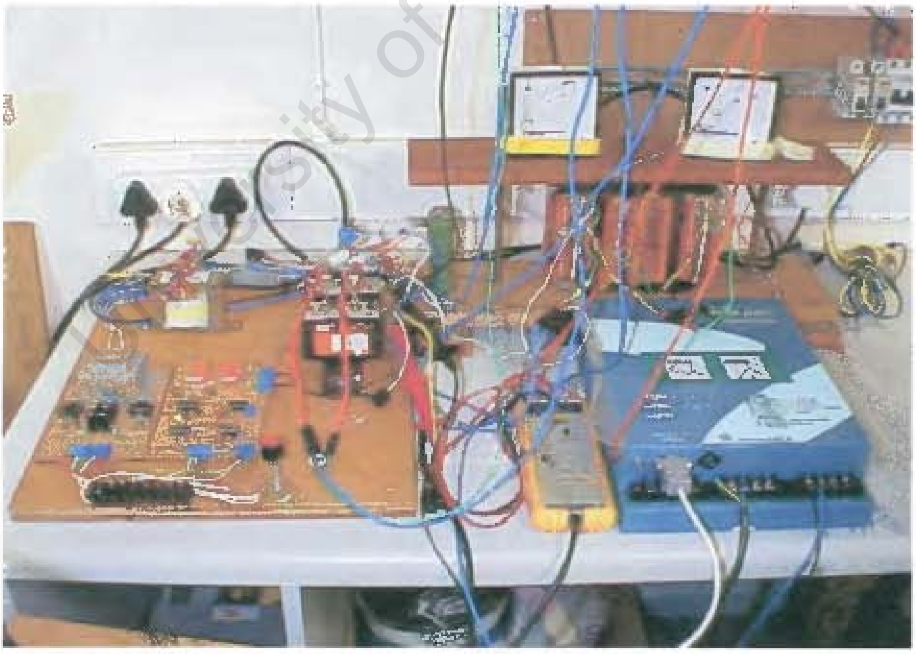

Fig: 7.47 Saturable Reactor and driving circuitry

Fig: 7.48 Data acquisition card

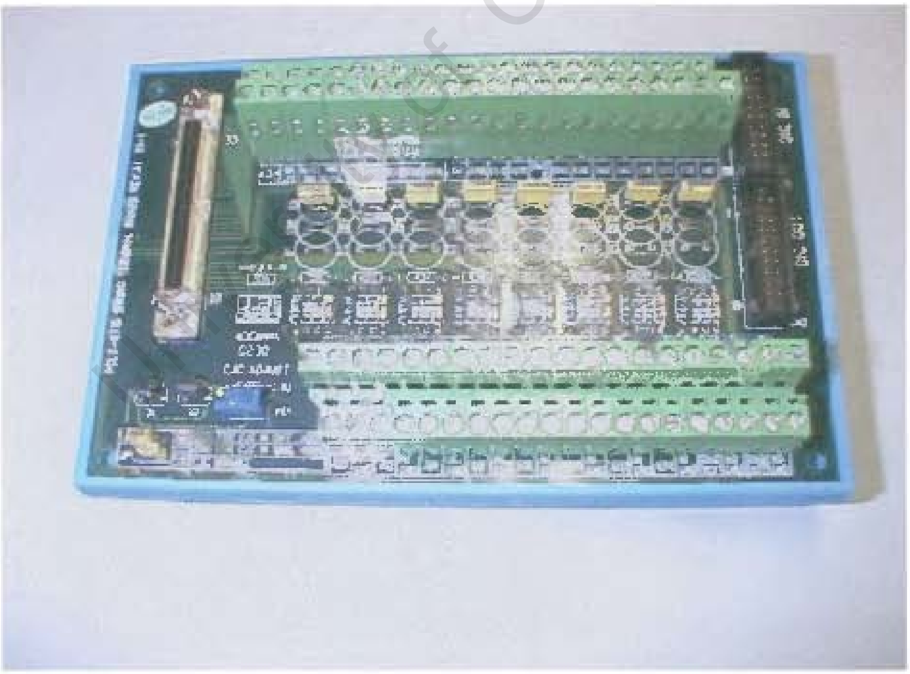

Fig: 7.49 Interfacing hardware and signal conditioning

Fig: 7.50 Saturable reactor

Appendix 1.8

Air-gap analysis and calculations

Introduction of air-gap reduces the permeability by causing the shearing over of the B-H loop and by doing this, effectively, replaces some of the amper-turns provided by the DC coil. Usually, inserting an air-gap is a permanent arrangement and since the objective of this practice is to vary the permeability of the core, air-gapping, was kept as the final tool to fine-tune the core permeability for the final steady state value of the AC coil reactance.

The calculation of the air-gap flux and length is as follows:

$$\Phi = B.A = 0.75 * 0.001 = 0.75 \quad mWb$$

The figure 0.75 T is the selected minimum flux density for the core material and air-gap in the complete absence of DC excitation.

In a magnetic circuit, the reluctance of any section is calculated from:

$$S = \frac{l}{\mu.A}$$

Where l is the average length of the flux path,

Hence for two air-gaps in each loop: $S_{AG} = \dfrac{2l_{AG}}{4\pi.10^{-7} * 0.001}$ At/Wb

$\mu_0 = 4\pi.10^{-7}$ is the permeability of free air.

So for the rest of the core: $S_{CORE} = \dfrac{0.333 - (2l_{AG})}{0.045 * 0.001} = 7400 - \dfrac{2l_{AG}}{4.5 * 10^{-5}}$

The figure 0.045 for permeability is from the B-H graph for B value of 0.75 T.

In general the mmf is related to reluctance and flux by $F = NI = Hl = S\Phi$

Hence: $NI = \Phi(S_{AG} + S_{CORE})$ At

In the complete absence of DC excitation which corresponds to minimum flux,

$$F = 250*1.37 = 0.75*10^{-3}\left(\frac{2.l_{AG}}{4\pi.10^{-7}*0.001} + 7400 - \frac{2.l_{AG}}{4.5*10^{-5}}\right)$$

$$456{,}666.67 - 7400 = \frac{2.l_{AG}}{1.257*10^{-9}} - \frac{2.l_{AG}}{4.5*10^{-5}}$$

$$449{,}266.67 = \frac{l_{AG}(9.0*10^{-5} - 2.514*10^{-9})}{5.6565*10^{-14}} = 1.591*10^{9}\, l_{AG}$$

$$l_{AG} = 2.823*10^{-4} \ m = 0.2823 \ mm$$

Experimentally, 0.3 mm of air-gap optimised the performance of the reactor.